



Kara Stariha, BSc, BEng

**An assessment of set-based joint parameters and their influence
on slope stability: A study of a carbonate outcrop near Kaili,
China**

Master's Thesis

Submitted in fulfilment of the requirements for the degree of

Diplom-Ingenieurin

Master's programme Geotechnical and Hydraulic Engineering

at

Graz University of Technology

Supervisor

Ao.Univ.-Prof. Dr. Qian Liu

Institute for Applied Geosciences

Graz University of Technology

Graz, December 2020

EIDESSTATTLICHE ERKLÄRUNG

AFFIDAVIT

Ich erkläre an Eides statt, dass ich die vorliegende Arbeit selbstständig verfasst, andere als die angegebenen Quellen/Hilfsmittel nicht benutzt, und die den benutzten Quellen wörtlich und inhaltlich entnommenen Stellen als solche kenntlich gemacht habe. Das in TUGRAZonline hochgeladene Textdokument ist mit der vorliegenden Masterarbeit identisch.

I declare that I have authored this thesis independently, that I have not used other than the declared sources/resources, and that I have explicitly marked all material which has been quoted either literally or by content from the used sources. The text document uploaded to TUGRAZonline is identical to the present master's thesis.

21/12/2020

Datum / Date



Unterschrift / Signature

Principle of equality

Due to reasons of legibility, this work does not include gender-specific formulations. It uses gender neutral terms they/them/theirs rather than expressly male pronouns, because it is not difficult to use gender neutral terms in the English language. The use of male expressions implies a subconscious gender bias which is not helpful in promoting gender equality.

Acknowledgements

I have received a great deal of support and assistance throughout the writing of this thesis, without which I would not have been able to complete this massive document.

Firstly, I would like to thank my supportive, enthusiastic and knowledgeable supervisor, Professor Qian Liu. He has been enormously flexible throughout this tumultuous year, and has always provided thorough feedback and a good chat from the other side of the world.

Secondly, I would like to acknowledge my colleagues, who have provided me with motivation and an endless supply of questionable jokes. Thank you so much for getting through my 8 line sentences. Your advice was invaluable. And my sentences are now much shorter.

Finally, I would like to thank my family for putting up with me, and my friends for keeping me sane. I would have had a miserable year without you.

Abstract

Rock mass behaviour is controlled by intact rock properties and by any defects present in the rock mass. When analysing the engineering implications of defects, it is necessary to numerically represent properties including orientation, spacing, persistence, termination, roughness and waviness.

The aim of this thesis was to develop a workflow to detect and characterise defect sets in rock slopes using 3D data sets. The effect of these defects on slope stability was then investigated through a kinematic analysis. The study area comprised a 140 m high sub-vertical carbonate slope face in the Kaili region of southern China. A 3D point cloud and a 3D real scene model were provided.

Three sub-vertical joint sets and one sub-horizontal bedding set were identified across four discrete domains. Defect properties were measured using CloudCompare, and quantified probabilistically. Existing methodologies for orientation and dilation angle measurement were adopted, while methods were proposed for measuring defect spacing and waviness amplitude. Spacing was measured using the “2-point thickness” tool in CloudCompare, along a virtual scanline. Waviness amplitude was measured as the offset from a mean orientation plane. A shear strength reduction back analysis was undertaken in RS3 on a block mould from a recent rockfall. This determined that the dilation angle had been overestimated. Throughout the characterisation process, limitations were found in the use of the available remote sensing data including resolution, noise, and the inability of point clouds to display joint traces.

DIPS was used to determine kinematically admissible failure mechanisms in each domain. Probabilistic analyses of dominant failure mechanisms were then undertaken in RocPlane, SWedge and RocTopple for planar sliding, wedge sliding and toppling respectively. The ability of 2D software to determine failure probability in the Study Area was found to be limited, as the complex slope geometry could not be modelled. As such, only a rough estimation of failure likelihood could be calculated. From the visual inspection of the slope face, the kinematic DIPS analysis, and the probabilistic analysis, it is considered that flexural toppling is the dominant form of failure in most domains. However, backwards toppling, base plane sliding/toppling and wedge sliding are also present.

Whilst the probabilistic analysis does not accurately reflect the likelihood of potential failure mechanisms, the problem does not rest purely with either the dataset or the analysis procedure. Rather, the dataset would lend itself to a different probabilistic method, capable of considering complex slope geometries and sub-vertical joint sets. This may include a 3D DEM analysis. The applied probabilistic method would be appropriate for a dataset with a simple slope geometry and non-vertical joint sets.

Kurzfassung

Das felsmechanische Verhalten von Gesteinsmassen wird durch die Eigenschaften des intakten Gesteins und durch eventuelle Trennflächen in der Gesteinsmasse bestimmt. Bei der Analyse der ingenieurtechnischen Auswirkungen von Trennflächen ist es notwendig, Eigenschaften wie Orientierung, Abstand, Persistenz, Termination, Rauigkeit und Welligkeit numerisch zu erfassen.

Das Ziel dieser Arbeit war es, einen Workflow zur Erkennung und Charakterisierung von Trennflächengefüge in Felsböschung anhand von den Datensätzen aus der Fernerkundung zu entwickeln. Die Auswirkung dieser Trennflächen auf die Hangstabilität wurde dann durch eine kinematische Analyse untersucht. Das Untersuchungsgebiet umfasste eine 140 m hohe, subvertikale Böschung aus karbonatischen Gesteinen in der Region Kaili in Südchina. Eine 3D-Punktwolke und ein 3D-Modell der realen Szene wurden erstellt.

Drei subvertikale Kluftscharen und eine subhorizontale Schichtungsschar wurden über vier diskrete Bereiche identifiziert. Die Trennflächeneigenschaften wurden mit CloudCompare gemessen und probabilistisch quantifiziert. Bestehende Methoden zur Messung der Orientierung und des Dilatationswinkels wurden übernommen, während die Methoden zur Messung des Kluftabstands und der Welligkeitsamplitude neu bearbeitet wurden. Der Abstand wurde mit dem Werkzeug "2-Point Thickness" in CloudCompare entlang einer virtuellen Scanlinie gemessen. Die Welligkeitsamplitude wurde als Offset von einer mittleren Orientierungsebene gemessen. Eine Rückanalyse der Scherfestigkeit wurde in RS3 an einer Blockform aus einem kürzlich erfolgten Felssturz durchgeführt. Dabei wurde festgestellt, dass der Dilatationswinkel während der digitalen Charakterisierung überschätzt worden. Während des gesamten Charakterisierungsprozesses wurden auch Einschränkungen bei der Verwendung der verfügbaren Fernerkundungsdaten festgestellt, inklusive den von Auflösung und Rauschen der Punktwolke bedingten Schwierigkeiten sowie der Unfähigkeit, aus Punktwolken Trennflächenspuren objektiv zu erfassen.

DIPS wurde verwendet, um kinematisch zulässige Versagensmechanismen in jedem Bereich zu bestimmen. Probabilistische Analysen der dominanten Versagensmechanismen wurden dann in RocPlane, SWedge und RocTopples für Planargleiten, Keilgleiten sowie Kippen durchgeführt. Die Fähigkeit der 2D-Software, die Versagenswahrscheinlichkeit im Untersuchungsgebiet zu bestimmen, erwies sich als begrenzt, da die komplexe Hanggeometrie nicht modelliert werden konnte. Daher konnte nur eine grobe Schätzung der Versagenswahrscheinlichkeit berechnet werden. Aus der visuellen Inspektion in dem 3D-

Modell der realen Szene, der kinematischen DIPS-Analyse und der probabilistischen Analyse geht es hervor, dass das Biegekippen in den meisten Bereichen die dominierende Versagensform ist. Allerdings sind auch Rückwärtskippen, Gleiten/Kippen auf der Schichtungsfläche sowie Keilgleiten entlang den Klufscharen vorhanden.

Während die probabilistische Analyse die Wahrscheinlichkeit potenzieller Versagensmechanismen nicht genau wiedergibt, liegt das Problem nicht nur am Datensatz oder am Analyseverfahren. Vielmehr würde sich der Datensatz für eine andere probabilistische Methode eignen, die in der Lage ist, komplexe Hanggeometrien und subvertikale Trennflächenscharen zu berücksichtigen. Dies kann mittels einer 3D-DEM-Analyse bewerkstelligt werden. Die angewandte probabilistische Methode wäre für einen Datensatz mit einer einfachen Hanggeometrie und nicht vertikalen Trennflächen geeignet.

Table of Contents

1	Introduction	21
1.1	Study Area	21
2	Literature Review	24
2.1	Data Collection and Measurement	24
2.1.1	Photogrammetry.....	25
2.1.2	Data Presentation.....	25
2.1.2.1	Point Clouds	25
2.1.2.2	Meshed Surfaces.....	27
2.1.2.3	Combined Datasets	28
2.1.3	Types of Processing.....	28
2.2	Geology of the Study Area	29
2.2.1	Karst Terrain	30
2.3	Genesis and Properties of Defects	32
2.3.1	Genesis and Nature of Defects.....	32
2.3.2	Joint Sets	33
2.3.3	Orientation.....	34
2.3.3.1	Measurement.....	34
2.3.3.1.1	Compass	35
2.3.3.1.2	FACETS	35
2.3.3.2	Analysis	36
2.3.3.2.1	Terzaghi Weighting.....	37
2.3.4	Spacing.....	38
2.3.4.1	Measurement.....	39
2.3.4.2	Analysis	40
2.3.5	Persistence and Geometry	40
2.3.5.1	Measurement.....	42
2.3.5.2	Analysis	42
2.3.5.3	Termination.....	42
2.3.6	Roughness and Waviness.....	43
2.3.6.1	Surface Condition	45
2.3.7	Sources of Error in Quantification.....	45
2.4	Shear Strength Assessment.....	47
2.4.1	Influences on Shear Strength	48

2.4.2	Numerical Definition of Shear Strength.....	51
2.4.3	Shear Strength Reduction Technique.....	51
2.4.4	SSR Analysis in RS3.....	52
2.5	Kinematic Analysis.....	53
2.5.1	Planar Sliding.....	54
2.5.2	Wedge Sliding.....	54
2.5.3	Toppling.....	55
2.5.4	Probabilistic Analysis.....	58
3	Data Collection and Processing	59
3.1	Data Collection.....	59
3.2	Processing.....	60
4	Characterisation of Defect Sets	63
4.1	Method of Orientation Measurement.....	63
4.2	Set Definition.....	70
4.2.1	Definition of Joint Sets.....	70
4.2.2	Segmentation of the Point Cloud.....	73
4.3	Domain Definition.....	75
4.4	Orientation.....	79
4.4.1	Joint Set Orientation.....	79
4.4.2	Bedding.....	81
4.5	Spacing.....	84
4.5.1	Virtual Scanline Method.....	84
4.5.1.1	Results.....	86
4.5.1.2	Sources of Error.....	94
4.5.2	Measurement of Fallen Blocks.....	96
4.6	Persistence.....	100
4.7	Roughness and Waviness.....	102
4.7.1	Joint Waviness.....	102
4.7.2	Joint Amplitude.....	102
4.7.2.1	Sources of Error.....	105
4.7.2.2	Comparisons with Existing Methods.....	109
4.7.3	Dilation Angle.....	110
4.7.3.1	Sources of Error.....	114
4.8	Defect Set Characteristics.....	116
4.8.1	Joint Nature and Formation.....	116
4.8.2	Numerical Characterisation Summary.....	117

4.8.3	Visualisation	117
5	Joint Shear Strength Assessment	119
5.1	Rockfall Reconstruction.....	119
5.1	RS3-SSR Analysis of Block 1.....	126
5.1.1	Model Definition.....	126
5.1.2	Results	130
5.1.3	Additional Analysis	133
6	Kinematic Analysis	135
6.1	DIPS Analysis	135
6.1.1	Domain D1	138
6.1.2	Domain D2	140
6.1.3	Domain D3	142
6.1.4	Domain D4	145
6.2	Probabilistic Analysis.....	147
6.2.1	Planar Sliding (RocPlane)	149
6.2.2	Wedge Sliding (SWedge)	150
6.2.3	Toppling Failure (RocTopple)	153
7	Conclusion	158
7.1	Characterisation of Defect Sets.....	158
7.2	Shear Strength Reduction Analysis.....	163
7.3	Kinematic Analysis	163
7.4	Potential Future Works.....	166
8	Bibliography	168
	Appendix A – RS3 SSR Analysis	172
	Appendix B – DIPS Kinematic Analysis	173
	Appendix C – RocPlane Probabilistic Assessment	174
	Appendix D – SWedge Probabilistic Assessment	175
	Appendix E – RocTopple Probabilistic Assessment	176

List of Figures

Figure 1-1: Location of Study Area in the Guizhou Province of southern China (Google Earth Pro, 2014-2020).....	22
Figure 1-2: Surveyed outcrop locations. The Study Area is located at “JK1” (Google Earth Pro, 2014-2020).....	22
Figure 1-3: Outcrop JK1, looking south. Study Area outlined in red.	23
Figure 2-1: Definition of the HSV colouring scheme proposed by Liu and Kaufmann (2015); a) the HSV colour cone; b) the HSV colour wheel; and c) representation of HSV coloured fractures, representing their geometry.	27
Figure 2-2: Distribution of karst types in southern China (Yuan, et al., 1995). Approximate location of Study Area indicated in red.....	30
Figure 2-3: Development of an inception doline with drainage focused by a cherty lens (Sauro, 2003). Drainage may also be focused by changes in lithology.	31
Figure 2-4: Proportional error of the Terzaghi correction factor for linear and planar sampling (Wang & Mauldon, 2006).....	38
Figure 2-5: Traces produced by sets of defects intersecting a plane surface (Liu, 2019); a) Persistent defect planes; b) Intermittent defect planes; c) Separately impersistent defect planes.....	41
Figure 2-6: Termination of joint sets (Liu, 2019).....	43
Figure 2-7: a) Diagram displaying the various features of a rough defect (Marcher & Potsch, 2019); and b) diagram displaying measurement of the first and second order irregularities, relative to the shear plane (Marcher & Potsch, 2019).....	44
Figure 2-8: The effect of surface roughness and normal stress on the friction angle of a discontinuity surface (Wyllie & Mah, 2004).....	50
Figure 2-9: Planar failure model (Norrish & Wyllie, 1996).....	54
Figure 2-10: Stereographic method of kinematic analysis; a) Planar sliding, with pole vectors; b) Wedge sliding, with intersection points.	55
Figure 2-11: Wedge failure model (Norrish & Wyllie, 1996).....	55
Figure 2-12: a) Direct toppling; and b) Flexural toppling (Hudson & Harrison, 1997).....	56
Figure 2-13: Sliding and toppling instability of a block on an inclined plane (Hoek & Bray, 1977).....	57

Figure 2-14: Stereographic method of Kinematic analysis (RocScience, 2020); a) Flexural toppling, with pole vectors; b) Direct toppling, with intersection points.	57
Figure 3-1: Representation of drone flight path and cloud of images.....	60
Figure 3-2: Point cloud from SfM, in Context Capture, looking south, top to first bench only. Viewed in Cloud Compare.	61
Figure 3-3: Rendered 3D real scene model, looking south, viewed in ContextCapture	61
Figure 3-4: Point cloud from SfM, in Context Capture, from above, top to first bench only. Viewed in Cloud Compare.	62
Figure 3-5: Rendered 3D real scene model, from above, viewed in ContextCapture	62
Figure 4-1: Study Area, with rockfill zone shown in red.	63
Figure 4-2: Delineation of "Rockfall Area". Regions with vegetation cover obscuring the rock surface have been excluded from the analysis, and are outlined in white.	64
Figure 4-3: Point cloud of Rockfall Area - colours indicating the orientation of Hough's Normal for each point.....	64
Figure 4-4: Location of measurement points from the Compass tool within the Rockfall Area	65
Figure 4-5: Output from the FACETS FM tool. Colours indicate the dip and dip direction of each facet.	67
Figure 4-6: Output from the FACETS Kd tool. Colours indicate the dip and dip direction of each facet.	67
Figure 4-7: Stereographic plot of measurements taken from the Rockfall Area point cloud. Processed in DIPS 8.0, without (left) and with (right) Terzaghi weighting. Data set obtained in CloudCompare from a) the Compass plugin, b) the FACETS FM plugin, and c) the FACETS Kd plugin, displaying only facets with a surface area $>0.5 \text{ m}^2$. All density contours set from 0 (white) to 10 (red).	69
Figure 4-8: Stereographic projection of measurements taken within the Study Area; a) no weighting applied; b) Terzaghi weighting applied. All density contours set from 0 (white) to 10 (red).	71
Figure 4-9: Sets defined on the stereographic projection of measurements taken within the Study Area. J1 (green), J2 (blue), J3 (red), and Bedding (grey). Confidence cones of 1 and 3 standard deviations displayed. All density contours set from 0 (white) to 10 (red).	71
Figure 4-10: Comparison of defined joint sets with orientation measurements taken from within the Rockfall Area. All density contours set from 0 (white) to 10 (red).	72

Figure 4-11: Segregated point clouds deflecting the processed joint sets, looking south. Viewed in Cloud Compare.	74
Figure 4-12: Hough-Normal colouring for each joint set.	75
Figure 4-13: Additional measurement planes, looking south.	75
Figure 4-14: Stereographic projection of measurements taken within the Study Area, with symbols representative of horizontal distance from west to east.	76
Figure 4-15: Occurrence of sets with horizontal distance and domain, where positive values are to the east, and negative values are to the west. a) J1; b) J2; c) J3	77
Figure 4-16: The four defined domains, looking south.....	78
Figure 4-17: Defect orientation measurements for each domain. Site-wide set windows shown for comparison. a) D1; b) D2; c) D3; d) D4.....	79
Figure 4-18: Comparison of mean poles by domain. Cones of confidence for the 95 th percentile displayed.	80
Figure 4-19: a) HSV colour wheel with overlay of proposed bedding set; b) Colour wheel applied to bedding points for visualisation purposes. Each colour represents a range of 60 ° in dip direction. All points have a dip between 0° and 30 °.....	82
Figure 4-20: Variation in bedding orientation a) on a large scale, viewed facing south; b) on a small to medium scale (viewed from above). Black box on a) represents the location of b).	82
Figure 4-21: Study Area (facing south) showing all points with dip less than 30°. Planes fit through traces of bedding planes visible in slope face.	83
Figure 4-22: Stereographic projections of bedding measurements; a) small-scale using the Compass tool; b) large scale, using surface traces with the Trace tool.	83
Figure 4-23: Virtual scanlines, sub-horizontal, striking as per slope face for each domain. Looking south.	84
Figure 4-24: Sketch comparing measurement lengths taken of defects (black) along a horizontal scanline (red) using the methodology of; a) the 1-point thickness tool; and b) the 2-point thickness tool.	85
Figure 4-25: Measurement of defect spacing along scanlines for Joint Set J1 within region D4, measured using the 2-point thickness tool along 5 horizontal scanlines. Facing along strike of Joint Set J1.....	86
Figure 4-26: Measurement of spacing for joint sets parallel to the slope face, Joint Set J2 in Domain D1, with increasing viewing rotation to fully display measurement locations. a)	

viewed from horizontal; b) viewed from approximately 30° from horizontal; c) viewed from approximately 70° from horizontal; d) vertical view.....	87
Figure 4-27: Histogram of scanline measured defect spacing, adopted upperbound limit marked in red; a) Joint Set J1; b) Joint Set J2; c) Joint Set J3; d) Bedding	91
Figure 4-28: Histograms representing defect spacing for each joint set, separated by domain. a) Joint Set J1. Not present in D2; b) Joint Set J2. Not present in D4; c) Joint Set J3. Not present in D1.	93
Figure 4-29: Comparison of defect visibility/apparent persistence in region D2 using a) CloudCompare point cloud; and b) ContextCapture 3D real scene model.....	95
Figure 4-30: Visible blocks from recent rockfalls; a) View of talus from above; b) Visible blocks >2 m, from top bench – looking south-east; c) Visible blocks >2 m, from base of slope – looking south-east;.....	97
Figure 4-31: Measured block dimensions blocks with one dimension above 2 m; a) face length; b) face area; c) block volume.	98
Figure 4-32: Markup of interpreted joint persistence; a) Joint Set J1, within Domain D4; b) Joint Set J3, within Domain D2; c) Joint Set J2, within domains D2 and D3. Note that the change in apparent dip of the joint set is due to the change in slope face orientation between Domain D2 and D3.	101
Figure 4-33: Measurement of amplitude above and below the mean plane line, with measurement points indicated in blue (Joint Set J2, plane 1); a) looking along plane strike; and b) looking directly at the plane face. The dashed line displays the extents of the point cloud which define the joint face.	103
Figure 4-34: Comparison of maximum amplitude (a) compared to measurement length (b).	106
Figure 4-35: Amplitude vs. Measurement area.....	106
Figure 4-36: J2 Plane 6; a) Showing only segmented point cloud from main joint set (J2), gaps visible; b) All defined (and segmented) joint sets showing. Small segment of Joint Set J3 (red) filling some of the gaps, additional gaps still present; c) Unsegmented point cloud, coloured by Hough Normal of each point;	108
Figure 4-37: Amplitude measurements using straight edge method (blue) and mean plane method (red).....	109
Figure 4-38: The Hough normal of each point on Plane 1 of Joint Set J2 plotted on a stereonet, where the plotted normals reflect surface roughness and the dilation angle is taken as the 95 th percentile variability cone (centre) from the mean joint plane.....	110

Figure 4-39: Peak dilation angle vs. measurement area for all joint sets	111
Figure 4-40: Stereonet plot of pole normals for Plane 6, Domain D2, Joint Set J2, showing the 68 th , 95 th and 98 th percentile variability cones; a) Plotting point normals from set J2 only; b) Plotting point normals from unsegmented point cloud.....	115
Figure 4-41: An example of a statistically possible rock mass, based on probabilistically defined parameters.....	118
Figure 5-1: Historic aerial imagery of the Rockfall Area; a) from December 2016; and b) from December 2017 (Google Earth Pro, 2014-2020).....	119
Figure 5-2: Horizontal layers, defined based on the nature of bedding.....	120
Figure 5-3: Interpolation of blocks which may have failed in the recent rockfall event along the bottom bed (plan view). Green blocks represent those which are considered likely to have fallen. Yellow blocks represent those which may have fallen based on the December 2016 profile, but were likely to have been attached to an observed joint surface.	122
Figure 5-4: Interpolation of blocks which may have failed in the recent rockfall event along the middle bed (plan view). Green blocks represent those which are considered likely to have fallen. Yellow blocks represent those which may have fallen based on the December 2016 profile, but were likely to have been attached to an observed joint surface.	123
Figure 5-5: Interpolation of blocks which may have failed in the recent rockfall event along the top bed (plan view). Green blocks represent those which are considered likely to have fallen. Yellow blocks represent those which may have fallen based on the December 2016 profile, but were likely to have been attached to an observed joint surface.	124
Figure 5-6: Side views of Block 1; a) as a point cloud in CloudCompare, with planes defining surface orientation; b) modelled block in RS3, with grey representing the rock mass, and red representing Block 1.....	126
Figure 5-7: Top view of Block 1; a) as a point cloud in CloudCompare, with planes defining surface orientation; b) with the extended planar joint surfaces imported into the RS3 model; c) Rock mass volume segmented along the joint surface in RS3. Block 1 shown in red.	127
Figure 5-8: Oriented view of Block 1 in RS3; a) with restraints applied at the back, base and sides of the model; b) with a 10-Noded Tetrahedra graded mesh	129
Figure 5-9: Displacement from completed RS3 SSR analysis, at failure with a SRF of 1.07. a) Total displacement, from 0 (blue) to 0.0035 m (red); b) x displacement, from -0.00049 m (blue) to 0.0012 m (red); c) y displacement, from 0 m (blue) to 0.0017 m (red); and d) z displacement, from -0.0031 m (blue) to 0 m (red).	131
Figure 5-10: combined meshes including the joint surface from remote imagery (blue), with	

the two planes projected past the edges of the plane, to ensure they properly intersect the slope volume; a) at full resolution, and b) at a reduced resolution, with 1000 points across the joint surface only.....	133
Figure 5-11: Rock mass block, and Block 1 wedge, defined by a reduced resolution surface. Mesh is a 10 noded tetrahedral, graded, with x,y,z restraints applied at the base, back and sides. The SSR region for analysis was trimmed directly around Block 1 to reduce processing time.....	134
Figure 5-12: Oriented view of Block 1 in RS3; a) with the full resolution surface mesh; b) with the reduced resolution surface mesh.....	134
Figure 6-1: Kinematic analysis undertaken in DIPS for Domain D1. Friction angle of 48, quantity of data points scaled based on relative joint quantity. a) Planar sliding; b) Wedge sliding; c) Flexural toppling; d) Direct toppling.	138
Figure 6-2: Example of wedge and toppling failure in Domain D1 along Joint Sets J1/J2 (green/blue) and J2 (blue) respectively. Viewed from a) perpendicular to slope face; b) from above.....	139
Figure 6-3: Kinematic analysis undertaken in DIPS for Domain D2. Friction angle of 30, quantity of data points scaled based on relative joint quantity. a) Planar sliding; b) Wedge sliding; c) Flexural toppling; d) Direct toppling.....	140
Figure 6-4: Example of the blocky nature of the surface in Domain D2, displaying wedge and toppling failures along joint sets J2 (blue) and J3 (red). Viewed from a) perpendicular to slope face; b) from above.....	141
Figure 6-5: Kinematic analysis in DIPS for Domain D3. Friction angle of 30, quantity of data points scaled based on relative joint quantity. a) Planar sliding; b) Wedge sliding; c) Flexural toppling; d) Direct toppling.	142
Figure 6-6: Example of typical slope face conditions in Domain D3, showing toppling failure along joint sets J3 (red), with release planes along J2 (blue); a) viewed perpendicular to slope; b) viewed approximately 70° from horizontal	143
Figure 6-7: Example of crown surface conditions within Domain D3, displaying wedge failure and toppling failure along joint sets J2 and J3, a) viewed perpendicular to slope; b) viewed vertically.....	144
Figure 6-8: Kinematic analysis in DIPS for Domain D4. Friction angle of 30, quantity of data points scaled based on relative joint quantity. a) Planar sliding; b) Wedge sliding; c) Flexural toppling; d) Direct toppling.	145
Figure 6-9: Typical slope face within Domain D4, presenting an example of toppling failure	

along Joint Set J3 (red) a) viewed perpendicular to slope; b) viewed from above;	146
Figure 6-10: Visualisation of planar sliding within Domain D1, along Joint Set J2.	150
Figure 6-11: Wedge sliding failures as modelled in SWedge; a) D1, standard slope; b) D1, overhanging slope; c) D2, standard slope; d) D2, overhanging slope; e) D3_1, standard slope; f) D3_1, overhanging slope; g) D3_2, standard slope; h) D3_2, overhanging slope;	152
Figure 6-12: Visualisation of toppling analysis by domain; a) D1 Direct Toppling (J2); b) D1 Flexural Toppling (J2); c) D2 Direct Toppling (J2/J3); d) D2 Flexural Toppling (J2/J3); e) D3 Direct Toppling (J3); f) D3 Flexural Toppling (J3); g) D4 Direct Toppling (J1); h) D4 Flexural Toppling (J1); i) D4 Direct Toppling (J3); j) D4 Flexural Toppling (J3).	157

List of Tables

Table 4-1: Settings used to run KD analysis attempts. Adopted analysis in grey.....	66
Table 4-2: Settings used to run FM analysis attempts. Adopted analysis in grey.	66
Table 4-3: Orientation ranges defined for each defect set.....	72
Table 4-4: Mean joint set orientations for unweighted and weighted data	72
Table 4-5: Ranges for set orientations as defined for point cloud segmentation.....	73
Table 4-6: Defect sets present for each domain.....	78
Table 4-7: Mean set orientation for sets within each domain, with Terzaghi weighting applied.....	80
Table 4-8: Variability and confidence for Joint Sets J1, J2, J3, across all domains. Terzaghi weighting applied to each data point based on the appropriate domain slope face.	80
Table 4-9: Bedding orientation as measured on a small and large scale.....	83
Table 4-10: Statistical summary of scanline measured set normal spacing, for all domains combined.....	88
Table 4-11: Difference between mean spacing and standard deviation	89
Table 4-12: Statistical summary of scanline measured set normal spacing, for all domains combined, with upperbound spacing limits applied.	94
Table 4-13: Statistical summary of measured block dimensions, for all domains and defect sets combined.....	96
Table 4-14: Measurement of blocks with dimensions >2 m in the Rockfall Zone.....	99
Table 4-15: Statistical summary of first order waviness, as amplitude.....	104
Table 4-16: Statistical summary of first order waviness, for joint surfaces with area less than 50 m ²	107
Table 4-17: Statistical summary of peak dilation angle, for joint surfaces with area less than 50 m ²	111
Table 4-18: Length, measurement area, maximum amplitude, peak dilation angles, and orientation for each measured plane.....	112
Table 4-19: Summary of probabilistic defect parameters	117
Table 5-1: Projected blocks from reconstructed rockfall	125

Table 5-2: Parameters defined for rock mass material - Limestone.....	128
Table 5-3: Parameters defined for joint material.....	129
Table 5-4: Summary of probabilistic defect parameters used in analysis	132
Table 6-1: Quantity of data points adopted for each joint set, by domain.	136
Table 6-2: Percentage of poles/intersections for which each failure mode is kinematically possible, colour coded in 5% intervals from >25% (maroon) to <5% (dark green).....	137
Table 6-3: Types of probabilistic analysis undertaken in each domain	147
Table 6-4: Summary of probabilistic defect parameters used in analysis	148
Table 6-5: Geometry as input into planar analysis for Domain D1.....	149
Table 6-6: Standard slope geometry as input into wedge sliding analysis for all domains.	151
Table 6-7: Geometry as input into wedge sliding analysis for each domain.....	151
Table 6-8: Percentage probability of wedge sliding in each domain.	151
Table 6-9: Standard slope geometry as input into toppling analysis for all domains.	154
Table 6-10: Geometry as input into toppling analysis for each domain.....	154
Table 6-11: Percentage probability for toppling failure for each domain	155
Table 6-12: Comparison of the percentage of intersections/normals kinematically able to fail (DIPS), and percentage probability for failure (RocTopple)	156
Table 7-1: Summary of domain slope orientation and dominant joint sets.....	159
Table 7-2: Summary of probabilistic defect parameters	160
Table 7-3: Summary of DIPS percentage of kinematically admissible poles/intersections, and probability of failure from RocPlane, SWedge and RocTopple.	164

1 Introduction

The behaviour of rock masses is controlled by both the properties of intact rock and the properties of joints and other defects present in the rock mass. Where sets of defects meet an open surface, such as a slope or excavation, the intersection of this surface with the defect sets will define the presence of kinematically removable blocks.

In slope engineering, it is therefore essential to have a thorough understanding of the properties of each present defect set, and the interaction between joints and open surfaces. The set-based orientation, location and 3-dimensional extent of block-forming defects are of particular importance (Dong, et al., 2020), as is the shear strength of the defect surface.

The aim of this thesis is to develop a workflow suitable to remotely characterise set-based joint parameters in slopes using three-dimensional datasets. This workflow was then employed to make an assessment as to the effect of defect sets on slope stability. A focus was taken on a steep carbonate slope face near Kaili, in the Guizhou province of southern China. To this end, the following tasks were undertaken:

- Definition of the set-based orientation, spacing, persistence and roughness for each defect set present in the Study Area, using three-dimensional datasets collected via DJI photo capturing (using CloudCompare and ContextCapture);
- Stochastic visualisation of defects within the rock mass (using FracMan);
- Back-analysis of recent rockfalls within the Study Area, to calculate the estimated shear strength of defects at equilibrium (using RS3); and
- Kinematic analysis of planar, wedge and toppling failures within the Study Area (using DIPS, RocPlane, SWedge and RocTopple).

1.1 Study Area

The Study Area consists of a carbonate outcrop in the karst area of southern China. The outcrop is close to the town of Long-Chang, near the city of Kaili in the Guizhou province. The location of the Study Area is displayed in Figure 1-1.

This region has a history of rockfalls, the most noteworthy of which occurred in 2013 at a neighbouring slope. On that occasion a pair of rockfalls resulted in five deaths, the damming of the Yudong river, and the evacuation of 79 residents (Dong, et al., 2020).

In 2018, eight slope faces within the Kaili region were surveyed using DJI photo capturing, including the original “New Rockfall” location. Figure 1-2 displays the “New Rockfall” and an additional three surveyed locations. This thesis utilises the dataset obtained from the survey of the outcrop designated “JK1”.

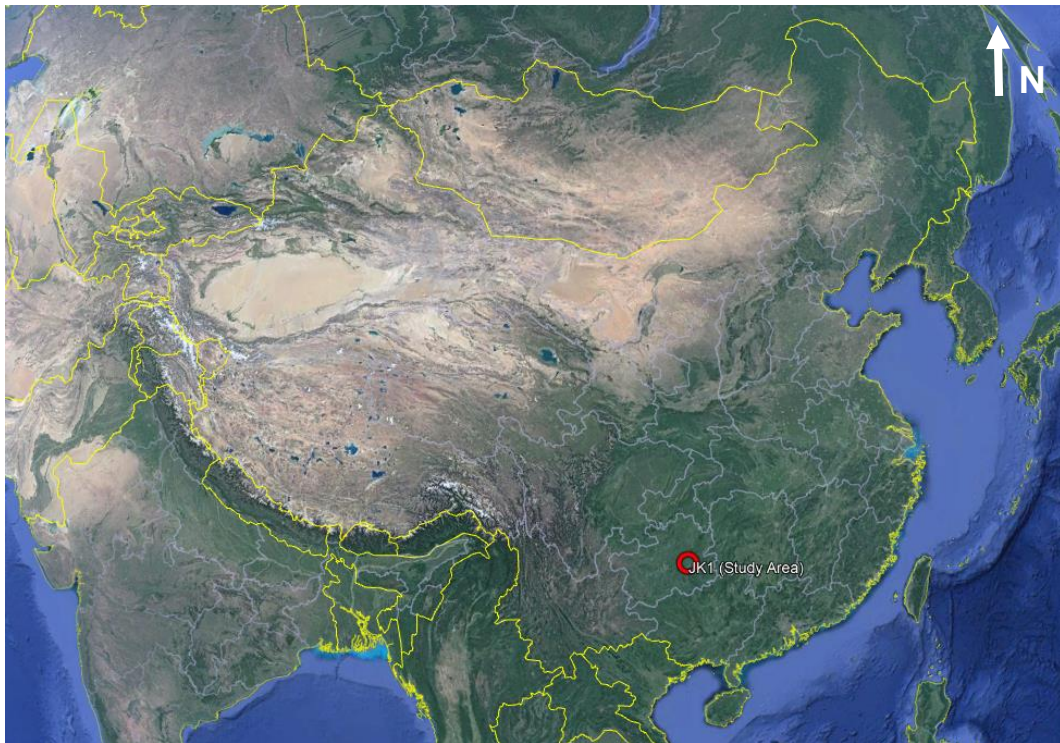


Figure 1-1: Location of Study Area in the Guizhou Province of southern China (Google Earth Pro, 2014-2020).

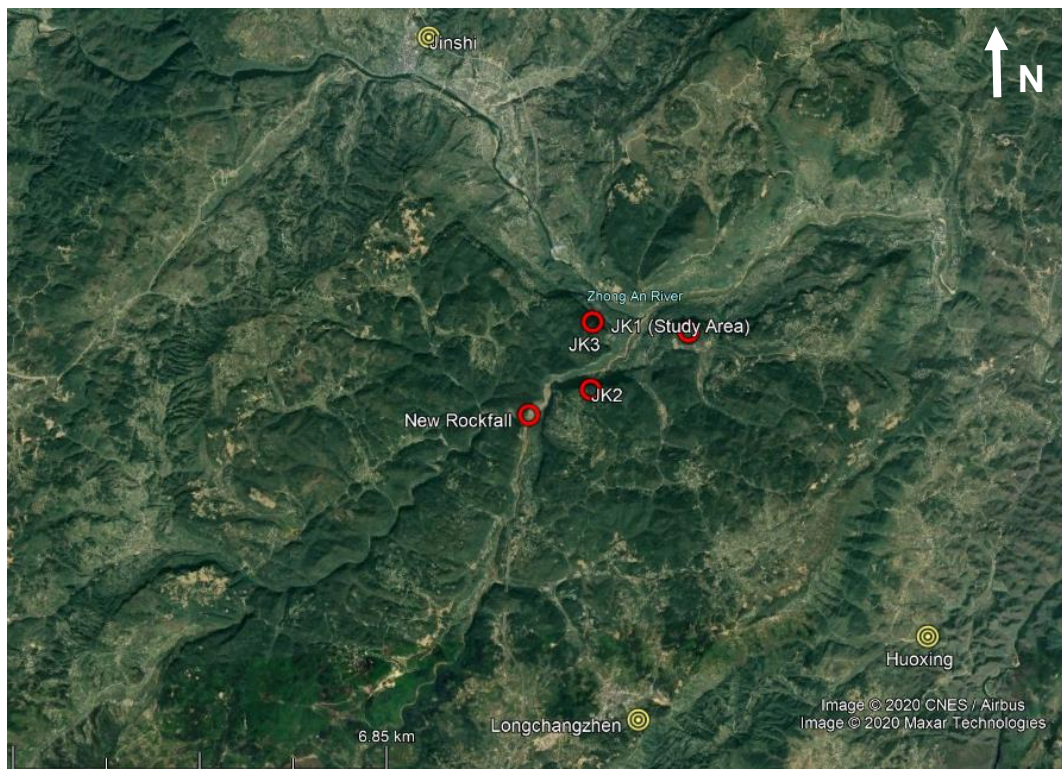


Figure 1-2: Surveyed outcrop locations. The Study Area is located at “JK1” (Google Earth Pro, 2014-2020)

The carbonate outcrop “JK1” is elongated in the east-west direction, with an approximate length of 600 m and width of 450 m (Figure 1-3). It is characterised by a sub-vertical, largely exposed rock face on the northern side and a smooth, vegetation covered slope on the southern side, inclined 25° to 30° from horizontal (28°/176°). The northern face has a total height of approximately 300 m, split by a sub-horizontal bench at a height of approximately 70 m. The Zhong An River lies approximately 600 m north of the outcrop, flowing east.

Historic rockfalls within this slope are evidenced in the irregular, blocky nature of the rock face. The topography below the slope face is covered in talus fans, as is the sub-horizontal bench. Most talus fans are covered in low vegetation, however one recent rockfall has scarred the vegetation and produced multiple fallen blocks of up to 220 m³ in volume. This rockfall appears to have occurred between December 2016 and December 2017, as indicated by historical satellite imagery (Google Earth Pro, 2014-2020).

Numerous karst cavities (dolines) up to 11 m in length are observable at the head of the outcrop. Depths of these cavities could not be ascertained from available data.

The exposed upper portion of the northern face is the region targeted by this thesis, and will hereby be referred to as the Study Area. This steep and unstable slope face has an approximate length of 700 m, a maximum height of 140 m, and a face area of 70,000 m².



Figure 1-3: Outcrop JK1, looking south. Study Area outlined in red.

The Kaili region has a subtropical humid climate, with a mean annual temperature between 15 and 21°C, and mean annual rainfall of approximately 1300 mm (Dong, et al., 2020).

2 Literature Review

In order to allow for the collection, processing, analysis and use of available data, it was necessary to build an understanding of established methodologies from existing literature.

This literature review considers the following:

- Methods of collecting data via remote sensing, and the presentation and processing of that data;
- The geological setting of the study area;
- The genesis of defects, and how this relates to their properties;
- Methods of characterising defect properties, including measurement and analysis of orientation, spacing, persistence, roughness and waviness;
- Factors influencing shear strength, methods of numerically defining shear strength, and the shear strength reduction technique; and
- Modes of kinematic failure, applying the defined defect properties. This includes methods of analysis and probabilistic assessments.

2.1 Data Collection and Measurement

Remote Sensing is the process of obtaining information about an area using a device which is not in contact with the surface. Kong et al. (2020) suggest that, compared to traditional survey, remote sensing techniques offer the following advantages:

1. Data is acquired in the form of high-precision 3D point clouds;
2. Fast and efficient data collection over large areas;
3. Contactless and safe investigations in inaccessible or hazardous areas; and
4. Reproducible and objective acquisition of data.

Additionally, many remote sensing techniques can be undertaken in any weather conditions. They can be more cost effective than traditional survey or mapping methods, depending on the scale of the project and the experience of personnel. Forms of remote sensing most regularly adopted for geological/geotechnical projects include LiDAR, photogrammetry, InSAR and electronic spectral sensors.

The platform holding remote sensing equipment can be varied to suit the required project, ranging from satellites to standard terrestrial setups. As technology improves, airborne platforms such as drones are becoming more popular. Typically, terrestrial platforms are able to collect a higher accuracy and resolution of data, whilst airborne platforms are ideal for larger areas which may be difficult to access.

2.1.1 Photogrammetry

Photogrammetry is an optical sensor method which generates a 3D reconstruction of a feature from 2D photos taken from multiple locations. The comparison of two or more images allows the calculation of the parallax angles between features, which can then be used to define distances and lengths. Three methods can be used:

- Digital Image Correlation generates a watertight model;
- Structure from Motion (SfM) generates a point cloud through feature matching; and
- Multi-View Stereo (MVS) generates a dense point cloud with dense image matching.

Modelling and texturing creates a 3D photorealistic model, which can be accurate down to a few centimetres. Photogrammetry is not good at determining texture, and struggles with vegetation cover. It is highly sensitive to variations in illumination, weather, damp spots etc. which can prevent image matching and feature correlation.

Unmanned Aerial Vehicles (UAVs) are often used to take images/readings remotely over large areas. Georeferencing of images can occur either directly, using an internal GPS system in the UAV, or by capturing ground control points in images which can be later used to correlate images. UAV tilt photogrammetry uses a UAV equipped with a tilt camera, which acquires images with the lens at a certain tilt angle relative the ground. This is able to better obtain rock structure information in areas with steep terrain.

This project utilises photogrammetry, with data recorded through UAV photo capturing. It has been processed as a point cloud using the Bentley program ContextCapture, utilising the Structure from Motion (SfM) method.

2.1.2 Data Presentation

Two main approaches can be used to present and analyse remote sensing data – point clouds or meshed surfaces (Gigli & Casagli, 2011).

2.1.2.1 Point Clouds

Laser scanning and photogrammetry are capable of producing extremely large datasets, containing millions of three-dimensional datapoints. Each data point contains an individual x, y, and z coordinate, with the accumulation of all points forming a “point cloud”. It is standard practice to combine data from multiple scans in order to improve accuracy and to prevent any shadowing of features which may occur from any one measurement location.

The open source program CloudCompare can be used to display, process and render point clouds (Anon., 2020). It includes several purpose-built plugins and algorithms which allow for specialist measurements and data processing applications. As detailed further below, international trends in remote sensing analysis are now leaning towards the direct extraction of features from point clouds, rather than from derivative surfaces such as meshes.

Visual recognition of 3D rock structure can be enhanced by assigning a HSV colour to each point in the cloud, representing the orientation of the normal vector of the point (Liu & Kaufmann, 2015). This visualisation highlights dominant surface orientations in an outcrop.

The normal vector for each point in space is typically determined using automated calculation processes, which consider the relationship of a point to its nearest neighbours. This process judges whether the points lie on the same defect plane, and if so, defines the orientation of that plane. Considering the irregular and often angular nature of jointed rock faces, an ideal algorithm must be able to accurately define edge intersections. Dong et al. (2020) state that the most appropriate algorithm for determining a point normal at edge intersections is the Hough transformation, as proposed by Boulch and Marlet (2012, 2016). This was the only transformation tested by Dong et al. (2020) which was capable of correctly reconstructing normals on the edges of plane intersections.

The Hough transformation is a tool for shape extraction, which applies deep learning to unstructured 3D data using a convolutional neural network (CNN) (Boulch & Marlet, 2016). Shape hypotheses are made by drawing the minimum number of points required to create a shape. Each “drawn” hypothesis creates one vote in a “bin” in an accumulator. After a certain number of hypothesised shapes are attempted, a CNN-based decision procedure selects the most highly voted bin from the accumulator, representing a plane and a normal orientation. This method is robust to noise, outliers, density variation and sharp edges (Boulch & Marlet, 2016).

Once the point normal has been determined, it is possible to segregate the data based on orientation (e.g. to create separate point clouds for each joint set), or to colour points based on orientation. Liu and Kaufmann (2015) proposed a HSV rendering technique which uses purpose-written MATLAB codes to assign a unique colour to each point. The colours’ hue (H) is linked to the dip direction of the normal, and the saturation (S) is linked to the dip of the normal, as displayed in Figure 2-1. Sub-vertical planes will present in bright tones, while horizontal planes will appear white. These models apply a “darkness” value V of 0.75, and have a resolution of 1 degree for each unique colour (Dong, et al., 2020).

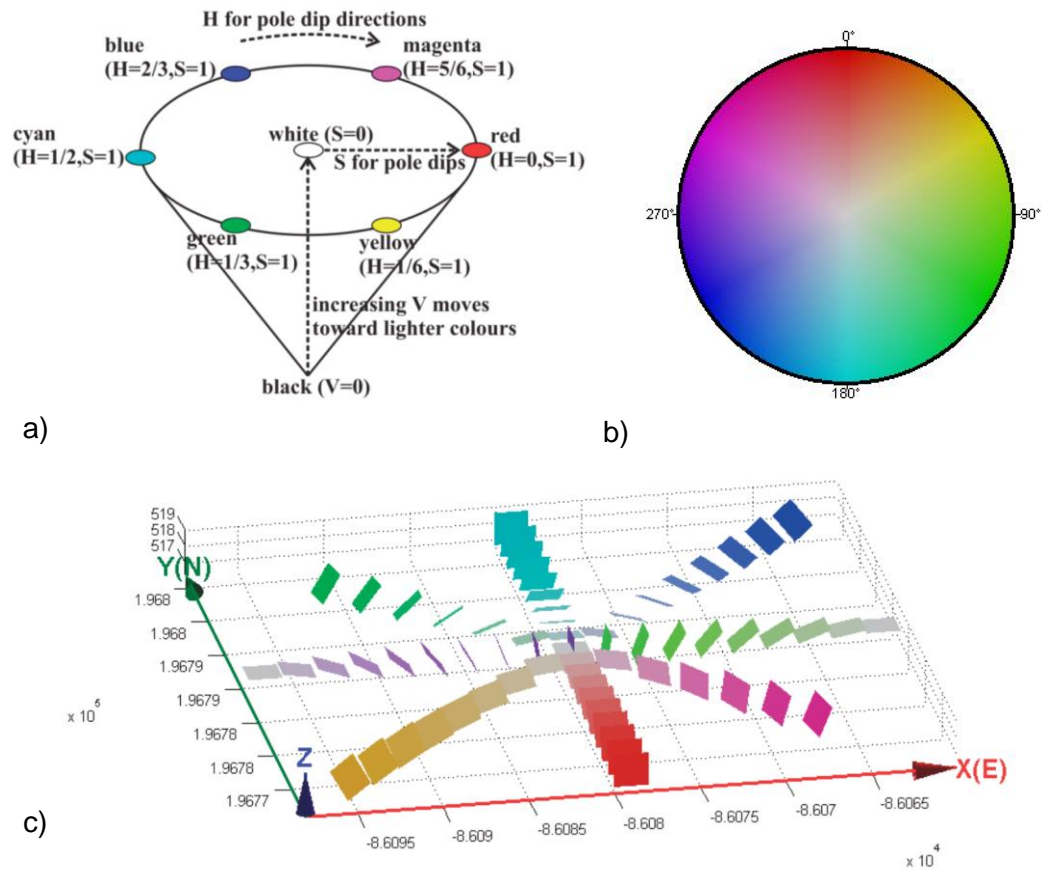


Figure 2-1: Definition of the HSV colouring scheme proposed by Liu and Kaufmann (2015); a) the HSV colour cone; b) the HSV colour wheel; and c) representation of HSV coloured fractures, representing their geometry.

Points which lie on the same defect will have similar direction values (and therefore colours) compared to their neighbours. This automated pre-processing step enables the visual discernment of defects from within an outcrop (Dong, et al., 2020).

2.1.2.2 Meshed Surfaces

Meshed surfaces may be generated either from interpolation of point cloud data, or through reconstructions of photogrammetry. 3D real scene models can be created directly from photogrammetry, using software such as Bentley's Context Capture. Georeferenced images are imported and aerial triangulation undertaken to reconstruct a watertight 3D scene.

The creation of a surface from a point cloud simplifies the original data, fitting points into elementary polygons with a known orientation (Gigli & Casagli, 2011). Neighbouring polygons with similar orientations can then be grouped into larger planes. The accuracy of defect surfaces is heavily dependent on the quality of triangulation processes forming the initial elementary polygons, and on the data resolution. Errors or inaccuracies here may neglect small features, and misrepresent complex shapes (Gigli & Casagli, 2011).

Measured surfaces may contain under-sampled domains due to limited sensor range, high light absorption, and occultations during scanning or imaging (Dong, et al., 2020). Although automated processes of cloud cleaning are constantly improving, the automatic removal of obstructions such as vegetation is still a challenge (Dong, et al., 2020). The variation in sampling density and the presence of obstructions affects meshing accuracy, and therefore raw point clouds utilised with vector statistical considerations are considered to be more accurate than derivative meshed surfaces (Ghosh, et al., 2010).

2.1.2.3 Combined Datasets

Where defects are oriented approximately perpendicular to a slope face, they may not be exposed as surfaces but may be visible as traces or cracks in the slope face (Turner, et al., 2006). Smooth rock faces may therefore yield very little defect information from 3D point clouds, while an image of the same rock face may identify prominent cracks. The combination of 3D laser scanning information with imagery allows for the analysis of defects present without surface relief by fitting planes to joint traces. In this case, the combination of 3D laser scanning and digital image analysis is able to produce a more complete structural analysis than either method can on its own (Turner, et al., 2006).

2.1.3 Types of Processing

There are two main ways to process remote imaging data (Gigli & Casagli, 2011):

- **Manual:** This procedure involves visually inspecting the point cloud or mesh, fitting local planes, and taking measurements utilising built-in tools. This procedure is typically non-systematic, time-consuming, subjective, and has a size bias which often misses the smallest features. This approach depends heavily on the quality of digital data and the judgement of the user; and
- **Automatic or Semi-Automatic:** Algorithms can be used to segment data into clusters or points along the same defect. This samples all detectable defects within the surveyed area, and can automatically calculate parameters such as orientation, number of sets, spacing and trace length. However, the computing time can be very long, and the process lacks engineering/geological judgement to sort important information from noise. There are numerous software packages available which are designed to extract 3D rock mass properties from high resolution LiDAR and photogrammetry, such as Vulcan, Jointmetrix3D, Surpac, Sirovision, 3DM analyst, Split-FX, 3DGeomech and Coltop3D (Gigli & Casagli, 2011).

Turner et al. (2006) state that a fully automated, computer-driven method of analysis is neither feasible or desirable, as geological and engineering judgement is required to extract meaningful geological structures and rock mass defects from the dataset in a way which cannot yet be replicated by existing algorithms. It is generally accepted that manual and automatic approaches should be used together (Gigli & Casagli, 2011).

2.2 Geology of the Study Area

The Study Area is located within the bare karst region of southern China, which covers the provinces of Yunnan, Guizhou and Guangxi. Within this karst region, deep marine carbonate rocks are continuously distributed over an area of approximately 500,000 km², with a mean thickness of 1500 m (Zhao, et al., 2012).

The Kaili carbonates were deposited during the Carboniferous and Permian periods. The calcareous strata present in the Study Area are the Qixia (P2q) and Maokou (P2m) Formations deposited in the Permian (Dong, et al., 2020).

The Study Area lies on the eastern edge of the Yunnan–Guizhou Plateau, which was uplifted during the Yanshan Movement in the Middle Jurassic and has an altitude of 1000 to 2000 m above sea level (Lu, et al., 2013). Further intermittent uplift episodes occurred throughout the Cenozoic. Erosion from surface and subterranean water caused deep incisions in the terrain, producing a landscape of karst hills and depressions, with a mean relief of 300 m (Lu, et al., 2013). The landforms in this part of southern China are strongly influenced by the physical and mechanical properties of carbonate rocks, producing tower landforms on the surface, and large halls and caverns underground (Yuan, et al., 1995).

Exposed bedrock near the Study Area comprises flatly bedded limestones with several thinly-bedded interlayers of calcareous shale (Dong, et al., 2020). Available remote sensing data indicates that this is comparable to the geology of the Study Area. No direct field observations have been made.

Fold axes and major faults in the Kaili area trend to the NNE, with faults typically dipping to the WNW and ESE at a mean dip angle in excess of 65° (Lu, et al., 2013).

2.2.1 Karst Terrain

In karst landscapes, mechanical erosion is secondary to surface and subsurface rock dissolution, where carbonate rocks are dissolved by slightly acidic water infiltrating the rock (Gutiérrez, et al., 2014). Dissolution processes may give rise to the formation of solutionally enlarged defect planes and three-dimensional void networks, which can form extremely complex aquifer systems. As a result, karst regions typically have high secondary permeability, and may transport large volumes of water quickly, with highly variable flow rates dependant on climatic conditions (Yuan, et al., 1995).

According to the karst divisions proposed by Lu (2003), and referenced by Lu et al. (2013), the Study Area lies within Region V: the Yunnan-Guizhou Plateau – South China Basin. This region largely features dissolution karst, tectonics-dissolution karst and dissolution-erosion karst. Karst development here is characterised by major underground rivers (Lu, et al., 2013). According to Yuan et al. (1995) the karst type in the Kaili region is “Bare Karst” (Figure 2-2), with a typical porosity of 2-4%, and compressive strengths in intact rock of over 100 MPa.

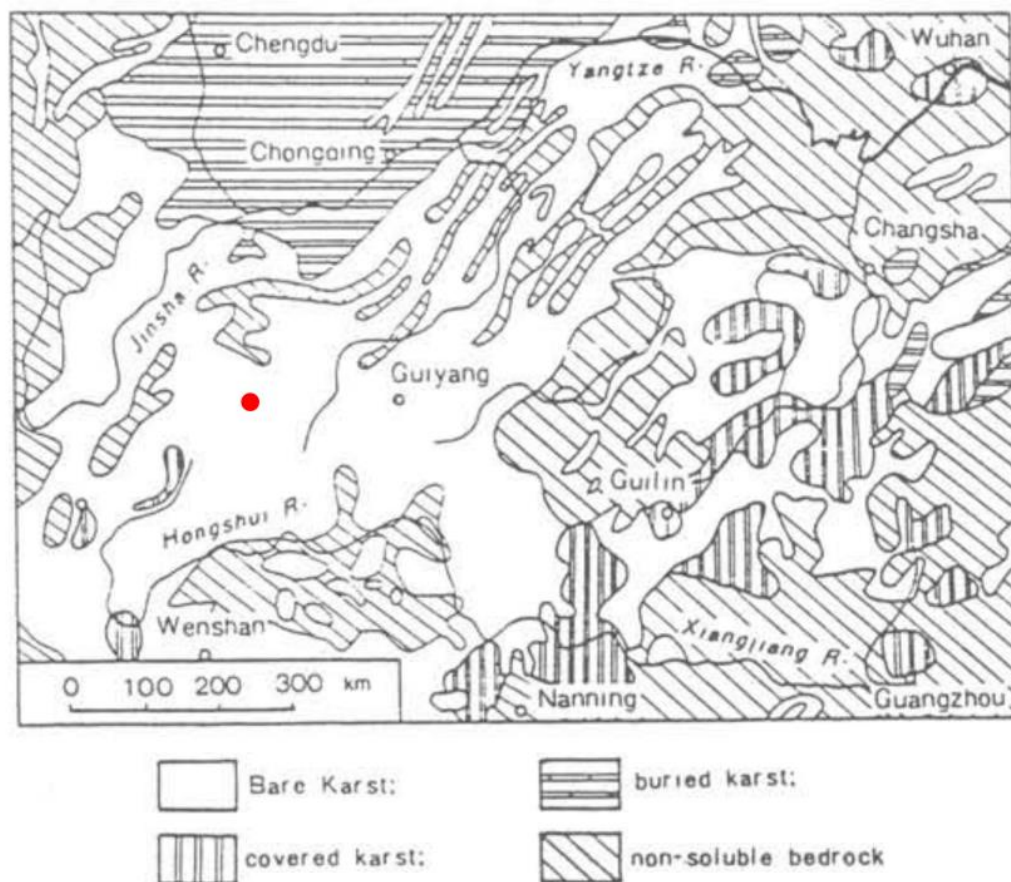


Figure 2-2: Distribution of karst types in southern China (Yuan, et al., 1995). Approximate location of Study Area indicated in red.

Karstic features are observable within the Study Area in the form of Dolines. Dolines are closed depressions with internal drainage. They may be up to hundreds of meters across and tens of meters deep (Gutiérrez, et al., 2014). The karst cavities observed at the crown of the Study Area are likely inception dolines, a type of accelerated corrosion doline (also known as a normal solution/dissolution doline). These particular dolines develop due to concentrations in surface runoff and subsurface flow which can occur in laminated strata where impermeable layers (such as shale) control the movement of flow. Any break in this impermeable layer (such as a defect) will cause a channelling of flow through the narrow opening, accelerating dissolution of soluble rock in this location (Sauro, 2003).

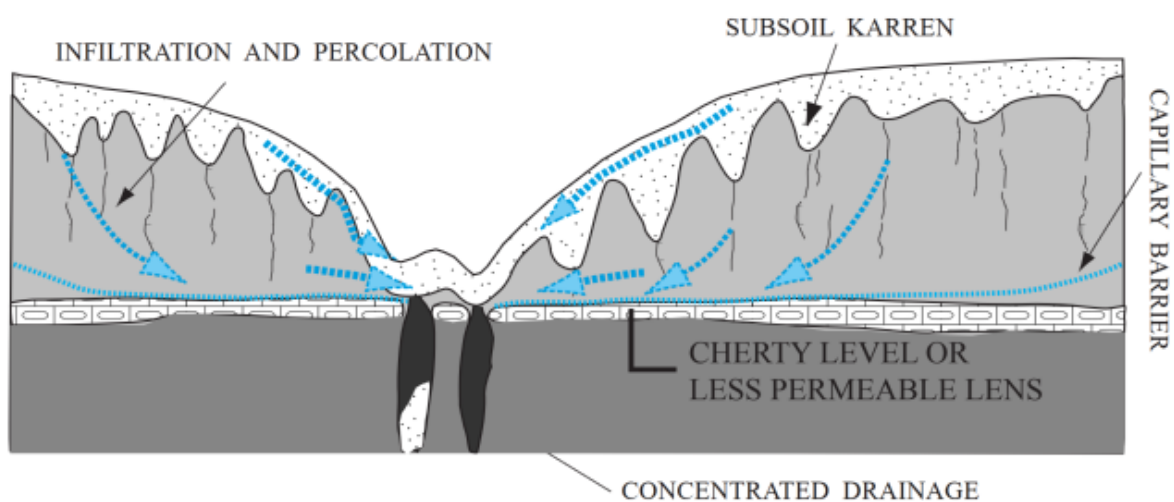


Figure 2-3: Development of an inception doline with drainage focused by a cherty lens (Sauro, 2003). Drainage may also be focused by changes in lithology.

The karst landscape is known to be susceptible to geohazards such as karst collapses, landslides, debris flows and water infiltration (Lu, et al., 2013). The effects of karst features on slope stability have not been thoroughly explored to date, largely due to complications in investigation and assessment. It is theorised that the occurrence, size and connectivity of voids may introduce additional instability to slopes either directly as voids, as solutionally enlarged defects, or by acting as preferential paths for groundwater flow (Gutiérrez, et al., 2014). Fluid pressures introduced into the rock mass through enlarged defects reduces the normal effective stress, reducing the shear strength of the defect. Solutionally enlarged defects may encourage frost weathering, which produces high pressures on the walls of defects (Gutiérrez, et al., 2014), potentially destabilising kinematically removable blocks.

2.3 Genesis and Properties of Defects

Defects are mechanical breaks in otherwise intact rock, encompassing joints, faults, bedding planes, foliations and schistosity. The presence and properties of defects in a rock mass can be a controlling factor in the overall rock mass behaviour, influencing deformation, hydraulics and stability of rock masses (Kong, et al., 2020).

Defects control rock mass behaviour by altering stresses and displacements within the rock mass as a response to loading. Where the considered portion of a rock mass is heavily fractured or there are low stress conditions the properties are governed largely by defects. However, where defects are widely spaced, material properties dominate (Liu, 2019).

The strength, deformation and stress-strain behaviour of a rock mass can be affected by defects in a non-linear and anisotropic fashion (Hammah, et al., 2008). Defects generally exhibit brittle (strain softening) behaviour, with residual strength much lower than the peak strength. This leads to the development of progressive failure mechanisms, where modifications to the stress regime from one failure can cause other regions to fail until an equilibrium state is achieved (Hammah, et al., 2008).

2.3.1 Genesis and Nature of Defects

In order to define the properties of a defect set, it is useful to understand the nature of the defects, and the processes behind their genesis. There are three geologically based groups of defects broadly recognised (National Research Council, 1996):

1. Dilating fractures/joints: normal displacement defects – where fracture surfaces move away from each other in a direction perpendicular to the surface. Tensile joints may originate even under high compressive stress, as flaws in the intact rock may cause local tensile stress (Ghosh, et al., 2018);
2. Shear fractures (faults): shear displacement defects – where fracture surfaces move predominantly parallel to each other (Ghosh, et al., 2018); and
3. Closing fractures/pressure solution surfaces (anti-cracks): where existing fractures are welded together by solution, occurring at grain contacts.

Mixed-mode fractures are possible, which occur as a combination of these modes. Rock masses which have complex deformational histories often have fractures produced sequentially by two or more of these modes. This results in overprinted displacement defects (National Research Council, 1996).

Dilatant joints propagate in the principal stress plane, normal to the maximum tensile or least compressive stress. Joints initiate and propagate as the stresses in intact rock are exceeded by external forces. The most common external forces are lithostatic changes in overburden weight, fluid pressure, tectonic forces and thermal cooling. Joints may also be initiated by extra-terrestrial impacts, volcanic activity, and salt intrusion (National Research Council, 1996).

The knowledge of joint initiation mechanism can assist in predicting persistence and orientation variation (Ghosh, et al., 2018). Regional joints form from states of constant stress, and have near-constant orientations. Their formation may relate to faulting or folding events. As more fracture sets are added to the network, the regional stress progressively decreases (Liu, 2019).

The particular location at which a joint will occur depends on stresses within the rock fabric. Even small-scale heterogeneities in a rock mass may lead to concentrations in the stress field at which joints may initiate. Heterogeneities may occur at grain contacts, lithological changes, or geological structures induced by previous deformations (National Research Council, 1996). Ghosh et al. (2018) suggest that joint arrest (the point at which the joint does not continue to grow) may be due to a decrease in pore pressure, an increase in remote stress perpendicular to the joint face, or interaction with obstacles such as other joints or local heterogeneities.

2.3.2 Joint Sets

Joints typically occur in groups with similar orientations, spacing and origins, known as sets. These sets may be localised, confined to narrow regions, or extended throughout a broader area. Joints may branch apart, splitting into separate surfaces. Adjacent joints may also join together. Both processes may lead to a fork-like appearance (Ghosh, et al., 2018).

The formation of joint sets changes the stress conditions within the rock mass, promoting and controlling the initiation of additional sets, and providing barriers to new joint propagation. This controls the spacing, clustering, and effective length of new joint sets, and tends to result in successive joint sets being shorter in length (National Research Council, 1996). Joint sets may cross each other in two circumstances:

1. When the first set is under a large normal compression and so slip along the defect surface is limited; and
2. When older fractures are cemented closed.

Joint orientation, location and 3-dimensional extent of block-forming defects (persistence) are of particular importance in determining rock mass behaviour (Dong, et al., 2020), and are the main parameters defined when characterising a joint set. When defining these parameters, it is vital to establish whether the rock mass under consideration is statistically homogeneous, or has location-dependent properties (Hudson & Priest, 1983). If the rock mass cannot be considered to be statistically homogeneous, two options may be adopted:

1. The rock mass may be segregated into structural regions, units or domains within which the properties are essentially homogeneous; or
2. The rock mass can be considered as continuously changing, requiring a geostatistical/probabilistic analysis.

2.3.3 Orientation

The direction of propagation and geometry of a defect is controlled by the stress field, which results from loading conditions and neighbouring defects. Joints tend to form along principal stress planes. Commonly the regional distributions of joint and fault patterns mirror regional geomorphological features, such as fold axis or mountain ranges which control the directions of principal stress (National Research Council, 1996). As principal stresses are orthogonal, orthogonal joint sets are common in isotropic rock masses under the same stress system. Varying intersection angles between sets may indicate a change in the stress regime, or anisotropy in the rock mass (National Research Council, 1996).

The shape of a defect may be described by “waviness”, or “curvature”, which Priest (1993) defines as “surface irregularities with a wavelength greater than about 100 mm”. When measuring defect orientation, if the size of the compass is small relative to the surface waviness the measured orientation will depend upon where on the “wavy” surface the compass is placed, and may not reflect the overall surface orientation (Sturzenegger & Stead, 2009). This error can be reduced by measuring orientation on a larger scale, estimating the mean defect orientation. This is easily achieved using remote sensing data, where measurements across larger surfaces are possible. Errors may also be reduced by selecting multiple orientation measurements at varying locations on a single defect, and finding the average orientation of these points (Sturzenegger & Stead, 2009).

2.3.3.1 Measurement

The orientation of a plane may be defined by three or more points within a point cloud. The orientation may be defined as dip and dip direction, dip and strike, or as the orientation of the plane normal. By plotting the orientations of all individual faces in a stereonet, it is

possible to visualise data clusters. Because of the high density of remote sensing data, it is possible to obtain the orientation of thousands of surfaces for a single rock outcrop, providing a solid basis for statistical analysis (Turner, et al., 2006).

CloudCompare contains two plug-ins which are designed to measure joint orientation – Compass, and FACETS.

2.3.3.1.1 Compass

Compass is a structural geology toolbox used to measure the orientation of planar features from point clouds. It contains a “Map Mode” which can delineate geological units, and a “Compass Mode”, which measures orientation and thickness (Thiele, et al., 2020).

The Compass Mode contains three tools, able to measure planes, traces and lineations:

- The plane tool measures surface orientation by fitting a plane to all points sitting within a user-defined measurement circle. This circle can be modified to increase or decrease the number of points included to define the plane. This tool is analogous to a geologist in the field applying a compass and clinometer;
- The trace tool estimates the orientation of a structure or contact using its interaction with a non-planar surface; and
- The lineation tool measures the trend and plunge of a line between two points.

2.3.3.1.2 FACETS

FACETS is also a structural geology plugin, however is designed to automatically extract planes from unstructured 3D point clouds and calculate their orientation (Dewez, 2020).

The data processing aspect of FACETS divides a point cloud into clusters, where adjacent points share some level of co-planarity. These “elementary planes” are then grouped into larger objects, using a coplanarity indicator and a roughness criterion. Data can be reported in interactive stereonet (Dewez, et al., 2016).

When initially dividing the point cloud, the division can be undertaken in one of two ways, both utilising a least-squares fitting algorithm (Dewez, et al., 2016).

- The Kd-Tree approach divides a point cloud into small planar patches, reducing in size until all points within a cell fit the best-fitting plane within a user-defined tolerance (root mean square threshold), or until the user-defined minimum number of points is reached. An algorithm is then applied in the opposite direction, merging all patches which share a common dip and dip direction into a “facet”, considering an input maximum angle tolerance and maximum relative distance from facet centre.

- The Fast-Marching (FM) approach uses a regular lattice subdivision with an octree structure. Adjacent patches will merge if doing so does not increase the merged patches retro-projection error beyond the maximum distance criteria. The fusion process is based on a fast-marching front propagation.

2.3.3.2 Analysis

The RocScience program DIPS 8.0 can be used to display orientation measurements, identify defect sets, determine set-based orientation and distributions, and undertake kinematic analysis (RocScience, 2020). To define the mean orientation for a defined defect set, DIPS utilises simple vector addition of all pole vectors within the defined set window. The resultant vector is then normalised with respect to its magnitude to obtain a mean unit pole vector for the defined set. For weighted datasets, the scalar weight for each pole is considered before including it in the vector summation (Diederichs, 1990).

DIPS provides information on the distribution of values about the mean value in three ways; Fisher's K, confidence limits and variability limits. Fisher's K value defines the clustering of each set, producing a constant defined based on the number of pole vectors in a set (N), and the length of the resultant vector created by the addition of all poles in a set (R). If there is low scatter and all defects are parallel to each other, K approaches infinity. If defects are randomly oriented, K approaches 0 (however is rarely below 5 in practice) (Priest, 1993). Fisher's K is a symmetric distribution (Priest, 1993). Fisher's K can be calculated as follows:

$$K = \frac{N - 1}{N - R}$$

For sample sizes exceeding 30, it becomes possible to calculate probabilistic approximations to show how well the distribution model fits a given group of orientation values (Priest, 1985). Priest (1985) defined two limits (confidence limits and variability limits), assuming that the mean vector represents the best estimate of the unknown true orientation.

Confidence limits are angular values which reflect the confidence in the mean value to a specified degree of certainty. This gives an indication of the reliability and size of the sample, and is best used where it is important to define the likely range for the mean orientation of the set (accuracy). The limit is expressed as the angle of a cone required to define a certain percentage of confidence in the mean value – e.g. 95%. This assumes the sample is symmetrically distributed (Lyman, et al., 2008). The following equation is used to define the angle of the confidence cone (alpha), for a certain probability P:

$$\cos(\alpha_{confidence}) = 1 + \frac{\ln(1 - P_R)}{R \cdot K}$$

Variability limits reflect the natural variability of the dataset from the mean value (precision). They can be used for probabilistic stability studies, and defines the likelihood of a sample falling within the variability cone. They are analogous to standard deviation, and are used where the main concern is the likely range of orientations of individual defects from the set mean. The limit is expressed as the angle of a cone required to contain a certain percentage of data – e.g. 95%, using the following equation:

$$\cos(\alpha_{variability}) = 1 + \frac{\ln(1 - P)}{K}$$

Other models have been developed which are able to provide better fitting distributions for asymmetric and girdle oriented data. Priest (1993) lists several of these models; Einstein and Baecher (1983), Kelker and Langenberg (1976), Mardia (1972) and Watson (1966). However, these models are extremely complex, both in parameter estimation and in the formulation of probabilistic results (Priest, 1993), and have not been considered in this thesis.

2.3.3.2.1 Terzaghi Weighting

The collection of measurement data from rock outcrops typically occurs in the form of lines or slope surfaces. The orientation of these linear or planar sampling methods relative to the orientation of the defects sets present will produce a directional bias. Terzaghi (1965) proposed a correlation factor (η) to correct for this bias, relating the measured defect frequency (λ_1') and the defect frequency measured along the defect normal (λ_1). Defect frequency is the inverse of defect spacing.

$$\eta = \frac{\lambda_1'}{\lambda_1}$$

In a planar sampling situation (such as the Study Area), defects sampled by a plane may be corrected based on the angle (β) between the plane normal and defect normal:

$$\eta_2 = \frac{1}{\sin\beta}$$

The magnitude of error in the value of the correction factor is dependent upon the relative orientations of the defect sets and measurement plane. Where the defect set is parallel to the sampling plane, a “blind zone” occurs where there are no intersections (Terzaghi, 1965). The proportional error increases dramatically, from 10% at a relative angle of 0° to 100% at an angle of 10° at an error in β measurement of $d\beta = 1^\circ$ (Wang & Mauldon, 2006).

A minimum bias angle is used to prevent the weighting factor from becoming excessively large and to reduce errors in proximity to the “blind zone”. Any planes which intersect a specified traverse at an angle less than the minimum bias angle will be limited to a specified maximum weighting factor. The larger the specified bias angle, the smaller the weighting factor applied.

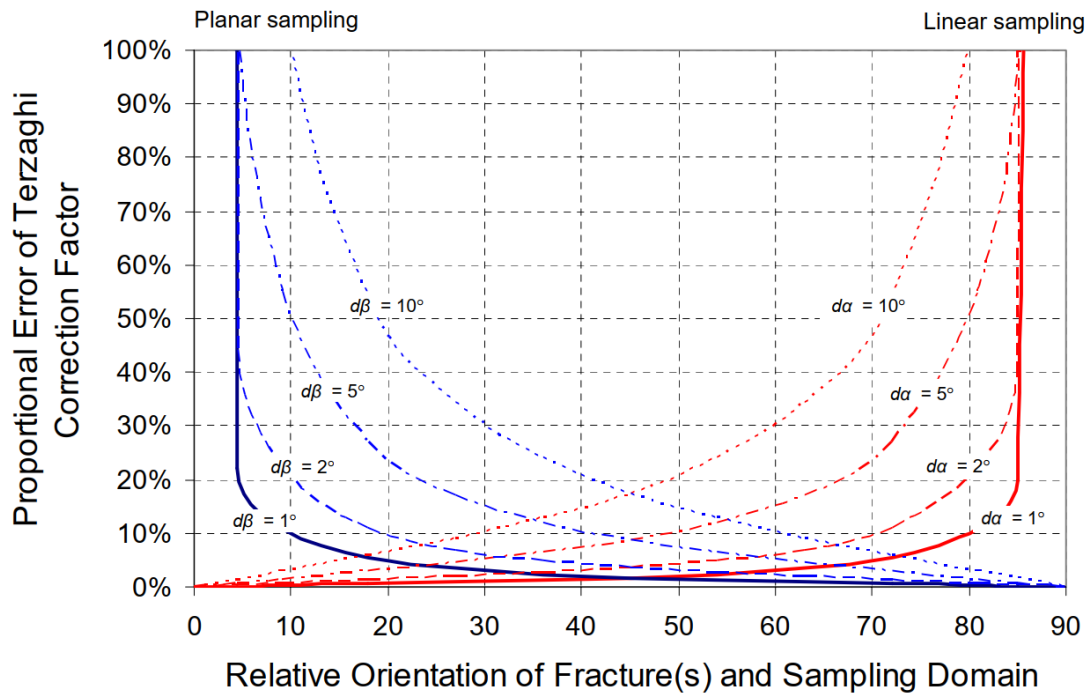


Figure 2-4: Proportional error of the Terzaghi correction factor for linear and planar sampling (Wang & Mauldon, 2006)

2.3.4 Spacing

Defect spacing is the measurement of the distance between two defects. This determines the shape and volume of rock blocks which, when compared to the geometry of an excavation or slope face, will impact overall slope stability (Devkota, 2019).

Joint spacing evolves with time, strain magnitude, strain rate and loading cycle (National Research Council, 1996). The spacing between joints of a particular set depends on the strength and stiffness of the rock mass and the interaction with existing joints.

The occurrence of defects in a set relates to the position of adjacent defects. For example, the formation of one joint may relieve the stress within the rock mass a certain distance to either side of the joint. Beyond this distance, where the stress exceeds the strength of the intact rock, an additional joint will form. This distance is approximately half of the mean spacing value, but may vary due to heterogeneities in the intact rock, or changes in the stress regime (Hudson & Priest, 1979). In general, joint spacing decreases with decreasing bed thickness in stratified rocks (Ghosh, et al., 2018).

2.3.4.1 Measurement

Measured defect spacing is highly dependent upon the direction of measurement. Defect spacing will appear maximised when measured parallel to the defect plane, while spacing will appear minimised when measured perpendicular to the defect plane. This variation has important implications for both defect measurement procedures, and engineering interpretation of spacing relative to the orientation of a structure. Priest (1993) proposed three forms of defect spacing measured along a scanline:

- Total spacing: distance between two adjacent defects;
- Set spacing: distance between adjacent defects from the same set; and
- Normal set spacing: spacing between joints of the same set, measured along a sampling line normal to the set mean orientation.

For kinematic analysis and engineering calculations, the set based normal spacing is the most important. Defect spacing is typically calculated in three-dimensional models by adopting a virtual scanline method, creating a straight line along which the intersections of planes are measured (Laux & Henk, 2015). Measurements can then be adjusted by defect orientation to obtain a normal set spacing. In a measurement procedure such as a scanline, measured values of defect spacing will incorporate the influence of joint impersistence.

Scanline methodologies are well understood and commonly utilised. Hudson and Priest (1983), consider that the following advice be adhered to when undertaking site surveys:

1. The survey should comprise a minimum of three orthogonal scanlines, to avoid missing any defect sets;
2. Scanlines should be long enough to include the heterogeneity of the rock mass; and
3. The basic spacing/frequencies should be corrected for scanline orientation;

The CloudCompare 'Compass' plug-in contains a "point thickness" tool which can be used to measure the distance between two points within a point cloud (Thiele, et al., 2020). The "point thickness" tool considers a plane of known orientation, and measures distances in the orientation of the plane normal. This can be completed in two ways:

- 1-point thickness: A plane is chosen, and a singular point is measured directly from this plane. This method therefore uses the orientation of a specific defect, which may vary somewhat from the mean set orientation; and
- 2-point thickness: A reference plane is chosen, and a distance is measured between two additional points in the direction of the reference plane normal. It is possible to use the mean set orientation to define the reference plane, and therefore to directly measure mean set spacing based on the mean set orientation.

2.3.4.2 Analysis

Defect spacing measurement data was described by Hudson and Priest (1979) to be distributed in three potential ways:

- Negative exponential distribution: randomly positioned defect spaces, independent of each other. Includes numerous small spacing values;
- Uniform distribution: all spacing values have an equal probability of occurrence; and
- Normal distribution: mean defect spacing is the most commonly occurring.

Set based normal spacing typically begins with a normal distribution. However, when considering multiple defect sets the total spacing converges to a negative exponential distribution (Hudson & Priest, 1979). The total spacing is calculated through the addition of each set based spacing, considering the angle of incidence between that set and the sampling line in question. The observable total defect spacing will generally be the result of the superposition of multiple set distributions. This increases the number of small spacings, and decreases those of large spacings. Hudson and Priest (1979) suggested that any arrangement of evenly spaced, clustered or randomly positioned defects will converge to a negative, exponentially distributed form.

If sufficient data is available, a goodness of fit test can be undertaken in order to measure the compatibility of a sample with the theoretical probability distribution function (Noroozi, et al., 2015). This level of rigorous probabilistic analysis is only meaningful when the dataset is known to be reliable, representative of the rock mass, and of an appropriate resolution.

2.3.5 Persistence and Geometry

Joint geometry considers joint shape and persistence, which is important in predicting joint behaviour. Defect geometry is complex, and is influenced by stress regime, rock mass heterogeneities, and existing defects. The analysis of surface markings on joints within massive rocks indicates that joints begin with a circular or elliptical shape, but can twist out of plane as they grow (National Research Council, 1996).

Persistence is defined as the extent or size of a discontinuity (Sturzenegger & Stead, 2009). It can be used to characterise the extent of fracturing in a rock mass. Typically, joints are modelled as flat discs, which can be used to define persistence in three dimensions by assigning a diameter to the flat disc (Lyman, et al., 2008). The diameter of this disc can be estimated from the trace length of joints presenting at intersections with slope faces.

Hudson & Priest (1983) divided the nature of defect persistence into three groupings:

- Persistent: where the defect trace continues uninterrupted;
- Intermittent: where the continuation of a defect trace is interrupted by rock bridges, but otherwise continues along the same plane; and
- Separately impersistent: each bounded defect is separate from the others.

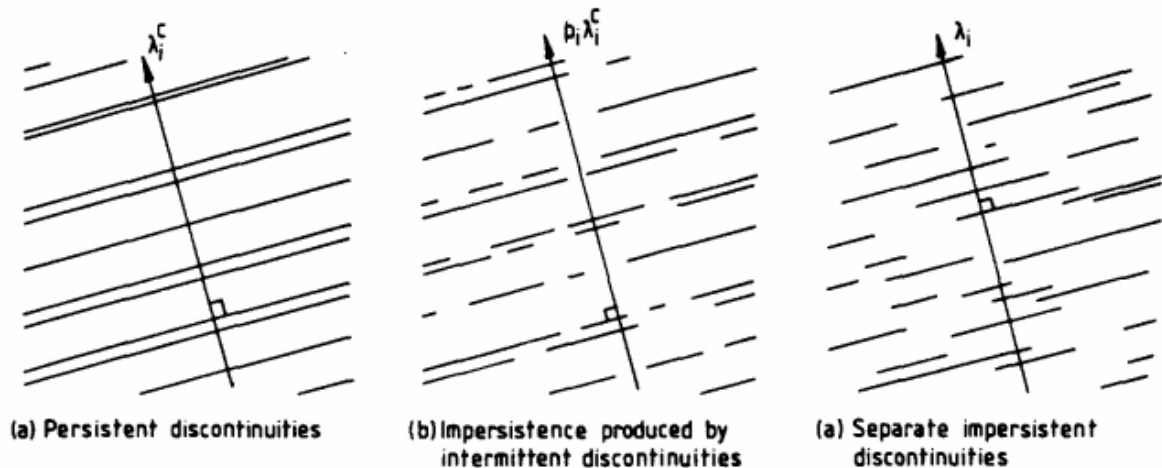


Figure 2-5: Traces produced by sets of defects intersecting a plane surface (Liu, 2019); a) Persistent defect planes; b) Intermittent defect planes; c) Separately impersistent defect planes.

Individual joints and defects may connect to form arrays with a long persistence. Joints which are adjacent to each other may overlap slightly, and where the stress regime is suitable, fractures may form in the intact rock between joints. This is common where there is little differentiation in principal stresses – i.e. an almost hydrostatic stress state. In highly differential stress states, the formation of these linkages is less common, and joint traces tend to be straight, linear, and parallel for long distances without connection (National Research Council, 1996).

The length of defects is influenced by unit thickness and stress regime, and may range from less than a meter to hundreds of meters. If thin laminae are present between layers, there may be offsets and breaks in the composite joints. Thicker units typically impede jointing, causing strata bound joint systems (National Research Council, 1996). Ghosh et al. (2018) suggested three bounding joint natures:

- Perfect bed bounded: joints traverse a single bed, terminating at boundaries on both ends;
- Unbounded: joints terminate abruptly without an apparent bed boundary; and
- Top bounded: joints are partially bound by beds on one end or the other.

2.3.5.1 Measurement

Classification of the type of persistence is important, because rock bridges between joints have a much higher resistance than the joints themselves, and thus effect block movement (Einstein, 1996). The forms of measurement for each type of persistence are:

- Persistent defects: persistence is typically obtained by assuming a flat disc shape, and assigning the diameter of this disc to be the “equivalent trace length” (Sturzenegger & Stead (2009), Lyman, Poropat, & Elmouttie (2008));
- Intermittent defects: the impersistence of a set can be quantified by a factor p_i , representing the proportion of the area of the actual defect plane compared to measurement length (including rock bridges). Spacing is then $1/p_i\lambda$; and
- For separately impersistent defects, the spacing will depend on both the number and size of separate fractures which are present.

Mean trace length can be estimated based on the following two main methodologies:

- Scanline: Measurement of semi-trace lengths along a scanline on an outcrop, measured either above or below the scanline.
- Window Sampling: End-point estimators from within any finite area, e.g. circular (Zhang & Einstein, 1998) or rectangular (Mauldon, 1998). These consider the quantity of joint traces terminating within and outside of the survey areas, and the size of the Study Area (Liu, 2019).

2.3.5.2 Analysis

For persistent jointing, if the defect shape is assumed as a flat disc, then measured trace lengths can be smaller than the joint diameter, but never larger. The actual mean diameter of the associated defects must therefore be determined from probabilistic distributions (Pahl, 1981). The most commonly applied probability functions are negative exponential, lognormal and gamma (Noroozi, et al., 2015).

2.3.5.3 Termination

The termination at each end of a fracture can be described as one of three types:

- Terminates in intact rock (i);
- Terminates on another fracture (a); and
- Obscured termination (o).

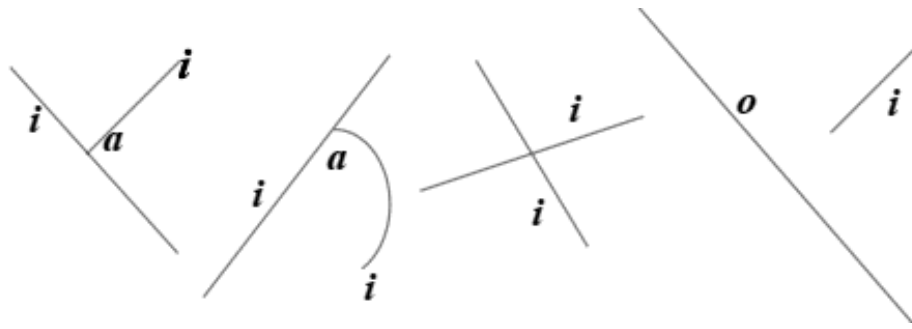


Figure 2-6: Termination of joint sets (Liu, 2019)

A termination index (T) can be defined, reflecting the percentage of joint ends terminating in intact rock. High values indicate there are many intact rock bridges, which would likely be stiffer and stronger than a rock mass with a lower index. T can be calculated based on window sampling (T_r) or the semi-trace approach (T_i), where $2T_r = T_i$ (Liu, 2019).

The type of termination which occurs for a joint can be used to determine the relative age of each joint set. The first defects to form (early defects) are typically long and straight. They depend on the regional stress field, and their development releases stress. Younger defects are typically shorter and more deflected. Hierarchical termination can be calculated for each set by comparing the termination index for each set. A lower termination index indicates an older, more pervasive set (Liu, 2019).

2.3.6 Roughness and Waviness

Defect roughness effects the mechanical behaviour of a rock mass by influencing the shear strength of a defect surface (Gigli & Casagli, 2011). The term “roughness” is typically used to describe the geometry of a defect surface, defined as a measure of the “unevenness” and “waviness” of a defect relative to its mean plane (Brady & Brown, 2005). There are two distinct components of surface roughness defined by ISRM (1978):

- Large scale waviness (first order), or curvature from planarity. This influences the direction of shear, and dilation of the surface during relative motion (Poropat, 2009). It can be qualitatively described as planar, undulating, or stepped. Henschler & Richards (2015) suggest this occurs at a scale of >500 mm; and
- Small-scale unevenness/roughness (second order), describing asparities in the joint surface. Henschler & Richards (2015) suggest this occurs at a scale of 10-100 mm.

Large scale waviness takes the form of undulations deviating from the mean plane, which due to their size are unlikely to shear off when subject to joint displacement. Under induced stress, interlocking and contact between these undulations provides additional shear resistance. Where there is shear movement, dilation will occur along these undulations.

There is some discussion around whether dilation occurs from the onset of displacement (Hencher & Richards (2015), Wyllie & Mah (2004)), or begins only after some displacement has occurred and the peak shear strength had been reached (Grasselli & Egger, 2003). Hencher & Richards (2015) state that dilation may be delayed if there is an infilling or veneer, or if the confining normal stress is high enough to prevent upwards movement.

Quantitatively, waviness in three dimensions may be sampled with a compass and inclinometer, or most commonly by placing a straight edge of length 1 m on an exposed joint plane, and measuring the maximum surface offset/amplitude at intervals along this edge (Morelli, 2014). This methodology is directionally-dependant.

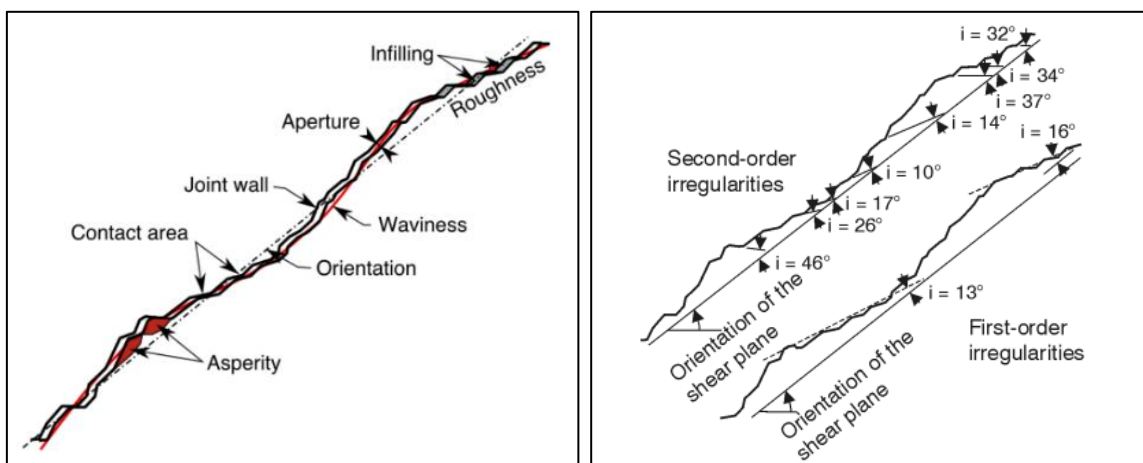


Figure 2-7: a) Diagram displaying the various features of a rough defect (Marcher & Potsch, 2019); and b) diagram displaying measurement of the first and second order irregularities, relative to the shear plane (Marcher & Potsch, 2019).

Small-scale unevenness/roughness influences the peak shear strength of the defect. If displacement occurs along the defect surface, asperities may be damaged or sheared, depending on the applied stress and the strength of the asperities. This form of roughness is typically expressed as a Joint Roughness Coefficient (JRC), measured with a profile comb and compared to standard roughness profiles proposed by Barton and Choubey (1977). This method is widely considered to be subjective and scale dependant, and does not account for the real 3D geometry of the surface, as it is looking along one direction only (Barton, 2012). Barton and Bandis (1982) proposed scale correction curves for JRC, relating laboratory size samples with insitu block sizes, however this is valid up to only 10 m in measurement length, with a maximum amplitude of 0.4 m.

The combined effect of roughness and waviness on the shear strength of a joint is often quantified as the angle at which dilation will occur if shear movement is applied to a joint surface. This dilation angle (i) is measured from the mean defect plane (Figure 2-7), and is discussed in Section 2.4.

2.3.6.1 Surface Condition

Joint roughness is influenced by surface texture, weathering and any mineral coating on the joint surface (Hencher & Richards, 2015). Weathering typically begins along and adjacent to defect surfaces, which may result in a reduced roughness value (Wyllie & Mah, 2004). Weathering processes may also cause progressive rock mass weakening, particularly in proximity to defects. For this reason, Schmidt hammer testing on defect surfaces may give a better approximation of joint rock strength than UCS testing of unweathered samples.

Water acts as the main erosive agent when penetrating through joints in limestones, working with constant dissolution and disgregation on the adjoining intact rock (Santo, et al., 2007). This can alter surface roughness, and can enlarge defects (increasing aperture). Joint surfaces may also separate when there is a reduction in confining stress.

2.3.7 Sources of Error in Quantification

It can be difficult to reduce geometrically complex situations into a concise and useful form (Hudson & Priest, 1979). It is not practically possible to take enough measurements to completely characterise a rock mass without uncertainty, and the quantification and understanding of that uncertainty is critical (Lyman, et al., 2008).

Lyman et al. (2008) suggested that a statistical estimation process be used to define joint properties as a range rather than a single value, accounting for uncertainties. They suggested that uncertainty may be separated into two components – stochastic variability, and the absence of knowledge. Stochastic variability is most commonly measured by estimating confidence limits for a given parameter, expressed as a probability distribution. Mathematical models of probability distributions then define the probability that a stochastic process will lie within certain ‘confidence’ limits (Lyman, et al., 2008).

Errors relating to classical measurement techniques are typically well understood, and methods of dealing with these errors have been developed in the past. However, new methods of measuring spatial data within 3D models raise new sources of uncertainty which have not yet fully been addressed (Lyman, et al., 2008). These uncertainties include:

- Resolution of remote imaging may not be fine enough to define smaller features;
- “Noise” from vegetation, talus or other objects may muddy results;
- Features which do not have a physical relief cannot be reflected in point clouds.

Using a fusion of image data and point cloud data improves the mapping of defects which appear as traces (Zhang, et al., 2019);

-
- Surfaces measured with LiDAR may contain under-sampled domains due to limited sensor range, high light absorption, and occultations during scanning (Dong, et al., 2020); and
 - Constructing meshed defect surfaces from point clouds may neglect small features, and distort and mis-represent complex shapes (Gigli & Casagli, 2011).

Virtual scanline mapping is often utilised in conjunction with 3D modelling. This methodology is subject the same forms of measurement bias as physical scanline measurements, although in different proportions. Zhang and Einstein (1998) outline the following forms of measurement biases relating to scanline measurements:

- Orientation Bias: The probability of a defect appearing in an outcrop depends on the relative orientation between the outcrop and the defect. It is best to view two perpendicular faces to view all defect sets;
- Size Bias: Larger defects are more likely to be sampled than smaller defects;
- Truncation Bias: Very small trace lengths are difficult to measure, and are typically not recorded below a cut-off length. In data from remote sensing sources the resolution of the source will impact the size of defect physically visible; and
- Censoring Bias: Long defect traces may extend beyond sight, so persistence and termination cannot be determined. The influence of censoring bias decreases as the size of the sampling window increases (Zhang & Einstein, 1998). In large-scale 3D models this bias is therefore reduced drastically.

A further source of error in any outcrop measurement is that joints observed at outcrops may not be reflective of joint conditions further within or underlying the outcrop. Joints at outcrop faces result from stress release, weathering, or a host of other surface activities (blasting, quarrying), which may obscure the relevant sub-surface joint related information. Consideration must be given to the differentiation of fractures which only exist at outcrops and those present in the shallow or deep subsurface (Ghosh, et al., 2018).

It can often be difficult to define whether a joint trace belongs to a single joint or multiple joints. This can change based on the scale of view. Looking from a large distance (e.g. satellite imaging) a joint trace may appear to be a single joint, however viewed up close it may be constructed of several joint traces formed from linked or unlinked segments (Ghosh, et al., 2018). Assessments of joint trace length and spacing in this case require significant geological/engineering judgement.

2.4 Shear Strength Assessment

The shear strength of defects influences the behaviour of rock masses by controlling the resistance to movement along a plane. Shear strength comprises both friction and cohesion, but whilst cohesion is broken at small strains, friction is mobilised at larger strains and remains to the end of shear deformation (Barton, 2012). Hencher and Richards (2015) list the components of shear strength as:

1. True cohesion: resulting from the shearing of intact rock bridges;
2. Roughness/waviness: field scale roughness, causing interlocking and dilation, comprising:
 - a. First order waviness: large-scale undulations and waviness (>500 mm); and
 - b. Second order waviness: surface roughness (10-100 mm).
3. Smaller asperity interaction and textural friction (basic friction) at the scale of rock core and laboratory test samples. This derives partly from adhesion at the areas of contact, and textural interlocking which leads to shearing and deformation. This is independent of the size of surface being tested.

Consideration of minor asperities over profile lengths less than 100 mm can be incorporated into JRC, and are typically measured in direct shear testing.

There are two potential approaches for determining the shear strength of joints –direct shear tests, and empirical estimation methods (Shigui, et al., 2011). Direct shear tests are expensive, time consuming and complex, and require a large number of tests to be considered representative. Hencher and Richards (2015) state that direct shear tests typically give inconsistent shear strength envelopes, even with the same JRC, and even for the same sample tested in different directions. They state that results from direct shear tests are unlikely to reflect the shear strength of defects insitu.

Considering the unreliable nature of shear strength testing, it is common for engineers to rely on empiricism and literature rather than sampling and direct analysis (Hencher & Richards, 2015). Empirical estimation methods are quick, inexpensive and simple, and can resolve issues of sample representation and shear strength anisotropy (Shigui, et al., 2011). However, these approaches also lack sensitivity with respect to geological variability (Hencher & Richards, 2015).

2.4.1 Influences on Shear Strength

Frictional joint shear resistance is influenced by several factors:

- Normal stress;
- Amount of shear displacement;
- Friction of the rock material: in the form of basic or residual friction angles;
- Roughness and waviness: as discussed in Section 2.3.2;
- Aperture: controls contact area, deformability and water pressure;
- Infilling: controls contact area;
- Strength and deformability of the intact rock;
- Boundary conditions: whether movement is constrained or unconstrained; and
- Petrographical properties: wear, hardness;

In an outcrop, normal stress is calculated based on block volume and surface area. For sub-vertical joints the normal stress may be minimal. When water pressure is present in joints it acts to reduce the normal stress, thus reducing the joint shear strength (Hoek, 2006).

The friction angle of a joint surface is typically described using the basic friction angle, the residual friction angle, and the dilation angle. The basic friction angle (ϕ_b) is empirical, based on scale and shear direction. It is a function of surface texture, weathering and mineral coating (Hencher & Richards, 2015). The basic friction angle can be highly variable even within samples of the same rock, cut in the same method (Hencher & Richards, 2015). Pötsch (2019) suggested that limestone has a basic friction angle of 25° to 40°, Hencher & Richards (2015) suggested 40° to 50°, whilst Singh & Geol (2012) suggested 31° to 37° and 27° to 35° for dry and wet surfaces respectively. Dong et al. (2020) assumed a base friction angle of 30° for Kaili Limestone.

The residual friction (ϕ_r) angle occurs after high shear displacements, with degraded asperities and an almost planar shear surface. For most rock types under low to intermediate normal stresses, the residual friction angle is equal to the basic friction angle (ϕ_b) (Morelli, 2014), unless foliation or slickensides are present (Marcher & Pötsch, 2019). Barton (2012) enthusiastically defended his analysis that the residual friction angle may indeed be several degrees lower than the basic friction angle, which he proposed initially in 1977 (Barton & Choubey), and which can be defined as:

$$\phi_r = (\phi_b - 20) + 20 \cdot \left(\frac{r}{R}\right)$$

where r is the Schmidt rebound number on wet and weathered surfaces, and R is the Schmidt rebound number on dry and unweathered surfaces.

Hencher and Richards (2015) stated that residual strength values reported from laboratory tests are generally arbitrary and very particular to the sample and testing procedure. They look poorly on numerical relationships between basic and residual friction angles, and recommend proper geological characterisation, testing and analysis.

The dilation angle (i) depends on surface roughness, asperity strength, and normal stress (σ_n). It includes both first and second degree roughness. The effective dilation angle is that through which the centre of gravity of the sliding mass moves, not the inclination angle of individual asperities on the defect surface (Hencher, 1995). Bandis et al. (1981) found that dilation was scale dependant, recording a rapid reduction in dilation with defect length. However, Hencher and Richards (2015) disagreed that the dilation angle is scale dependant, maintaining that an entire block of any size may dilate over an asperity.

Dong et al. (2020) suggested a method of calculating the dilation angle (i) from high resolution point cloud data. After calculating the Hough's normals for each point within the surface, the normals are plotted on an equal area stereonet. The peak dilation angle is then estimated as the angle between the cone axis (mean joint plane) and the surface formed by the maximum scatter of the surface normals. Dong et al. found a peak dilation angle of 14° in Kaili Limestone.

The friction angle mobilised in a certain situation depends on surface roughness and normal stress. When defects with roughness or waviness undergo shear, asperities resist movement. As shear occurs the sample displaces along asperities, dilating perpendicular to the shearing direction. If the shear stress exceeds the strength of the asperities (σ_{ns}) they are degraded or may be completely sheared. The degree of shearing depends on the magnitude of normal stress compared to the joint rock strength, and the amount of shear displacement. With increasing normal stress and displacement asperities are sheared. The dilation angle decreases, and the mobilised friction angle reduces to the residual friction angle (Figure 2-8).

Small scale asperities are often completely sheared, while larger scale undulations are unlikely to fully shear but provide resistance only until dilation carries the block over the undulation. Therefore, in high stress conditions, first order waviness only should be used for design calculations, as the smaller second order asperities will quickly shear (Wyllie & Mah, 2004).

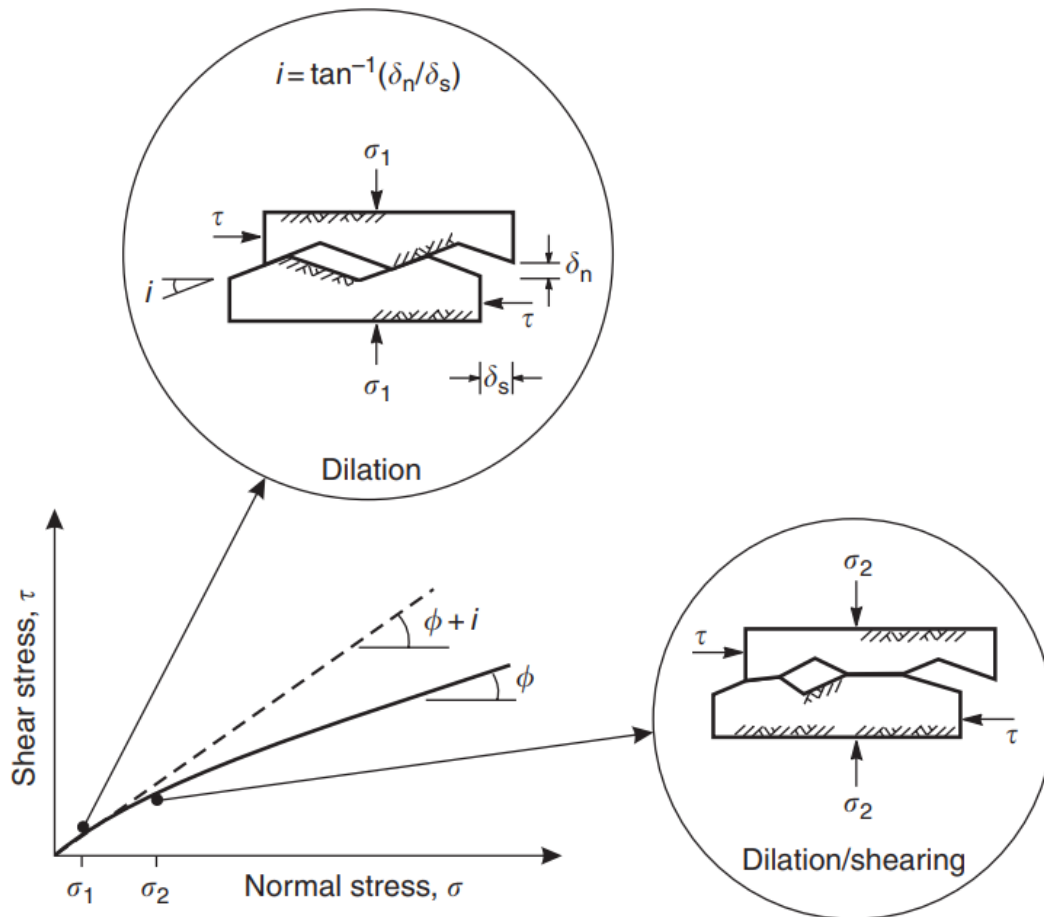


Figure 2-8: The effect of surface roughness and normal stress on the friction angle of a discontinuity surface (Wyllie & Mah, 2004).

The strength of asperities is typically defined by the Joint Compressive Strength (JCS). JCS can be taken as the Unconfined Compressive Strength (UCS) of intact rock, or can be tested using a Schmidt hammer rebound test (Hoek, 2006). Dong et al. (2020) investigated representative strength values for Kaili limestone, and found that slightly weathered limestone had a mean UCS of 75 MPa, and that moderately weathered limestones have a mean UCS of 33 MPa. Slightly weathered samples had only slight discolouration, and were taken from the interior of failed blocks. Moderately weathered samples were taken from the weathered and altered intact rock adjacent to highly weathered joint surfaces. These surfaces had brownish-red colours from the passage of water through open joint systems, where calcites had been removed by dissolution.

Dong et al. (2020) also undertook shear strength testing along joint surfaces in Kaili limestone, deriving a friction angle of 58° and cohesion of 11.89 MPa for fresh samples, and a friction angle of 35° and cohesion of 9.56 MPa for weathered samples, with an assumed residual friction angle of 30° . They adopted a density of 2.5 g/cm^3 (unit weight of 24.5 kN/m^3) for weathered blocks.

2.4.2 Numerical Definition of Shear Strength

The shear strength (τ_{max}) of a defect with joint roughness was described by Patton in 1966 as dependant on the base friction angle (ϕ_b) and the peak dilation angle (i) as follows:

$$\tau_{max} = \sigma_n \cdot \tan(\phi_b + i)$$

This approach did not account for the gradual change in shear strength with normal stress (Hoek, 2006), so in 1977 Barton and Choubey suggested a curved failure envelope for rough defect surfaces, which was refined further by Barton and Bandis (1990). This relationship considers the normal stress, JRC and JCS in an empirical relationship. This includes the second order roughness of a joint surface (in the form of JCS), but does not account for first order waviness, or the effect of rock bridges where present.

$$\tau_{max} = \sigma_n \cdot \tan\left(\phi_r + JRC \cdot \log\left(\frac{JCS}{\sigma_n}\right)\right)$$

As discussed in Section 2.3.5.1, the cohesive component of shear resistance along a joint plane will be a function of the quantity of rock bridges which are present (Einstein, 1996).

2.4.3 Shear Strength Reduction Technique

The shear strength reduction technique in finite element slope stability analysis involves the search for a stress reduction factor (SRF) which brings a slope to the very limit of equilibrium – i.e. on the edge of failure (Hammah & Corkum, 2004).

The factor of safety (F) in slope stability analysis is defined as by Duncan (1996), as:

$$F = \frac{\text{Shear strength of material}}{\text{Shear strength required for equilibrium}} = \frac{\tau}{\tau^*}$$

Situations with a factor of safety above one are considered to be stable (under current conditions) while those with a factor of safety below one are unstable and should not exist under the modelled conditions. Situations with a factor of safety of one are considered to be in equilibrium.

Hammah & Corkum (2004) state that Shear Strength Reduction (SSR) techniques assume a Mohr-Coulomb strength envelope, defined through cohesion (c') and friction angle (ϕ'). This linear envelope can easily be factored to find a reduced shear strength, as follows:

$$\frac{\tau}{F} = \frac{c'}{F} + \frac{\tan\phi'}{F}$$

Hammah & Corkum (2004) outlined the following steps of the SSR technique:

1. Develop a model of a slope, using the appropriate material deformation and strength properties. Compute the model and record maximum total deformation;
2. Increase the value of F (or SRF) and calculate the factored Mohr-Coloumb material parameters as per the equation above;
3. Re-enter new Mohr-Coulomb parameters. Rerun. Record maximum deformation;
4. Repeat steps 2 and 3 until the finite element model does not converge on a solution – i.e. continues to reduce the material parameters until slope failure; and
5. The critical F will be that just beyond where failure occurs.

Hammah et al. (2005) investigated the influence of Young's modulus and Poisson's ratio on deformations and factors of safety when undertaking a shear strength reduction analysis. They determined that although these parameters affect the magnitude of deformation, they had limited impact on the factor of safety. Additionally, they found that the angle of dilation (large-scale waviness) does not have a significant impact in slope problems, due to the low confinement environment. This lack of normal stress means that dilation is free to occur, and that contact and interlocking of undulations is reduced. These factors do, however, have a large impact on deformation values.

2.4.4 SSR Analysis in RS3

The SSR method lends itself well to automated calculations, and has long been adopted in Finite Element Modelling (FEM) software, particularly for soils and heavily jointed rock. As FEM software is a continuum analysis method, there was some question as to its suitability to calculate large displacements of blocks, which would be more readily modelled in Discrete Element Modelling (DEM). However, as FEM programs have evolved it has become possible to incorporate joint elements into FEM models, substantially increasing the allowable degrees of freedom (Hammah, et al., 2007).

Hammah et al. (2007) determined that FEM SSR methods accurately determine stability results for both unreinforced and reinforced slope problems. They state that FEM SSR is a credible alternative to DEM in slope stability problems with blocky rock masses (including planar, wedge and toppling regimes), being able to automatically determine critical failure mechanisms with no prior assumptions as to modes, shapes or locations of these mechanisms. Additionally, FEM allows the consideration of both movement along defects, and shear failure of intact rock, which can allow it to model rock bridges.

The RocScience program RS3 is a 3D Finite Element Modelling software program used for modelling slopes, tunnels and support design, foundations and groundwater. It includes a fully-automated shear strength reduction feature, which allows it to be used in complex slope stability analysis (RocScience, 2020). This feature automatically iterates through reduced Mohr-Coulomb parameters, converging to define the critical reduction factor to achieve a factor of safety at equilibrium.

2.5 Kinematic Analysis

Defect controlled rock slope failures occur where structural defects in rocks and a topographic slope intersect in such a way that block movement is kinematically possible. The type and likelihood of rock slope failure is determined by the geometrical relationship between defects and the slope face, and the shearing strengths of structural defects.

Varying topographical and structural conditions can lead to the occurrence of multiple failure modes, meaning that in larger Study Areas a spatially distributed deterministic assessment of rock slope instability is required (Ghosh, et al., 2010). Data on the orientation of structural defects in rocks, and terrain geometry, is essential in the kinematic testing of defect-controlled rock slope faces, and thus in rock slope instability assessments (Ghosh, et al., 2010).

An assessment of kinematically possible failure mechanisms can be undertaken on a stereographic projection, considering the slope angle, defect sets, and shear strength of the defects. The major rock slope failure modes are:

- Planar sliding;
- Wedge sliding;
- Flexural toppling; and
- Direct toppling.

In rock masses with a high density of stress release cracks in the outer zone, toppling failures are the most common (Gutiérrez, et al., 2014). All rock slope failure mechanisms require release surfaces on either sides of the block to facilitate kinematic failure development, unless intact rock failure occurs. These may take the form of joint surfaces or other defects within the rock mass.

2.5.1 Planar Sliding

Planar sliding involves slip along a persistent defect plane or surface. Failure is kinematically constrained to certain directions by the orientation of bedding or joints. Planar failure is kinematically possible if the dip of a controlling structural defect is steeper than the residual friction angle of that defect, but shallower than the apparent inclination of the slope face relative to defect plane normal (Goodman & Bray, 1976). Lateral limits on planar sliding are typically set to 20° , meaning that the slope face and defect plane must have a strike of within 20° of each other (Norrish & Wyllie, 1996). Lateral release planes are also required.

The planar failure model as outlined by Norrish and Wyllie (1996) is included in Figure 2-9 below. A representation of the planar failure mechanism in stereographic projection is included in Figure 2-10 below.

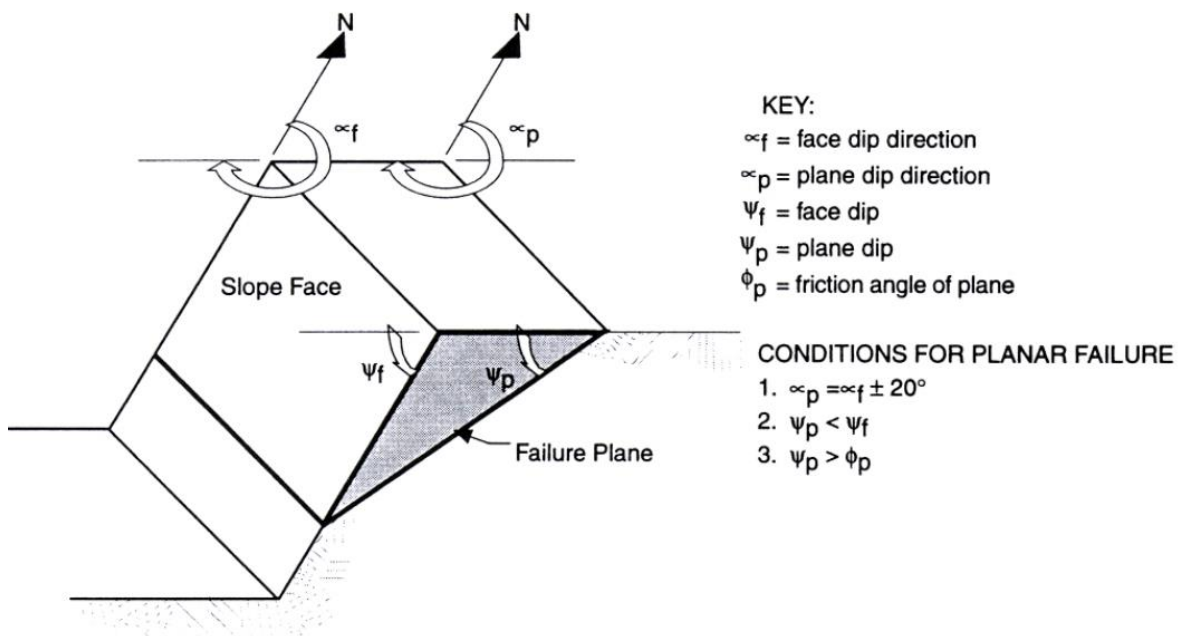


Figure 2-9: Planar failure model (Norrish & Wyllie, 1996)

2.5.2 Wedge Sliding

Wedge sliding involves the simultaneous slip of a block along the intersection line of two defect planes. Wedge failure is kinematically possible if the plunge of the intersection line is larger than the residual friction angle of the defect surfaces, but smaller than the apparent inclination of the slope face relative to defect plane normal (Norrish & Wyllie, 1996). The dip direction of the two defect planes controls which plane sliding will occur along.

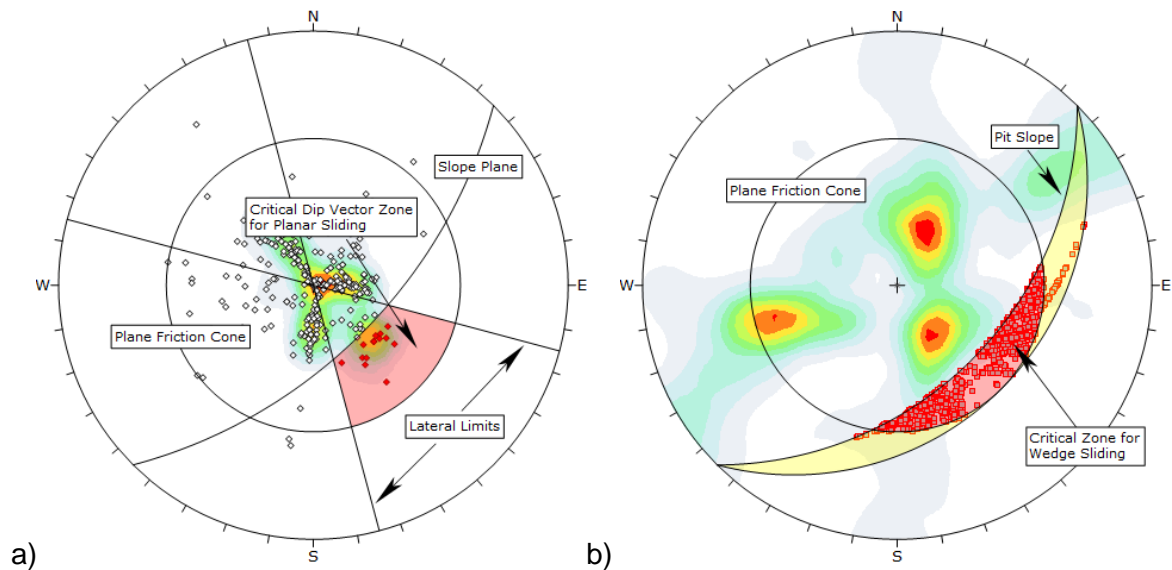


Figure 2-10: Stereographic method of kinematic analysis; a) Planar sliding, with pole vectors; b) Wedge sliding, with intersection points.

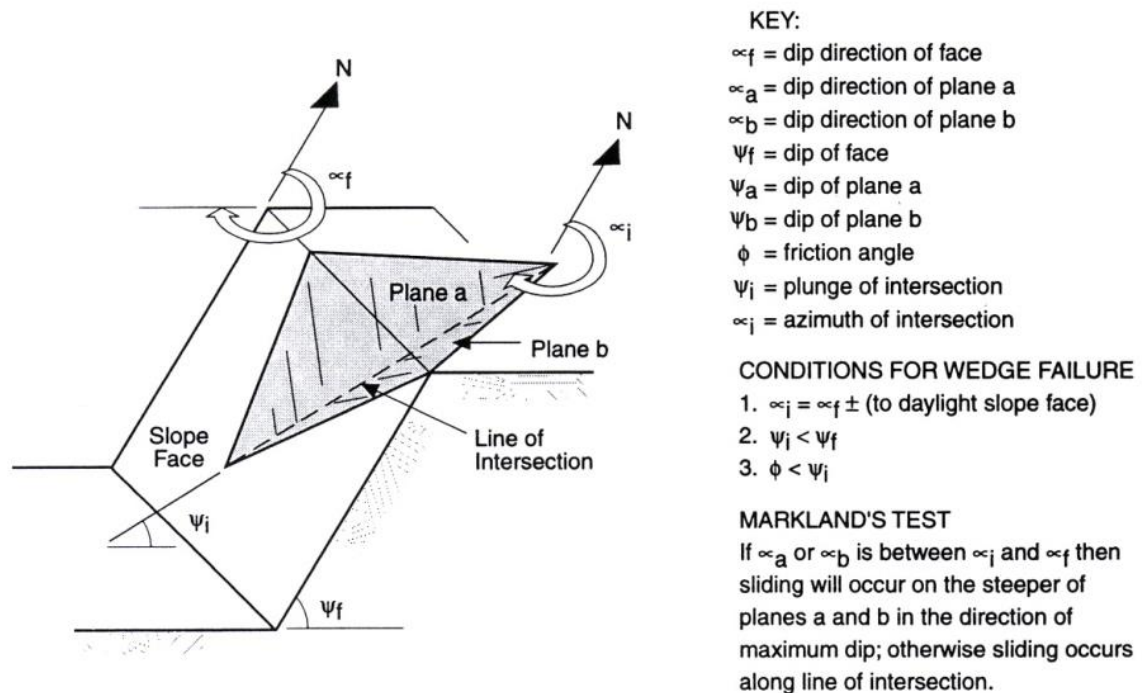


Figure 2-11: Wedge failure model (Norrish & Wyllie, 1996)

2.5.3 Toppling

Toppling is a failure mode involving the forward rotation of a block about an edge. This mode typically occurs where there are regularly spaced, parallel defects or foliation dipping into the slope, or tension cracks from the surface (Goodman & Bray, 1976). Toppling is particularly heightened by the presence of high-inclination defect planes, especially where these joints are open. Release surfaces are required for toppling to occur.

Two main modes of toppling may occur (Goodman & Bray, 1976):

- Flexural toppling; and
- Direct toppling.

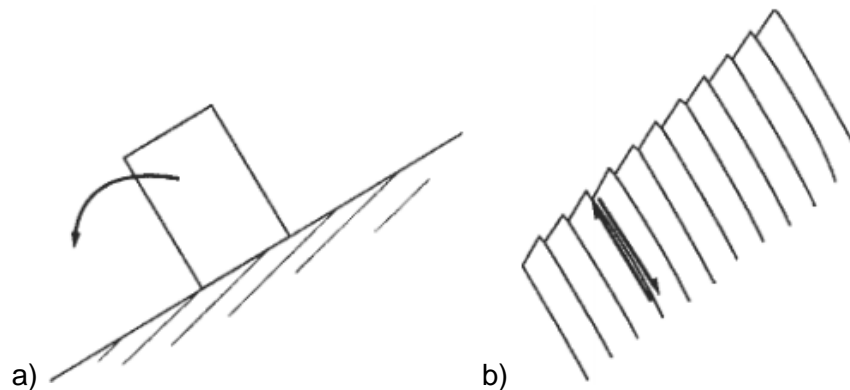


Figure 2-12: a) Direct toppling; and b) Flexural toppling (Hudson & Harrison, 1997)

Flexural toppling occurs due to bending stresses in interacting rock columns, each formed by a single set of steeply dipping defects. Columns act as cantilevers, and are free to bend forward under their own weight. This induces inter-layer slip, and causes tensile and compressive bending stresses (Goodman & Bray, 1976). Failure is initiated when the tensile stress in the column toe exceeds the tensile strength of the rock. Flexural toppling is kinematically possible where the slope dip is larger than the defect plane normal plus the friction angle. Exposed lower surfaces of overhanging beds are common. Analyses for flexural toppling are often run with lateral limits of 30° , from the normal to the slope plane (Norrish & Wyllie, 1996).

Direct block toppling occurs where the centre of gravity of a block lies outside the outline of the block base, developing a critical turning moment. This occurs where joints are widely spaced. Blocks towards the base of the slope are loaded by blocks above, creating a “stairway” rising upwards from each progressive layer (Goodman & Bray, 1976).

Base joints/defects delineate the base of blocks, and the inclination and shear strength of this base surface together with the block geometry (aspect ratio), will determine the nature of the instability. Sliding of blocks can also occur, where the inclination of the base joint is above the surface friction angle. The combination of sliding and toppling results in four kinematic possibilities, displayed in Figure 2-13 below, and outlined as follows:

- No sliding and no toppling (stable);
- Sliding but no toppling;
- No sliding, but toppling; and
- Sliding and toppling.

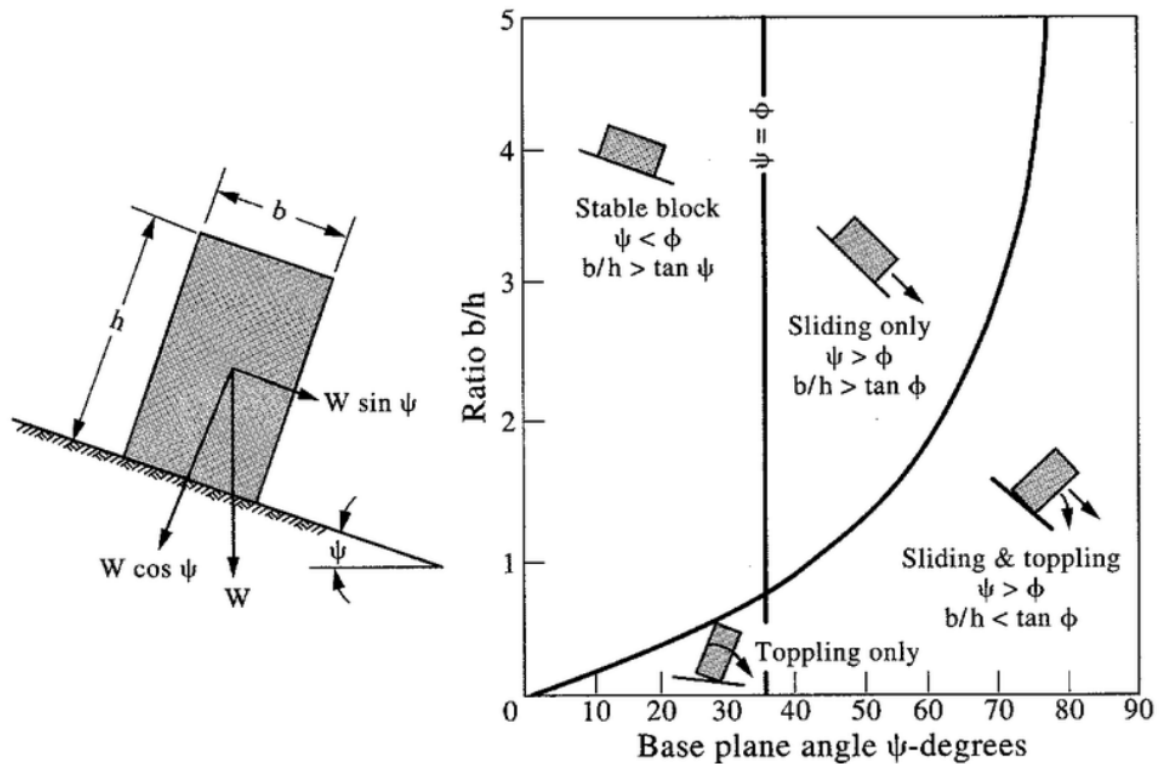


Figure 2-13: Sliding and toppling instability of a block on an inclined plane (Hoek & Bray, 1977)

Analyses for direct toppling are typically run with lateral limits of 20° , from the normal of the slope plane (Norrish & Wyllie, 1996). Outside of these limits oblique toppling may occur. A representation of flexural and direct toppling failure mechanisms in stereographic projection is displayed in Figure 2-14.

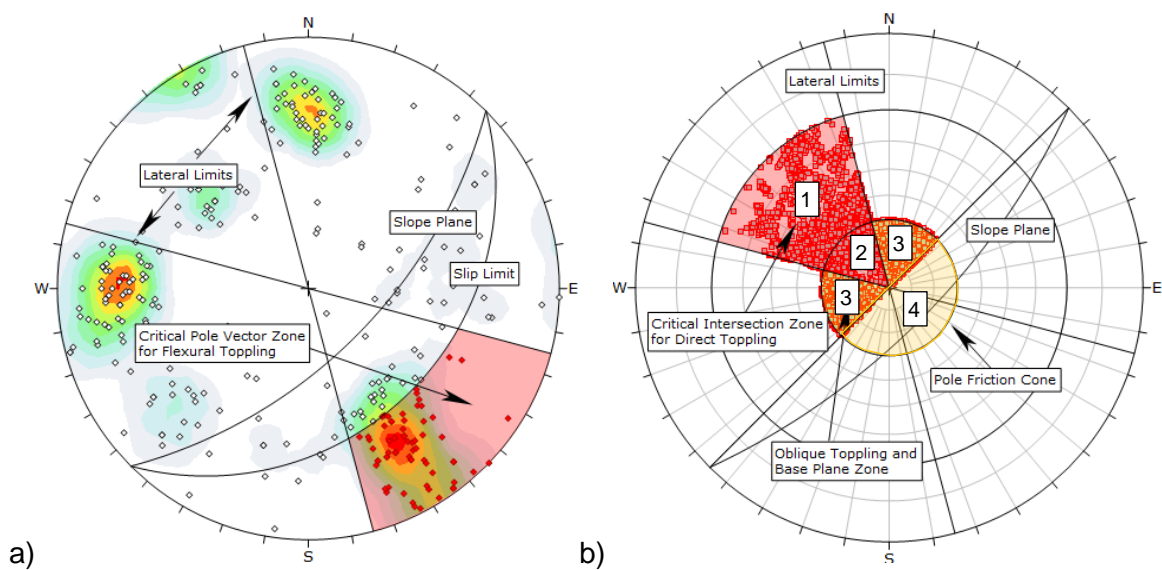


Figure 2-14: Stereographic method of Kinematic analysis (RocScience, 2020); a) Flexural toppling, with pole vectors; b) Direct toppling, with intersection points.

Stereographically, a direct toppling analysis can be separated into four modes of failure, each represented in Figure 2-14:

- Base Plane Sliding: Zone 1. Includes intersections which lie outside of the friction cone, but within the lateral limit, representing toppling release planes which are also sliding planes. Combined sliding and toppling modes may occur here simultaneously;
- Direct Toppling: Zone 2. Includes intersections which are both within the friction angle and the lateral limits, and so are subject to direct toppling;
- Oblique Toppling: Zone 3. Includes intersections which are sub-vertical, where toppling in a direction outside of the lateral limits is possible; and
- Backward Direct Toppling: Base planes which dip into the slope may still act as release planes for direct toppling blocks. The half-circle region opposite zones 2 and 3 (zone 4), within the friction cone, may also represent potential base planes (RocScience, 2020). DIPS does not calculate these poles in the direct toppling analysis results.

2.5.4 Probabilistic Analysis

Probabilistic analysis allows the consideration of the statistical distribution of geometric and joint set parameters, including slope orientation, joint orientation, spacing, persistence and shear strength. These input parameters may be defined using probabilistic distributions such as Fisher's K for orientation, normal distributions, logarithmic distributions etc. The resulting analysis considers combinations of these variables, then returns a factor of safety distribution from which a probability of failure is calculated for the given failure mechanism.

The RocScience suite of software designed for slope stability analysis includes RocPlane, SWedge and RocTopple for planar sliding, wedge sliding and toppling failure mechanisms respectively. The programs allow the evaluation of geometry and stability of formed blocks. These programs are predominately two-dimensional (other than SWedge), and are limited in the geometries which can be modelled. Nonetheless, they provide a simple and straightforward analysis for multiple failure mechanisms.

3 Data Collection and Processing

In December 2018 a data collection campaign was undertaken in the Kaili region, Guizhou Province, Southern China. This campaign focused on slope faces which had a pronounced risk of rockfall, and was completed under the leadership of Qian Liu. The aim of the campaign was to allow for remote outcrop characterisation using UAV photogrammetry. Field investigations were focused on the site of a 2013 rockfall near Long-Chang and an additional seven locations. The focus of this thesis is the site named “JK1”, the Study Area.

A data set was provided as reference for this thesis, comprising both a 3D point cloud of the Study Area, and a 3D real scene model generated from UAV photo capturing.

The following sections outline the collection and processing of this data, as completed by others. This information was provided by Qian Liu as part of the dataset for this thesis.

3.1 Data Collection

Preliminary site inspections determined that the area to be imaged had a length of approximately 1260 m and a width of approximately 820 m.

Data was recorded with DJI photo capturing, based on tilt photogrammetry. DJI (Dai-Jiang Innovations) supplies approximately 70% of the consumer drone market, and provide unmanned aerial vehicles for aerial photography and videography (Joshi, 2019). Considering the large slope height difference in the Study Area, the DJI Phantom4 Pro drone was chosen to carry out the tilt photogrammetric survey. Phantom has the advantages of strong photography performance, high flight flexibility and long endurance. In order to ensure a thorough coverage of the slope object, UAV Manager was used to plan and design the flight route. After starting up, the DJI Phantom4 Pro drone entered the planned route mission to carry out oblique photogrammetric surveys.

The flight route was crossed and contoured, with an overlap rate of 80% and a sensor tilt angle of 45°. The flight route is displayed in Figure 3-1 below. The line height is 270 m, with a total flight length of 17.7 km. A total of 463 oblique images were captured in a 30 minute flight, with a ground sampling distance of 10 cm per pixel. GPS coordinate information and camera attitude were recorded for each image, using the WGS84 coordinate system and ellipsoid. The imaged area lay in the elevation range of 500 m to 900 m.

After the pre-defined flight mission was completed, and prior to leaving site, the image data was checked to find any locations which may not have been properly imaged. In order to get a complete coverage of the whole slope surface, manual flight was used for the supplementary shooting of an additional 74 images.

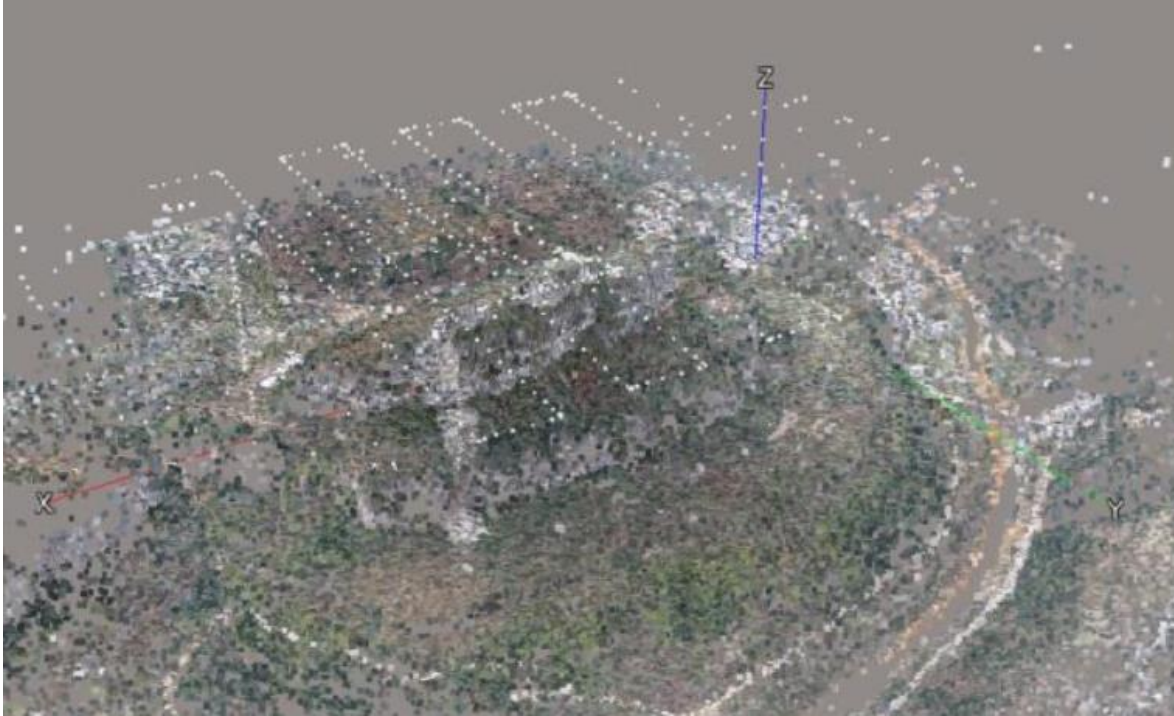


Figure 3-1: Representation of drone flight path and cloud of images

3.2 Processing

The 3D real scene model was reconstructed from collected images using Bentley's Context Capture software. A project was created into which images containing spatial location information were imported. Aerial triangulation was completed, modelling boundaries were set, and the coordinate system was defined. Reconstructions of the 3D real scene model and 3D point cloud were then undertaken.

The open source program CloudCompare Version 2.9.1 was used to display, process and render the collected point cloud (Anon., 2020), assigning HSV colourings as outlined in Section 2.1.2.1.

Figure 3-2 to Figure 3-5 below compare the two provided datasets – the HSV coloured point cloud, and the rendered 3D real scene model.

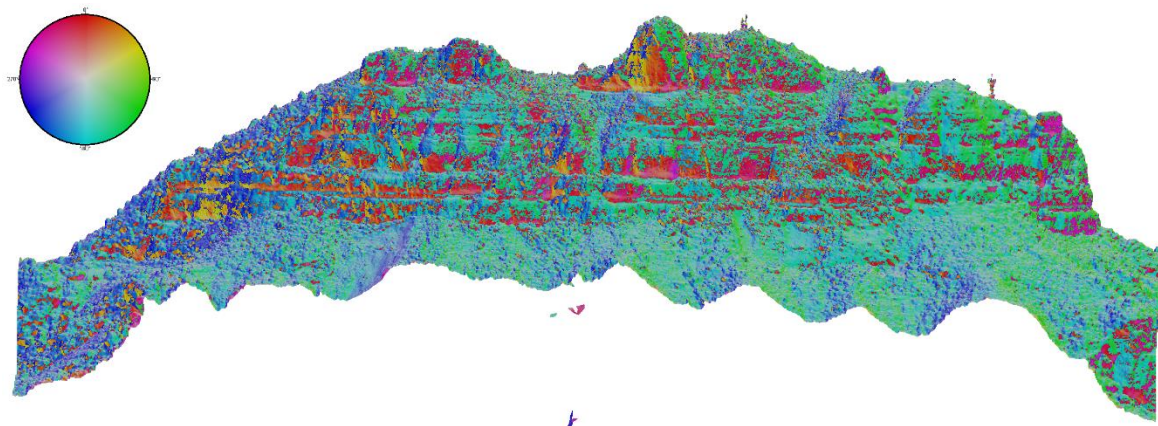


Figure 3-2: Point cloud from SfM, in Context Capture, looking south, top to first bench only. Viewed in Cloud Compare.



Figure 3-3: Rendered 3D real scene model, looking south, viewed in ContextCapture

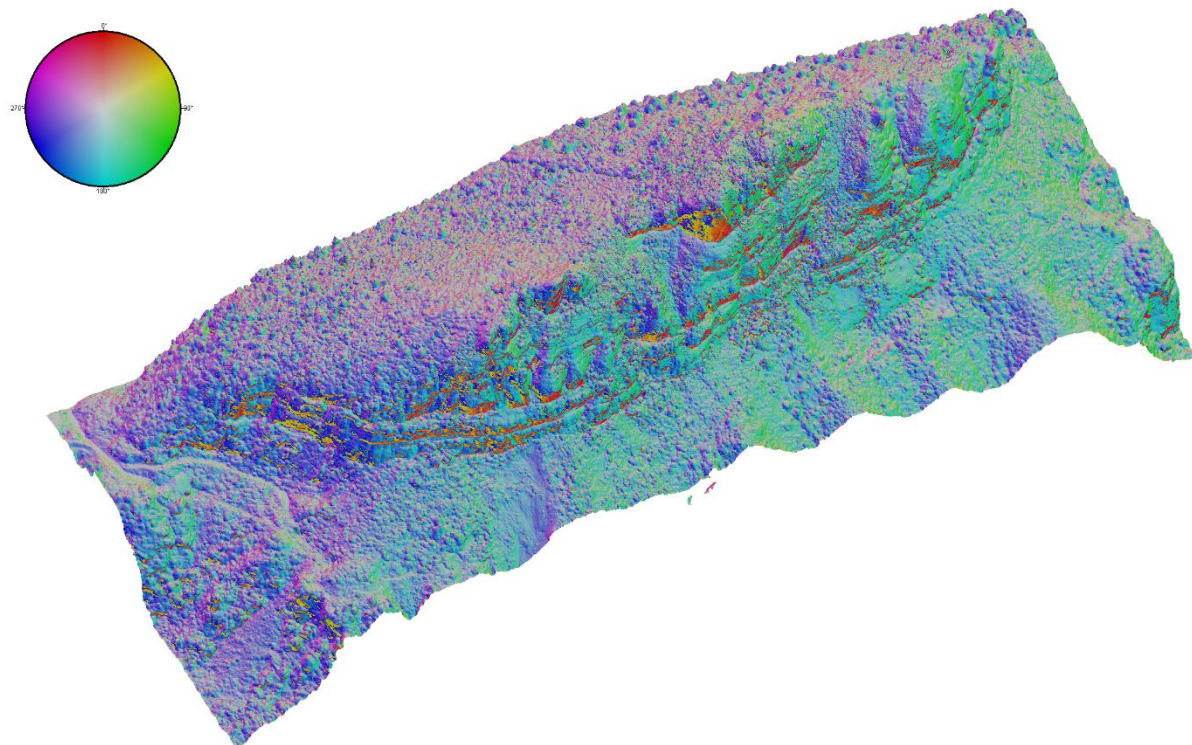


Figure 3-4: Point cloud from SfM, in Context Capture, from above, top to first bench only. Viewed in Cloud Compare.



Figure 3-5: Rendered 3D real scene model, from above, viewed in ContextCapture

4 Characterisation of Defect Sets

When modelling the engineering implications of defects within a rock mass, it is necessary to numerically represent defect properties.

Defects within a rock mass can typically be grouped into sets, with characteristics relating to the geometric attributes of that set (orientation, length, spacing, persistence, roughness, waviness) (Hammah, et al., 2008). An understanding of these numerical characteristics allows the generation of defect networks in numerical modelling, and can allow the simulation of mechanical behaviour for each member of a network (Hammah, et al., 2008).

4.1 Method of Orientation Measurement

To determine the most appropriate form of orientation measurement for this dataset, three different measurement methods were trialled on a small sub-set of the site area. Although data had been pre-processed, obstructions such as vegetation were still present. Automated cloud cleaning is still a challenge (Dong, et al., 2020), and considering the size of the Study Area, the manual removal of such obstructions was not feasible. As such, the focus on a small segment of the Study Area allowed the manual removal of vegetation and a thorough assessment of appropriate measurement techniques. This area, referred to as the “Rockfall Area”, covers a portion of the slope where a rockfall has recently occurred.

The location of the Rockfall Area is displayed in Figure 4-1. The point cloud from this area has been trimmed to remove vegetation, as displayed in Figure 4-2 and Figure 4-3.



Figure 4-1: Study Area, with rockfall zone shown in red.



Figure 4-2: Delineation of "Rockfall Area". Regions with vegetation cover obscuring the rock surface have been excluded from the analysis, and are outlined in white.

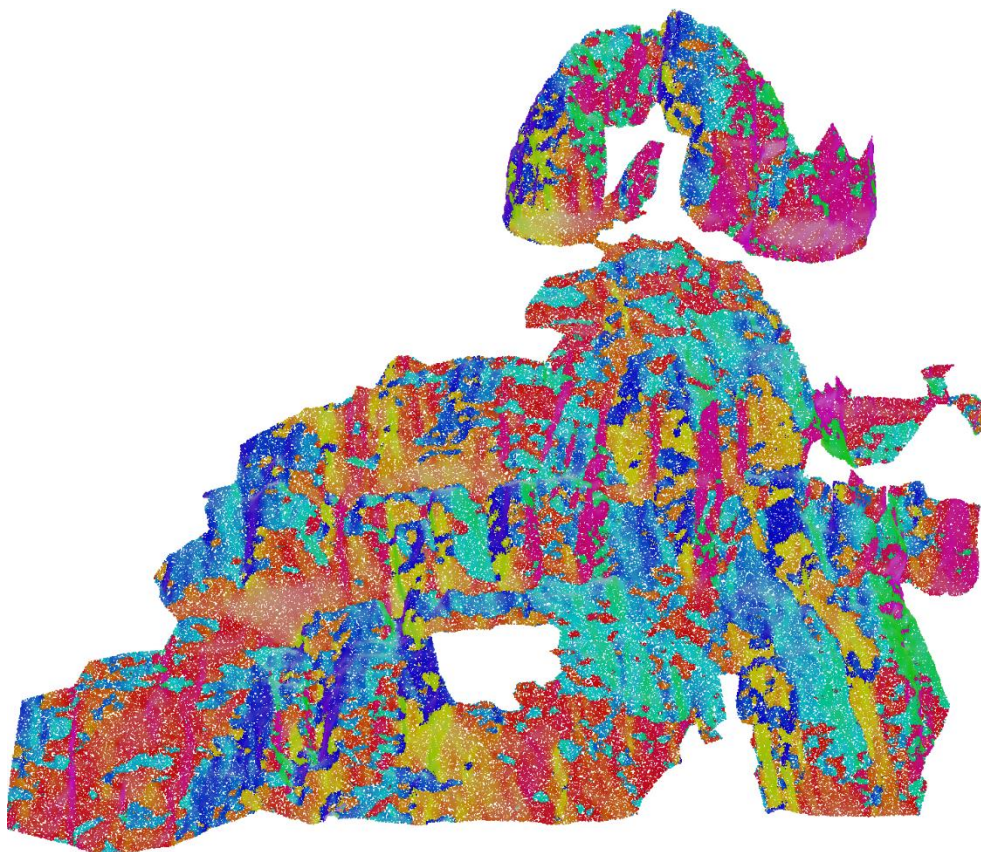


Figure 4-3: Point cloud of Rockfall Area - colours indicating the orientation of Hough's Normal for each point

Orientation was measured using three methods, using measurement tools available as plug-ins in the CloudCompare program (outlined in Section 2.3.3.1), as follows:

- Compass tool (manual);
- Facets (KD) tool (automatic); and
- Facets (FM) tool (automatic).

The Compass tool was used to manually capture 315 measurements from the point cloud in this test region. The raw point cloud was compared with the ContextCapture 3D real scene model to ensure that measurement locations were representative of exposed joint surfaces. Measurements were taken on a range of large and small defects. Where defects had an apparent waviness, the measurement plane was extended to take an average orientation across the surface. The compass tool generated a numerical list of measurement information (dip and dip direction) which was exported to csv. Measurement locations are shown in Figure 4-4 below.

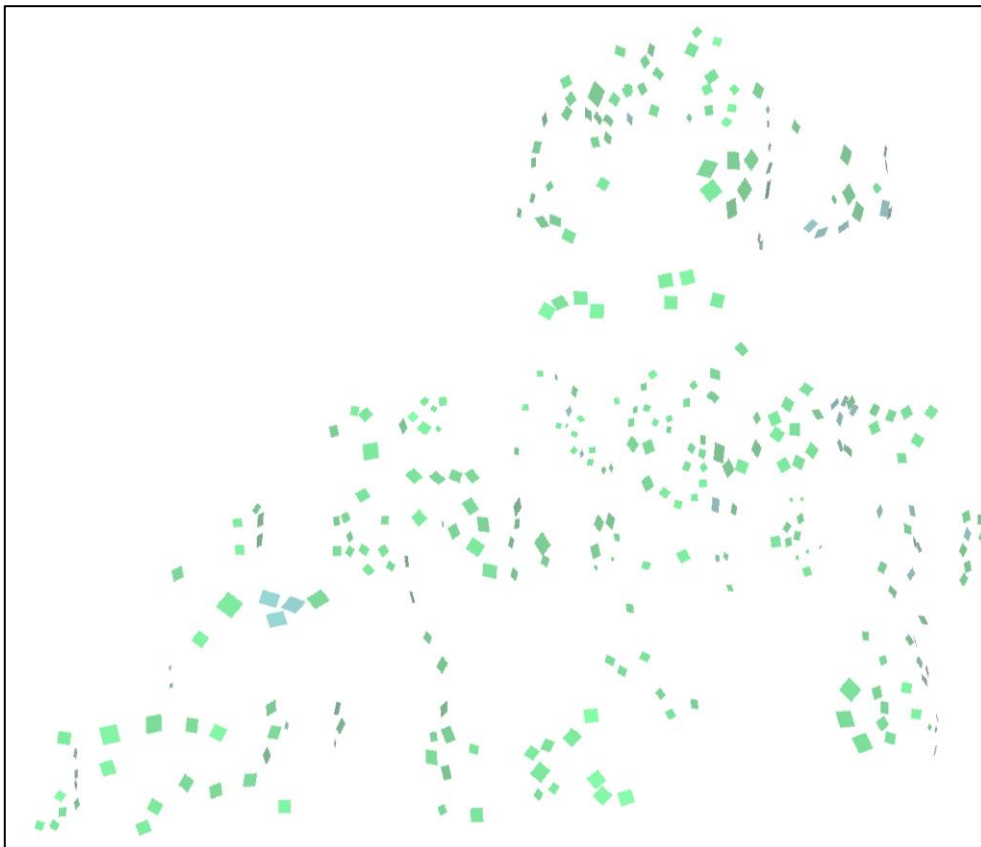


Figure 4-4: Location of measurement points from the Compass tool within the Rockfall Area

Both FACETS tools (KM and FD) automatically segregate the point cloud into multiple “facets” representing defect faces, as discussed in Section 2.3.3.1.2.

For the FACETS KM analysis, ten variations of input settings were utilised (Table 4-1). The adopted settings judged to provide the most representative results are highlighted.

Table 4-1: Settings used to run KD analysis attempts. Adopted analysis in grey.

Attempt	Maximum Angle	Max. Relative Distance	Max. Distance	Min. Points per Facet	Max. Edge Length
1	20	1	0.2	10	0.78
2	20	1	0.2	50	20
3	20	10	5	50	20
4	10	10	5	10	5
5	10	5	3	10	50
6	5	5	3	50	5
7	5	3	0.1	30	50
8	7	2	0.5	30	8
9	7	1.5	0.2	20	10
10	7	1.5	0.5	20	12

For the FACETS KM analysis, eight variations of input settings were utilised (Table 4-2). The adopted settings judged to provide the most representative results are highlighted.

Table 4-2: Settings used to run FM analysis attempts. Adopted analysis in grey.

Attempt	Octree Level	Max. Distance	Min. Points per Facet	Max. Edge Length
1	8	5	50	20
2	1	10	10	5
3	20	10	10	50
4	20	1	100	5
5	10	1	100	50
6	5	0.5	20	1
7	8	0.5	70	1
8	8	0.2	50	1.5

The FACETS tools both generated a visual representation of the facets into which the outcrop was segregated (Figure 4-5 and Figure 4-6). The colour of the facets reflect the dip vector of the facet plane, which represents the maximum dip orientation of a plane and is orthogonal to the pole vector of a plane. For this reason, the colours of the facet planes are 180° from the HSV colours of the standard point cloud dataset, which are based on Hough normal directions. The orientation of facets was exported to csv.

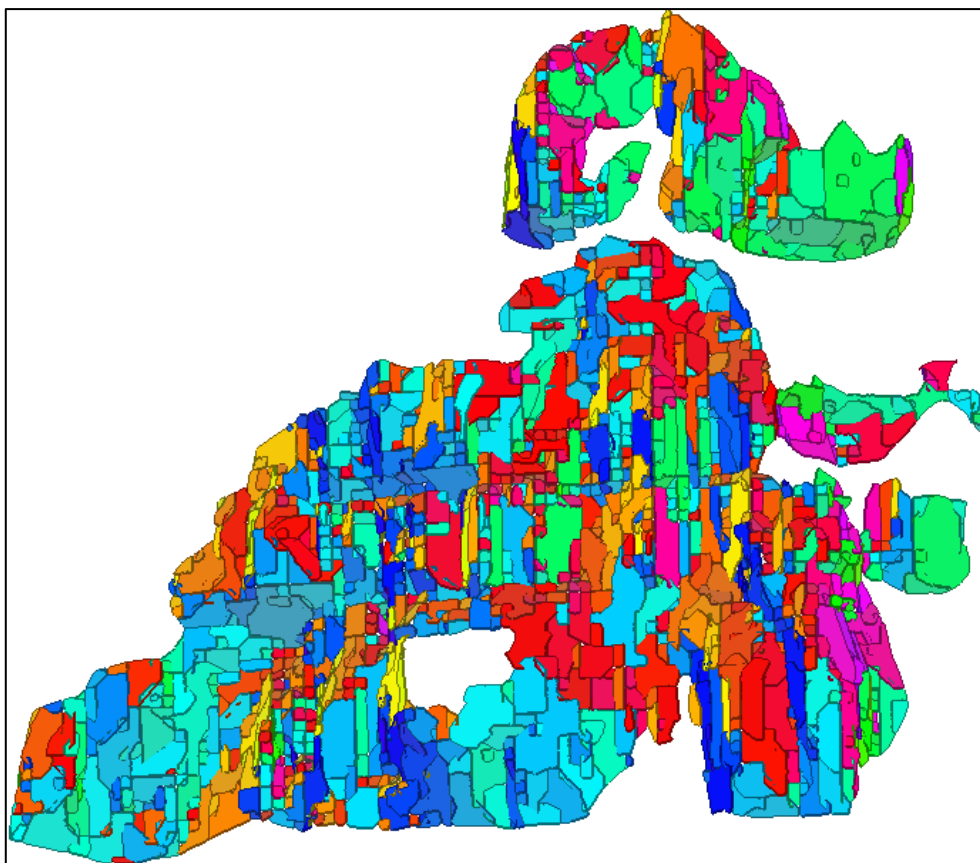


Figure 4-5: Output from the FACETS FM tool. Colours indicate the dip and dip direction of each facet.

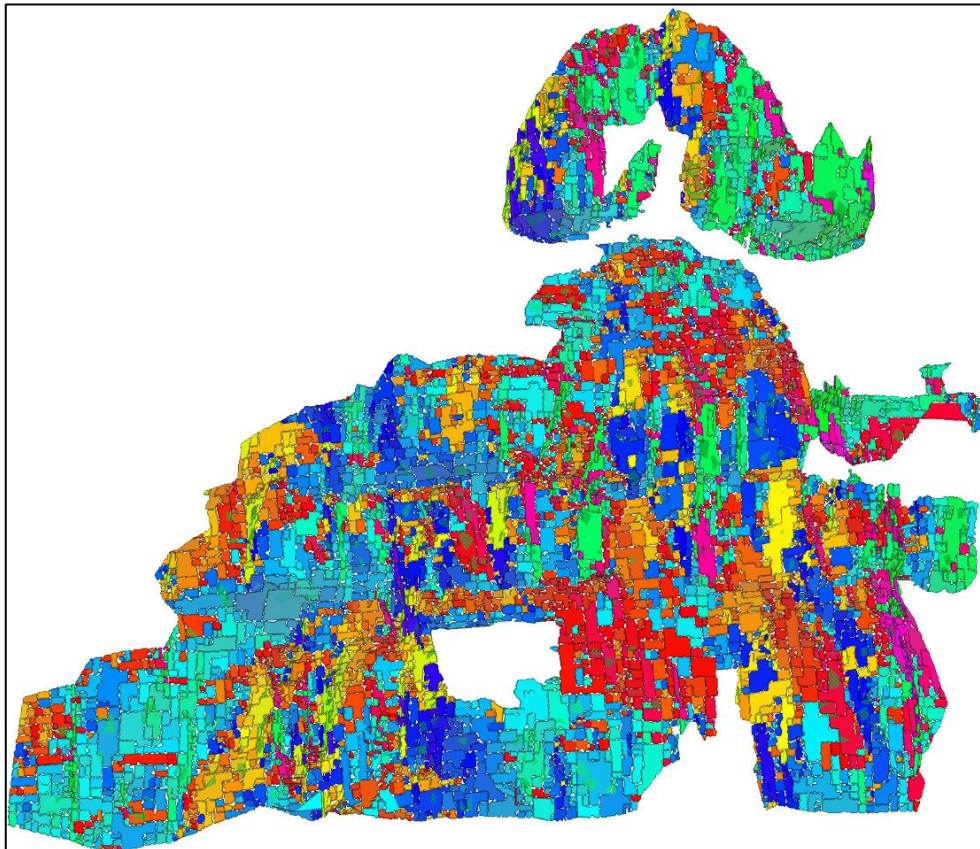


Figure 4-6: Output from the FACETS Kd tool. Colours indicate the dip and dip direction of each facet.

Dip and dip direction measurements were imported into the Rocscience software DIPS 8.0 and plotted on an equal angle, lower hemisphere stereographic projection. The exposed slope face of the Study Area was approximated as a planar surface, dipping 80° to the north. This was entered into DIPS as a planar traverse, and a Terzaghi weighting applied to account for measurement bias due to the orientation of the measurement plane relative to defect orientations. A minimum bias angle of 15° was adopted.

A comparison of the stereographic projections from each measurement method is displayed in Figure 4-7, with and without Terzaghi weightings applied. The stereonet all broadly show steeply dipping defects, typically greater than 70° from horizontal. Whilst the Compass-measured defects clustered in more discrete sets, the FACET analyses each formed two broader groupings of defects, or, rather, one wrapped set which was roughly consistent with the overall orientation of the slope face. Minor variation was apparent in these two broad groupings, however this the variation was not distinct enough to identify separate defect sets.

From this comparison of measurement data from the rockfall zone, it was determined that the compass tool was, although more labour intensive, the most appropriate form of orientation measurement when compared to the FACETS plugin. It was determined that the FACETS tools (both Kd and FM) were unable to distinguish between defect sets in an effective manner, even when vegetation was removed, and the Compass tool was adopted for all further orientation measurements within the site area.

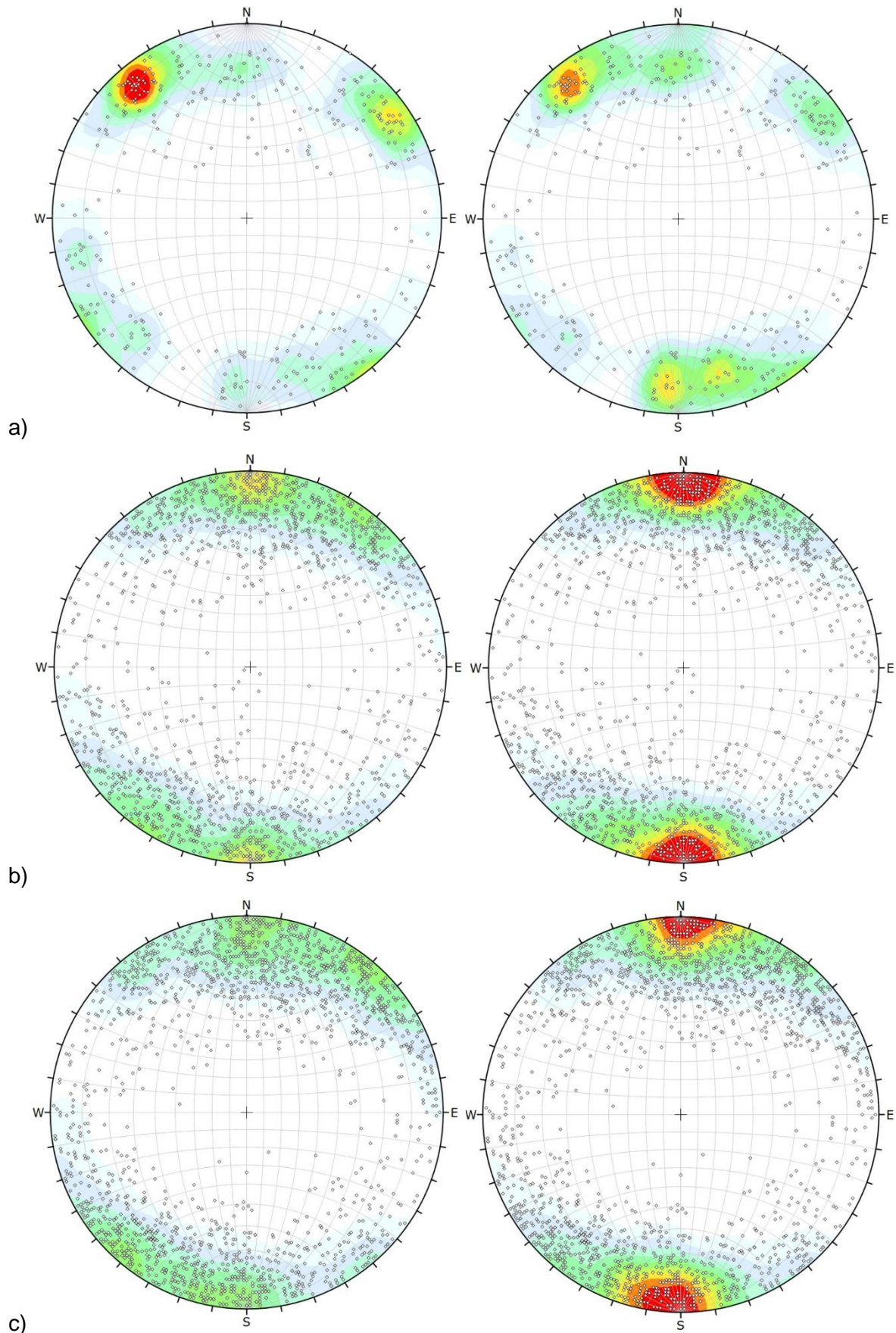


Figure 4-7: Stereographic plot of measurements taken from the Rockfall Area point cloud. Processed in DIPS 8.0, without (left) and with (right) Terzaghi weighting. Data set obtained in CloudCompare from a) the Compass plugin, b) the FACETS FM plugin, and c) the FACETS Kd plugin, displaying only facets with a surface area $>0.5 \text{ m}^2$. All density contours set from 0 (white) to 10 (red).

4.2 Set Definition

Defect sets within the Study Area were defined based on orientation, such that defects exhibiting similar orientations were grouped together as a set.

4.2.1 Definition of Joint Sets

In order to characterise defect sets within the Study Area as a whole, 848 measurements were manually taken from the point cloud using the Compass plugin in CloudCompare. The raw point cloud was compared with the ContextCapture 3D real scene model, in order to ensure that measurement locations were representative of exposed joint or bedding surfaces. Measurement points were distributed across the site area, and were taken on a range of large and small defects. Where defects had an apparent waviness, the measurement plane was extended to take an average orientation. The azimuth and dip of each plane was exported as a csv file, as were the local coordinates of the centre of each plane in the form of x, y and z coordinates.

The normal vector of each plane was plotted onto a stereonet using the RocScience software DIPS. The exposed surface of the Study Area was approximated as a planar surface, dipping 80° to the north. This surface was entered into DIPS as a planar traverse, and a Terzaghi weighting was applied to account for any measurement bias due to the orientation of the measurement plane relative to each defect orientation. A minimum bias angle of 15° was adopted.

Figure 4-8 displays the stereographic plot of measured planes, both unweighted, and with Terzaghi weighting applied. Seven clusters of poles may be observed, which have been interpreted to belong to three sub-vertically wrapped joint sets, and one sub-horizontal set representing bedding (Figure 4-9).

The stereonet with applied Terzaghi weighting has been used to define the range for each defect set, as displayed in Figure 4-9. It is apparent that although the Terzaghi weighting changes contour shape and colour, it does not change the quantity, distribution or definition of defect sets. The orientation range allocated for each defect set is displayed in Table 4-3. A value of strike has been displayed rather than dip direction, as each set is sub-vertical and so dip directions fluctuate 180 degrees for each set. A comparison of the mean set orientations for unweighted and weighted datasets is included in Table 4-4. A further analysis of bedding is undertaken in Section 4.4.2.

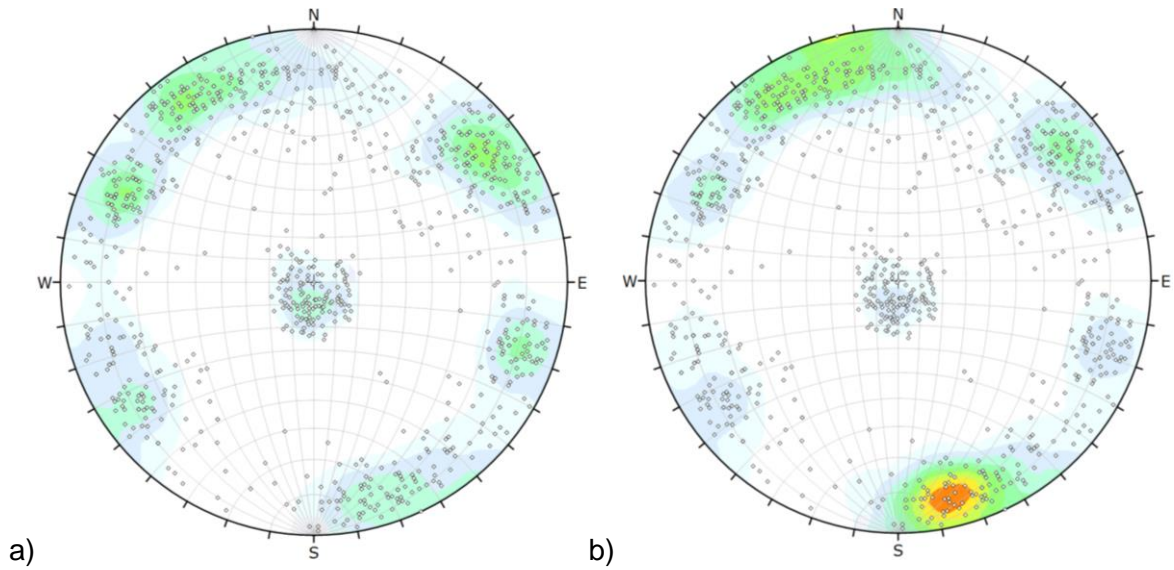


Figure 4-8: Stereographic projection of measurements taken within the Study Area; a) no weighting applied; b) Terzaghi weighting applied. All density contours set from 0 (white) to 10 (red).

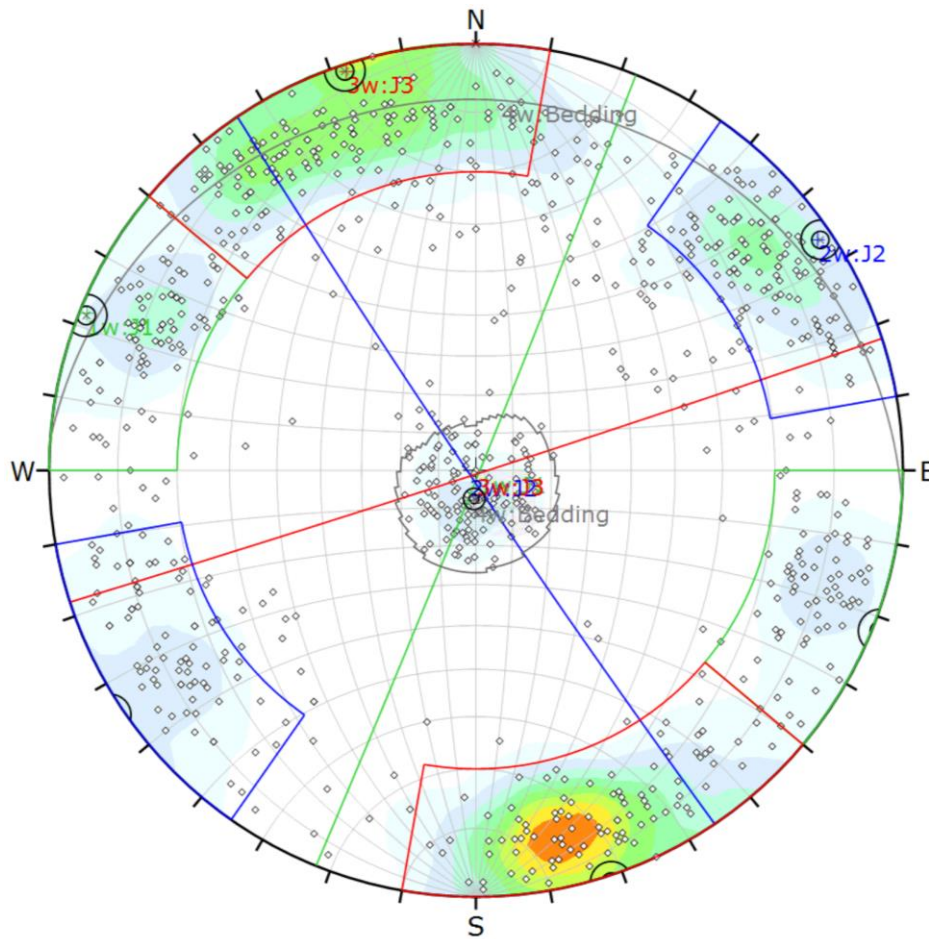


Figure 4-9: Sets defined on the stereographic projection of measurements taken within the Study Area. J1 (green), J2 (blue), J3 (red), and Bedding (grey). Confidence cones of 1 and 3 standard deviations displayed. All density contours set from 0 (white) to 10 (red).

Table 4-3: Orientation ranges defined for each defect set

Set Name	Set Colour	Dip		Strike	
		Maximum	Minimum	Maximum	Minimum
J1	Green	70	90	180	220
J2	Blue	70	90	125	170
J3	Red	70	90	40	100
Bedding	Grey	0	30	Sub-horizontal	

A comparison of defined joint sets with measurements undertaken in the Rockfall Area displayed a strong correlation, as shown in Figure 4-10 below, although Joint Set 1 (green) was not observed within this area due to the orientation of the slope face.

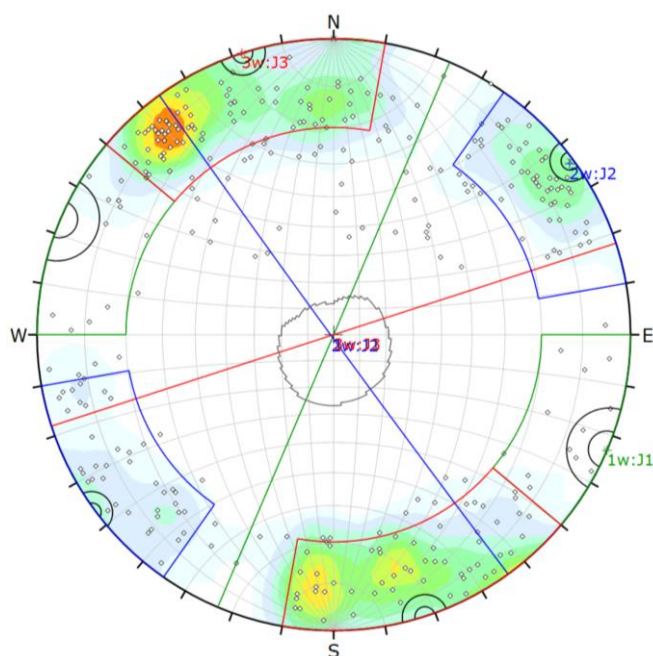


Figure 4-10: Comparison of defined joint sets with orientation measurements taken from within the Rockfall Area. All density contours set from 0 (white) to 10 (red).

Table 4-4: Mean joint set orientations for unweighted and weighted data

Set Name	Set Colour	No Weighting		Terzaghi Weighting	
		Mean Dip	Mean Dip Direction	Mean Dip	Mean Dip Direction
J1	Green	89.0	111.2	89.0	111.7
J2	Blue	88.3	237.4	88.3	236.2
J3	Red	87.5	157.3	89.1	161.8
Bedding	Grey	7.3	3.8	7.7	3.7

4.2.2 Segmentation of the Point Cloud

In order to undertake further analysis regarding spacing and persistence, the point cloud was segmented into point clouds for each set. The qFacets plugin in CloudCompare was used to segregate the dataset, generating two clouds for each joint set (each representing one half of the sub-vertically wrapped set) which were then merged to create one point cloud for each wrapped set. Table 4-5 outlines the dip and dip direction values used to segregate the point cloud.

Ranges for data segmentation were set to the outer limits of the expected set orientations. This ensured that exposed defect faces would be fully displayed, allowing for an accurate measurement of spacing, trace length and exposed face area.

Table 4-5: Ranges for set orientations as defined for point cloud segmentation.

Set		Dip		Dip Direction	
		Min	Max	Min	Max
J1 (green)	1	70	90	90	130
	2	70	90	270	310
J2 (blue)	1	70	90	35	80
	2	70	90	215	260
J3 (red)	1	70	90	310	10
	2	70	90	130	190
Bedding (black)	-	0	30	0	360

The point cloud for each set was assigned a solid colour. The chosen colour was not directly representative of the orientation of the set, but was chosen for clarity in order to plainly display the different sets. The Hough Normal based colouring system made it difficult to visualise the relationships between data points within a set. Because the sets were sub-vertical, each set would be represented by colours on opposite sides of the colour wheel (Figure 4-12). Similarly, the sub-horizontal bedding set would be so pale in colour as to be invisible, with variations in orientation particularly difficult to observe. As such, the bedding set was coloured black.

The segmented point clouds are displayed in Figure 4-11 below.

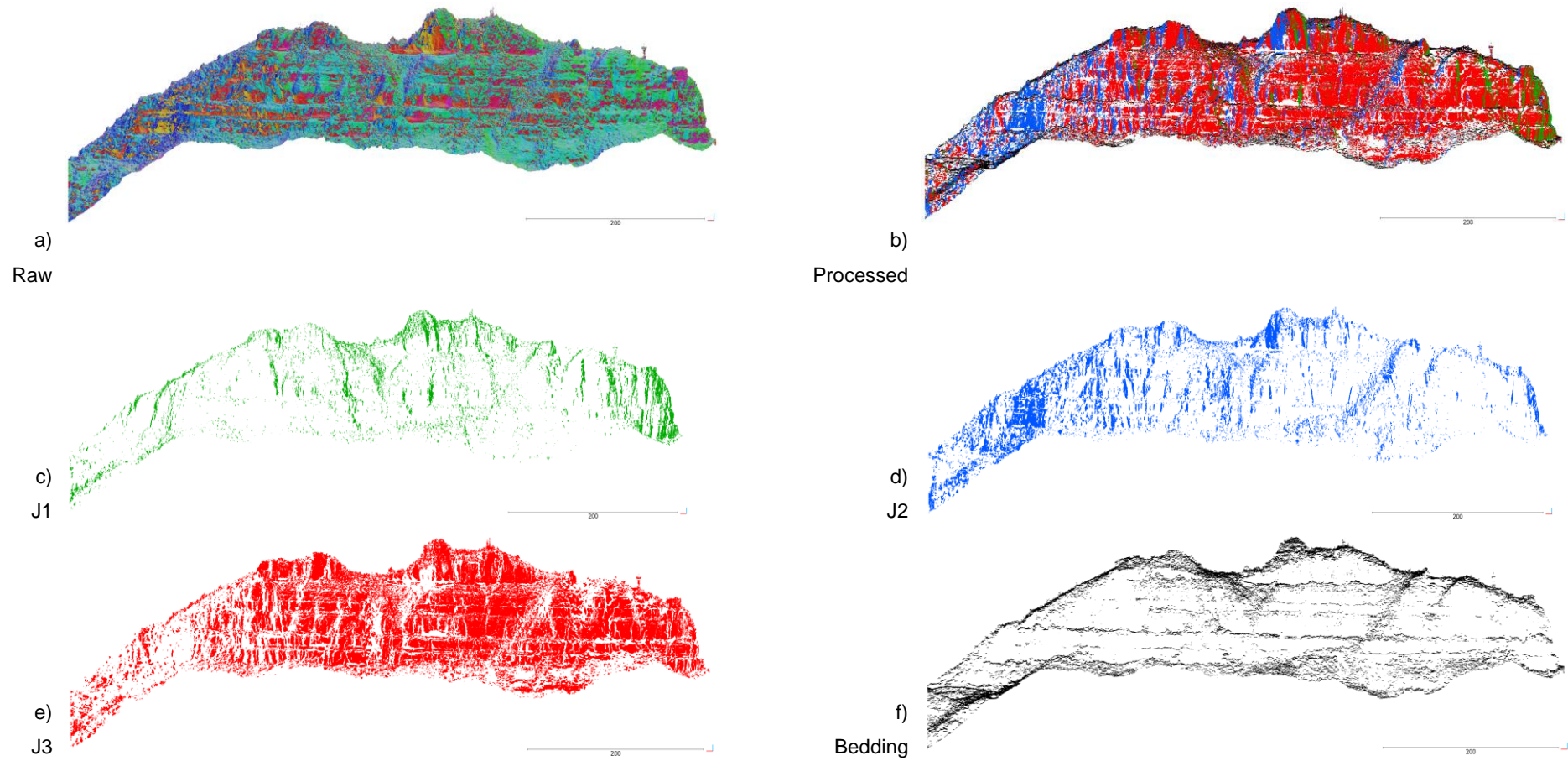


Figure 4-11: Segregated point clouds deflecting the processed joint sets, looking south. Viewed in Cloud Compare.

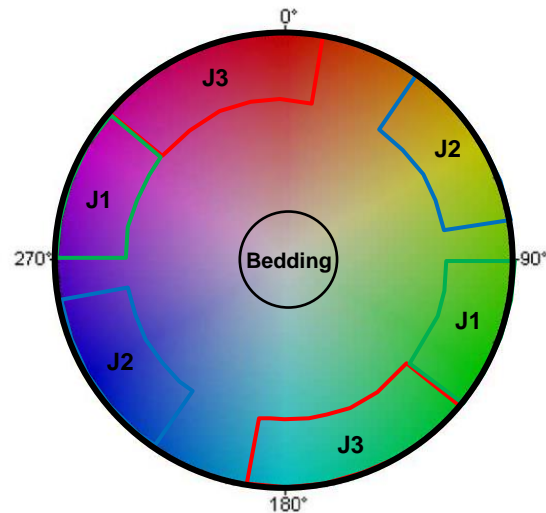


Figure 4-12: Hough-Normal colouring for each joint set.

4.3 Domain Definition

A number of analyses were conducted to find any potential variation in location-based set distribution across the Study Area.

As the exposed surface could be approximated with an east-west strike, the exported x coordinate of each measurement point reflected the horizontal distance from one end of the outcrop to the other. Positive x coordinates represent those to the east and negative x coordinates represent those to the west. An additional 2,277 orientation measurements were taken in an attempt to capture each visible defect plane (Figure 4-13), generating a larger dataset from which to analyse the geographical distribution of defect sets, and any variation in defect characteristics with location. Bedding orientation was derived from results of the large-scale trace lineation methodology discussed in Section 4.4.2.

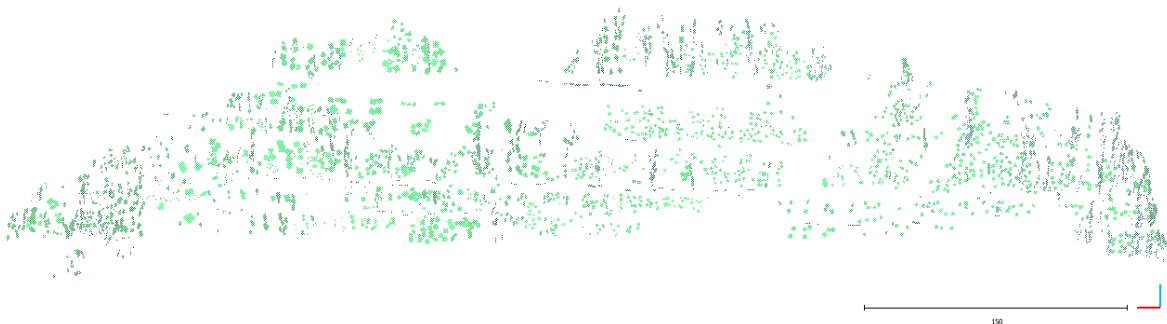


Figure 4-13: Additional measurement planes, looking south.

Figure 4-14 symbolically displays the distance along the face of the outcrop (x coordinate) for each set. It can be seen that different defect sets are dominated by different x-coordinate ranges, indicating a location-dependant occurrence of defect sets.

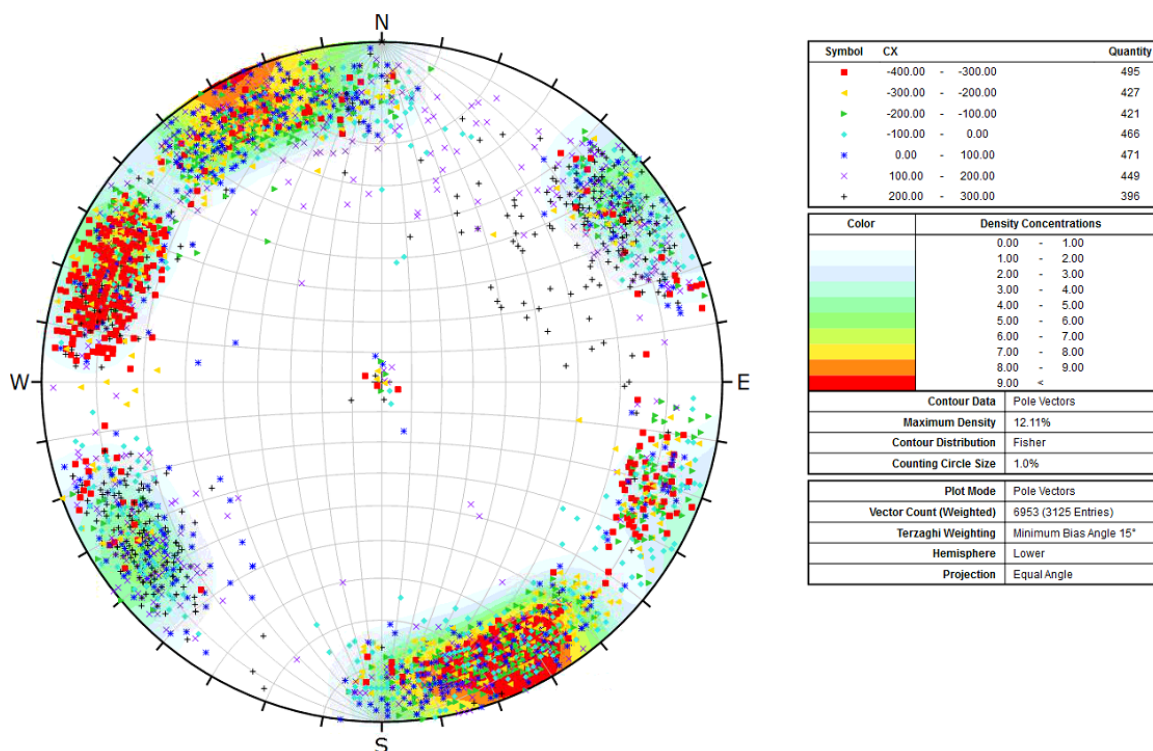


Figure 4-14: Stereographic projection of measurements taken within the Study Area, with symbols representative of horizontal distance from west to east.

Histograms were created to visualise the distribution of each defect set horizontally across the Study Area (Figure 4-15). Each set clearly displays a change in set frequency with horizontal distance along the slope face. The location dependant visibility of sets is considered to be due to the relative orientation of the slope face compared to each set.

Based on an assessment of the histogram distribution, and a visual assessment of the CloudCompare model, four domains were defined. Each domain has a consistent slope face strike, and each is dominated by unique combinations of defect sets. The four domains are displayed in Figure 4-16 and are outlined as follows:

- D1: on the far eastern side of the outcrop. The slope face strikes approximately 150° . This exposes primarily set J2, which has a strike of 146° ;
- D2: slightly further west than D1. The slope face strikes approximately 110° , and exposes primarily joint sets J2 and J3;
- D3: the largest domain, in the centre of the outcrop. The slope face strikes approximately 75° , and exposes primarily Joint Set J3, with J1 and J2 also present. The slope face strike is similar to J3, which has a strike of 72° ; and
- D4: on the far western side of the outcrop. The slope face strikes approximately 50° , and exposes primarily Joint Set J1 and J3.

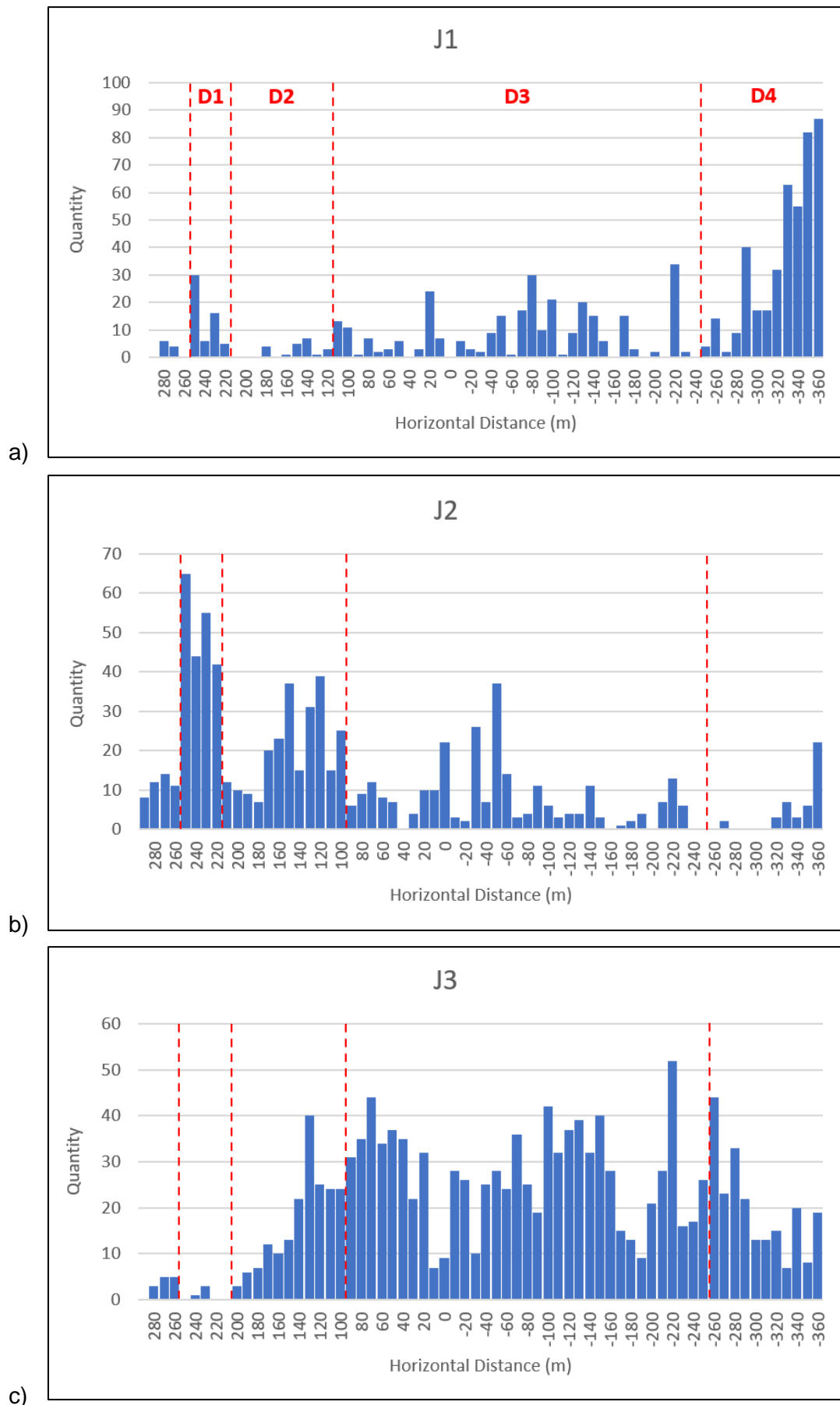


Figure 4-15: Occurrence of sets with horizontal distance and domain, where positive values are to the east, and negative values are to the west. a) J1; b) J2; c) J3

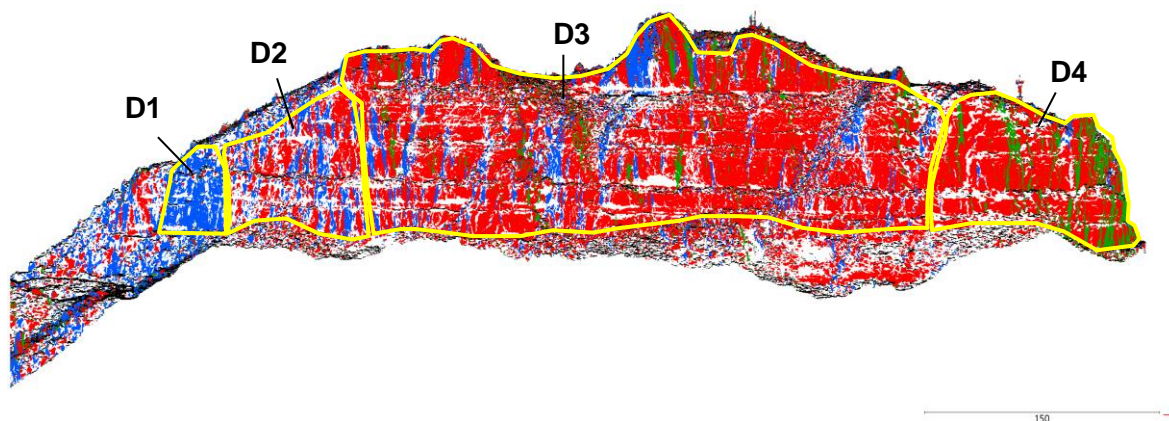


Figure 4-16: The four defined domains, looking south

A summary of the joint sets present in each domain is included in Table 4-6 below. Joint sets within each domain have been classed as:

- Dominant: Joint set which controls the orientation of the slope face, and controls the failure mechanism within the domain;
- Present: Joint set is present in approximately equal proportions to other sets within the domain. Set has an impact on the failure mechanism within the domain; and
- Minor: Joint set is present in only minor quantities. Although it may be visible in one or two failures or defect planes, it does not influence the main failure mechanism of the domain.

Table 4-6: Defect sets present for each domain

Set	D1	D2	D3	D4
J1	Present	Minor	Present	Present
J2	Dominant (sub-parallel)	Present	Present	Minor
J3	Minor	Present	Dominant (sub-parallel)	Present
Bedding	Present	Present	Present	Present

Further joint set characterisation (spacing, surface area etc.) was calculated separately for each of these domains.

4.4 Orientation

An analysis of defect set orientation was undertaken for each individual domain. This was used to define whether mean set orientations were location dependant.

4.4.1 Joint Set Orientation

Stereonet were plotted of measurement data contained within each domain, taken as a subset from the site-wide, detailed measurement dataset displayed in Figure 4-13. A Terzaghi weighting was applied adjusting for the angle of each domain slope face. These stereonet are displayed in Figure 4-17 below.

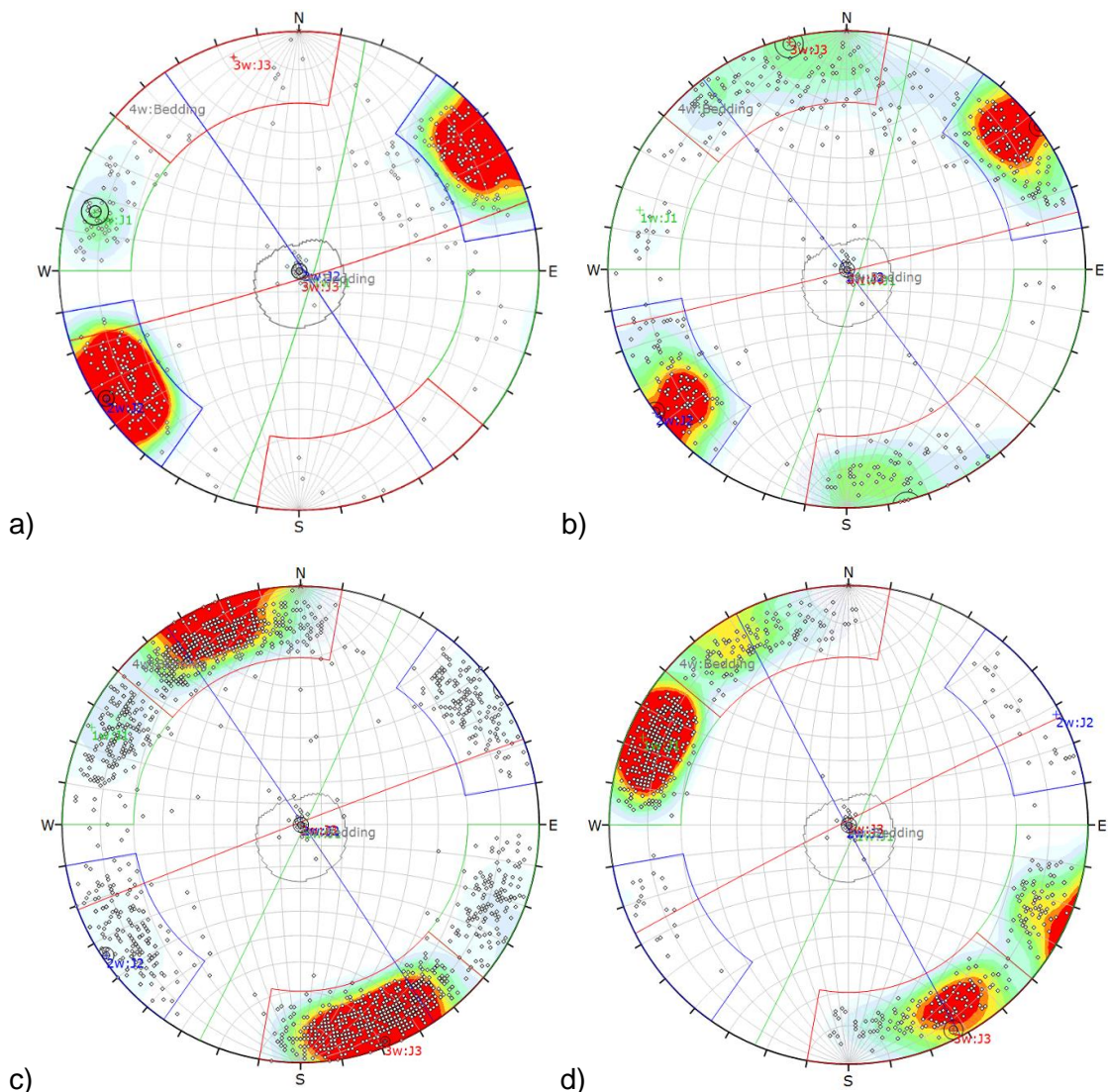


Figure 4-17: Defect orientation measurements for each domain. Site-wide set windows shown for comparison. a) D1; b) D2; c) D3; d) D4

A summary of mean set orientation for each domain is included in Table 4-7. Figure 4-18 graphically displays the mean set orientation for each domain, compared to the 95th percentile cone of confidence of the site-wide set orientation. Although the domain-

segregated means are outside the cone of confidence of the site-wide data, there is no overall trend in orientation from one side of the outcrop to the other. As such, it is considered that variations in mean orientation are due to random fluctuations and measurement bias. Site-wide mean orientation values have therefore been adopted for all further analyses.

Table 4-7: Mean set orientation for sets within each domain, with Terzaghi weighting applied.

Domain	Slope Face		J1		J2		J3	
	Dip	Dip Direction	Dip	Dip Direction	Dip	Dip Direction	Dip	Dip Direction
D1	79°	61°	83°	106°	88°	56°	-	-
D2	82°	22°	-	-	90°	53°	89°	166°
D3	81°	344°	88°	115°	89°	56°	89°	339°
D4	76°	320°	86	113°	-	-	88°	333°
All	80°	0°	86.2°	113.0°	88.7°	55.7°	88.8°	338.3°

Table 4-8: Variability and confidence for Joint Sets J1, J2, J3, across all domains. Terzaghi weighting applied to each data point based on the appropriate domain slope face.

Set Name	K	Confidence (68%)	Variability (68%)	Confidence (95%)	Variability (95%)	Qty Data Points
J1	45.72	0.46°	12.86°	0.75°	21.18°	808
J2	37.74	0.51°	14.17°	0.83°	23.34°	796
J3	27.33	0.46°	16.66°	0.75°	27.50°	1374

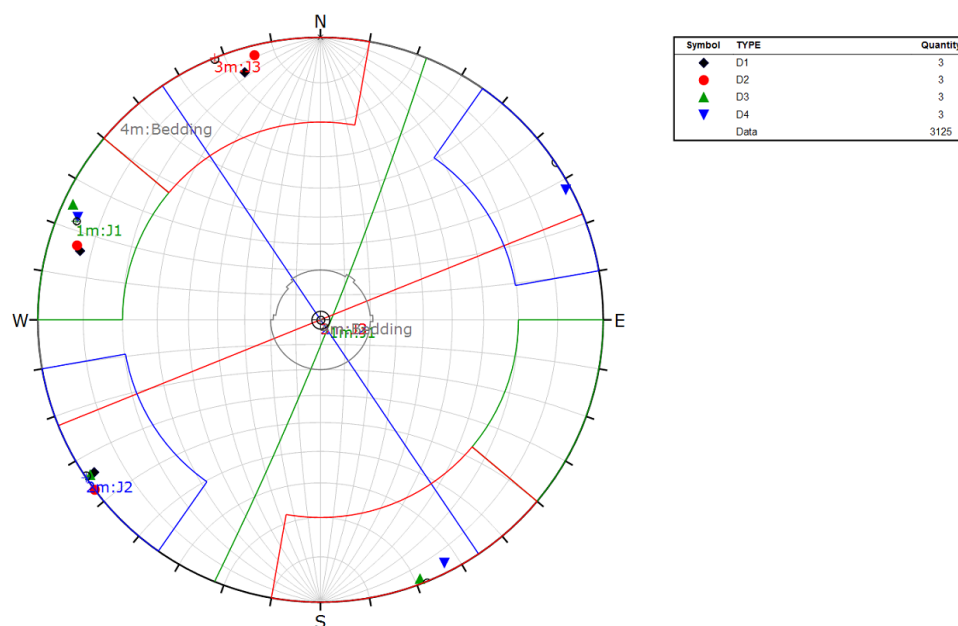


Figure 4-18: Comparison of mean poles by domain. Cones of confidence for the 95th percentile displayed.

There are several possible methods of quantifying the variation defect set orientation, as outlined in Section 2.3.3.2. For the purposes of this analysis, data is assumed to be symmetrically distributed, and therefore the Fisher's K, confidence cone and variability limits are all considered to be appropriate quantifiers of variation. Table 4-8 above outlines these quantifications, from which the following conclusions may be drawn:

- Joint Set J1: A moderately high Fisher's K value and a small variability limit indicates low scatter and low variability within the sample. A very small confidence cone allows a high degree of confidence in the mean value. Of all joint sets, this set has the lowest scatter and variability, and the highest confidence;
- Joint Set J2: A moderately high Fisher's K value and a small variability limit indicates low scatter and low variability within the sample. A very small confidence cone allows a high degree of confidence in the mean value; and
- Joint Set J3: A lower Fisher's K value and larger variability limit indicates that this set has a higher scatter and variability compared to the other two joint sets. This can visually be observed in the set distribution shown in the stereographic projection in Figure 4-17. The confidence cone remains very small, indicating that there can be a high degree of confidence that the mean value is correct.

4.4.2 Bedding

The definition of bedding orientation is vital in determining possible failure modes within the Study Area. Visual inspection of the slope face and available literature indicates that bedding is sub-horizontal. Bedding presents with sub-horizontal traces and was clear within both the point cloud model and the 3D real scene model.

The 3D real scene model shows alternating sequences of massive, blocky limestone and thinly bedded limestone. It is likely that some bedding structure still exists within the "massive" zones, but that this is not visible from the 3D real scene model with the current image resolution. Weathering and erosion within the thinly bedded zones visually appears to have occurred at a higher rate than the massive zones, which has acted to undercut the massive zones. This undercutting, together with failure of the overlying massive blocks, has resulted in a stepped face upon which talus and vegetation have built up.

Obtaining direct measurements of bedding orientation from the point cloud using the Compass tool proved challenging due to a high variation in orientation. This variation was due predominately to the obstruction of bedding surfaces by vegetation and talus, and waviness within the bedding planes themselves.

In an attempt to visually characterise bedding orientation, the point cloud was segmented into six datasets, all with a dip between 0° and 30° . Each dataset represented a range of 60° in dip direction, covering a full 360° . Each data set was coloured as per the Hough Normal colour wheel, but adjusted such that colours were shown at full saturation regardless of dip (Figure 4-19). Figure 4-20 visually displays the variation in bedding orientation on a large and small scale.

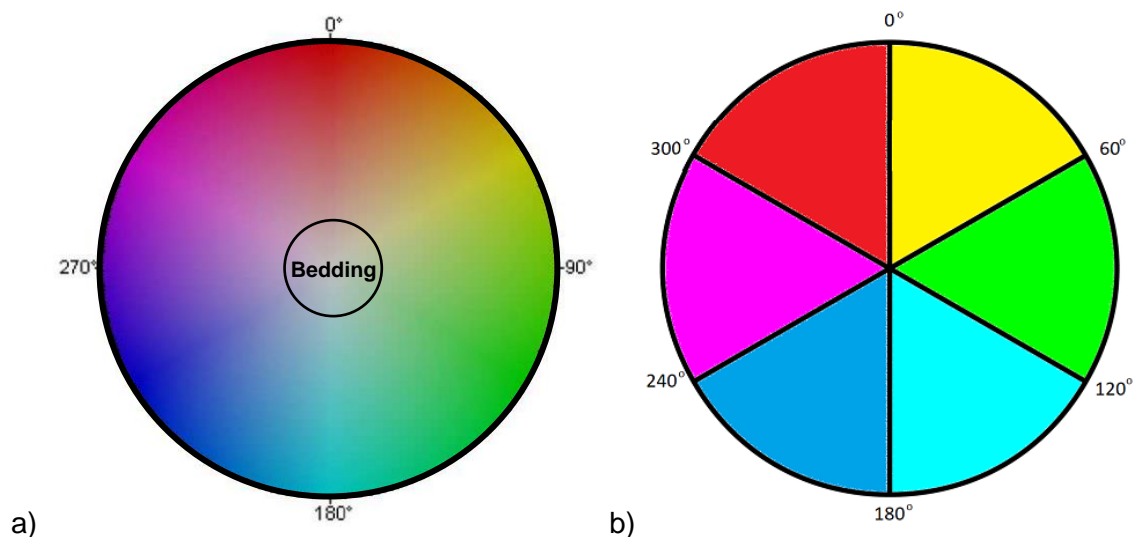


Figure 4-19: a) HSV colour wheel with overlay of proposed bedding set; b) Colour wheel applied to bedding points for visualisation purposes. Each colour represents a range of 60° in dip direction. All points have a dip between 0° and 30° .

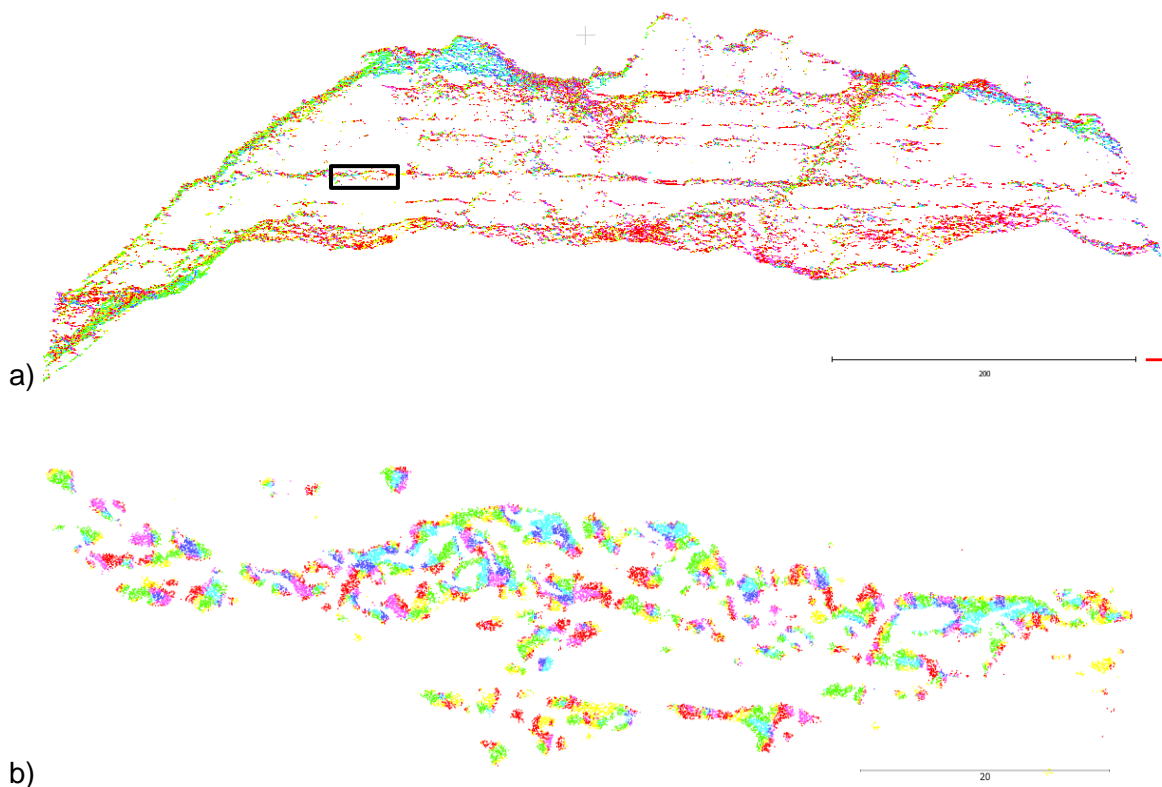


Figure 4-20: Variation in bedding orientation a) on a large scale, viewed facing south; b) on a small to medium scale (viewed from above). Black box on a) represents the location of b).

In order to characterise the large-scale orientation of bedding, the trace of bedding planes was outlined across the face of the slope. Each visible bedding plane was traced with a polyline in three dimensions, and the CloudCompare “fit plane” function utilised to define the plane of best fit through the polyline. Figure 4-21 displays the fitted planes.

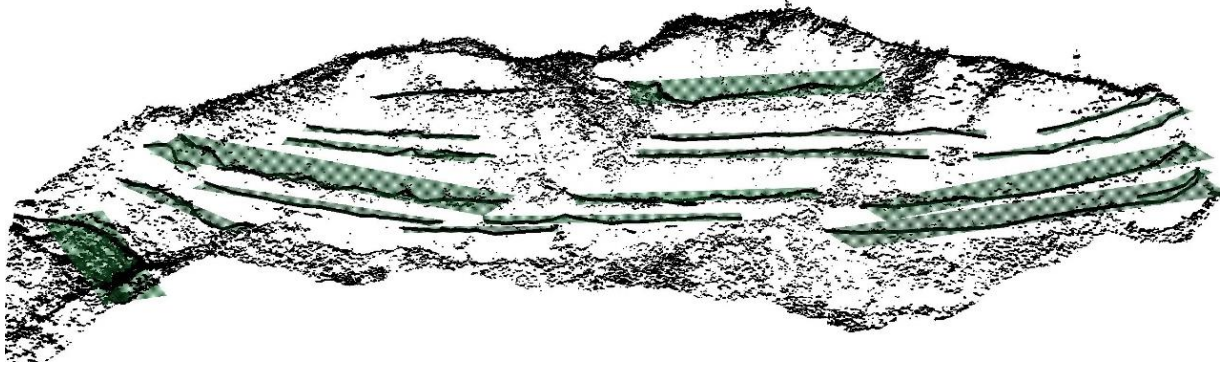


Figure 4-21: Study Area (facing south) showing all points with dip less than 30°. Planes fit through traces of bedding planes visible in slope face.

A comparison of stereonet projections of small-scale and large-scale bedding measurements are included in Figure 4-22, and tabulated in Table 4-9.

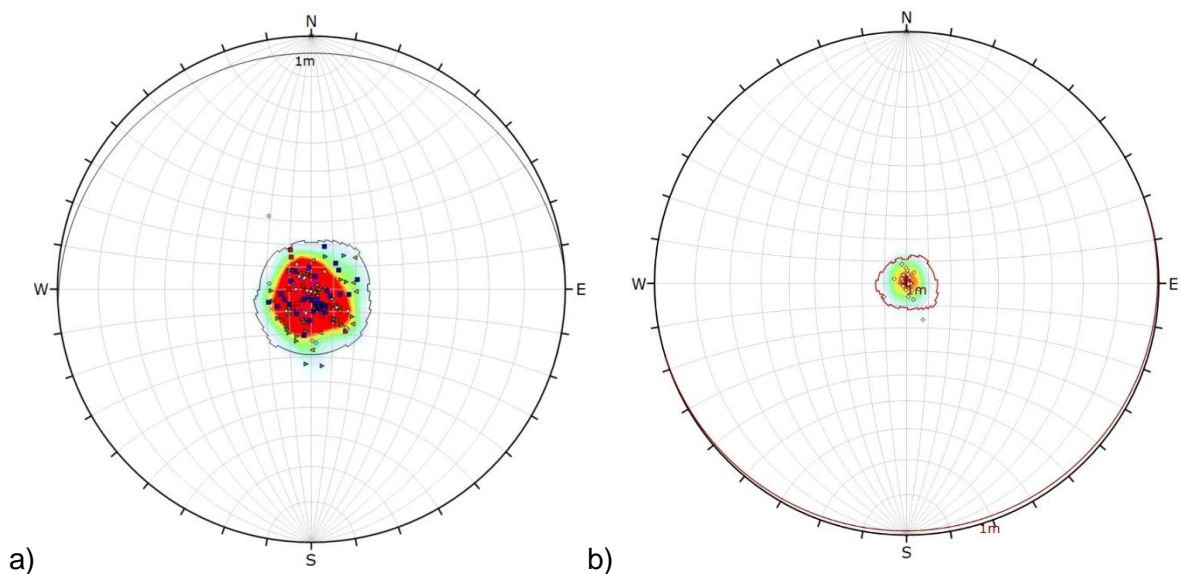


Figure 4-22: Stereographic projections of bedding measurements; a) small-scale using the Compass tool; b) large scale, using surface traces with the Trace tool.

Table 4-9: Bedding orientation as measured on a small and large scale

Method	Mean Dip	Mean Dip Direction	K	Qty	Variability Limit	Confidence Limit
Small Scale (Compass)	4.2°	355.6°	37.9	145	23.3°	1.9°
Large Scale (Trace)	0.7°	163.2°	209.0	20	9.9°	2.2°

The sub-horizontal nature of bedding within the Study Area leads to a wide variation in measured dip direction. Both methods of analysis indicate that bedding dips at less than 5° , although the mean dip direction between methods is inconsistent. There can be bias in the imaging of sub-horizontal planes, due to the aerial nature of the image capturing. Additionally, exposed bedding surfaces are largely overlain by talus and vegetation. As such, large-scale orientation is considered to be more representative of the slope. Bedding orientation was not observed to be location-dependant across the Study Area.

4.5 Spacing

Normal set spacing was measured in two ways, in order to limit the influence of sources of error inherent in each technique:

1. The virtual scanline method, adopted across the entire Study Area; and
2. Measurements of dimensions of fallen blocks below the Rockfall Area;

4.5.1 Virtual Scanline Method

The virtual scanline method was adopted to calculate defect spacing across the Study Area. Five sub-horizontal scanlines were generated in each of the four domains, as displayed in Figure 4-23 below. Scanlines were placed parallel to the strike of the slope face at elevations which minimised the influence of vegetation and talus build-up.

As all three joint sets within the Study Area are sub-vertical, adopting horizontal scanlines with an azimuth reflecting the strike of the slope face is appropriate for all joint sets. Spacing between sub-horizontal bedding planes was measured vertically.

The distance between defects of each set intersecting the scanline was measured, taking the mid-point of defects where waviness of the plane caused an apparent thickness. Large spacings where joints were covered by vegetation or talus build-up were disregarded.

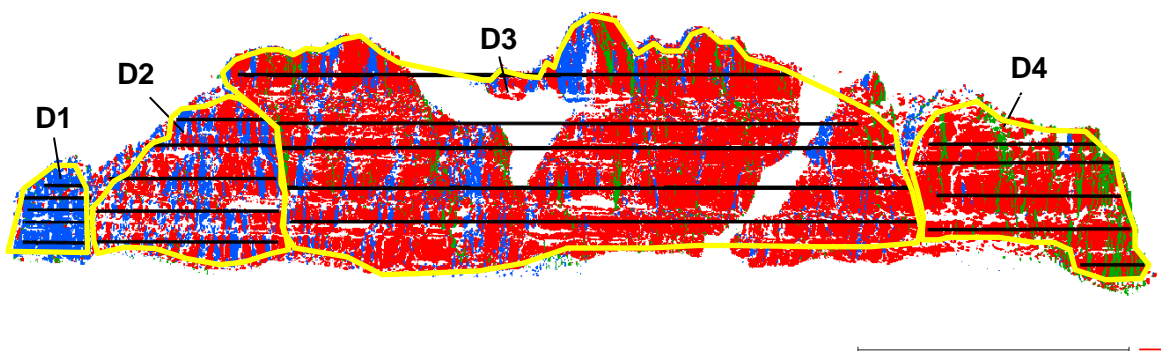


Figure 4-23: Virtual scanlines, sub-horizontal, striking as per slope face for each domain. Looking south.

The “2-point thickness” tool from within the CloudCompare “Compass” plugin was used to directly measure the normal spacing between defects of the same set along each scanline, rather than measuring set spacing and then back calculating normal set spacing. The “2-point thickness” methodology was adopted rather than the “1-point thickness” methodology, with the mean set plane orientation used as a reference plane.

The 1-point method causes the measured spacing between two defects of slightly different orientation to be heavily biased by which of the two defects is chosen as the measurement plane. The defect spacing would therefore be different if it were measured from left to right along the scanline compared to right to left. The 2-point method prevents this by using the mean set orientation to define the direction of measurement. This essentially follows the standard scanline methodology, calculating spacing based on mean set orientation rather than individual defect planes. Additionally, processing and measuring using the 2-point method introduced here is far faster in practice, as a reference plane has to be selected only once in any series of measurements. For a 1-point method, a plane must be selected for each individual measurement.

This concept is displayed in Figure 4-24 below, where the spacing between two planes is measured from left to right (green) and right to left (blue) respectively, using both the 1-point and 2-point thickness methods. Spacing values using the 1-point method can be observed to vary between the two measurement directions, based on which plane is chosen to designate the orientation of measurement. Spacing values in the 2-point method are independent of individual plane orientation or direction of measurement.

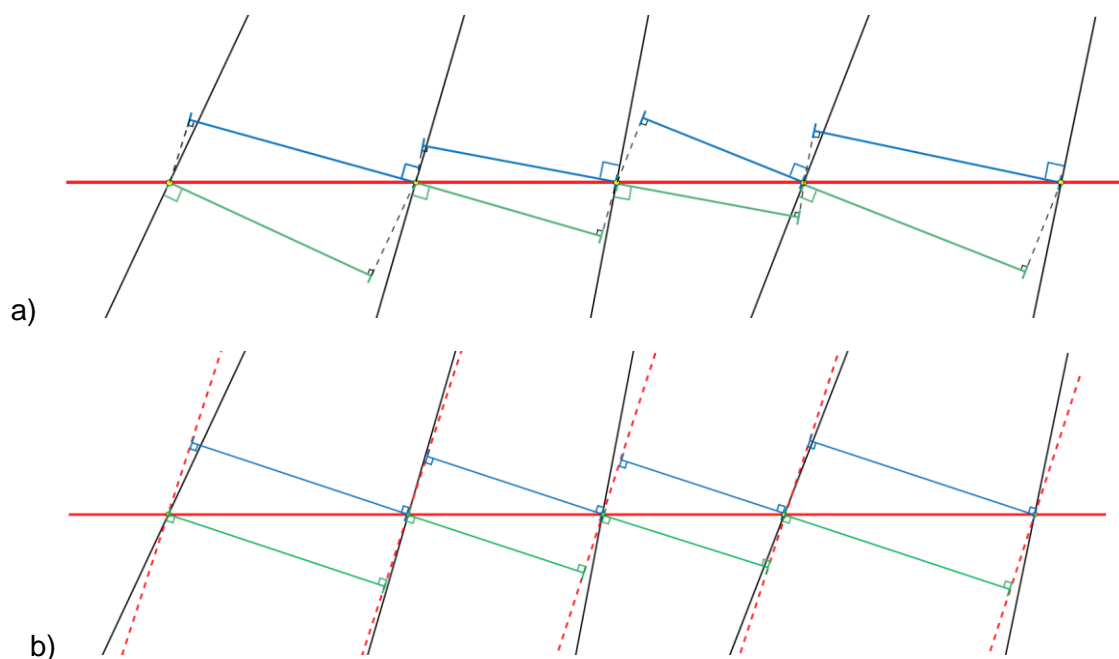


Figure 4-24: Sketch comparing measurement lengths taken of defects (black) along a horizontal scanline (red) using the methodology of; a) the 1-point thickness tool; and b) the 2-point thickness tool.

An example of spacing measurements using the 2-point thickness tool is shown in Figure 4-25. The raw point cloud was compared with the ContextCapture 3D real scene model, in order to ensure that measurement locations were representative of exposed joint or bedding surfaces. Where the scanline sat external to the slope face, defects were projected horizontally to the location of intersection with the scanline.

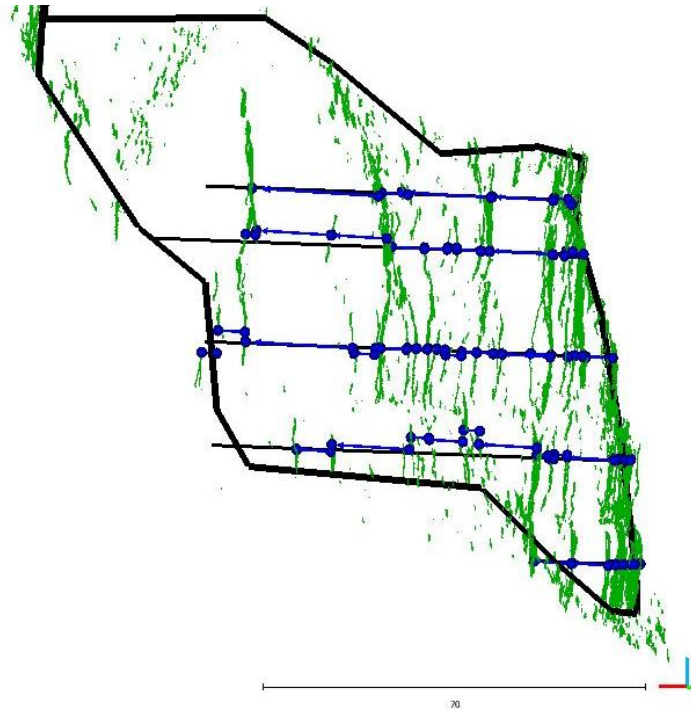


Figure 4-25: Measurement of defect spacing along scanlines for Joint Set J1 within region D4, measured using the 2-point thickness tool along 5 horizontal scanlines. Facing along strike of Joint Set J1.

Where joint sets were sub-parallel to the scanlines, spacing measurements were taken perpendicular to the slope. As the number of suitable measurement points were typically limited, these measurements were taken ad hoc where possible, rather than along scanlines. This most regularly took the form of measuring the depth of “steps” which occurred at bedding surfaces, or where wedges had previously fallen and caused voids in the slope face. An example from D1 is displayed in Figure 4-26 below.

4.5.1.1 Results

When numerically analysing the defect spacing for each set, consideration was given to each domain separately. Because each domain has a slope face which intersects the defect plane at a different angle, the different domains are each susceptible to the exposure of defects in different ways. Histograms in Figure 4-27 display the defect set normal spacing across all domains, as measured by the virtual scanline method. Figure 4-28 displays the defect set spacing measurements for each domain. A statistical evaluation of defect spacing across all domains is included in Table 4-10 below.

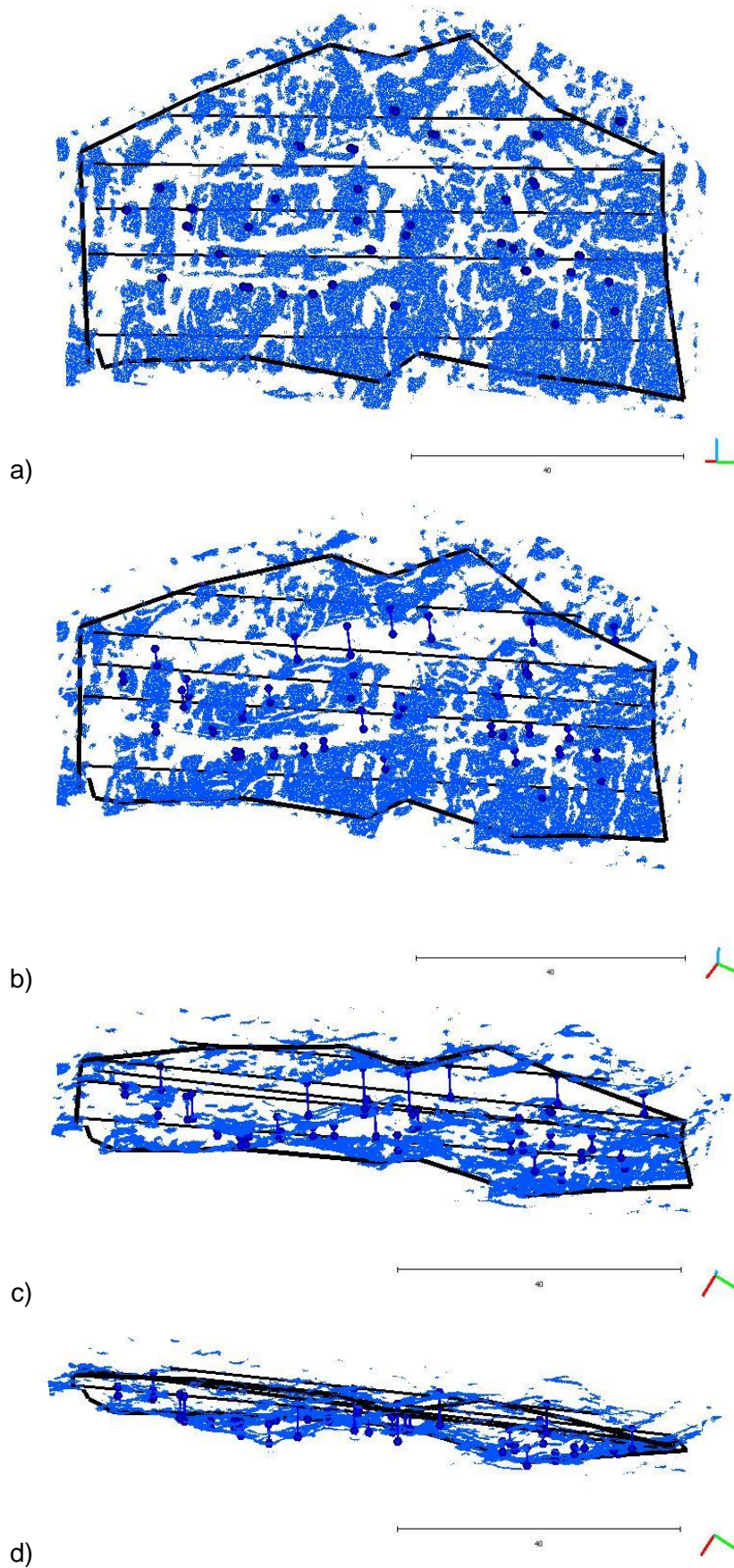


Figure 4-26: Measurement of spacing for joint sets parallel to the slope face, Joint Set J2 in Domain D1, with increasing viewing rotation to fully display measurement locations. a) viewed from horizontal; b) viewed from approximately 30° from horizontal; c) viewed from approximately 70° from horizontal; d) vertical view.

The reliability of the spacing data was not considered sufficient to warrant a rigorous goodness of fit test to determine probabilistic distribution. It is more appropriate to apply engineering and geological judgement in this case than to apply rigorous mathematical modelling.

The distribution of histograms is observed to be positively skewed, with a long tail towards longer spacing values and median values smaller than the mean values. This is the case for all joint sets. Bedding shows more of a uniform distribution, although this likely reflects large-scale boundaries between bedding units/stratum, rather than smaller laminations or bedding within units, which are likely to be more closely spaced.

It was observed that where dominant defect sets control the geometry of the slope, the measured defect spacing is typically slightly smaller. This may be due to waviness within the defects being measured more in this case, which may have caused the positive skew to the data. Conversely, it may represent the true spacing in that more surfaces are exposed for measurement, making the results more representative. Joints perpendicular to the slope face are much simpler to measure, however they risk presenting as joint traces, rather than surfaces, and may not be reflected in the point cloud.

Table 4-10: Statistical summary of scanline measured set normal spacing, for all domains combined.

Measure	Spacing (m)	Spacing (m)	Spacing (m)	Spacing (m)
	J1	J2	J3	Bedding
Min	0.12	0.07	0.07	0.35
Max	39.23	41.67	23.06	36.13
Mean	7.22	5.68	4.11	14.88
Mode (rounded to 0.5)	1.50	1.00	1.50	13.50
5%	0.50	0.85	1.00	3.51
25%	2.00	1.84	1.94	10.49
50%	4.50	3.50	3.00	15.00
75%	9.52	6.50	5.00	19.70
95%	23.13	17.51	10.00	25.20
Std. Dev.	7.64	6.12	3.43	7.13
Skew	2.03	2.48	2.37	0.19

The statistical summary in Table 4-10 indicates a sampling issue – the mean spacing value is smaller than the standard deviation for Joint Sets J1 and J2. For Joint Set J3, although the standard deviation is not larger than the mean it is only marginally smaller, as summarised in Table 4-11 below.

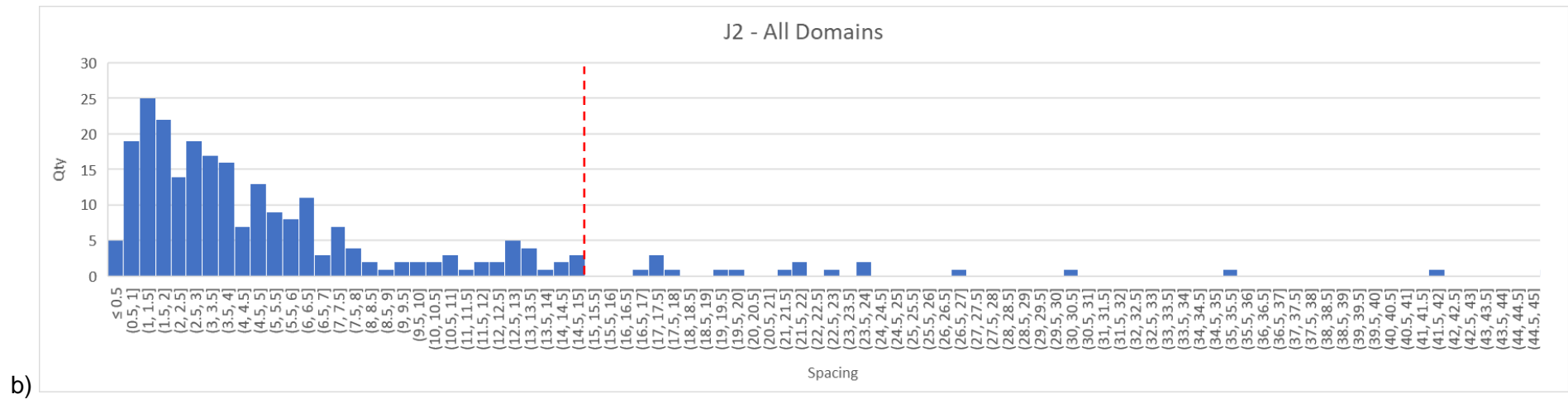
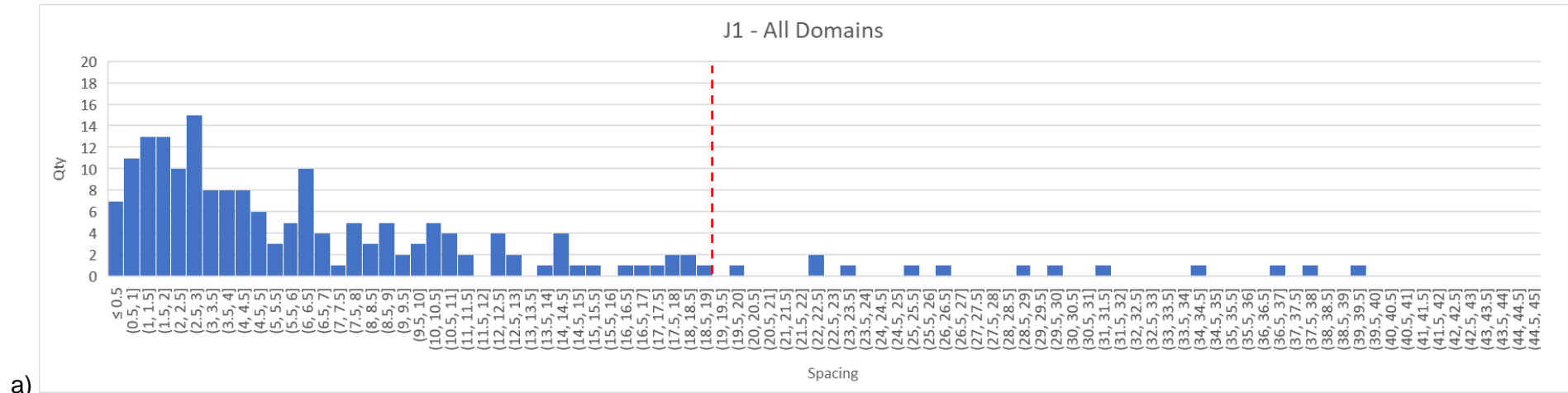
Table 4-11: Difference between mean spacing and standard deviation

Set	Median Spacing (m)	Mean Spacing (m)	Standard Deviation (m)	Mean Minus Standard Deviation (m)
J1	4.50	7.22	7.64	-0.42
J2	3.50	5.68	6.12	-0.44
J3	3.00	4.11	3.43	0.68
Bedding	15.00	14.88	7.13	7.75

This difference is due to the few extremely (and unrealistically) large values of spacing which were measured. These values were likely measured where joints were present as traces, not surfaces, or where joints were obscured by vegetation or talus, and therefore will be higher than the true spacing at this location. Mean values were also significantly larger than the median, pulled upwards by a few unrealistically high spacing values. In order to reduce the effects of this error, engineering and geological judgement was used to apply an upperbound limit to spacing values. This limit was assessed for each joint set as follows:

- Joint Set J1: 19 m;
- Joint Set J2: 15 m;
- Joint Set J3: 11 m; and
- Bedding: 20 m.

This results in a statistical summary as outlined in Table 4-12 below. Small variations in measured spacing between joints were observed between domains. This is not considered to reflect fluctuations in actual spacing values. It is considered to show the impact of the relative orientation between a slope face and defect set, and how this influences the way in which defects present. Values adopted for further calculations are therefore derived from a combination of spacing measurements for each joint set, with upperbound limits applied.



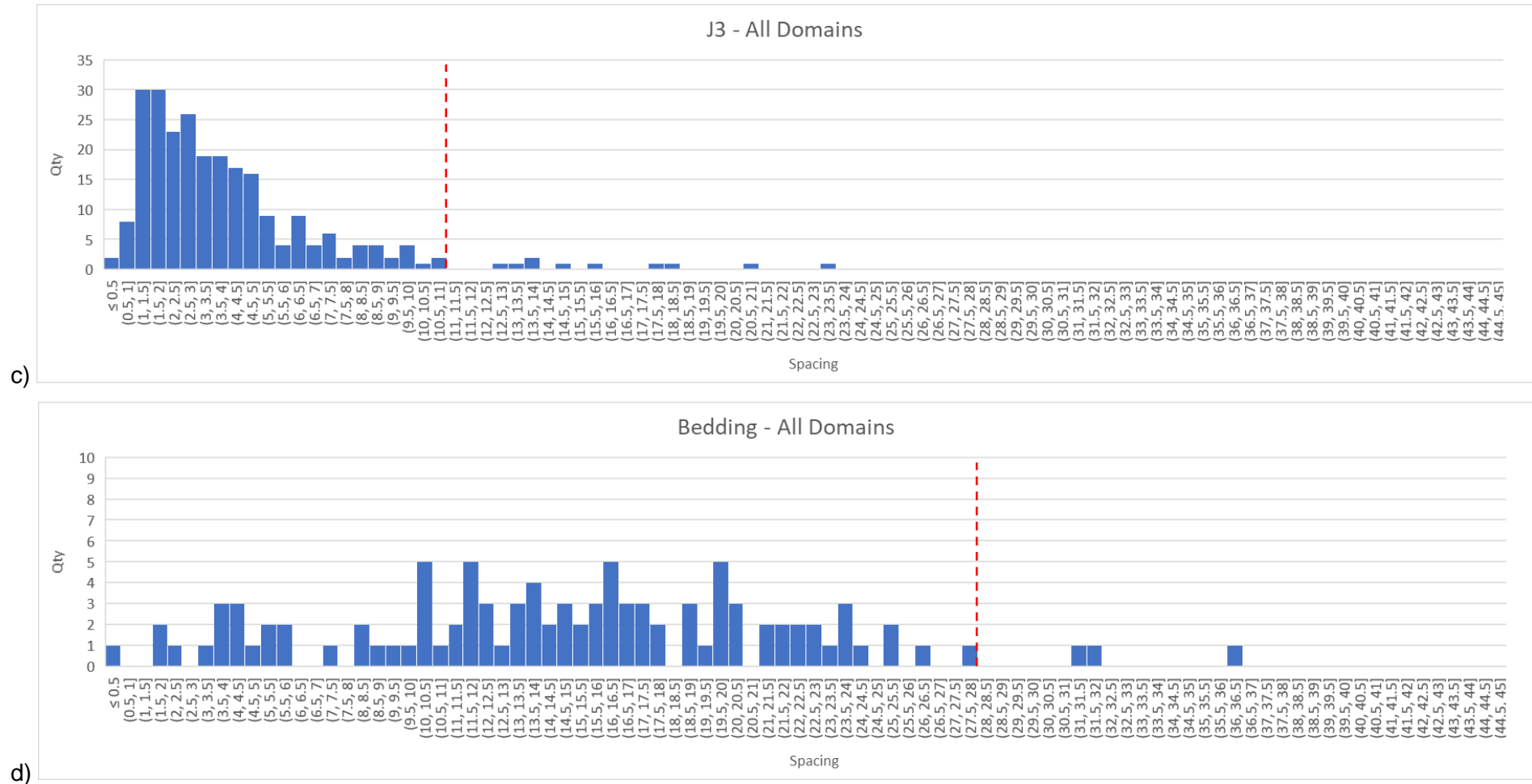
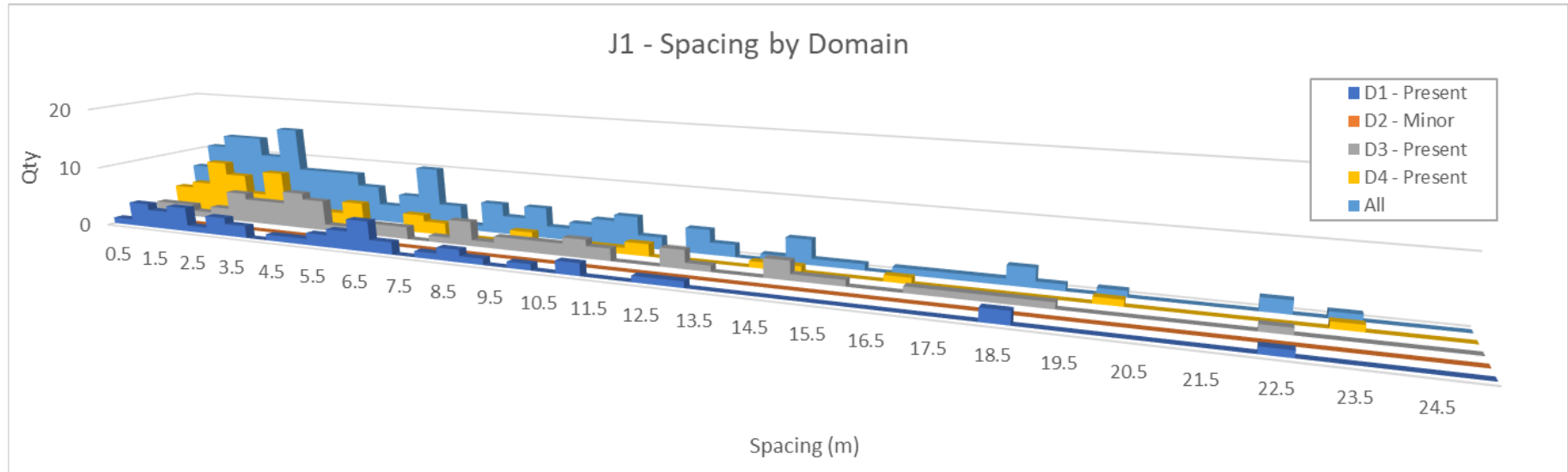
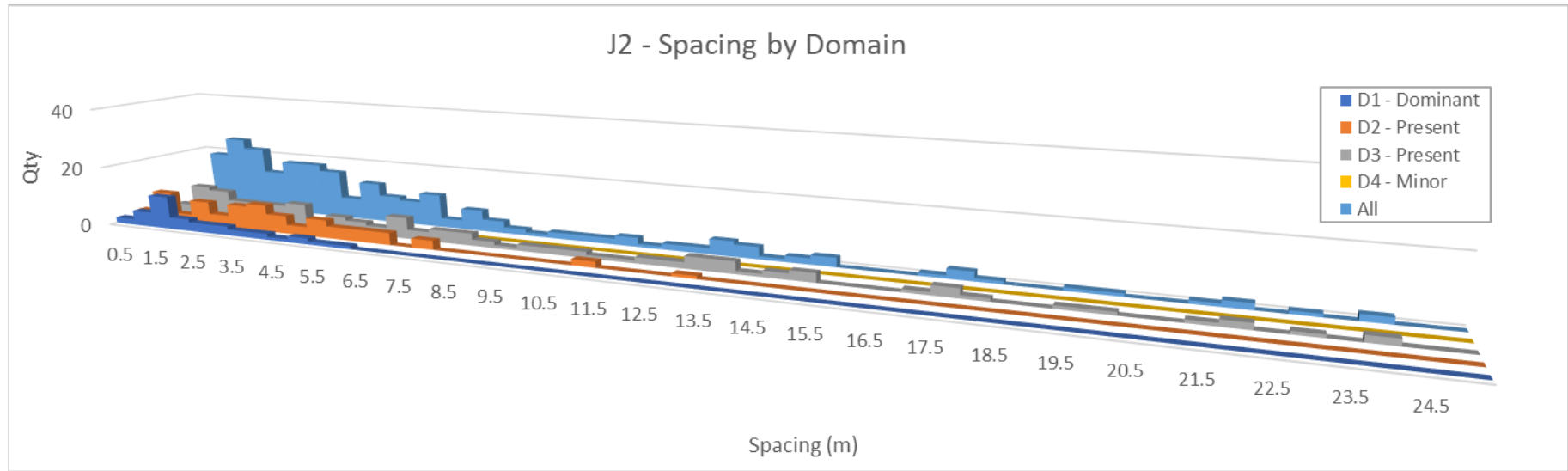


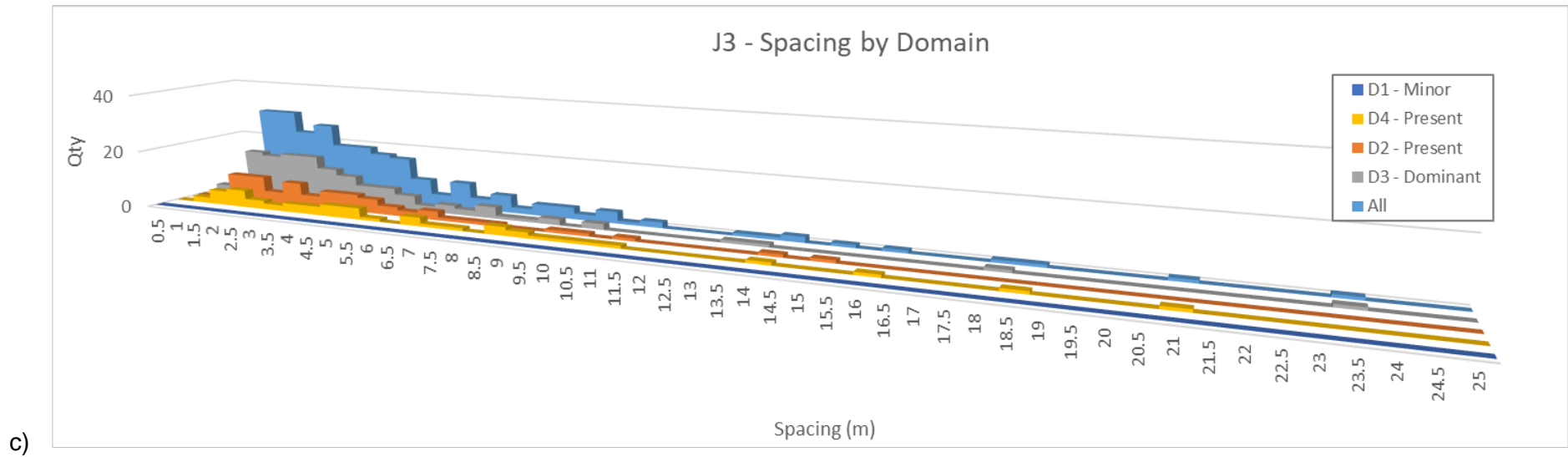
Figure 4-27: Histogram of scanline measured defect spacing, adopted upperbound limit marked in red; a) Joint Set J1; b) Joint Set J2; c) Joint Set J3; d) Bedding



a)



b)



c) Figure 4-28: Histograms representing defect spacing for each joint set, separated by domain. a) Joint Set J1. Not present in D2; b) Joint Set J2. Not present in D4; c) Joint Set J3. Not present in D1.

Table 4-12: Statistical summary of scanline measured set normal spacing, for all domains combined, with upperbound spacing limits applied.

Measure	Spacing (m)	Spacing (m)	Spacing (m)	Spacing (m)
	J1	J2	J3	Bedding
Min	0.12	0.07	0.07	0.35
Max	18.75	14.84	10.72	19.99
Mean	5.58	4.39	3.60	12.09
Mode (rounded to 0.5)	1.50	1.00	1.50	13.50
5%	0.50	0.73	1.00	3.12
25%	2.00	1.67	1.86	8.64
50%	4.00	3.41	3.00	13.00
75%	8.40	6.00	4.80	16.37
95%	14.96	12.70	8.68	19.50
Std. Dev.	4.61	3.55	2.30	5.22
Skew	1.06	1.29	1.09	-0.47

4.5.1.2 Sources of Error

Several limitations of the measurement methodology were recognised, as outlined below:

- The resolution of the 3D real scene model is not high enough to visually follow traces of joints in most cases;
- Point cloud resolution limits the minimum size of defect surfaces which can be represented. When determining the Hough Normal of a point, there may not be enough points along the surface to accurately define a plane and its orientation;
- When measuring defect spacing it can be challenging to judge the difference between waviness and defect spacing. On a highly undulous or irregular surface it may be difficult to define whether the exposed surface was created by a single irregular joint, or a set of joints at a small spacing. This is particularly difficult to define in joint sets which control the slope face orientation. In this case, as can be seen in Figure 4-26d, the stepped or irregular face may be due to waviness in the dominant joint set, or due to separate joints of the same set. This error could be reduced by quantifying and accounting for the waviness of joint planes;
- Spacing between non-parallel planes is location dependant. This error is reduced by completing several scanlines at various locations within each domain;
- If using the 1 or 2-point thickness tool, the orientation of the measurement plane will have a large impact on the calculated spacing value (as discussed above). This impact is reduced by taking measurements in the orientation of the set mean plane, using the 2-point thickness tool

- The point cloud within CloudCompare displays only defect surfaces, and is not capable of showing defect traces where a plane is not exposed. As such, where defect planes did not precisely cross the scanline but were observed directly above or below the scanline, geological judgement was applied (in conjunction with the ContextCapture 3D real scene model) as to whether the defect extends across the scanline as a trace rather than as a plane. An example is displayed below in Figure 4-29 for Joint Set J2, in Domain D2. Although the point cloud does not indicate a continuous defect surface, when compared to the 3D real scene model it becomes apparent that the joint is continuous, and that a trace is present.

This defect was visually assessed because the point cloud had displayed a defect surface which was then further investigated. If no defect surface had been observable in the point cloud at all, a visual assessment of the trace would not have been made, and the defect spacing in this region would not have been accurately measured. The resolution of the point cloud and the 3D real scene model is not high enough to accurately characterise the trace of defects where surfaces are not present, or when they are obscured by vegetation, talus etc. This issue could be solved by increasing the resolution of the point cloud data and 3D model, and then merging the 3D real scene model with the point cloud such that defect traces are also visible for measurement within the same model.

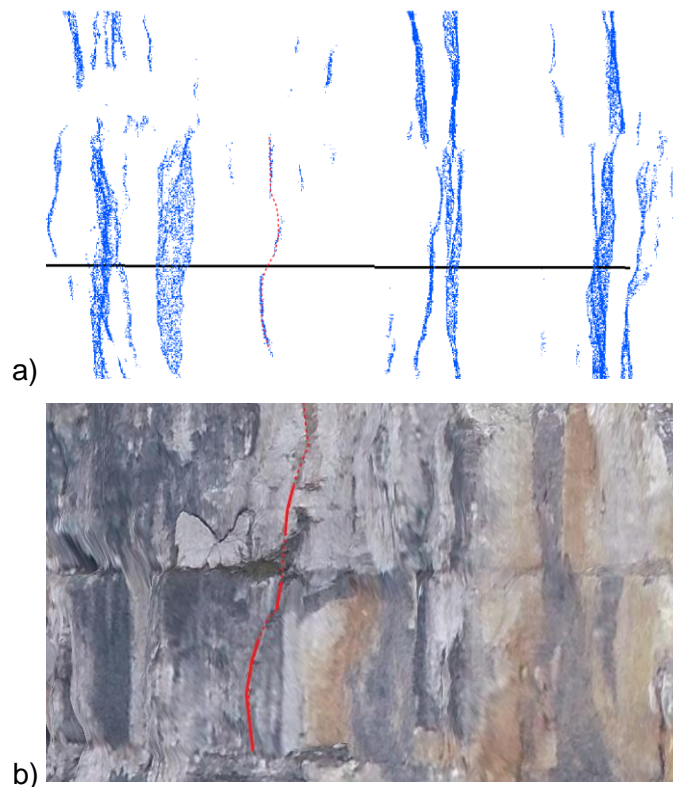


Figure 4-29: Comparison of defect visibility/apparent persistence in region D2 using a) CloudCompare point cloud; and b) ContextCapture 3D real scene model.

4.5.2 Measurement of Fallen Blocks

Fallen blocks located at the base of the Rockfall Area were measured in order to approximate defect spacing, surface area and block volume. All blocks with a dimension above 2 m were measured, with a basic description of the block shape and weathering recorded. It is noted that these blocks are estimated to comprise less than half of the overall rockfall, with the remaining material being less than 2 m in dimension.

Figure 4-30 displays the fallen blocks at the base of the slope, and the identifiers assigned to each visible block with a dimension above 2 m. As joints are all orthogonal to bedding, and all at equal orientation relative to each other ($\sim 60^\circ/120^\circ$), it is not practically possible to determine which joint sets comprised each block face. As such, all spacing, area and volume information has been combined for all defect sets, as displayed in Table 4-13.

Table 4-13: Statistical summary of measured block dimensions, for all domains and defect sets combined.

Measure	Edge length (m)	Area (m ²)	Volume (m ³)
Min	0.63	0.98	2.05
Max	7.51	50.45	252.65
Mean	3.02	10.74	45.60
5%	1.26	1.95	4.56
25%	1.90	3.82	7.14
50%	2.58	6.51	13.31
75%	3.55	12.06	38.74
95%	6.48	38.48	164.24
Std. Dev.	1.59	11.04	65.96

Histograms of dimensions are displayed in Figure 4-31. They show that typically block face lengths are below 4.5 m, volumes are below 25 m³, and face areas are below 9 m². The mean block edge length (3.02 m) was smaller than the mean spacing values for any joint set (4.1 m to 7.2 m). This indicates that spacing measured from the point cloud may be overestimated. It is possible that blocks broke up as they fell or landed. However, the shape of the fallen blocks was typically sub-rectangular, suggesting that blocks broke along joint or bedding planes. It is considered most likely that bedding spacing was overestimated. Point cloud data indicated a bedding spacing of 10 m to 20 m in this area. However, the largest observed fallen block edge length was 7.5 m. The larger measured spacing is believed to reflect the distance between beds of a significantly different nature – i.e. thinly bedded zones vs. massive zones. Bedding structure likely still exists within the “massive” zones, but is not visible with the current imaging resolution.

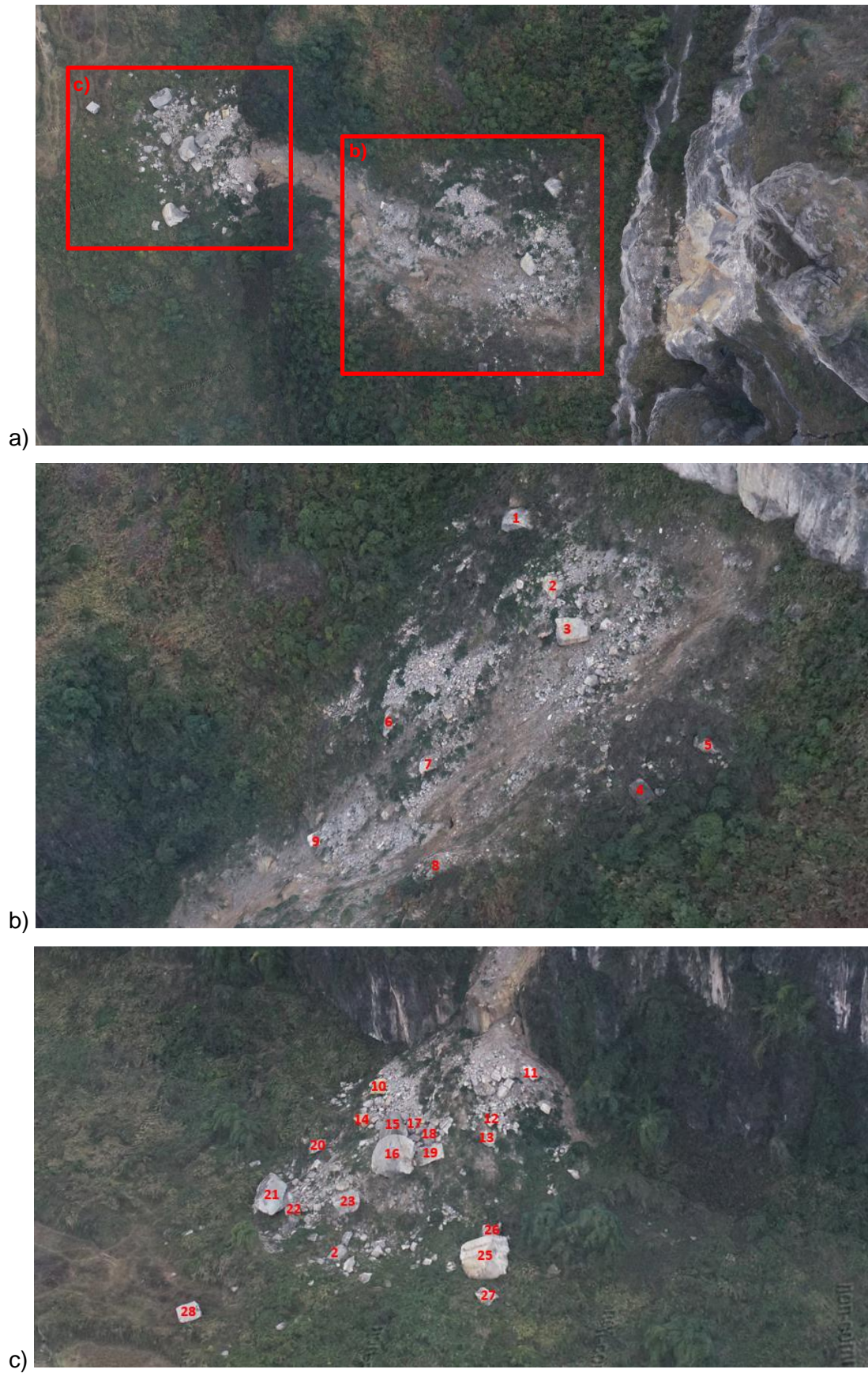


Figure 4-30: Visible blocks from recent rockfalls; a) View of talus from above; b) Visible blocks >2 m, from top bench – looking south-east; c) Visible blocks >2 m, from base of slope – looking south-east;

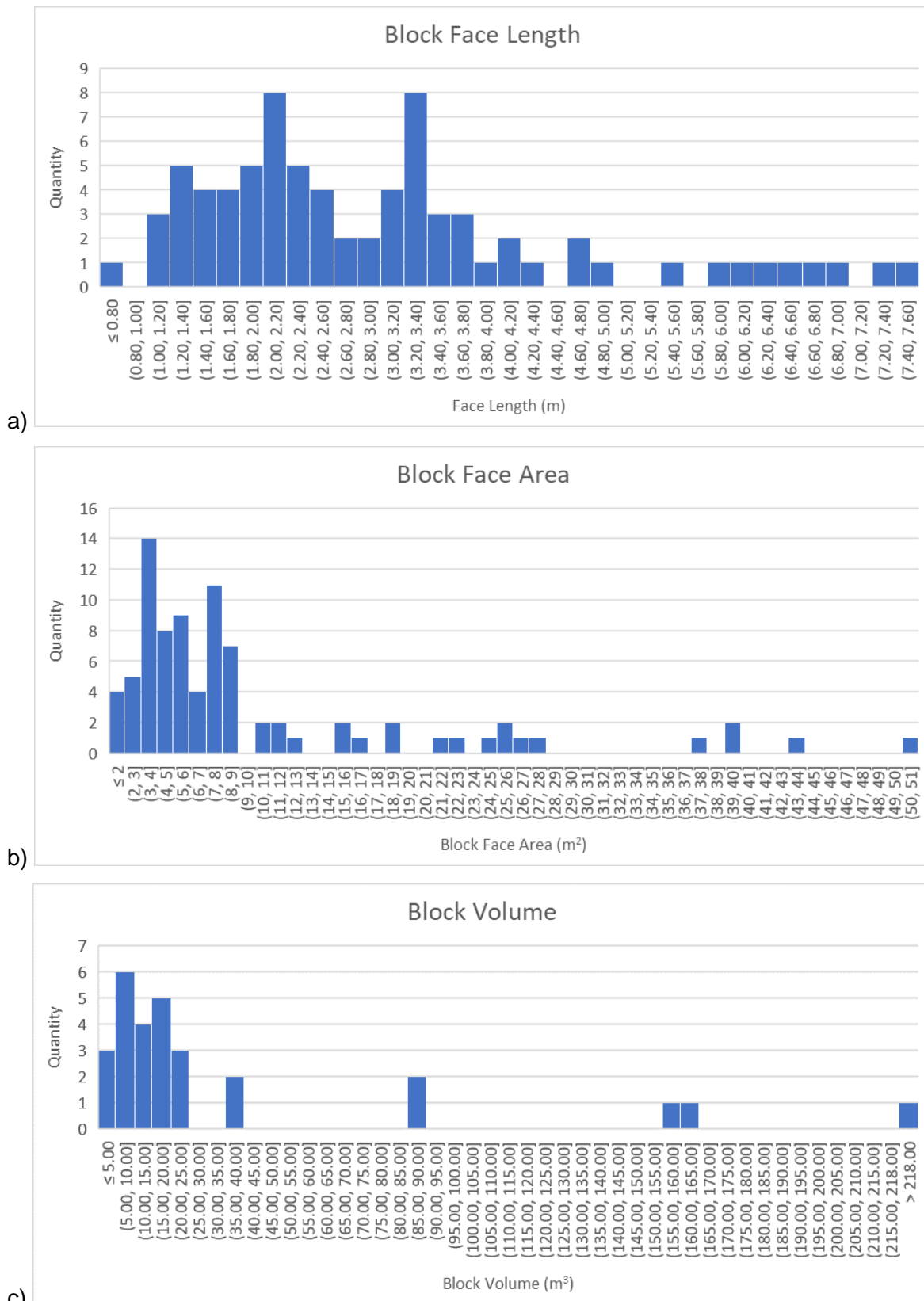


Figure 4-31: Measured block dimensions blocks with one dimension above 2 m; a) face length; b) face area; c) block volume.

The total volume of fallen blocks with a dimension above 2 m was 1090 m³.

Table 4-14: Measurement of blocks with dimensions >2 m in the Rockfall Zone.

Block	Length (m)	Width (m)	Height (m)	Volume ⁴ (m ³)	Age	Shape	Weathering
1	4.87	3.77	2.11 ¹	38.74	New	Sub-rectangular	Fresh
2	3.99	2.16	1.80	15.51	New	Sub-rectangular	Fresh
3	4.63	3.35	1.55 ¹	24.04	New	Sub-rectangular	Fresh
4	3.30	2.09	1.93	13.31	Old ³	Sub-rectangular	Weathered ³
5	3.05	1.30	1.15 ¹	4.56	Old ³	Irregular	Weathered ³
6	3.22	1.40	1.10 ¹	4.96	Old ³	Irregular	Weathered ³
7	3.45	2.37	1.31	10.71	New	Sub-rectangular	Fresh
8	7.28	3.10	6.93 ¹	156.40	Old ³	Irregular	Weathered ³
9	2.09	1.56	0.63 ¹	2.05	New	Sub-rectangular	Fresh
10	2.89	2.54	1.09 ¹	7.97	New	Sub-rectangular	Fresh
11	3.14	1.67	-. ²	-. ²	New	Sub-rectangular	Fresh
12	2.15	1.31	-. ²	-. ²	New	Sub-rectangular	Fresh
13	3.08	2.65	-. ²	-. ²	New	Sub-rectangular	Fresh
14	2.72	1.90	1.28	6.65	New	Sub-rectangular	Fresh
15	5.49	4.69	3.37	86.73	New	Planar but not orthogonal.	Fresh
16	6.37	6.14	4.20	164.24	New	Sub-rectangular	Fresh
17	2.49	2.24	1.86	10.36	New	Irregular	Fresh
18	2.58	1.83	1.51 ¹	7.14	New	Irregular	Fresh
19	4.40	3.77	-. ²	-. ²	New	Sub-rectangular	Fresh
20	2.26	2.08	1.60 ¹	7.50	New	Sub-rectangular	Fresh
21	7.51	3.71	3.23	89.87	New	Sub-rectangular	Fresh
22	2.31	1.77	1.64 ¹	6.73	New	Sub-rectangular	Fresh
23	4.11	2.94	1.97	23.86	New	Sub-rectangular	Fresh
24	3.38	2.39	-. ²	-. ²	New	Irregular	Fresh
25	6.42	5.87	6.70	252.65	New	Sub-rectangular	Fresh, bedding visible.
26	3.43	2.43	-. ²	-. ²	New	Sub-rectangular	Fresh
27	3.27	2.15	-. ²	-. ²	New	Sub-rectangular	Fresh

Notes:

1. Block is partially buried. Measured height may underestimate block dimensions.
2. Block is completely buried, with only the top exposed. Block height cannot be determined.
3. The block may present as weathered due to the age of its fall, or the block may have fallen in such a way as to present the initially outward facing, weathered, surface.
4. Volume was calculated on the assumption that all block planes were orthogonal, representing a rectangular block.

4.6 Persistence

Determining persistence using point cloud data is difficult, particularly where joints continue as traces rather than as surfaces. Due to the highly irregular, non-vertical and blocky nature of the slope face (including vegetation-covered benches), and due to the wavy surface of joint planes, it is difficult to trace neat planar continuations for each joint. Assessments on the nature of joint persistence were undertaken using engineering and geological judgement, by comparing the point cloud and 3D real scene models.

The quantitative assessment of persistence is orientation dependent. The persistence of each joint set was assessed in domains where the set could be viewed along strike, as displayed in Figure 4-32. The following determinations were made for each defect set:

- Joint Set J1: Highly persistent. Extends typically beyond outcrop limits.
 - Assessment based on domains D1, D3 and D4, oblique to Joint Set J2.
- Joint Set J2: Highly persistent. Extends typically beyond outcrop limits.
 - Assessment based on domains D2 and D3, oblique to Joint Set J2.
- Joint Set J3: Highly persistent. Extends typically beyond outcrop limits.
 - Assessment based on Domain D1, oblique to Joint Set J3.
- Bedding: Highly persistent. Extends beyond outcrop limits.

On the rare occasions that point cloud data displayed seemingly isolated planes, it is considered likely that these continue as traces throughout the outcrop.

Kulatilake et al. (2003) suggest that where semi-traces have terminations beyond the boundary of the exposure, reliability of the estimated corrected mean trace length is reduced. They state that for high reliability, the percentage of semitraces terminating outside of the exposure should be below 50% (Kulatilake, et al., 2003). All defect sets (J1, J2, J3 and bedding) have over 50% (closer to 90%) of trace lengths terminating outside of the exposure. As such, it is considered that a numerical assessment of defect persistence on joint sets is not possible, as the scale of persistence is significantly larger than the scale of the dataset for all defect sets. All that can be said is that the mean vertical trace length is larger than the height of the outcrop – which is approximately 140 m. These joint sets should be therefore considered to be continuously persistent on the outcrop scale.

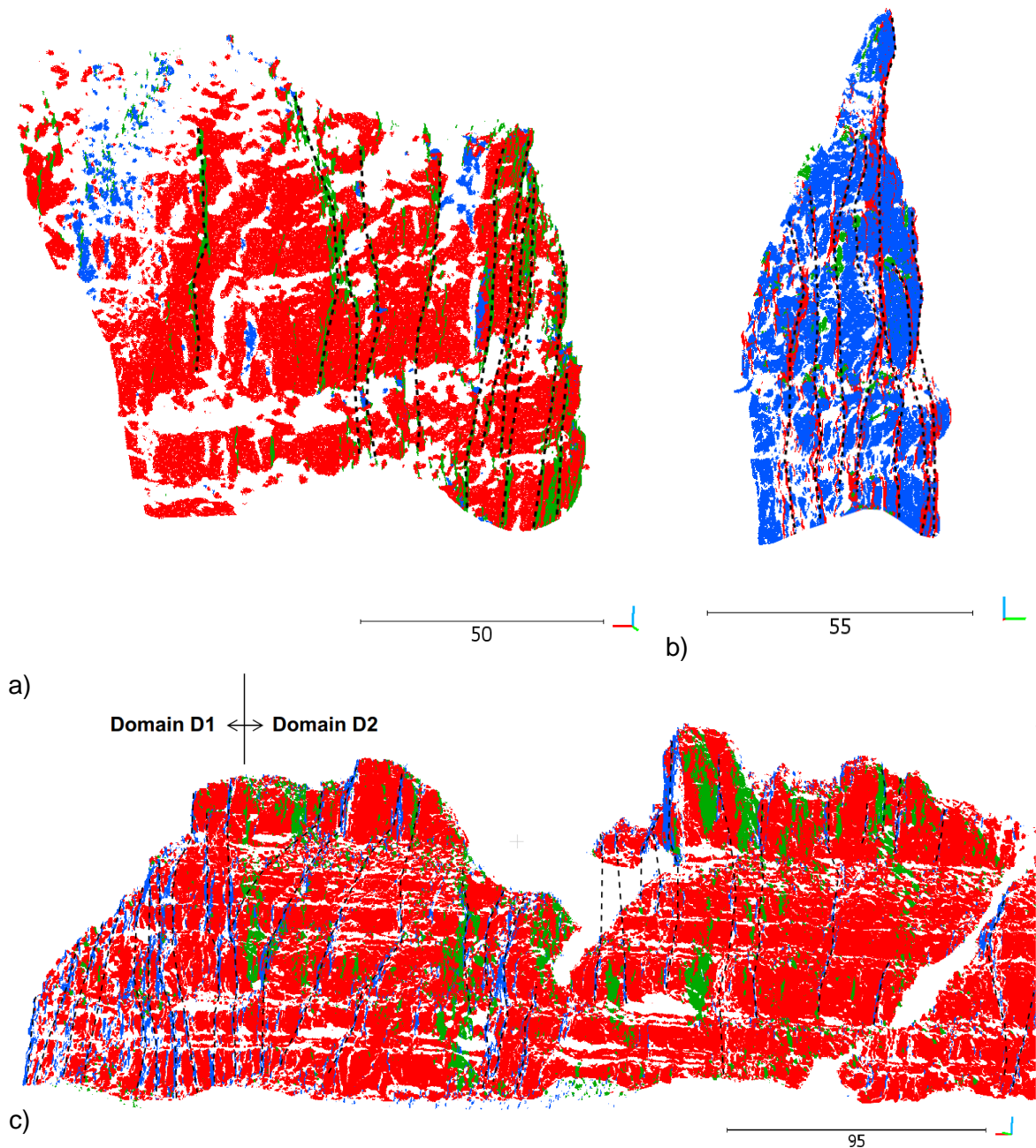


Figure 4-32: Markup of interpreted joint persistence; a) Joint Set J1, within Domain D4; b) Joint Set J3, within Domain D2; c) Joint Set J2, within domains D2 and D3. Note that the change in apparent dip of the joint set is due to the change in slope face orientation between Domain D2 and D3.

Similarly, there was no evidence of joint termination against other joints or bedding planes. The three joint sets and bedding were observed to regularly cross each other, and no termination against one another was observed. All joint sets are considered to be unbound by bedding structures. The vast majority of observable joint planes terminated outside the Study Area (type: obscured). Any rare small planes which did not extend outside the Study Area are believed to form a part of larger joints which do not show a physical relief, as discussed in Section 4.5.1.

4.7 Roughness and Waviness

Waviness and roughness were measured for representative exposed joint planes for each joint set. A focus was given to planes within the Rockfall Area, with the aim that all fresh surfaces in this zone be thoroughly investigated in terms of surface area, dilation angle, amplitude and orientation. Three assessments were made as to joint roughness/waviness:

- Qualitative large-scale assessment of the waviness of entire joints, across the height of the outcrop;
- Quantitative assessment of the amplitude of first order waviness on exposed defect planes; and
- Quantitative assessment of the dilation angle on exposed defect planes.

The available resolution of data was not sufficient to quantify the second order roughness in the form of Barton's JRC.

4.7.1 Joint Waviness

The large-scale assessment of joint waviness across the height of the slope face was qualitatively undertaken by observing the shape of the joint trace when viewed parallel to the strike of that joint. The shape was described according to ISRM (1978) as planar, undulating or stepped. Each joint set was classified as follows:

- Joint Set J1: Stepped, some undulations;
- Joint Set J2: Undulating, on the scale of tens of meters. Planar at <5 m scale; and
- Joint Set J3: Undulating, on the scale of tens of meters. Planar at <5 m scale.

All joint sets (but particularly Joint Set J1) exhibit locations in which joints appear to split and re-join, resulting in apparent "stepped" features. The long joint traces observed likely formed from the connection of individual adjacent joints, through fracturing of intact rock or from intersecting joint surfaces. The large-scale waviness of joints can be observed in Figure 4-32 above.

4.7.2 Joint Amplitude

The amplitude of first order waviness was calculated on the scale of exposed surfaces using a planar method. This proposed method is analogous to the straight edge method, but utilises a best fit plane, measuring maximum amplitude as offset from that plane. This method is considered to more appropriately reflect the movement of a block along a surface, and recognises that the whole block will dilate over an asperity.

The planes considered for the quantitative assessment of each joint set are outlined below:

- Joint Set J1: Three planes from each of the four domains (12 in total);
- Joint Set J2: One plane from each of D1, D3 and D4, with an additional 9 planes from within the Rockfall Area in Domain D2 (12 in total);
- Joint Set J3: One plane from each of D1, D3 and D4, with an additional 9 planes from within the Rockfall Area in Domain D2 (12 in total); and
- Bedding: Analysis was not undertaken on bedding planes, due to the lack of suitable planes for measurement.

For each joint set, the selected defect plane was cropped from the segmented joint set point cloud (Section 0), and a mean orientation plane was fitted. The view was oriented to be looking along strike of the plane (Figure 4-33a). The one-point thickness tool was used to measure the maximum distance of the joint surface to the left and right of the mean orientation plane. The addition of these two height values was taken as the amplitude. At the same time, the length and width of the defect surface was measured, and the orientation of the mean plane recorded.

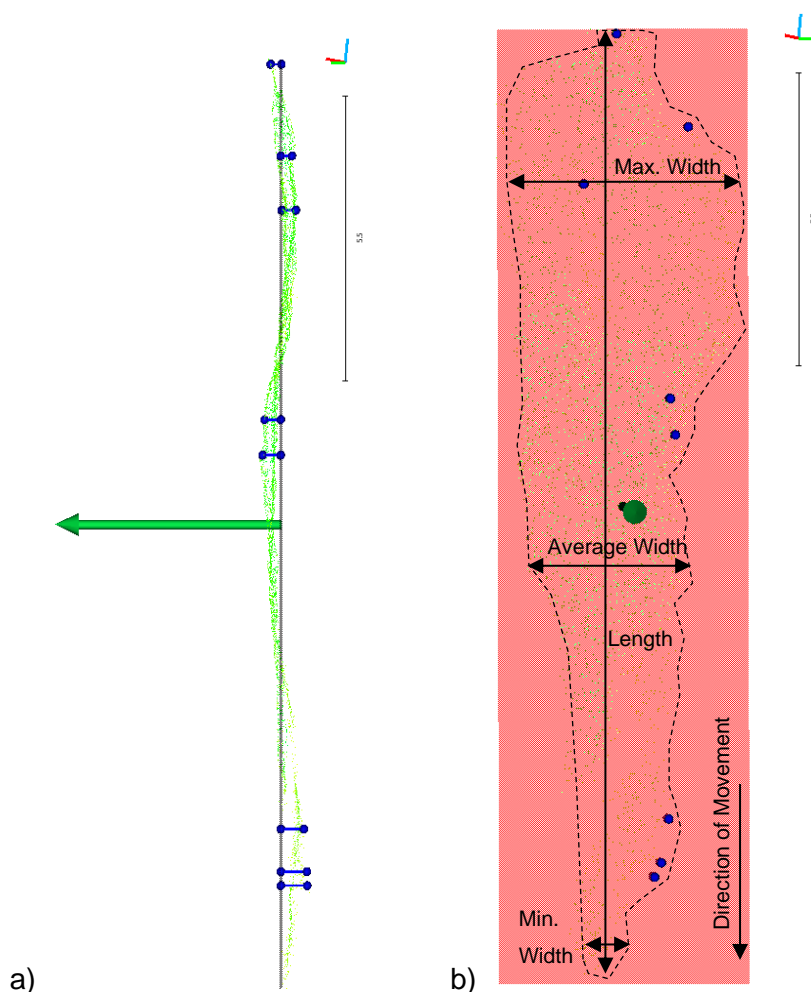


Figure 4-33: Measurement of amplitude above and below the mean plane line, with measurement points indicated in blue (Joint Set J2, plane 1); a) looking along plane strike; and b) looking directly at the plane face. The dashed line displays the extents of the point cloud which define the joint face.

Roughness is known to be a directionally-dependent property. However, the planar measurement technique considers the plane as a whole, and does not account for the main direction of movement (which is assumed to be sub-vertical in these joint sets). In order to allow an analysis of amplitude compared to length and area of measurement, the length was recorded in the direction of assumed shear (vertical).

A statistical summary of the amplitude measured for each joint set is outlined in Table 4-15 below. A summary of the measured length, area and amplitude for each assessed plane is included in Table 4-18. Note that the numerical naming conventions of blocks relate to the block numbers analysed as part of the rockfall reconstruction discussed in Section 4.7.3.1.

Table 4-15: Statistical summary of first order waviness, as amplitude.

Measure	Amplitude J1 (m)	Amplitude J2 (m)	Amplitude J3 (m)
Min	0.23	0.34	0.35
Max	3.09	2.33	4.26
Mean	1.26	0.95	1.06
5%	0.40	0.38	0.38
25%	0.68	0.51	0.48
50%	1.12	0.90	0.64
75%	1.71	1.14	1.23
95%	2.47	1.86	2.84
Std. Dev.	0.75	0.54	1.04

Joint Set J1 was observed to have the largest maximum amplitude, with a mean of 1.26 m and median of 1.12 m. Joint Set J2 exhibited a lower maximum amplitude, with a mean of 0.95 and median of 0.90 m. Joint Set J3 exhibited the smallest amplitude, although it was highly variable with a mean of 0.35 m, but a median of 0.64 m, and a standard deviation of 1.04 m. This is broadly consistent with the quantitative assessment, which found that Joint Set J1 was stepped, and therefore would present with larger, more irregular, amplitudes.

The range of waviness amplitude values overlaps with the range of spacing values discussed in Section 4.5. This implies that there may have been some contamination of spacing values with waviness. However, it has already been determined (through the comparison with fallen block dimensions), that spacing values likely overestimate rather than underestimate the real set normal spacing. As such, no correction will be applied to spacing values on the basis of waviness, although future investigations are recommended.

4.7.2.1 Sources of Error

All surfaces in the model occur where blocks previously failed. If this failure occurred in sliding, the shear movement along the joint surface may already have degraded any asperities along the surface. Without first assessing the failure mechanism at a given surface, it cannot be known for certain whether the plane has undergone shear or not, and therefore whether the surface represents a lower (possibly residual) waviness.

There was an overall high variability in amplitude, which was observed to relate to the surface area over which amplitude was measured. Those defects with the highest measured amplitude were typically also those of the largest area. Note that this is opposite to the scale effect discussed by Barton (1982), who stated that the JRC reduces with increasing measurement size. A comparison between measured amplitude and defect area is included in Figure 4-34 and Figure 4-35 below.

It is believed that this size bias indicates a large-scale waviness to the jointing which is evident only in surfaces over a certain area. Sub-sampling the amplitude of waviness within smaller planes cannot reflect the waviness of the joint surface over a scale of tens of meters. Once waviness or undulations reach a certain scale relative to block size, they no longer control shear strength. This is because at a block scale the surface can be estimated as roughly planar. Extremely large scale waviness would best be assessed by measuring interlimb angles or using qualitative descriptors such as those outlined in Section 4.7.1. However, waviness of this scale is judged to have little bearing on defect shear strength at a block scale, and so it will not be discussed further in this thesis.

In order to determine an appropriate scale at which to measure waviness, an attempt was made to define the upperbound block face area. Looking at the dimensions of fallen blocks at the base of the slope face (Section 4.5.2), the block face area is likely to be less than approximately 50 m². To that end, Table 4-16 presents a revision of the statistical amplitude summary, considering only those surface areas below 50 m². The mean, median and standard deviation values for each joint set are significantly smaller looking at this block-size scale. Joint Set J1 still displayed the most waviness (median 0.91 m), while Joint Sets J2 and J3 were quite similar, with medians of 0.53 m and 0.56 m respectively.

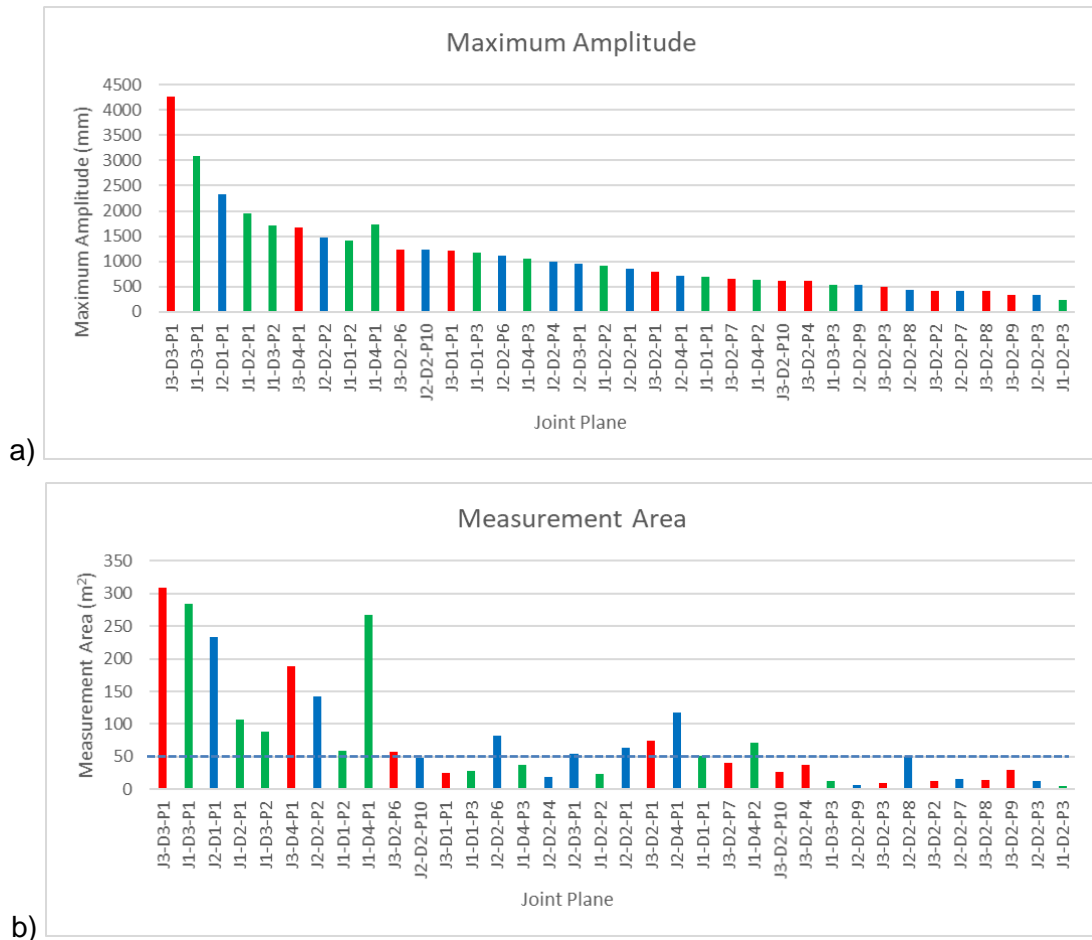


Figure 4-34: Comparison of maximum amplitude (a) compared to measurement length (b).

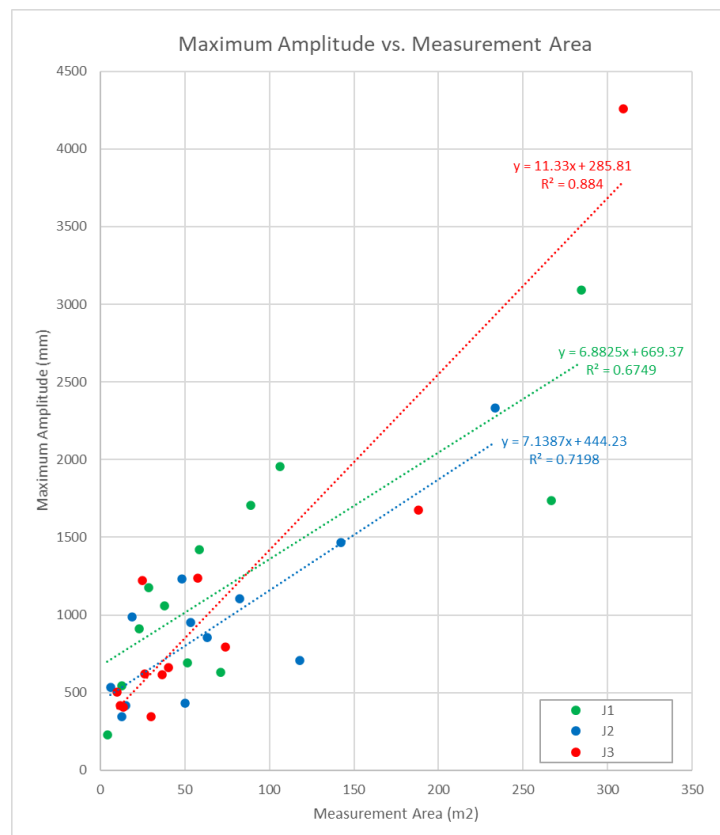


Figure 4-35: Amplitude vs. Measurement area

Table 4-16: Statistical summary of first order waviness, for joint surfaces with area less than 50 m².

Measure	Amplitude J1 (m)	Amplitude J2 (m)	Amplitude J3 (m)
Qty Planes <50m ²	5	5	8
Min	0.23	0.34	0.35
Max	1.18	1.23	1.22
Mean	0.78	0.70	0.60
5%	0.29	0.36	0.37
25%	0.54	0.42	0.42
50%	0.91	0.53	0.56
75%	1.06	0.99	0.63
95%	1.15	1.18	1.03
Std. Dev.	0.35	0.35	0.26

It should be noted that the planes measured in this procedure utilise only the points from the segmented point cloud for the joint set of interest – e.g. for a plane of Joint Set J2, the segmented point cloud for the set J2 is analysed. This means that there may be gaps in the point cloud (as can be seen in Figure 4-36), which occur where the normal orientation of a data point is not within the orientation range of the particular joint set. There are three possible reasons for these gaps:

1. A joint from another set intersected the plane;
2. Waviness/undulations in the joint at that location are so extreme that they present an orientation outside of the orientations defined for the joint set in question; or
3. The joint surface was discontinuous in this location, and a “rock bridge” was present, which broke as the block dislodged.

An inspection of a joint surface which exhibited these “voids” was undertaken in order to determine their cause. Plane 6 of Joint Set J2 was inspected. As displayed in Figure 4-36b below, numerous “voids” can be observed in the segmented J2 point cloud.

Figure 4-36 compares the plane with only Joint Set J2 showing (Figure 4-36a) to the plane with all sets showing (Figure 4-36b). It is clear that there is a small region where the J2 joint plane has been split by set J3 (red). This supports point 1 above. However, additional voids are still present. Inspection of the unsegmented HSV coloured point cloud (Figure 4-36c) shows that the void region has a similar colour to the surrounding points. This indicates that the void is likely due to extreme waviness, with the normal orientation of the points falling just outside of the segmented set window. On this plane, no rock bridges are obvious.

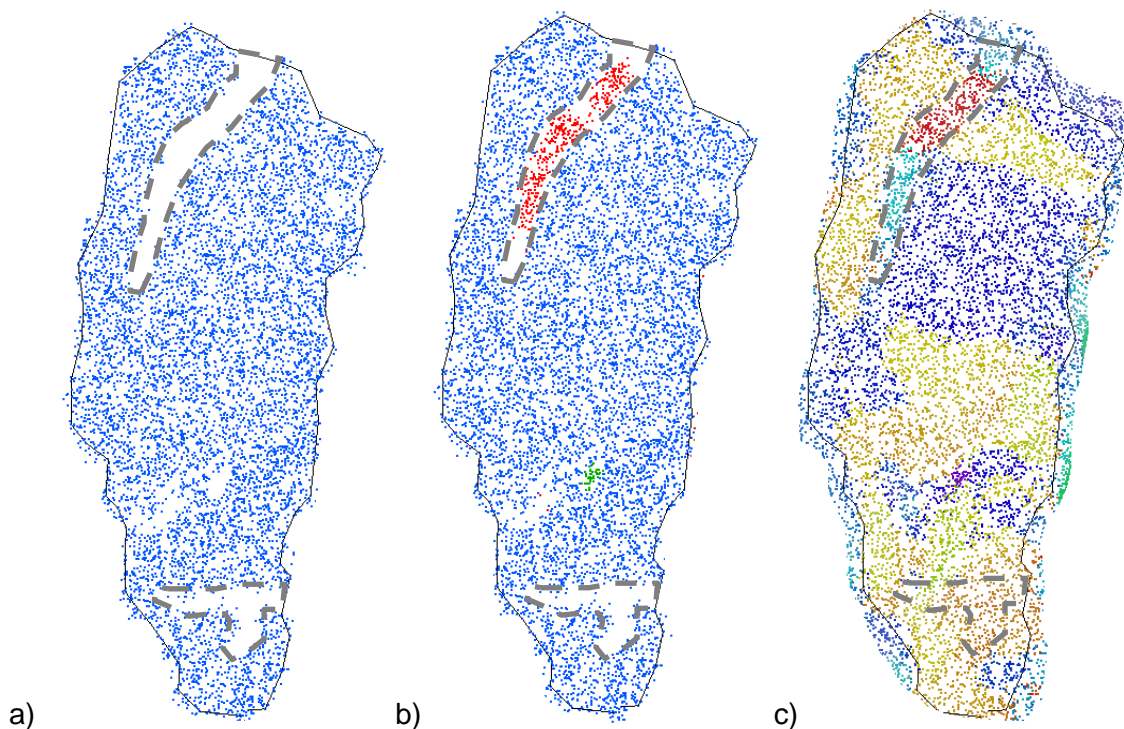


Figure 4-36: J2 Plane 6; a) Showing only segmented point cloud from main joint set (J2), gaps visible; b) All defined (and segmented) joint sets showing. Small segment of Joint Set J3 (red) filling some of the gaps, additional gaps still present; c) Unsegmented point cloud, coloured by Hough Normal of each point;

The presence of these gaps does not significantly alter the amplitude of a defect plane measured using the procedure outlined above. This is because gaps are still surrounded by points which are visible, and so the overall surface of the joint when observed in profile is similar. However, the mean plane will change slightly based on the addition of these points within the voids. A comparison of amplitude along Plane 6, J2, calculated an amplitude of 1105 mm when only points from the J2 cloud were considered, and an amplitude of 1090 mm when all points were considered along the surface. This difference of 15 mm (or 1.36%) is considered negligible, particularly when considering the resolution of available data.

Because movement along an existing joint would offer significantly less resistance to shear than a rock bridge, it would be ideal to quantify the presence of any rock bridges. However, it was not possible to determine the proportion of alternate jointing, rock bridges and extreme waviness using the available data. On joint surfaces which were inspected, voids were largely judged to be due to extreme waviness, with some smaller instances of intersecting joints. No rock bridges were directly observed.

Higher resolution imagery may have enabled a visual assessment of exposed rock bridges on surfaces. However, for the purposes of this thesis, rock bridges are disregarded, and gaps in the point cloud of joint surfaces are omitted when calculating waviness amplitude and dilation angle.

4.7.2.2 Comparisons with Existing Methods

There are differences between the planar measurement method proposed in this thesis and the standard straight edge method for measuring waviness amplitude proposed by ISRM (1978). This means that the results are not directly comparable, because:

- The plane areas under consideration are significantly larger than the 1 m straight edge typically used in site measurements. Roughness is scale-dependant, and scale factors must be considered;
- The planar method measures roughness across an area rather than a singular line (as per the straight edge method). However, considering that blocks slide across planes rather than singular lines, this is believed to appropriately reflect block movement. The straight edge method was designed for simple field use based on limited available equipment.
- Measuring along the full area of a plane means that the likelihood of intersecting extreme amplitude values is more likely. Therefore, amplitude measured with this method would be higher than measured along a straight edge. However, as Hencher and Richards (2015) stated, an entire block may dilate over an asperity, whatever the length of surface;
- The straight edge method rests a straight line on the highest two peaks of a surface, and measures amplitude perpendicularly downwards to the lowest point. The method utilised in this thesis fits a mean plane to the defect surface, and measures amplitude both above and below the mean plane, summing these values to obtain the amplitude. Depending on the overall orientation of the mean plane as compared to the straight edge, this may lead to a slight difference in amplitude readings, as displayed in Figure 4-37; and
- The amplitude measured from the mean orientation plane is directly dependant on the point cloud itself. If the resolution of the point cloud is too coarse to determine troughs and peaks in the surface, if shadowing from the angle of measurement prevented imaging of troughs, or if noise or errors in measurement produced outlying datapoints, the amplitude as measured would not be correct.

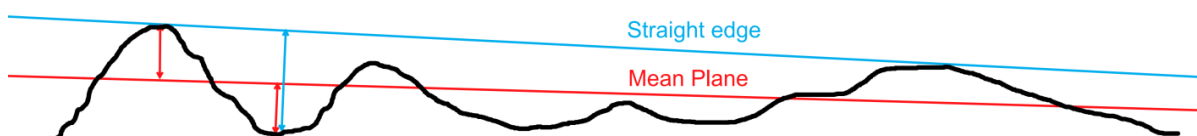


Figure 4-37: Amplitude measurements using straight edge method (blue) and mean plane method (red)

4.7.3 Dilation Angle

Dilation angle was measured according to the methodology of Dong et al. (2020), whereby the Hough normal of each point was exported (as dip and dip direction), and plotted on a stereonet using DIPS 8.0 (Figure 4-38). The peak dilation angle was then taken as the angle between the cone axis (mean joint plane) and the surface formed by the scatter of the surface normals.

The 95th percentile variability cone was used to define this scatter, rather than the furthest outlier. The stereonet was plotted using the “scatter” mode, whereby the diameter of the plotted point reflects the quantity of pole vectors it represents. Outlying points were typically very small, representing only a small number of pole vectors, therefore representing a small planar surface. It was judged that these outliers would not control the dilative behaviour along the plane, and so the 95th percentile variability cone was adopted.

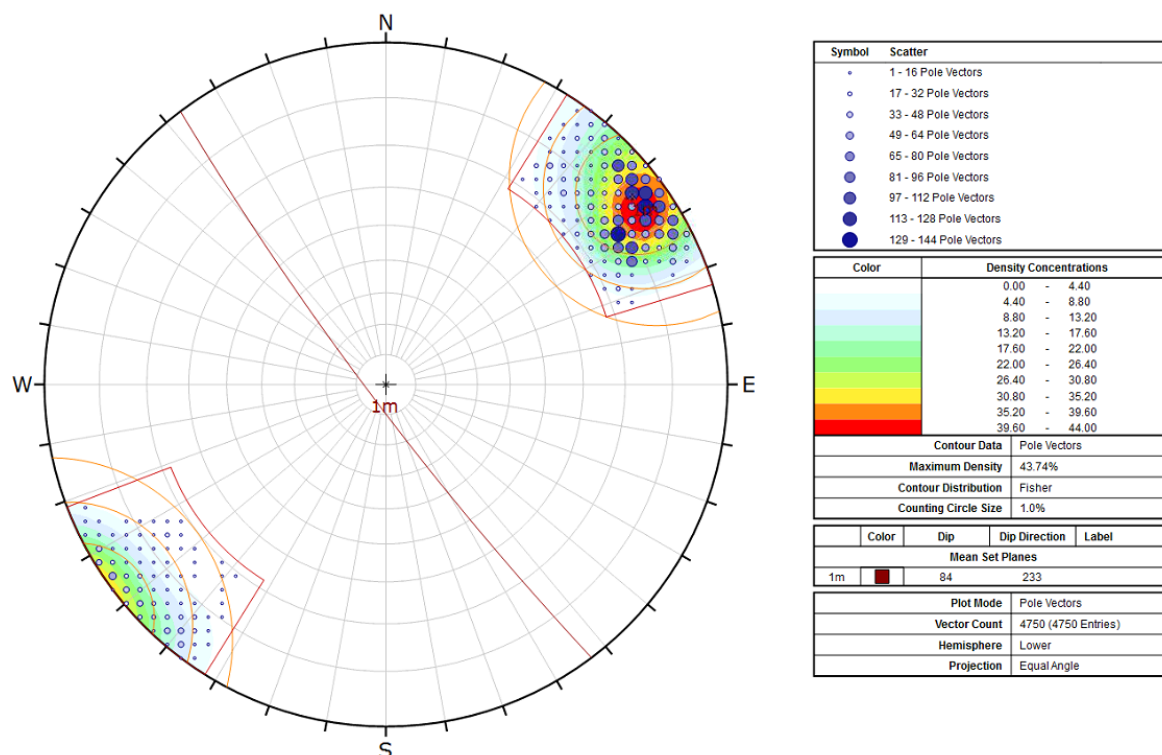


Figure 4-38: The Hough normal of each point on Plane 1 of Joint Set J2 plotted on a stereonet, where the plotted normals reflect surface roughness and the dilation angle is taken as the 95th percentile variability cone (centre) from the mean joint plane.

A statistical summary of the dilation angle measured for each joint set is outlined in Table 4-17 below. A summary of the measured length, area and dilation angle for each plane assessed is included in Table 4-18. Note that the numerical naming conventions of the blocks relate to the block numbers analysed as part of the rockfall reconstruction discussed in Section 5.1.

Generally, the joint sets were observed to all have similar peak dilation angles, with mean and median values between 18.42° and 22.30°. Joint sets all had a standard deviation of between 4.01° and 5.63°. When the peak dilation angle was plotted against measurement area (Figure 4-39), a slight size bias emerged where larger planes had slightly higher dilation angles. This was not as pronounced as for waviness amplitude (Section 4.7.2).

Table 4-17: Statistical summary of peak dilation angle, for joint surfaces with area less than 50 m².

Measure	Dilation Angle	Dilation Angle	Dilation Angle	Dilation Angle
	J1 (°)	J2 (°)	J3 (°)	All (°)
Min	10.25	15.26	16.77	10.25
Max	25.31	27.16	29.77	29.77
Mean	18.42	20.99	22.30	20.86
5%	10.91	16.07	17.62	13.05
25%	13.54	19.30	19.25	19.20
50%	20.57	19.92	20.45	20.34
75%	22.39	23.30	24.94	23.53
95%	24.73	26.39	29.48	29.06
Std. Dev.	5.63	4.01	4.44	4.96

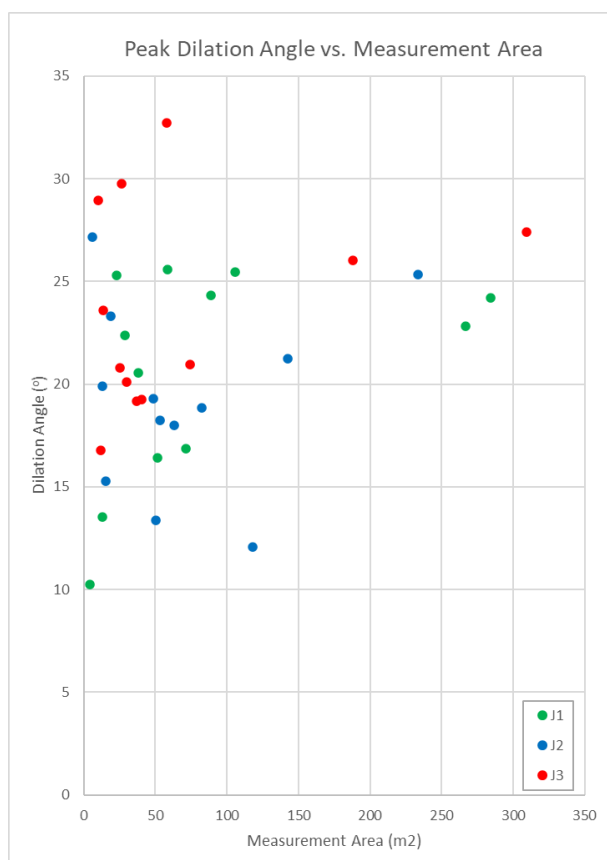


Figure 4-39: Peak dilation angle vs. measurement area for all joint sets

Table 4-18: Length, measurement area, maximum amplitude, peak dilation angles, and orientation for each measured plane.

Set	Plane	Length	Area (m ²)	Maximum Amplitude (mm)	Peak Dilation Angle (°)	Plane Dip (°) (Compass)	Plane Azimuth (°) (Compass)	Mean Dip (°) (DIPS)	Mean Azimuth (°) (DIPS)
J1	D1-P1	17.15	51.49	692	16.42	78	105	80	104
J1	D1-P2	15.39	58.48	1422	25.58	89	109	88	109
J1	D1-P3	10.06	28.67	1176	22.39	81	106	85	103
J1	D2-P1	18.85	106.05	1953	25.45	83	289	87	292
J1	D2-P2	10.03	22.86	912	25.31	86	284	89	101
J1	D2-P3	6.39	4.19	228	10.25	84	124	82	125
J1	D3-P1	41.88	284.23	3091	24.21	81	287	86	289
J1	D3-P2	18.86	88.97	1706	24.31	82	122	86	289
J1	D3-P3	8.76	12.76	543	13.54	88	116	90	118
J1	D4-P1	28.34	266.72	1735	22.85	88	105	90	289
J1	D4-P2	14.31	71.17	630	16.87	86	119	87	120
J1	D4-P3	14.71	37.82	1057	20.57	85	289	86	294
J2	D1-P1	29.77	233.40	2330	25.35	85	56	90	57
J2	D2-P1	17.82	63.44	857	18.01	84	233	84	233
J2	D2-P10	13.69	48.46	1232	19.30	88	229	89	231
J2	D2-P2	25.00	142.50	1467	21.24	88	231	89	233
J2	D2-P3	8.05	12.95	344	19.92	87	235	90	228
J2	D2-P4	14.32	19.05	989	23.30	86	241	80	50

Set	Plane	Length	Area (m ²)	Maximum Amplitude (mm)	Peak Dilation Angle (°)	Plane Dip (°) (Compass)	Plane Azimuth (°) (Compass)	Mean Dip (°) (DIPS)	Mean Azimuth (°) (DIPS)
J2	D2-P6	16.48	82.40	1105	18.83	88	229	89	223
J2	D2-P7	9.25	15.08	417	15.26	81	44	83	44
J2	D2-P8	10.84	50.19	433	13.37	84	225	86	226
J2	D2-P9	8.69	6.17	533	27.16	89	220	83	223
J2	D3-P1	15.55	53.49	950	18.24	86	228	86	231
J2	D4-P1	26.13	118.16	708	12.06	82	77	84	75
J3	D1-P1	20.17	24.98	1221	20.79	81	13	89	360
J3	D2-P1	14.33	74.03	794	20.97	85	335	86	353
J3	D2-P10	10.80	26.46	621	29.77	84	140	86	149
J3	D2-P2	5.29	11.84	417	16.77	81	359	82	359
J3	D2-P3	5.47	9.93	504	28.93	86	338	86	344
J3	D2-P4	10.78	36.66	616	19.18	84	168	87	171
J3	D2-P6	11.28	57.74	1237	32.74	89	337	89	154
J3	D2-P7	8.75	40.49	664	19.27	88	143	89	147
J3	D2-P8	8.96	13.66	407	23.60	84	145	85	151
J3	D2-P9	8.18	30.02	346	20.11	86	138	86	142
J3	D3-P1	32.82	309.40	4258	27.40	86	159	88	158
J3	D4-P1	16.05	188.23	1674	26.01	89	335	89	336

4.7.3.1 Sources of Error

The methodology proposed for the determination of the dilation angle considers all parts of the plane in all directions with equal weighting, and does not account for a predicted direction of shear. It also does not consider the scale effect of roughness, and is measured across an entire defect surface rather than a 1 m interval, or other standard dimension. The accuracy of the dilation angle is dependent on the resolution of the point cloud, and the appropriateness of the derivation of point normals (as described in Section 2.1.2.1).

As discussed in Section 4.7.2.1, in some instances there are gaps in the point cloud defining plane surfaces. Additional analysis was undertaken to find the reason for, and the effect of, the data gap. The analysis used the data for plane P6, in Domain D2, which occurs along Joint Set J2. Figure 4-40 below displays the stereographic plot of point normals, one including those classified as Joint Set J2 only, and the other including all point normals. Both cases have the same high-density centre. However, the scatter of poles from the second case is observed to be much larger – extending up to 60° from the mean set orientation. The first case defines a dilation angle of 18.83° , whilst the second case defines a dilation angle of 30.37° (at the 95th percentile).

The second case may reflect extreme waviness, intersections of other joint sets, or rock bridges which have fractured. The scatter of poles in this case indicates that some points have a normal orientation within the window of Joint Set J3. This is in line with the visual assessment in Figure 4-36, suggesting that the set J3 intersected this plane. As all joint sets are sub-vertical and the direction of movement is likely sub-vertical, the intersection of J3 is unlikely to cause significant dilation. Any rock bridges represented by the scatter would represent a cohesive component of shear strength and therefore would not be considered in calculations of dilation angle.

The first case corresponds reasonably well with the dilation angle of 14° suggested by Dong et al. (2020) for Kaili Limestone. As such, the dilation angle for all analysed joint planes has been calculated from the segmented plane point cloud only.

Interestingly, it was observed that the plane orientation derived from fitting a plane to the point cloud of a surface was similar, but not equal to, the mean set orientation when all Hough normals were plotted on a stereonet in DIPS. The fitted plane is believed to be more accurate, as it considers the relative location of each point, and is therefore able to account for variations in the intensity of the point cloud at various locations.

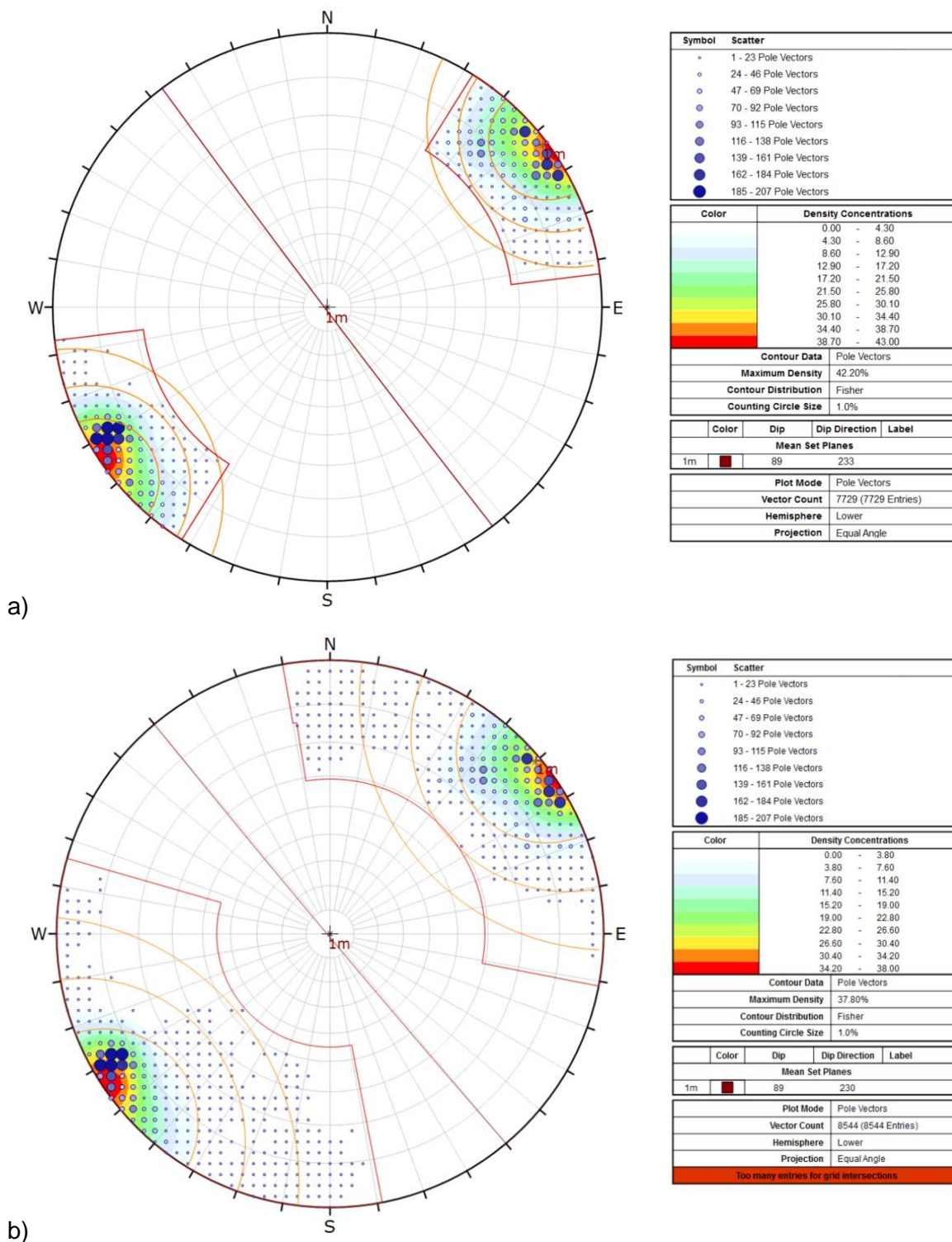


Figure 4-40: Stereonet plot of pole normals for Plane 6, Domain D2, Joint Set J2, showing the 68th, 95th and 98th percentile variability cones; a) Plotting point normals from set J2 only; b) Plotting point normals from unsegmented point cloud.

4.8 Defect Set Characteristics

4.8.1 Joint Nature and Formation

Joints across the study area were observed to be highly persistent, unbound in termination, and with an orientation which was not locationally dependant. Literature describing other outcrops within the Kaili region (Dong, et al., 2020) defines joint sets with a similar orientation. Together, this points to the joint sets being regional in nature, forming from a state of near constant stress (Ghosh, et al., 2018).

The high jointing persistence (at least in the vertical direction) is not unexpected. The reasons for joint arrest outlined by Ghosh et al. (2018) (increase in stress perpendicular to the joint face and interaction with obstacles) were not present in this area during joint formation. Joint sets do not do not truncate each other, and there was no evidence of joint termination against bedding planes.

Considering the lack of tectonic activity in this region, it is likely that the joint sets formed from lithostatic changes in overburden weight. This is supported by the fact that all three joint sets are orthogonal to the bedding, and would have been parallel to the major stress direction under overburden weight. Assuming no horizontal regional stress, the minor and intermediate stresses may have been equal, both in the horizontal plane. The joints would therefore have been able to form with their current $\sim 60^\circ$ relative strike and high persistence. This implies that the stress regime was almost hydrostatic during joint formation.

Long joint traces likely formed from the connection of individual adjacent joints, allowing fractures to form through intact rock between joints, or along joint surfaces from other sets. This is supported by the classification of Joint Set J1 as stepped, and the undulating nature of all three joint sets. This more stepped nature of J1 may indicate that J1 is slightly younger than J2 and J3, having been fragmented by pre-existing J2 and J3 sets.

Uplift episodes, weathering, and erosion from the surface have created the current topography, where open joint sets can be observed often leading from diatremes at the top of the slope. The slope face is highly irregular, with overhangs, block features, and steps. It can be theorised that joint surfaces on the smaller scale may be at least partially open, due to the dissolution of the carbonate rocks by the movement of water. A reduction in lateral stress from removal or vertical burial loads would also likely have led to an increased joint aperture.

4.8.2 Numerical Characterisation Summary

A numerical summary of probabilistic parameters for each defect set is included in Table 4-19. These parameters were not found to be location dependant, and have been adopted for all domains.

Table 4-19: Summary of probabilistic defect parameters

Parameter	J1	J2	J3	Bedding
Mean Dip	86.2°	88.7°	88.8°	0.4°
Mean Dip Direction	113.0°	55.7°	338.3°	330.7°
Fishers K	45.72	37.74	27.33	136.78
Mean Spacing	5.58 m	4.39 m	3.60 m	12.09 m
Spacing Standard Deviation	4.61 m	3.55 m	2.30 m	5.22 m
Persistence	>140 m	>140 m	>140 m	>140 m
Mean Amplitude (waviness)	783 mm	703 mm	600 mm	-
Amplitude Standard Deviation	350 mm	347 mm	259 mm	-
Mean Peak Dilation Angle	18.42°	20.99°	22.30°	20.86°
Reduced Dilation Angle	16.61°	18.93°	20.12°	18.81°
Dilation Standard Deviation	5.63°	4.01°	4.44°	4.96°

4.8.3 Visualisation

Obtaining statistical information around the distributions of joint orientation, spacing and persistence provides information on the uncertainty of joint sets. However, this form of joint characterisation ignores the location of the defects themselves (Einstein, 1996). Stochastic models represent the spatial character of joint patterns by constructing a rock mass with joints distributed according to the input statistical parameters. However, whilst they may represent a statistically possible rock mass, they do not represent a “real” situation, such as a particular outcrop. To represent the aggregate characterization of the in-situ fracture system (Liu, 2020), the probabilistic properties of the joint sets and bedding within the Study Area were modelled in FracMan 7.70. Figure 4-41 below displays the results.

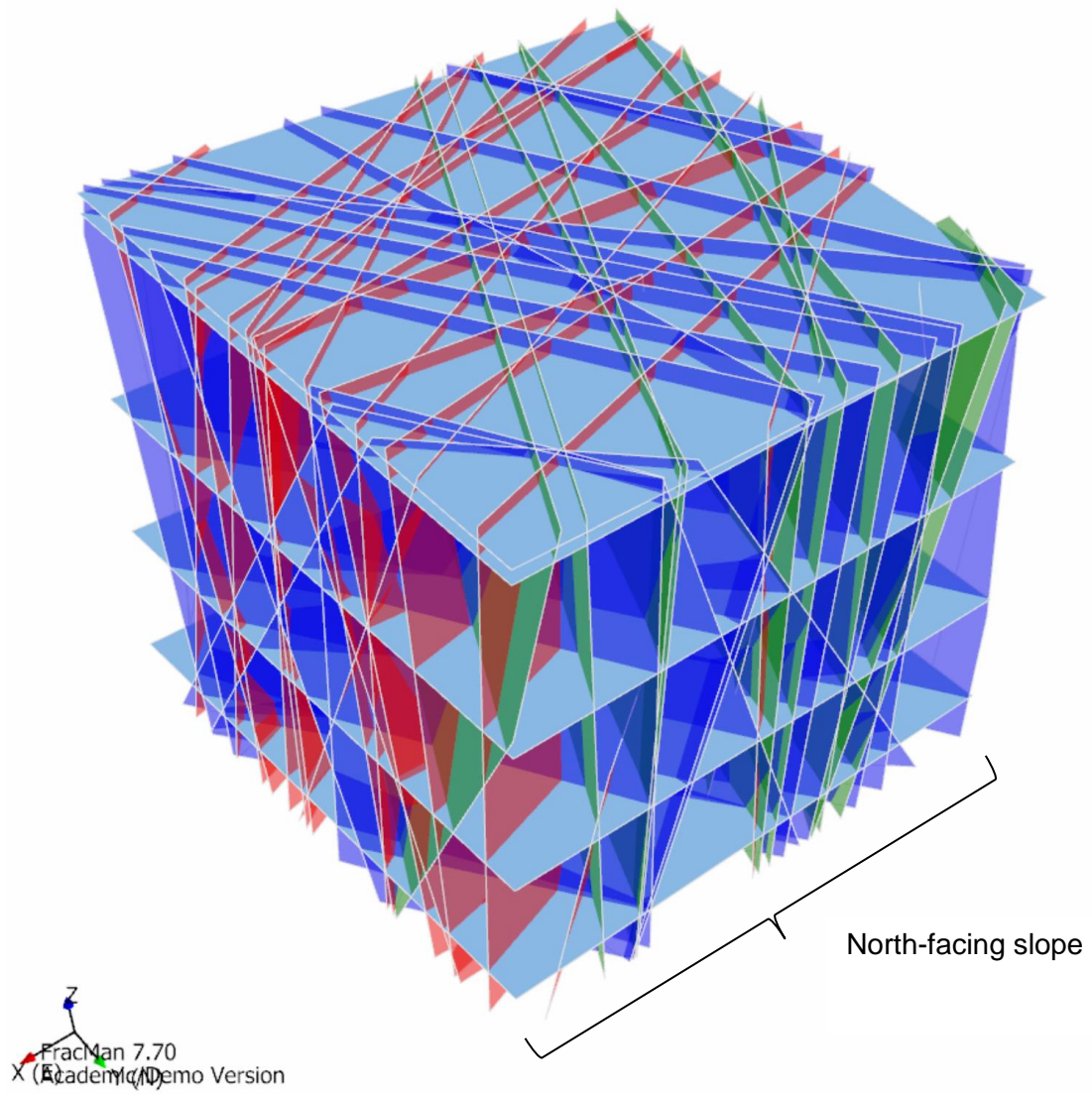


Figure 4-41: An example of a statistically possible rock mass, based on probabilistically defined parameters.

5 Joint Shear Strength Assessment

In order to define joint shear strength, an assessment was made of a recent rockfall, previously defined as the “Rockfall Area” (Section 4.1). An analysis was made of the jointing and freshly exposed surfaces within this region, in an attempt to determine the locations and dimensions of recently fallen blocks. One block (the first judged to have failed) was further assessed with the Shear Strength Reduction (SSR) method, to back-calculate the shear strength of the joint planes upon which it moved.

5.1 Rockfall Reconstruction

Comparing historic aerial images, it appears that the rockfall occurred between December 2016 and December 2017. Imagery from December 2016 indicates that the orientation and overall shape of the slope face in this area has not changed drastically.

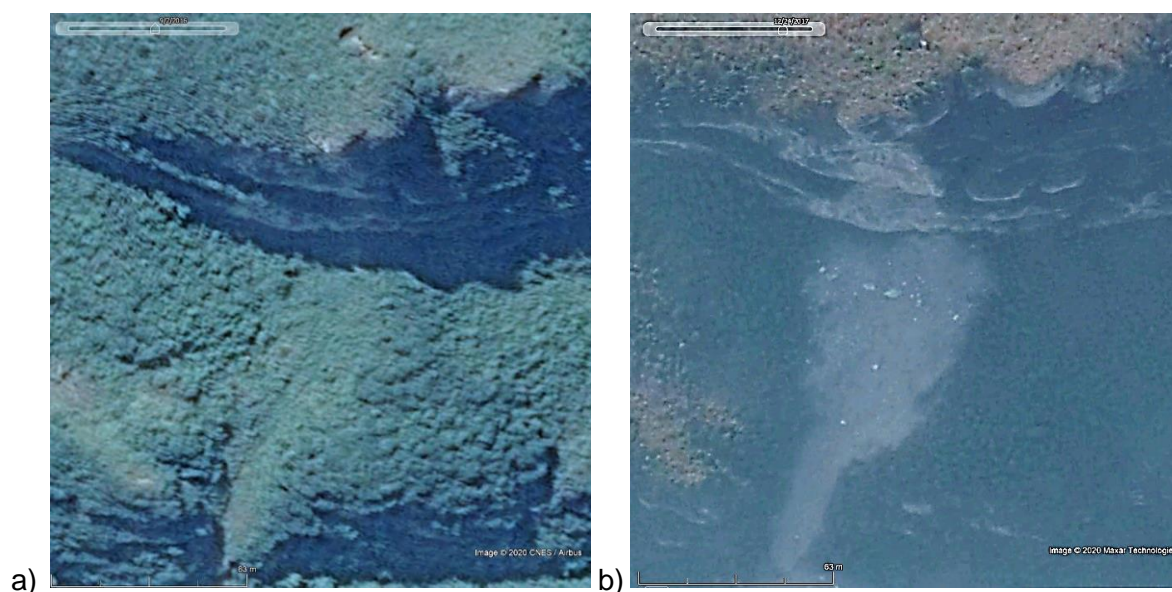


Figure 5-1: Historic aerial imagery of the Rockfall Area; a) from December 2016; and b) from December 2017 (Google Earth Pro, 2014-2020)

The face of the Rockfall Area was split into five horizontal layers, representing major beds. Three main massively bedded zones were defined, and two thinly bedded zones. In the massive zones, orthogonal joint surfaces indicate that blocky failures have occurred. In the thinly bedded zones failure appeared to have occurred in more of a spalling fashion, where major joint surfaces were not visible.

The slope face in the rockfall area was irregular, with moulds observed from which blocks are judged to have fallen. The slope face (and block moulds) was generally defined by Joint Sets J2 and J3. Joint Set J1 was not observed to be present. A slight overhang was present underlying the Rockfall Area, with an orientation of $64^{\circ}/190^{\circ}$.

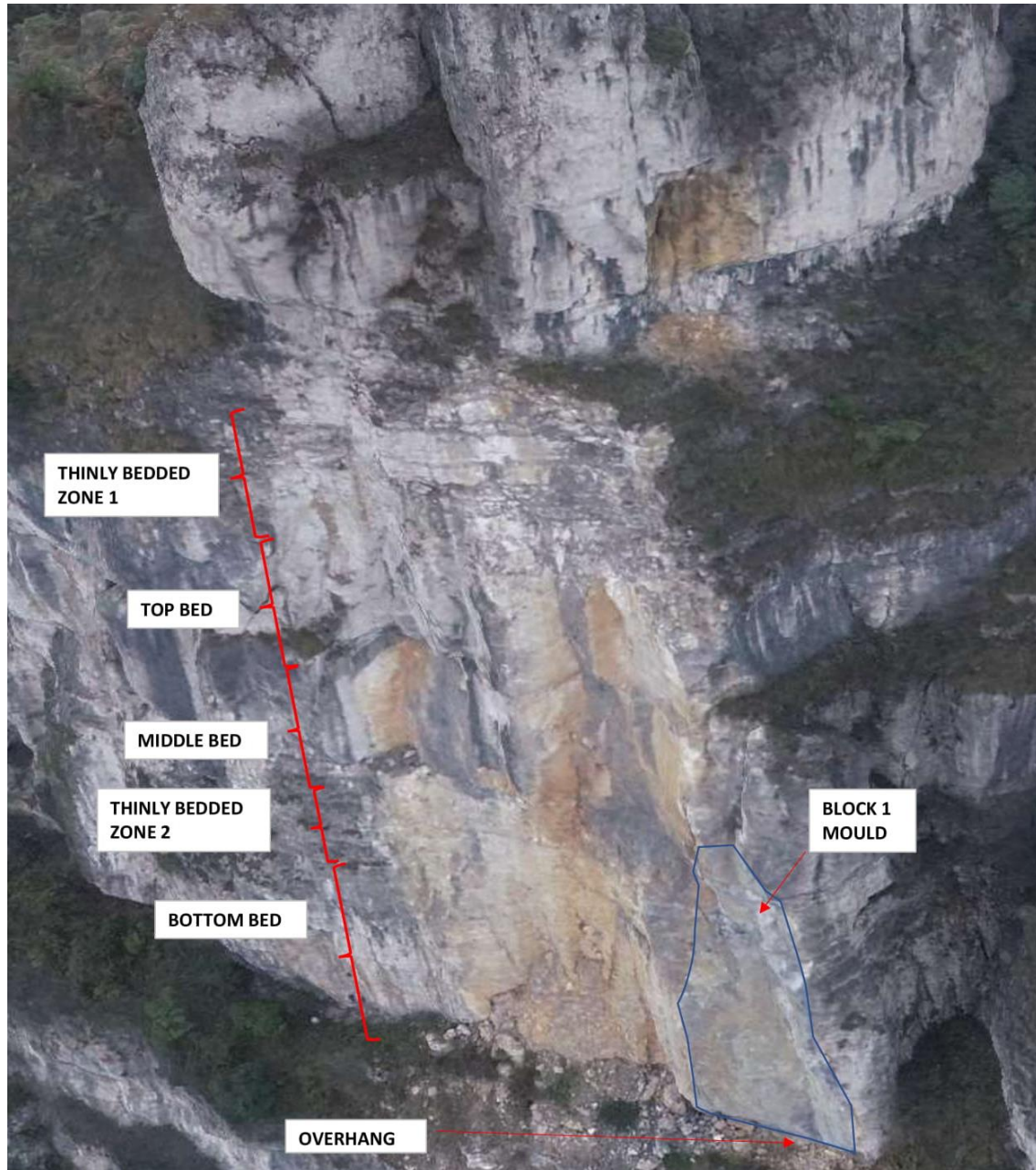


Figure 5-2: Horizontal layers, defined based on the nature of bedding.

An attempt was made to recreate the order in which the rockfall would have taken place. Segments of the point cloud were taken in CloudCompare as a strip for each massive zone. The exposed joint surfaces were defined and projected outwards from the existing face, to estimate the shape of fallen blocks along those joints (Figure 5-3 to Figure 5-5). Point clouds were compared to the 3D real scene model to determine which surfaces appeared freshly exposed, indicating where a block had recently fallen.

The overhang underlying the bottom bed is theorised to have caused the blocks in that bed to fail, potentially through wedge sliding, or toppling. This undermined blocks in the upper layers, allowing them to fail either by direct falling, or in sliding along one or two planes.

Figure 5-3 to Figure 5-5 display (in green) the blocks theorised to have fallen in the most recent rockfall. As the exact shape of the original rockface is unknown, the full extent of the rockfall cannot be determined, and the shape of the blocks cannot precisely be known. However, the comparison with images from prior to the rockfall shows that the historic surface is similar in shape and orientation to the current surface. Based on this, potential additional blocks are marked in yellow, indicating those which are likely to have fallen, but are not attached to a fresh joint surface.

The blocks are named roughly in order of the theorised failure sequence, beginning with Block 1. For each of the newly exposed joint surfaces, the spacing between joint sets was measured in addition to plane orientation, surface area, amplitude of waviness, and dilation angle (as per Section 4.7). A summary of the results for each surface is displayed below in Table 4-18.

The total volume of predicted blocks from the reconstruction is 2025 m³. The total volume of fallen blocks with a dimension above 2 m was approximately 1090 m³. A difference between these values is not unexpected. It can be visually assessed that more than half of the fallen material is less than 2 m in diameter, and was therefore not included in the volume estimation.

Blocks observed at the base of the rockfall area were significantly smaller than expected based on measured spacing values – particularly the bedding spacings, which were measured between 10 m to 20 m in this area. It is likely that blocks formed along minor bedding partings which were not measured in the spacing calculations, as they did not present as exposed surfaces. It was therefore not possible to match fallen blocks with their moulds on the slope face.

Based on this geometric data (block volume and joint orientation), a kinematic analysis and shear strength reduction analysis was undertaken in order to determine the shear strength of the planes along which Block 1 moved.

BOTTOM BED: POTENTIAL BLOCK DIMENSIONS

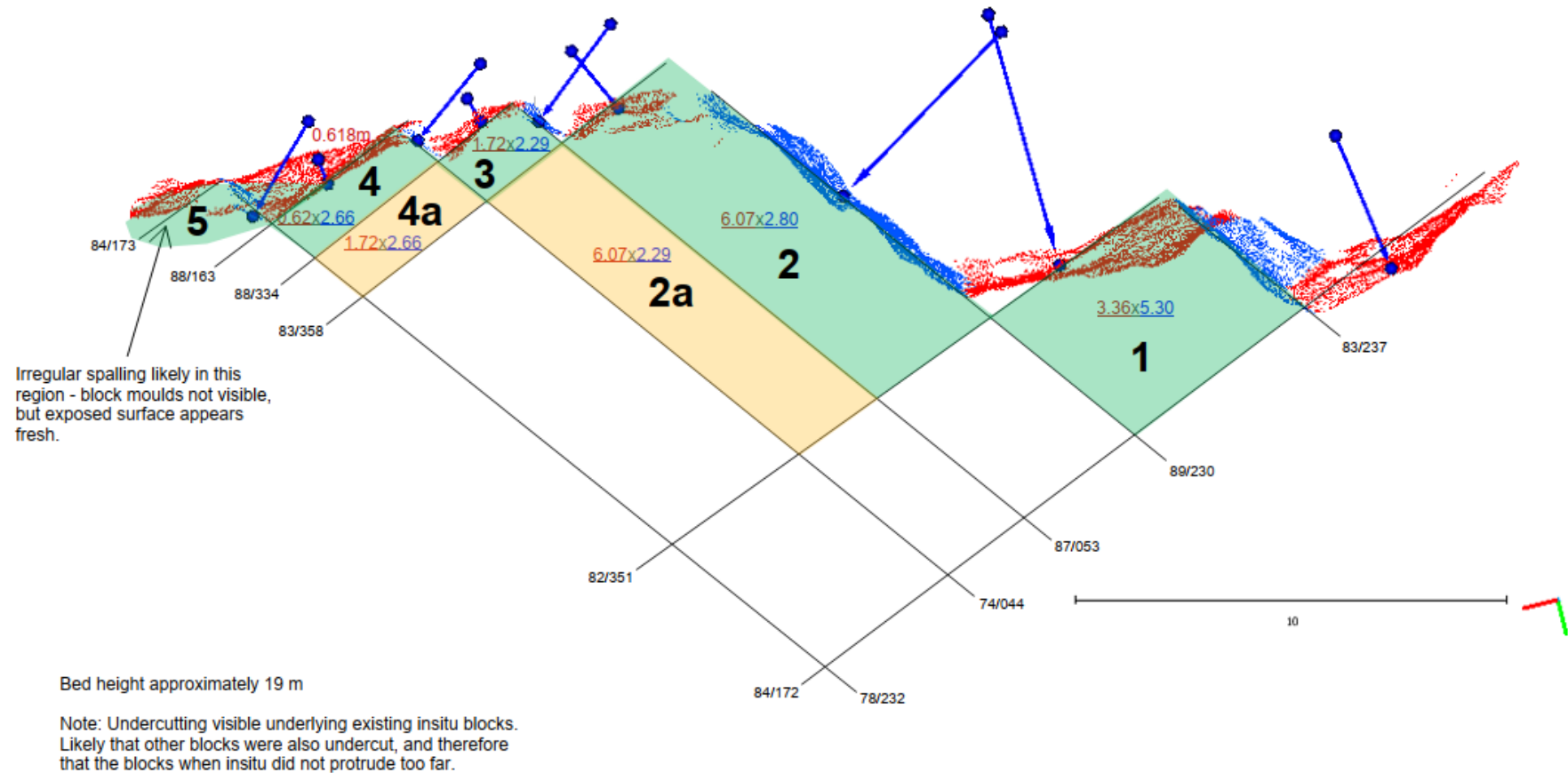


Figure 5-3: Interpolation of blocks which may have failed in the recent rockfall event along the bottom bed (plan view). Green blocks represent those which are considered likely to have fallen. Yellow blocks represent those which may have fallen based on the December 2016 profile, but were likely to have been attached to an observed joint surface.

MIDDLE BED: POTENTIAL BLOCK DIMENSIONS

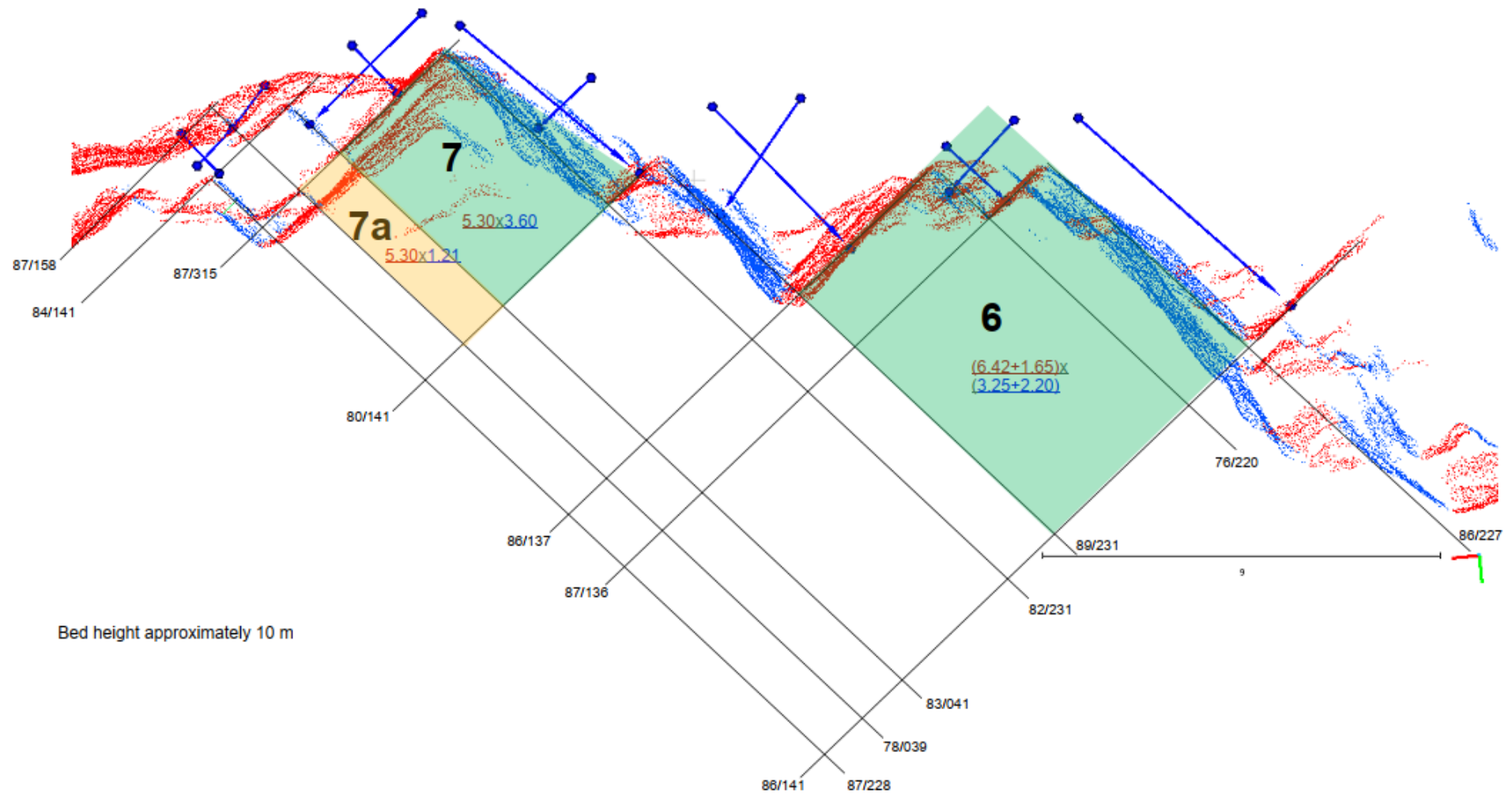


Figure 5-4: Interpolation of blocks which may have failed in the recent rockfall event along the middle bed (plan view). Green blocks represent those which are considered likely to have fallen. Yellow blocks represent those which may have fallen based on the December 2016 profile, but were likely to have been attached to an observed joint surface.

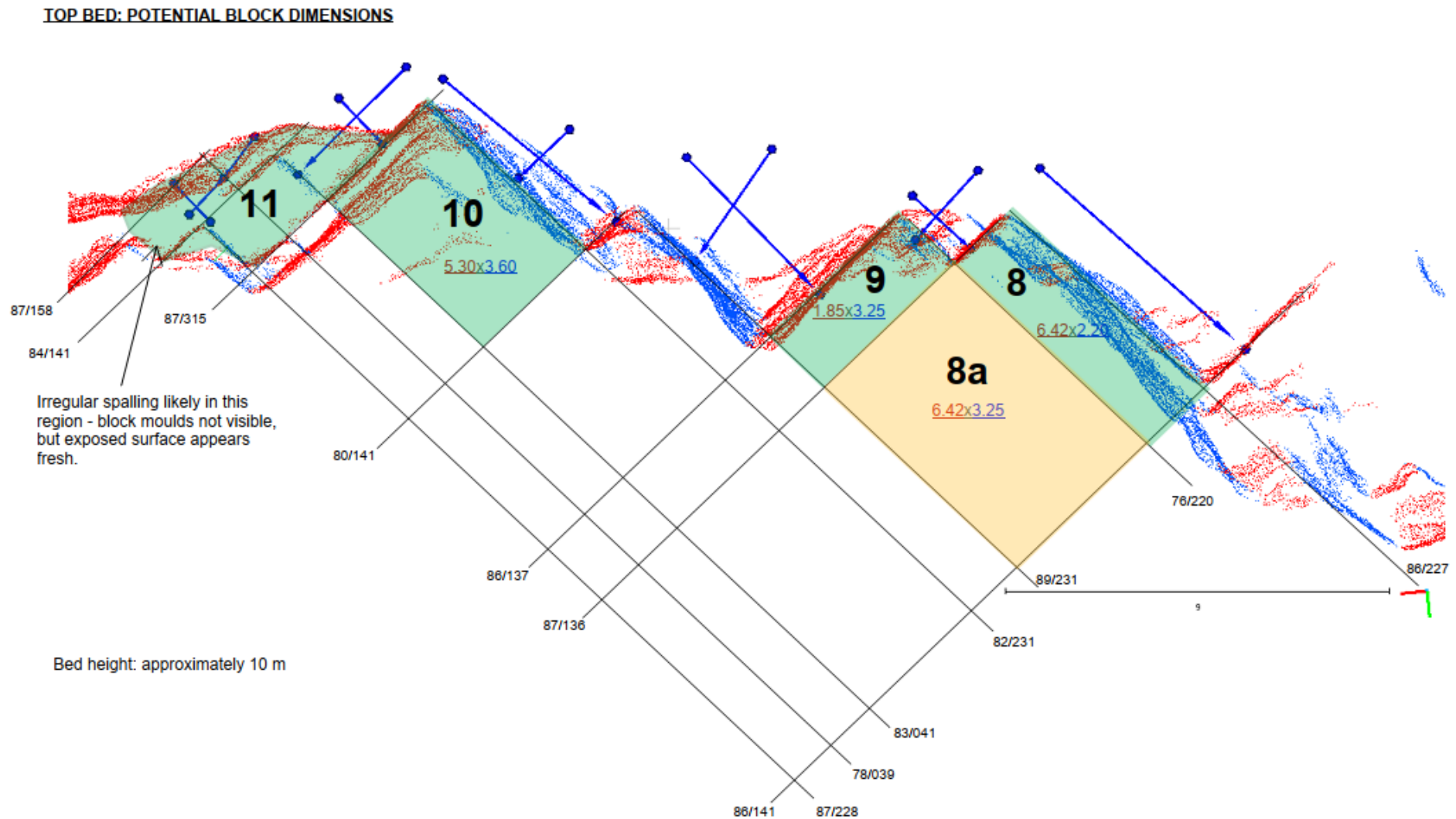


Figure 5-5: Interpolation of blocks which may have failed in the recent rockfall event along the top bed (plan view). Green blocks represent those which are considered likely to have fallen. Yellow blocks represent those which may have fallen based on the December 2016 profile, but were likely to have been attached to an observed joint surface.

Table 5-1: Projected blocks from reconstructed rockfall

Block	Distance J2 (m)	Distance J3 (m)	Bedding (m)	Volume (m3)	Dip J2	Azimuth J2	Dip J3	Azimuth J3	Dip Bedding Base	Azimuth Bedding Base	Dip J2	Azimuth J2	Dip J3	Azimuth J3	Dip Bedding Top	Azimuth Bedding Top	Status ¹	Shape
1	5.30	3.36	15.0	267.12	83	237	82	351	64	190	89	230	84	172	3	189	Likely	Irregular elongated
2	2.80	6.07	14.0	237.94	89	230	83	358	64	190	87	53	82	351	3	189	Likely	Irregular
2a	2.29	6.07	14.0	194.60	87	53	83	358	3	189	74	44	82	351	3	189	Possible	Irregular
3	2.29	1.72	13.0	51.20	87	53	88	334	3	189	74	44	83	358	3	189	Likely	Sub-rectangular
4	2.66	0.62	11.0	18.14	74	44	88	163	3	189	78	232	88	334	3	189	Likely	Sub-rectangular
4a	2.66	1.72	11.0	50.33	74	44	88	334	3	189	78	232	83	358	3	189	Possible	Sub-rectangular
5	9.40	2.90	17.0	77.24 ²	-	-	-	-	-	-	-	-	-	-	-	-	Likely	Irregular - Spall?
6	5.45	8.10	10.0	441.45	86	227	87	136	3	189	76	220	86	141	3	189	Likely	Sub-rectangular
7	3.60	5.30	10.0	190.80	82	231	87	315	3	189	32	41	80	141	3	189	Likely	Irregular one side
7a	1.21	5.30	10.0	64.13	83	41	87	315	3	189	78	39	80	141	3	189	Possible	Sub-rectangular
8	2.20	6.42	10.0	141.24	86	227	87	136	3	189	76	220	86	141	3	189	Likely	Sub-rectangular
8a	3.25	6.42	7.3	152.31	76	220	87	136	3	189	89	231	86	141	3	189	Possible	Sub-rectangular
9	3.25	1.85	7.3	43.89	76	220	86	137	3	189	89	231	87	136	3	189	Likely	Sub-rectangular
10	3.60	5.30	9.0	171.72	82	231	87	315	3	189	83	41	80	141	3	189	Likely	Irregular one side
11	7.20	1.73	20.0	41.52 ²	-	-	-	-	-	-	-	-	-	-	-	-	Likely	Irregular - Spall?

Notes:

1. Status indicates whether blocks are considered likely to have fallen in this most recent rockfall.
2. In locations where spalling is judged to have occurred, no plane orientations are provided. Volume is assessed based on a triangular pyramid, interpolated from the edges of known points

5.1 RS3-SSR Analysis of Block 1

In order to assess the shear strength of joint planes, a back analysis was made of Block 1 and the shear strength required for it to have been at equilibrium. The RocScience program RS3 was utilised for this back analysis, due to the complex geometry of the slope face, including underhanging below the block mould.

5.1.1 Model Definition

In order to create the RS3 model, planes were created and exported from CloudCompare, projecting the main plane of each surface of the existing slope face to recreate the expected initial slope face (Figure 5-6 and Figure 5-7). Once planes were imported, an external box was created around the planes, and the 3D Boolean operation utilised to segmented the box volume using the planes. This generated a block representing the overall slope surface, prior to the failure of Block 1. This was saved as a volume in an .obj format, and imported into future analysis files as required. This volume was “set as external” to constrain the limits of the analysis area to this volume.

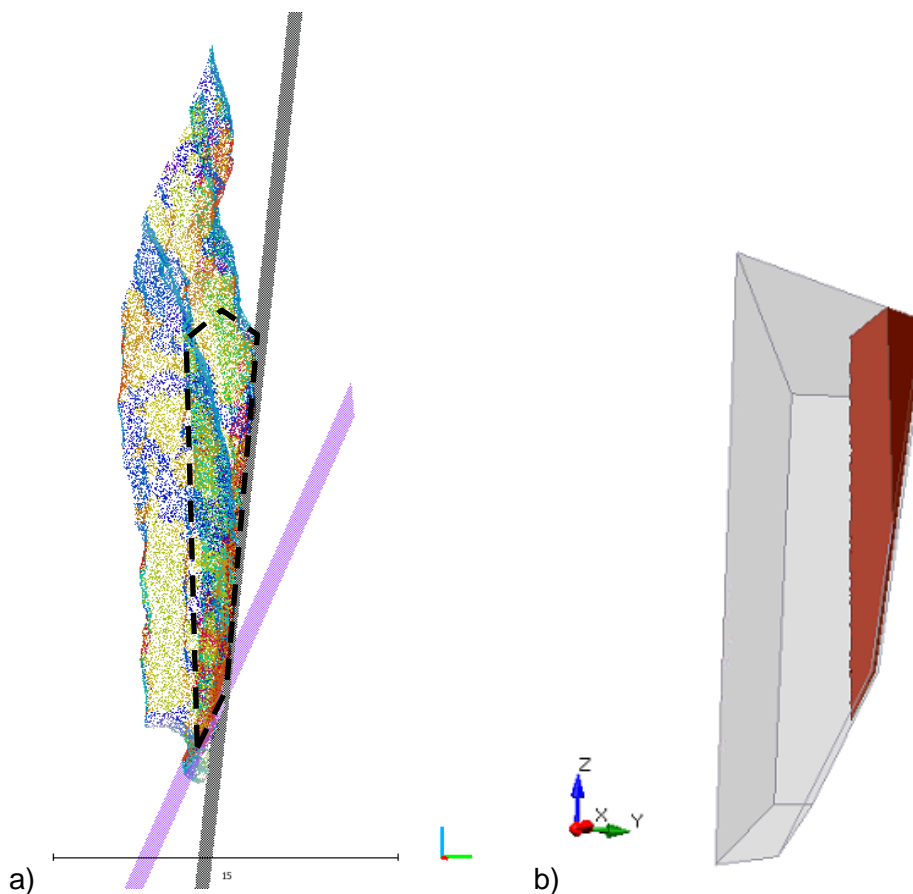


Figure 5-6: Side views of Block 1; a) as a point cloud in CloudCompare, with planes defining surface orientation; b) modelled block in RS3, with grey representing the rock mass, and red representing Block 1.

The planes representing joints from the sets J2 and J3 along which Block 1 moved were merged into a single mesh to import into RS3. This was done in CloudCompare by defining planes to fit to the point cloud joint surfaces (both J1 and J2), and increasing the extents of the planes beyond the boundaries of the model volume. They were then turned into point clouds, trimmed to end at the plane intersection, and merged again before being turned back into a mesh. This mesh representing the combined joint surfaces was then imported into RS3 as a surface, and designated to be a Joint. Once the joint surface was defined, the 3D Boolean tool was used to segment the rock mass volume along the joint surface, creating a separate Block 1. This process is displayed in Figure 5-7 below.

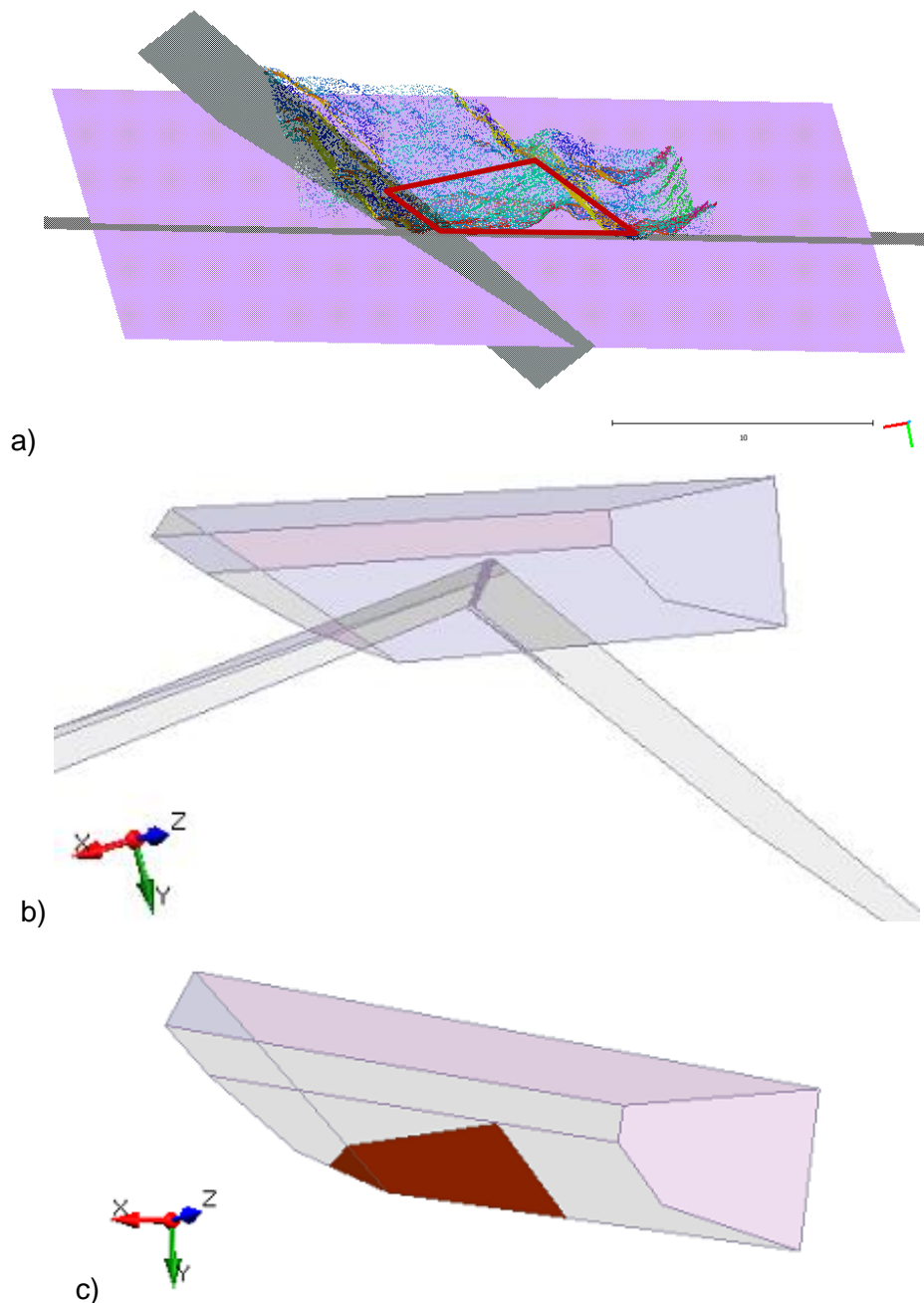


Figure 5-7: Top view of Block 1; a) as a point cloud in CloudCompare, with planes defining surface orientation; b) with the extended planar joint surfaces imported into the RS3 model; c) Rock mass volume segmented along the joint surface in RS3. Block 1 shown in red.

It is possible that what has been named Block 1 is comprised of multiple blocks, split by bedding planes, as discussed in Section 4.5.2. However, for the purposes of this calculation, it is assumed to have failed in a singular block. It was also assumed, that no rock bridges were present, due to the continuous nature of the point cloud defining the joint surfaces.

The rock mass and Block 1 were both assigned the material type “Limestone”, which was modelled using a Hoek-Brown failure criterion with properties as outlined in Table 5-2. The joint surface was modelled with Mohr-Coulomb materials, to simplify the shear strength reduction process, with properties as outlined in Table 5-3.

Table 5-2: Parameters defined for rock mass material - Limestone.

Parameter	Value	Units	Comment
Initial Element Loading	Field Stress & Body Force	-	Modelling gravity only.
Unit Weight	24.5	kN/m ³	As per Dong et al., 2020 for Kaili Limestone.
Poisson’s Ratio	0.3	-	The upper 75 th percentile of Limestone values from RocScience’s RocData program, due to the weathered nature of the rock mass.
Young’s Modulus	33.4	GPa	The lower 25 th percentile of Limestone values from RocScience’s RocData program, due to the weathered nature of the rock mass.
Intact UCS	33	MPa	As per Dong et al., 2020, for weathered material around joints.
m_b	0.844	-	Hoek Brown Parameters: - M_i taken as 10 (RocData, 2020) - Assumed GSI range between 45 – 65, taken as 55, from: <ul style="list-style-type: none"> ▪ Blocky nature ▪ JCond89 = 16 (poor to fair) <ul style="list-style-type: none"> • Persistent = 0 • Aperture open 1-5 mm = 1 • Roughness very rough = 6 • No infilling = 6 • Weathering moderate = 3
s	0.001	-	- $D = 0.7$ due to stress release and movement of water along joints.

Poisson’s ratio and Young’s Modulus have little impact upon the factor of safety (and therefore the SSR process), although they do impact the deformation (Hammah 2005). The adoption of stiffness parameters based on literature (RocData, 2020) is therefore considered appropriate.

Table 5-3: Parameters defined for joint material.

Parameter	Value	Units	Comment
Tensile Strength	0	KPa	-
Cohesion	25	KPa	See discussion below.
Friction Angle	30	Degrees	As per Dong et al., 2020.
Dilation Angle	19.5	Degrees	Averaged from the measured dilation angles for the J2 and J3 planes bordering Block 1.
Normal Stiffness	100	MPa	Default value used.
Shear Stiffness	10	MPa	Default value used.

Without any cohesive component (friction only) the RS3 model would not converge under any circumstances. This is due to a flaw in the RS2 software, where “if material properties are set to zero, this can cause numerical issues” (RocScience, 2020). The lowest cohesion value found not to cause numerical issues was 0.025 MPa, which was adopted.

Restraints in the x, y and z directions were applied to the back face, orthogonal side face, and base face of the model (Figure 5-8). No restraints were applied to surfaces which were not fully constrained by insitu rock, including the main slope face, overhanging face, inclined side plane, and top surface. The volume was meshed with a 10 noded tetrahedral mesh, graded to increase element intensity in the geometrically complex regions.

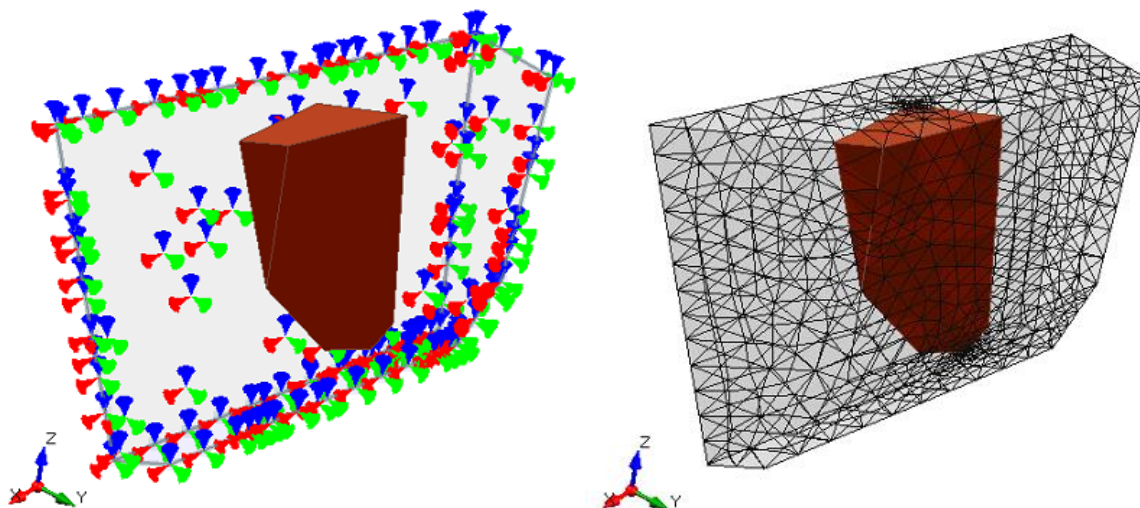


Figure 5-8: Oriented view of Block 1 in RS3; a) with restraints applied at the back, base and sides of the model; b) with a 10-Noded Tetrahedra graded mesh

5.1.2 Results

The SSR analysis returned a reduction factor of 1.07. The analysis resulted in a total displacement profile indicating that the top of the block underwent significantly more displacement than the base of the block (Figure 5-9). Values of x and y displacement were positive at the top. At the toe, there were negative values of x displacement and zero values of y displacement. These results may reflect either the forwards rotation of the block top in toppling, rotating the base back towards the slope, or they may reflect the onset of wedge failure from the top of the block. Visual inspection of model outputs from Hammah (2008) indicate that wedge sliding may be represented by larger displacement contours at the top of a block. As this is exactly at the onset of failure, the displacements are extremely low (<3.5 mm). Without allowing for the detachment of the failed block, it is challenging to judge the mode of failure based on the displacement results.

It is extremely difficult to determine the mode of failure at this location due to its complex sub-vertical and undercut geometry, including two overhangs of varying dip. Failure cannot therefore be assessed using a simple kinematic assessment. It is possible that toppling, wedge sliding, or a combination of the two occurred in this location. Further investigations could include modelling the slope in a DEM program, which would allow for the failed block to detach and would clearly define the mode of failure.

If toppling did occur, then the component of shear stress affecting the failure would be reduced, as there would have been less movement along the joint surfaces. It would logically follow that the SSR analysis may return non-representative results in this case because FEM is unable to consider the detachment of blocks. However, Hammah et al. (2007) undertook a comparison of DEM analysis in the program UDEC and FEM-SSR, and found results to be comparable for forward toppling, backward toppling and flexural toppling.

The reduction factor of 1.07 can be used with the original input parameters (Table 5-2 and Table 5-3). At equilibrium, it can therefore be calculated that:

$$c^* = \frac{0.025}{F} = \frac{0.025}{1.07} = 0.023 \text{ MPa}$$

and:
$$(\varphi_b^* + i^*) = \tan^{-1} \left(\frac{\tan(\varphi_b + i)}{F} \right) = \tan^{-1} \left(\frac{\tan(30+19.5)}{1.07} \right) = 47.57^\circ$$

Output pages from the SSR analysis undertaken in RS3 are included in Appendix A.

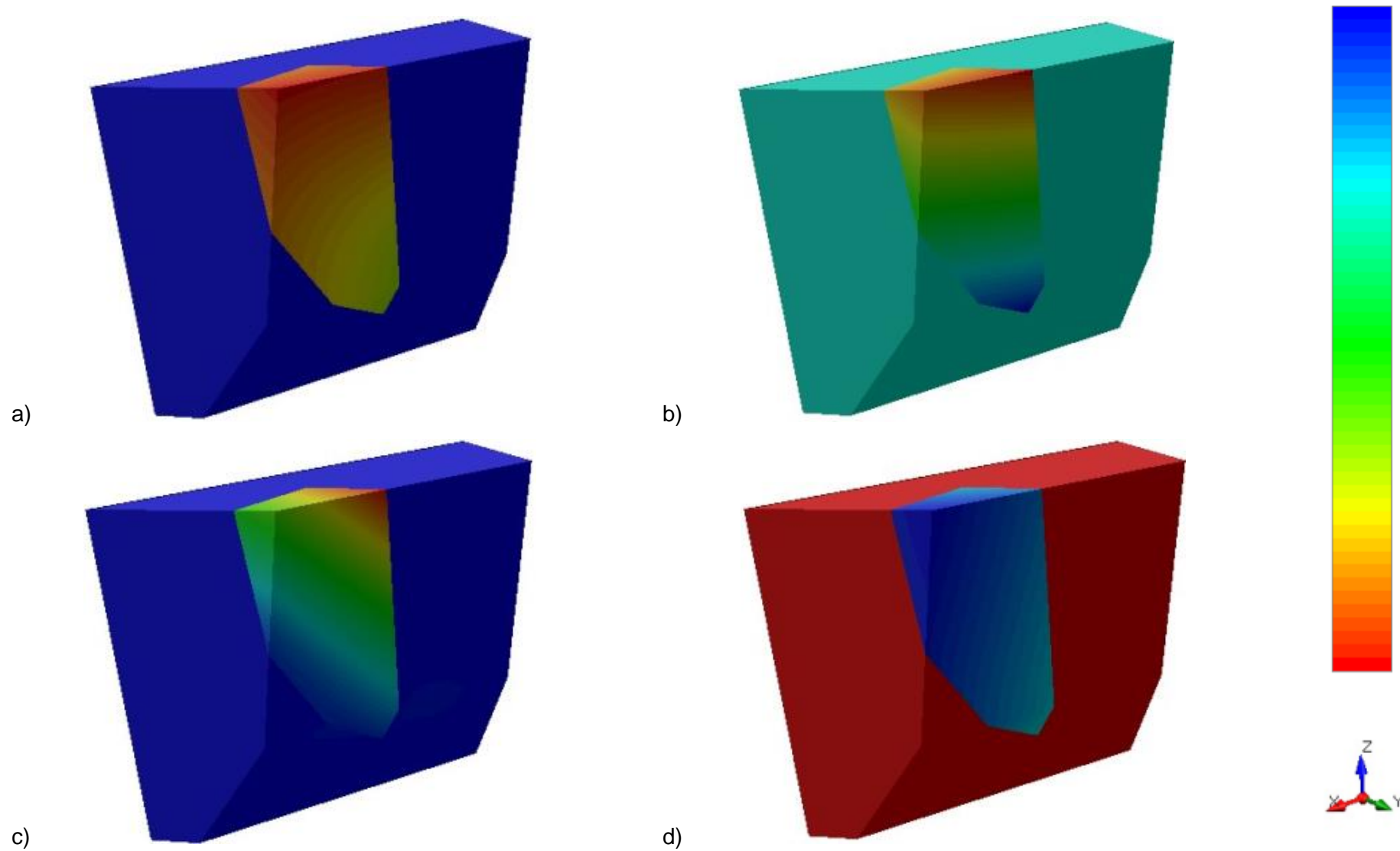


Figure 5-9: Displacement from completed RS3 SSR analysis, at failure with a SRF of 1.07. a) Total displacement, from 0 (blue) to 0.0035 m (red); b) x displacement, from -0.00049 m (blue) to 0.0012 m (red); c) y displacement, from 0 m (blue) to 0.0017 m (red); and d) z displacement, from -0.0031 m (blue) to 0 m (red).

The reduction of shear strength required for failure implies that at least one of several possible scenarios must have occurred:

1. The estimate of base shear strength was too high;
2. The estimate of the peak dilation angle was too high;
3. The shape of block 1 may have been incorrectly estimated – it may have projected further from the presumed rock face, or may have extended further up the slope;
4. There may have been surcharge loading from blocks above;
5. There may have been seismic loading at the time of the rockfall;
6. There may have been water pressure built up behind the block (considered unlikely, due to the elevated slope, and the predicted open, free draining nature of the joints);
7. There is an error in another input parameter, such as stiffness or strength; or
8. There was an error in modelling or meshing geometry.

For the purposes of this thesis, it is assumed that the reduction of shear strength is valid, and is due to an overestimation of the peak dilation angle. This results in a reduction in dilation angle of 1.92° , representing a 9.8% decrease from 19.5° to 17.6° . Dong et al. (2020) suggested a dilation angle of 14° for a surface in Kaili limestone, although this is understood to vary significantly from surface to surface. A dilation angle of 17.6° still reflects a high degree of waviness/roughness, but is closer to the value proposed by Dong et al.

Ideally, this calculation would be repeated on several blocks to determine the average SRF. However, due to time and computational restrictions, further calculations are undertaken on the assumption of a base friction angle of 30° , and no cohesive component to shear strength. Applying the 9.8% reduction indicated by the SSR analysis, the reduced peak dilation angle for all defect sets is outlined in Table 5-4. In absence of available measurement data, an overall average value has been adopted for bedding.

Table 5-4: Summary of probabilistic defect parameters used in analysis

Parameter	J1	J2	J3	All/Bedding
Mean Peak Dilation Angle	18.42°	20.99°	22.30°	20.86°
Reduced Dilation Angle	16.61°	18.93°	20.12°	18.81°

Although it would be ideal to model a block which has a clear mode of failure (preferably sliding), the sub-vertical nature of jointing, irregular nature of the slope face, and frequent overhangs makes it remarkably difficult to determine whether wedge sliding or toppling occurred. Within the Rockfall Area, many blocks are believed to have fallen as the blocks below them failed, meaning that any meaningful back analysis cannot be undertaken on any but the first block to fail (Block 1). It also means that a surcharge load was likely present.

5.1.3 Additional Analysis

An additional analysis was attempted in RS3, whereby the exposed joint surfaces adjoining Block 1 were imported into the geometry as a mesh created from the 3D point cloud. The idea was that the dilation angle would be directly reflected in the surface topography, and could be removed as an unknown. Any reduction in shear strength would therefore be in the base friction angle only.

The mesh of the joint surface was spliced with meshes continuing the joint surface orientation beyond the extents of the imaged surface, to ensure that the mesh properly intersected with the estimated initial surface. This was done by extruding all meshes to point clouds, editing the point clouds, and re-meshing them as a combined whole. In practice, these extended zones make up only a small component of the modelled joint surface. However, the extended zones are required to fully encapsulate the block within the rock mass volume when modelling RS3, without leaving any undefined areas.

Combined joint surfaces were developed both at full resolution (controlled by the resolution of the original imaging), and at a reduced resolution of 1000 points across the joint surface. Figure 5-10 below displays the combined meshes, including the joint surface from remote imagery (blue) with the two planes projected past the edges of the plane. Although both combined meshes import well into RS2, their refined nature makes computing highly intensive, which is particularly the case for the full resolution mesh. A comparison of the two surfaces as imported into RS3 is included as Figure 5-12 below.

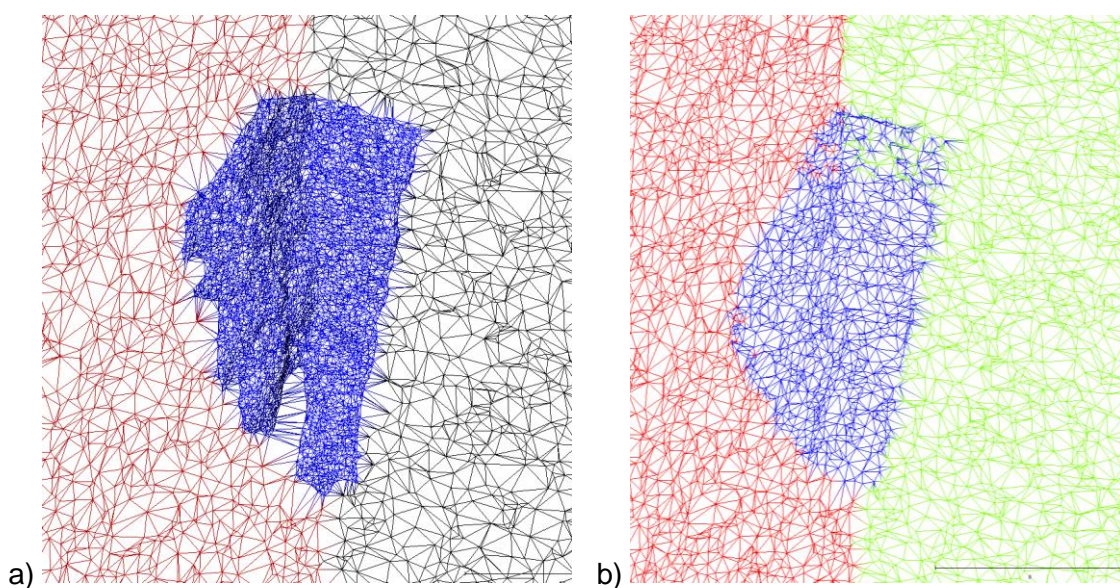


Figure 5-10: combined meshes including the joint surface from remote imagery (blue), with the two planes projected past the edges of the plane, to ensure they properly intersect the slope volume; a) at full resolution, and b) at a reduced resolution, with 1000 points across the joint surface only.

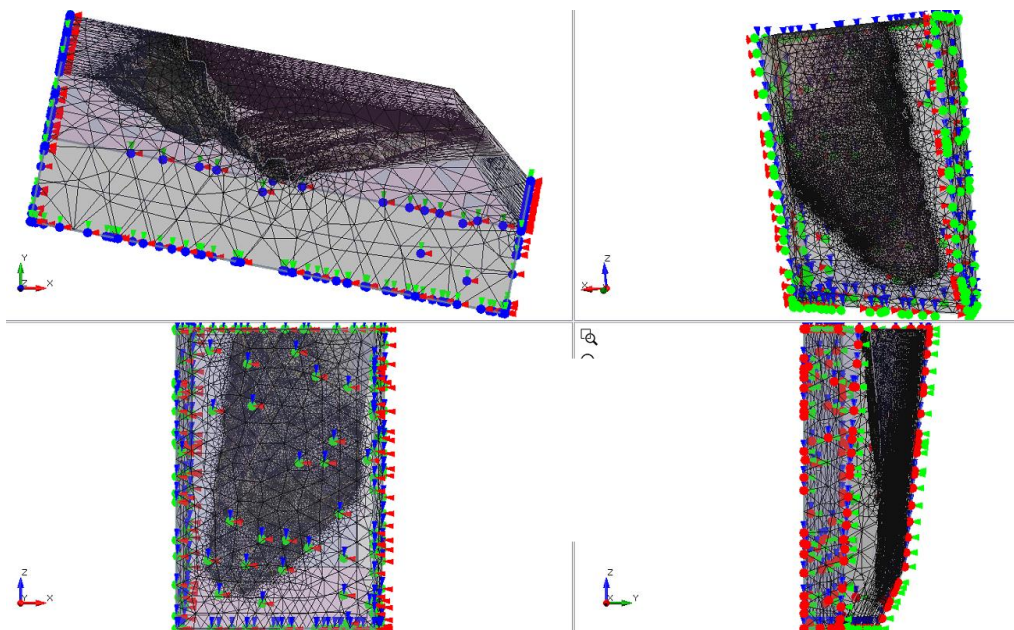


Figure 5-11: Rock mass block, and Block 1 wedge, defined by a reduced resolution surface. Mesh is a 10 noded tetrahedral, graded, with x,y,z restraints applied at the base, back and sides. The SSR region for analysis was trimmed directly around Block 1 to reduce processing time.

An attempt was made to run the full resolution model. However, after little progress was made over the space of 24 hours (<10%), the attempt was abandoned. The reduced resolution model was then run for over 7 days without completing the calculation, and this attempt was also abandoned.

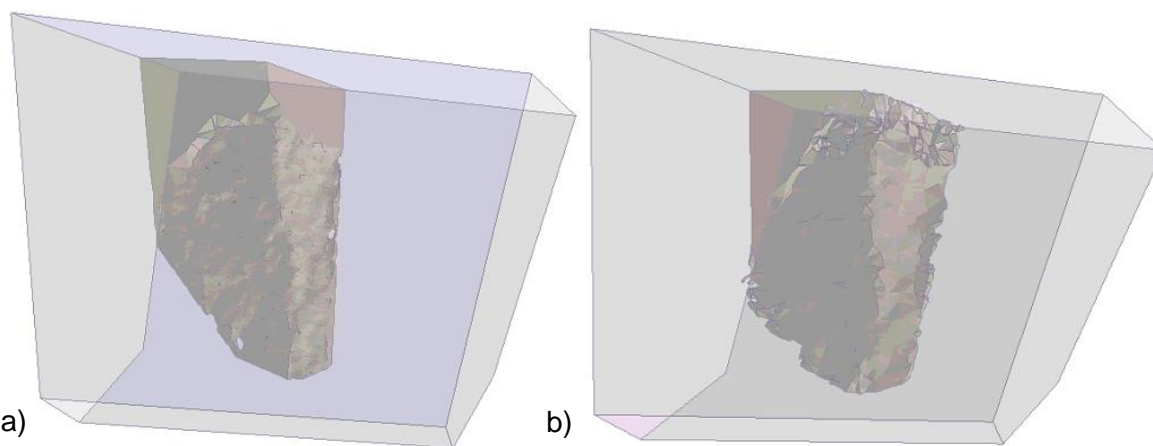


Figure 5-12: Oriented view of Block 1 in RS3; a) with the full resolution surface mesh; b) with the reduced resolution surface mesh

Although this model could account for some level of surface roughness and dilation, it cannot fully include any dilation which may occur, for the following reasons:

1. The mesh is not of sufficient resolution to model the small-scale roughness of the joint surface. Any smoothing of the mesh reduces this resolution even further; and
2. If the block failed in wedge sliding, there would already have been movement along the joint surfaces, damaging the asperities. The joint roughness along the modelled surface would therefore be reflective of residual roughness.

6 Kinematic Analysis

For the purposes of fracture system definition and kinematic analysis, the Study Area has been broken into four domains, as discussed in Section 4.3. Each domain has a distinct slope face strike, and each is dominated by unique combinations of defect sets. Typical failure mechanisms have been analysed for all domains, and representative images have been generated to display those failure mechanisms.

Due to the diverse nature of the joint set orientations, the failure mechanisms vary throughout the slope face – changing between and within domains based on which joint sets are dominant. Two analyses were undertaken:

- Basic kinematic analysis in DIPS, showing possible failure mechanisms in each domain. Scaled to account for the presence of each set within each domain; and
- Probabilistic modelling in the RocScience software packages RocPlane, SWedge and RocTopple. This was undertaken in each domain where the DIPS analysis indicated the planar sliding, wedge sliding and toppling failure mechanisms were present respectively. This provided a probability of failure for each failure mode.

6.1 DIPS Analysis

A basic kinematic analysis was undertaken in DIPS to determine the possible failure mechanisms within each domain, considering joint set orientations and the slope face orientation. Analyses were undertaken for each domain, for the following failure modes:

- Planar Sliding;
- Wedge Sliding;
- Flexural Toppling; and
- Direct Toppling (including direct, oblique, base plane and backwards toppling).

As observed in the Rockfall Area, one block falling may undercut overlying blocks, which may fail just by falling. No analysis has been undertaken for this progressive failure mode, and no account had been made for potential surcharge loading from overlying blocks.

DIPS automates kinematic analyses, allowing the input of the slope angle, friction angle of the surface, and lateral limits to sliding. Together these components are used to define regions of kinematic removability on the stereonet, as discussed in Section 2.5. The location

of plotted plane normals and intersection points relative to the kinematically removable regions determines whether a certain failure mode is possible.

The average slope angle was adopted for each domain. Based on the results of the SSR analysis, a friction angle of 48.8° was adopted, comprising a base friction angle of 30° , and a dilation angle of 18.8° . As DIPS does not allow a variation in friction angle for different surfaces, this angle was adopted for all defect sets. A lateral limit of 20° was adopted for all failure mechanisms other than flexural toppling, for which 30° was adopted.

DIPS provides results displaying the percentage of poles/intersections on the stereonet for which each failure mode is kinematically possible. This result is directly related to the quantity of points plotted for each set. For example, planar failure along 50% of the bedding set would be under-represented as a percentage of all poles, because it was measured on a large scale and has only 21 data points. Planar failure along 50% of Joint Set J3, with a higher number of measured planes, would represent a much higher percentage of poles. This does not accurately reflect the relative influence of the two defect sets.

This influencing effect of measurement quantity was reduced by scaling the relative quantity of measurements for each set. The quantity of data points for each set were selected based on engineering judgement, and on the quantity of measurement points available for all sets (limited by the quantity of measurements available for the bedding, being 21). Data points from each set were assigned a number, and a random number generator (Excel RANDBETWEEN function) was employed to determine which points would be utilised in an unbiased fashion. Within each given domain, the number of data points for each set were:

- ‘Dominant’ set: 30 data points;
- ‘Present’ set: 20 data points; and
- ‘Minor’ set: 5 data points.

Table 6-1 below displays the number of data points randomly selected from each set, for kinematic analysis.

Table 6-1: Quantity of data points adopted for each joint set, by domain.

Domain	J1	J2	J3	Bedding
D1	20	30	5	20
D2	5	20	20	20
D3	20	20	30	20
D4	20	5	20	20

Table 6-2 displays the percentage of poles/intersections for which each failure mode is kinematically possible, calculated for each region, and assuming a friction angle of 49°.

Table 6-2: Percentage of poles/intersections for which each failure mode is kinematically possible, colour coded in 5% intervals from >25% (maroon) to <5% (dark green).

	D1	D2	D3	D4
Planar Sliding	12.8%	3.9%	6.9%	3.6%
Wedge Sliding	14.8%	17.4%	12.7%	5.9%
Flexural Toppling	22.4%	13.9%	21.0%	27.2%
Direct Toppling	1.1%	4.3%	4.5%	5.7%
Oblique Toppling	14.1%	16.3%	20.9%	24.3%
Base Plane Sliding	18.2%	12.9%	12.9%	11.0%
Backward Toppling (into slope) ¹	15.2%	20.6%	25.4%	30.0%

Notes:

1. Percentages for backward toppling calculated as the sum of oblique and direct toppling. Discussed below.

As discussed in Section 2.5.3, base planes which dip into the slope may still act as release planes for direct toppling blocks, and may result in backward direct toppling. Stereographically, this occurs where plane normals lie within the semi-circle opposite the regions of oblique and direct toppling. DIPS does not calculate this mode of failure directly. Due to the symmetrical nature of intersections and planes within this Study Area, it has been assumed that additional backward direct toppling has a percentage equal to the sum of oblique and direct toppling modes.

It is clear that all domains have a broad range of failure mechanisms present. However, toppling was the dominant failure mechanism for all domains, having the highest relative percentage of kinematically admissible poles/intersections. This was particularly the case for backwards, flexural and oblique toppling. The dominance of toppling is not unexpected, considering the sub-vertical jointing, the blocky nature of the massive limestone beds, and the pervasive base plane generated by the sub-horizontal bedding. Wedge sliding was also kinematically admissible for over 10% of intersections in Domains D1, D2 and D3.

It should be noted that the DIPS analysis is incapable of considering the highly complex geometry of the slope face. This geometry (including overhangs and undercutting) would significantly impact the failure mechanisms which can be considered kinematically admissible. To reflect the geometric complexity of the slope face and to determine the modes of failure in a more rigorous fashion, a 3D DEM model would be required.

Results and stereographic projections for each domain are included in the sections below.

6.1.1 Domain D1

A diverse range of failure mechanisms were present within Domain D1. All mechanisms other than direct toppling presented as kinematically possible for over 10 percent of poles/intersections. Toppling was kinematically possible for 48.6% of intersections either through direct, oblique, backward or base plane mechanisms. The single most dominant failure mechanism was flexural toppling (22.4% of plane normals), which occurred along Joint Set J2. The dominance of toppling along Joint Set J2 is evidenced in the face of the slope itself, which is approximately equal to the mean set orientation of J2.

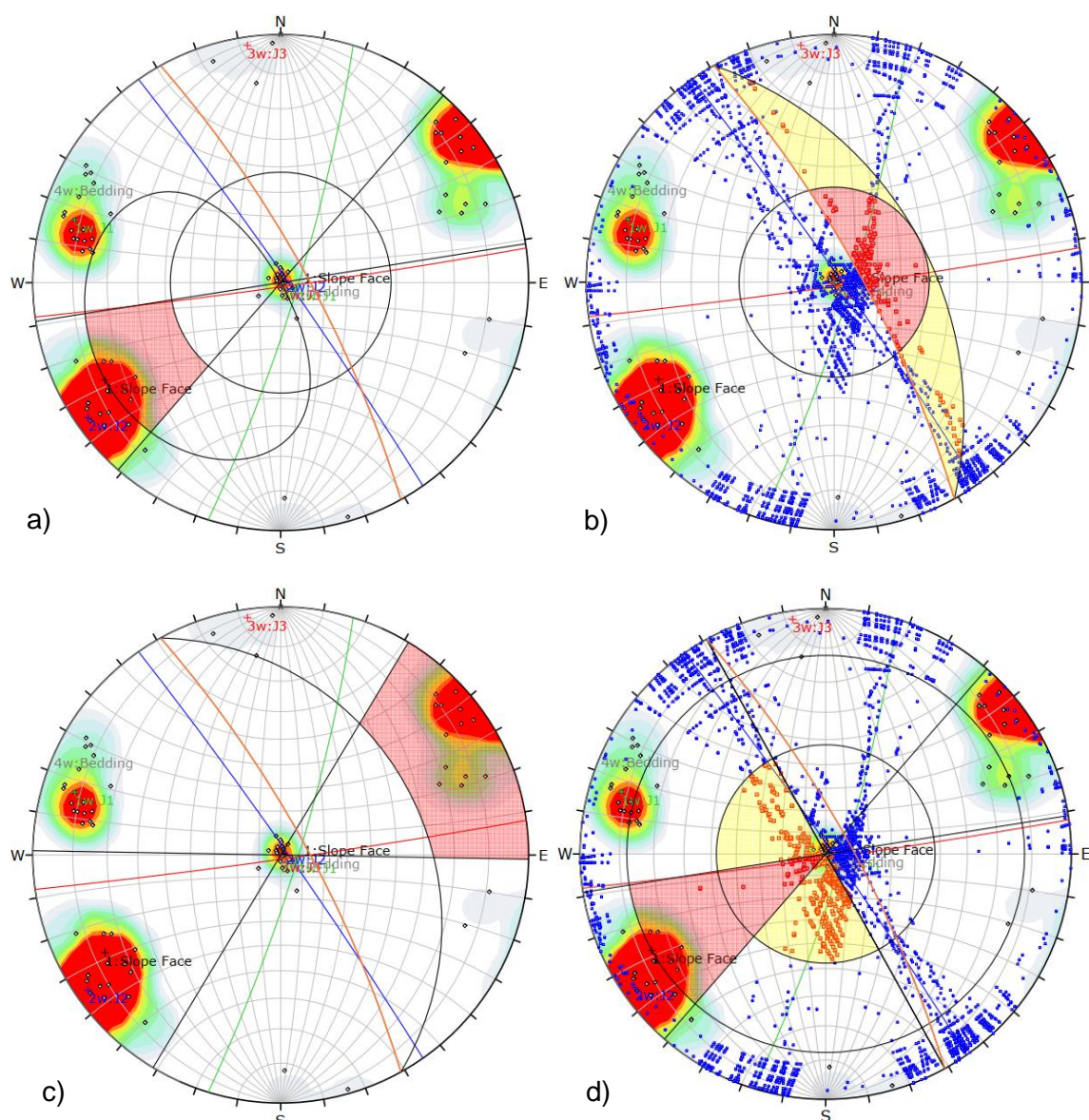


Figure 6-1: Kinematic analysis undertaken in DIPS for Domain D1. Friction angle of 48, quantity of data points scaled based on relative joint quantity. a) Planar sliding; b) Wedge sliding; c) Flexural toppling; d) Direct toppling.

Figure 6-2 presents locations within Domain D1 in which toppling and wedge failure were judged to have occurred. Output pages from the D1 DIPS Kinematic analysis are included in Appendix B1.

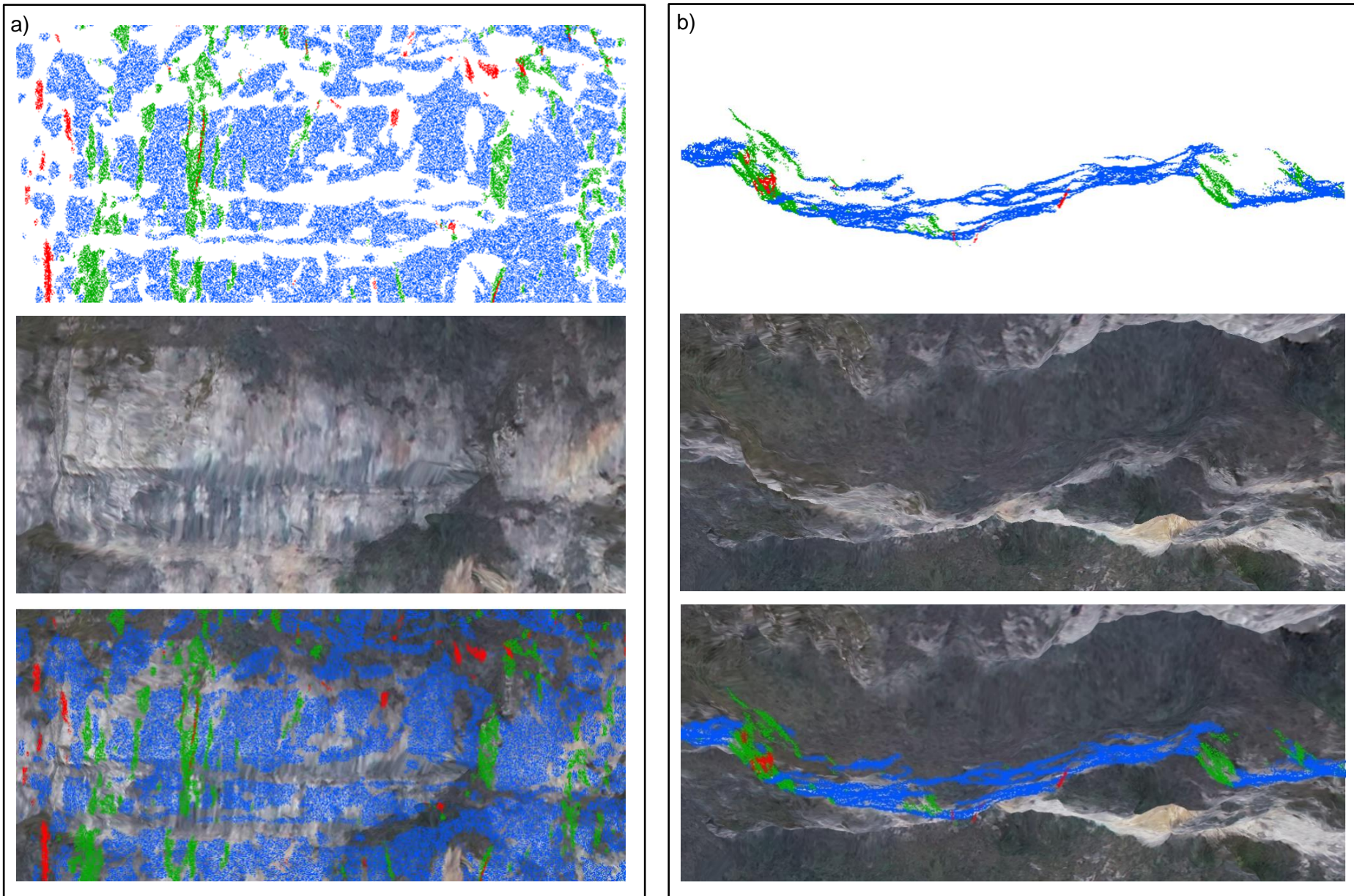


Figure 6-2: Example of wedge and toppling failure in Domain D1 along Joint Sets J1/J2 (green/blue) and J2 (blue) respectively. Viewed from a) perpendicular to slope face; b) from above

6.1.2 Domain D2

A diverse range of failure mechanisms were present within Domain D2, with all mechanisms other than planar sliding and direct toppling presenting as kinematically possible for over 10 percent of poles/intersections. Toppling was kinematically possible for 49.8% of intersections either through direct, oblique, backward or base plane mechanisms. The single most dominant failure mechanism was backward toppling (20.6% of poles), then wedge sliding (17.4% of poles). The variability of failure mechanisms within this domain is evidenced by the extremely irregular nature of the slope face, which contains large overhangs and a blocky, zig-zag like surface. There is no dominant set in this region. Sets J2 and J3 are present in roughly equal proportions, which provides the basis for wedge sliding failure.

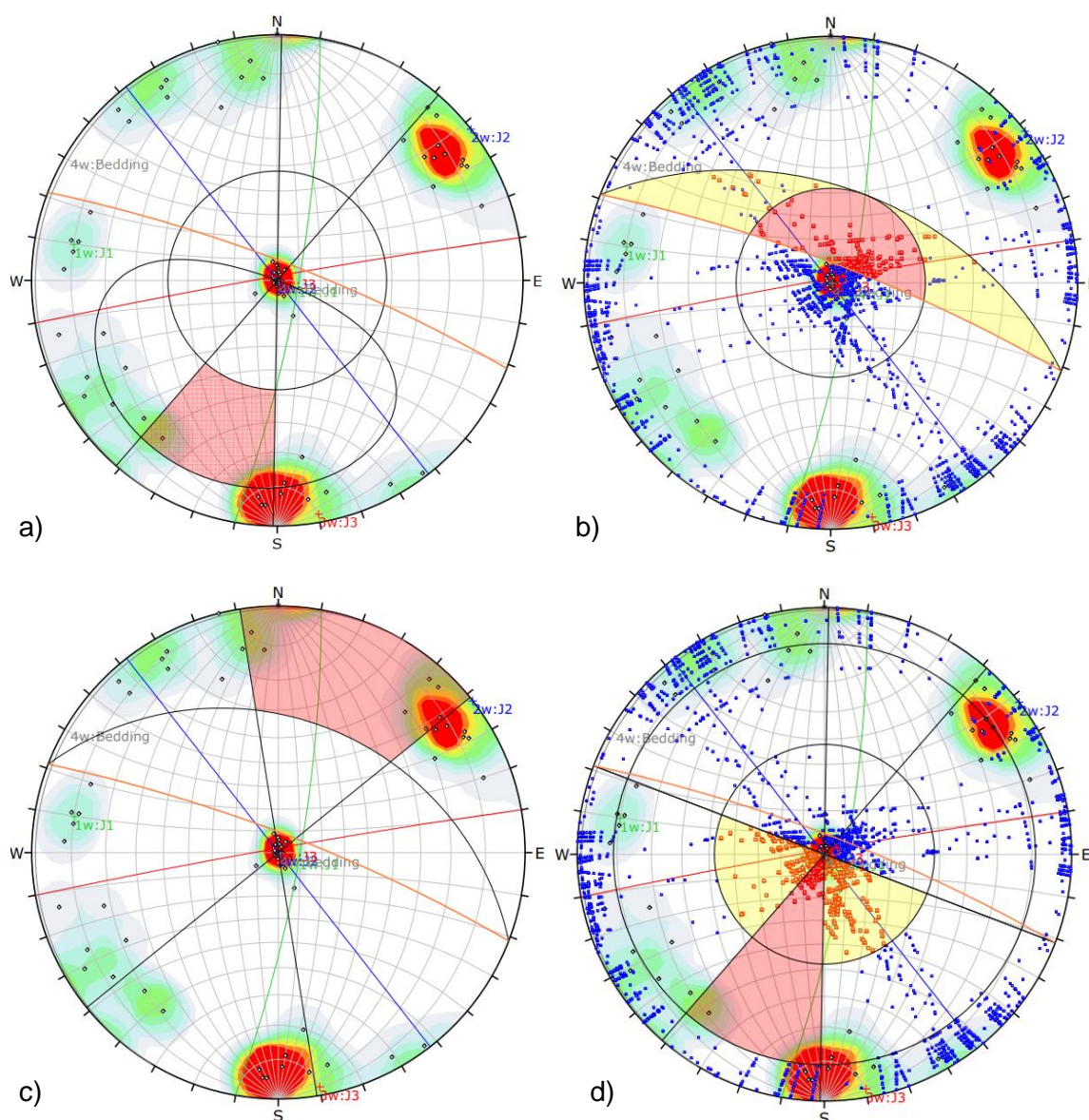


Figure 6-3: Kinematic analysis undertaken in DIPS for Domain D2. Friction angle of 30, quantity of data points scaled based on relative joint quantity. a) Planar sliding; b) Wedge sliding; c) Flexural toppling; d) Direct toppling

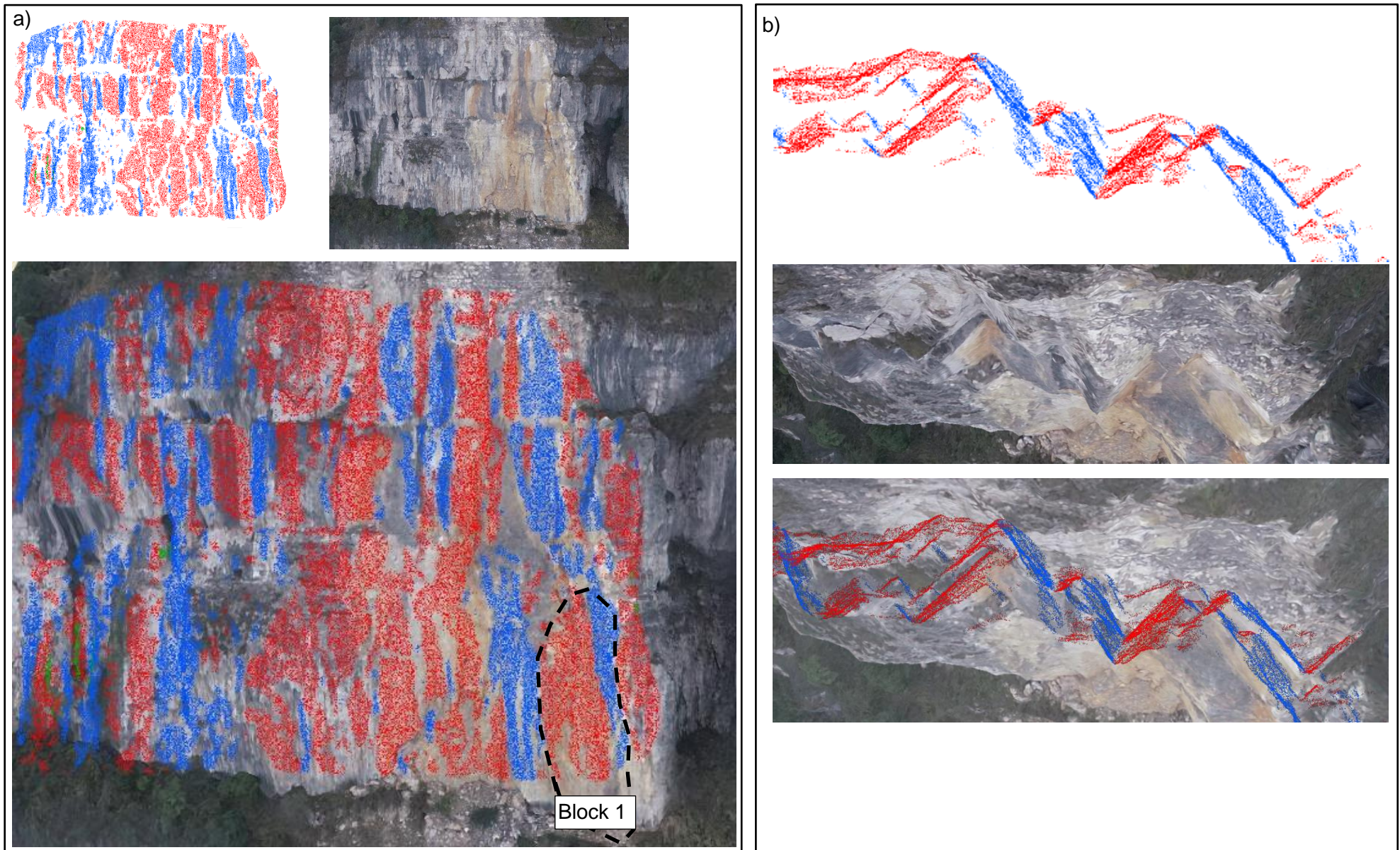


Figure 6-4: Example of the blocky nature of the surface in Domain D2, displaying wedge and toppling failures along joint sets J2 (blue) and J3 (red). Viewed from a) perpendicular to slope face; b) from above

Figure 6-4 presents the Rockfall Area within Domain D2 in which toppling and wedge failure were judged to have occurred. As discussed in Section 5.1, it is believed that Block 1 failed first (bottom right), through either wedge sliding or toppling (or a combination of the two), and that the overlying blocks were undercut and failed predominately through falling. Output pages from the D2 DIPS Kinematic analysis are included in Appendix B2.

6.1.3 Domain D3

Domain D3 was heavily dominated by three forms of toppling – backward toppling, flexural toppling and oblique toppling (25.4%, 21.0% and 20.9% of intersections respectively). Base plane sliding/toppling and wedge sliding also occurred (12.9% and 12.7% respectively). The dominance of toppling along Joint Set J3 is evidenced in the face of the slope itself, whose orientation is approximately equal to the mean set orientation of J3.

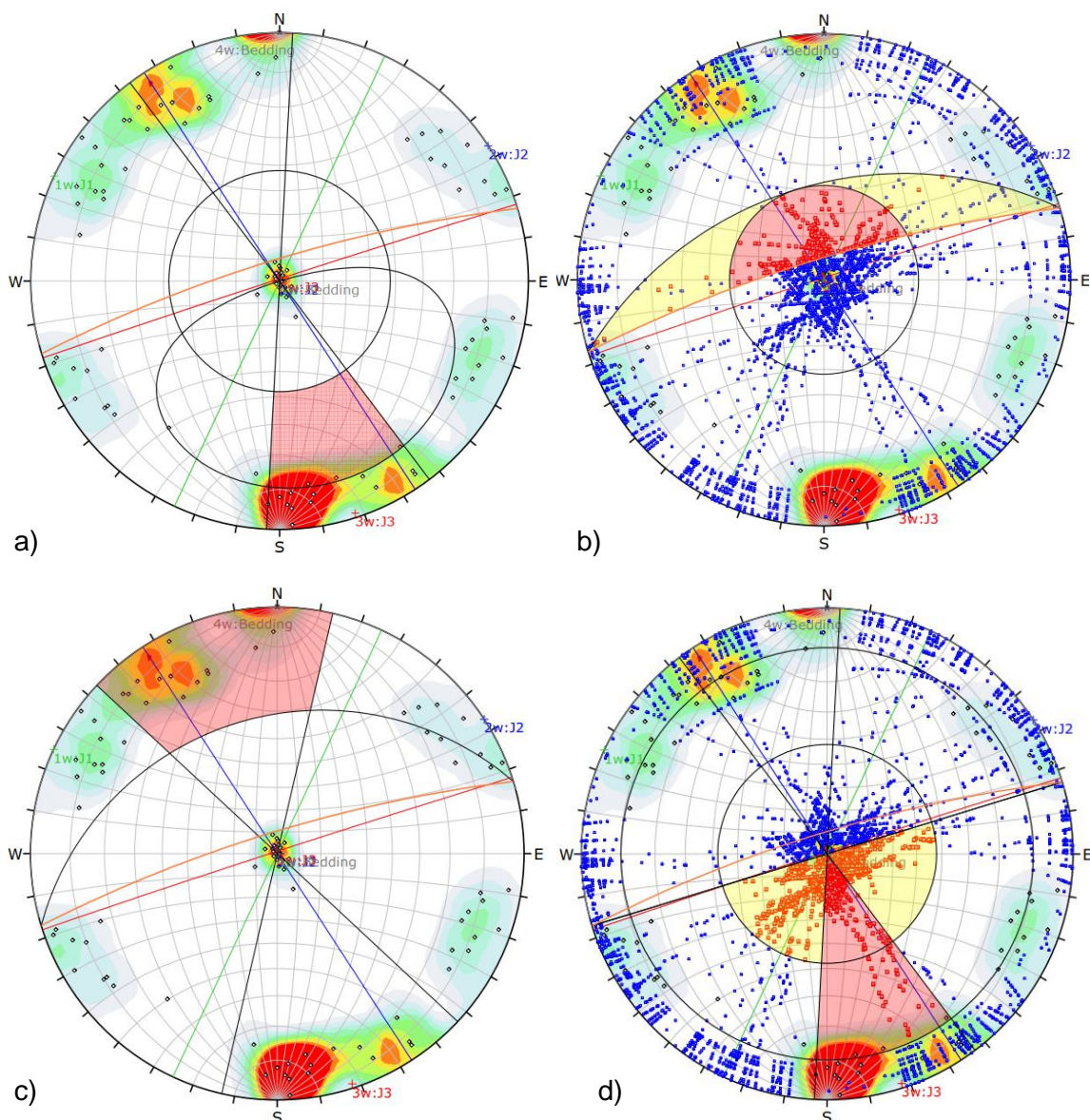


Figure 6-5: Kinematic analysis in DIPS for Domain D3. Friction angle of 30, quantity of data points scaled based on relative joint quantity. a) Planar sliding; b) Wedge sliding; c) Flexural toppling; d) Direct toppling.

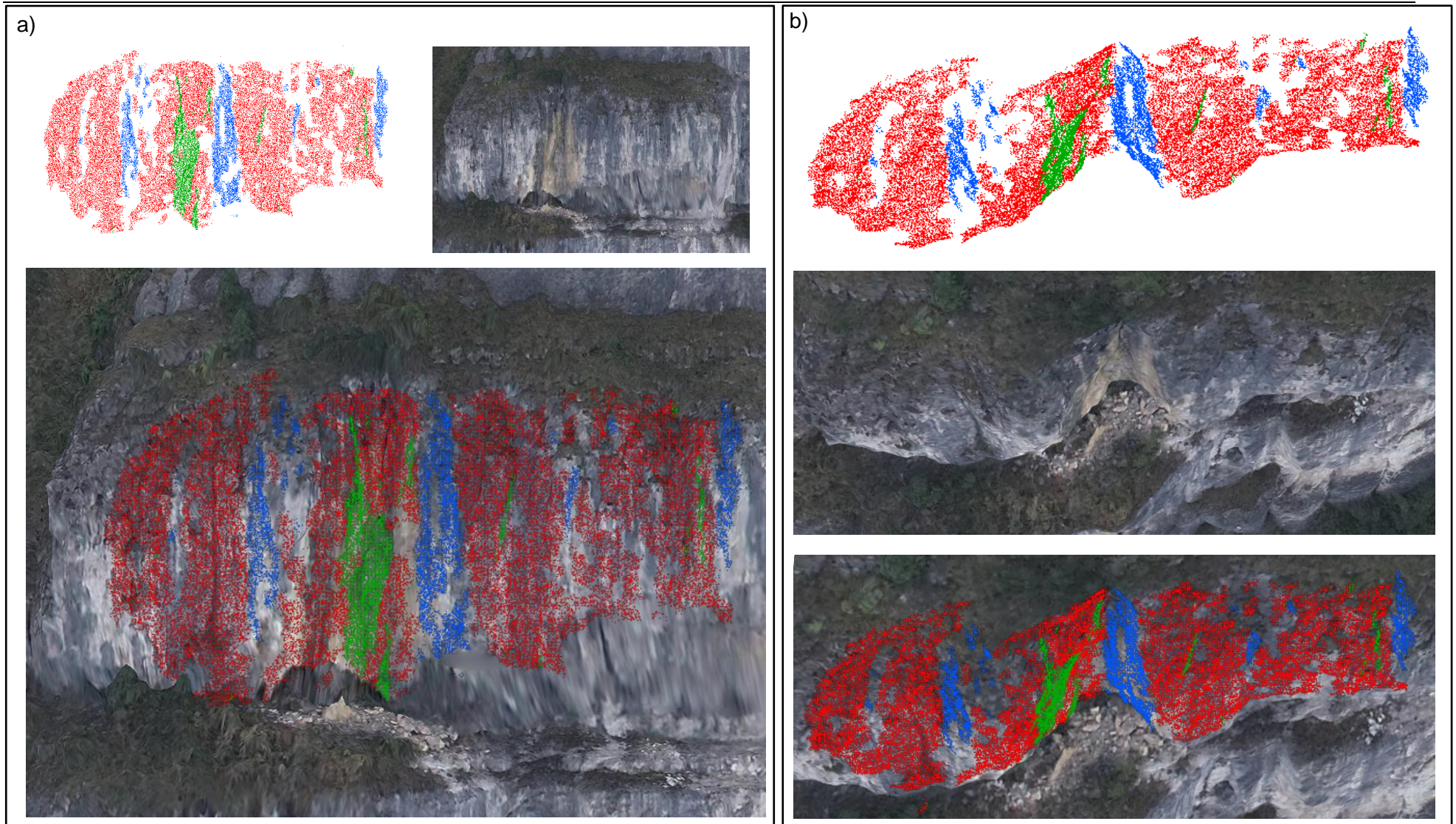


Figure 6-6: Example of typical slope face conditions in Domain D3, showing toppling failure along joint sets J3 (red), with release planes along J2 (blue); a) viewed perpendicular to slope; b) viewed approximately 70° from horizontal

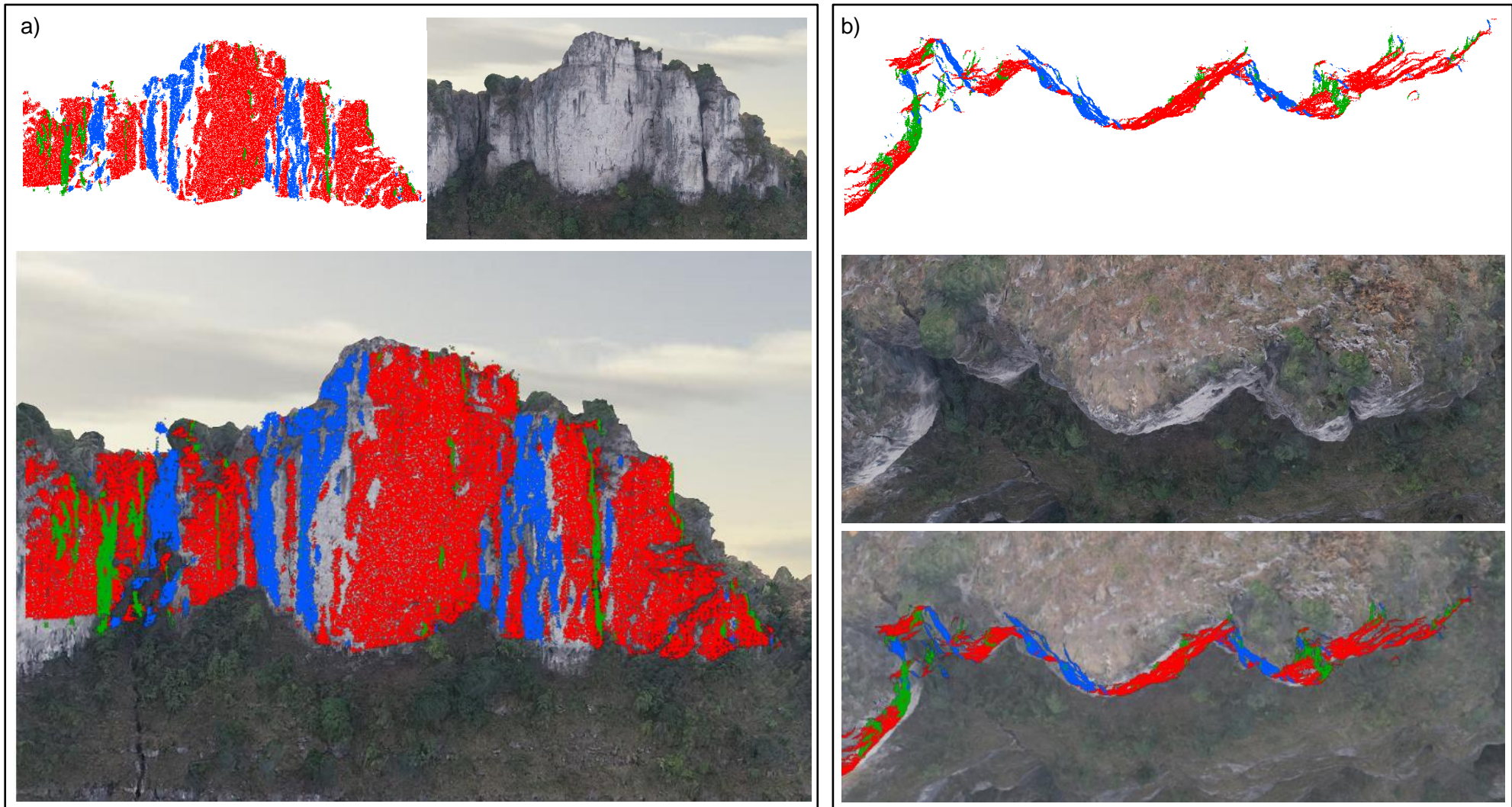


Figure 6-7: Example of crown surface conditions within Domain D3, displaying wedge failure and toppling failure along joint sets J2 and J3, a) viewed perpendicular to slope; b) viewed vertically

Figure 6-6 and Figure 6-7 present typical slope faces representative of Domain D3. Figure 6-6 reflects conditions throughout the majority of the slope face, while Figure 6-7 displays representative conditions at the crest of the slope. It is extremely difficult to define whether toppling or wedge sliding occurred at these locations, due to the highly vertical nature of the defect sets and the undercutting of the slope face. The basic kinematic analysis in DIPS indicates that toppling failure was most common. Output pages from the D3 DIPS Kinematic analysis are included in Appendix B3.

6.1.4 Domain D4

Domain D4 was heavily dominated by three forms of toppling – backward toppling (30.0% of intersections), flexural toppling (27.2% of plane normals) and oblique toppling (24.3%). Base plane sliding/toppling also occurred (11.0%). However, planar sliding, wedge sliding and direct toppling were all present only in minor quantities (<6%).

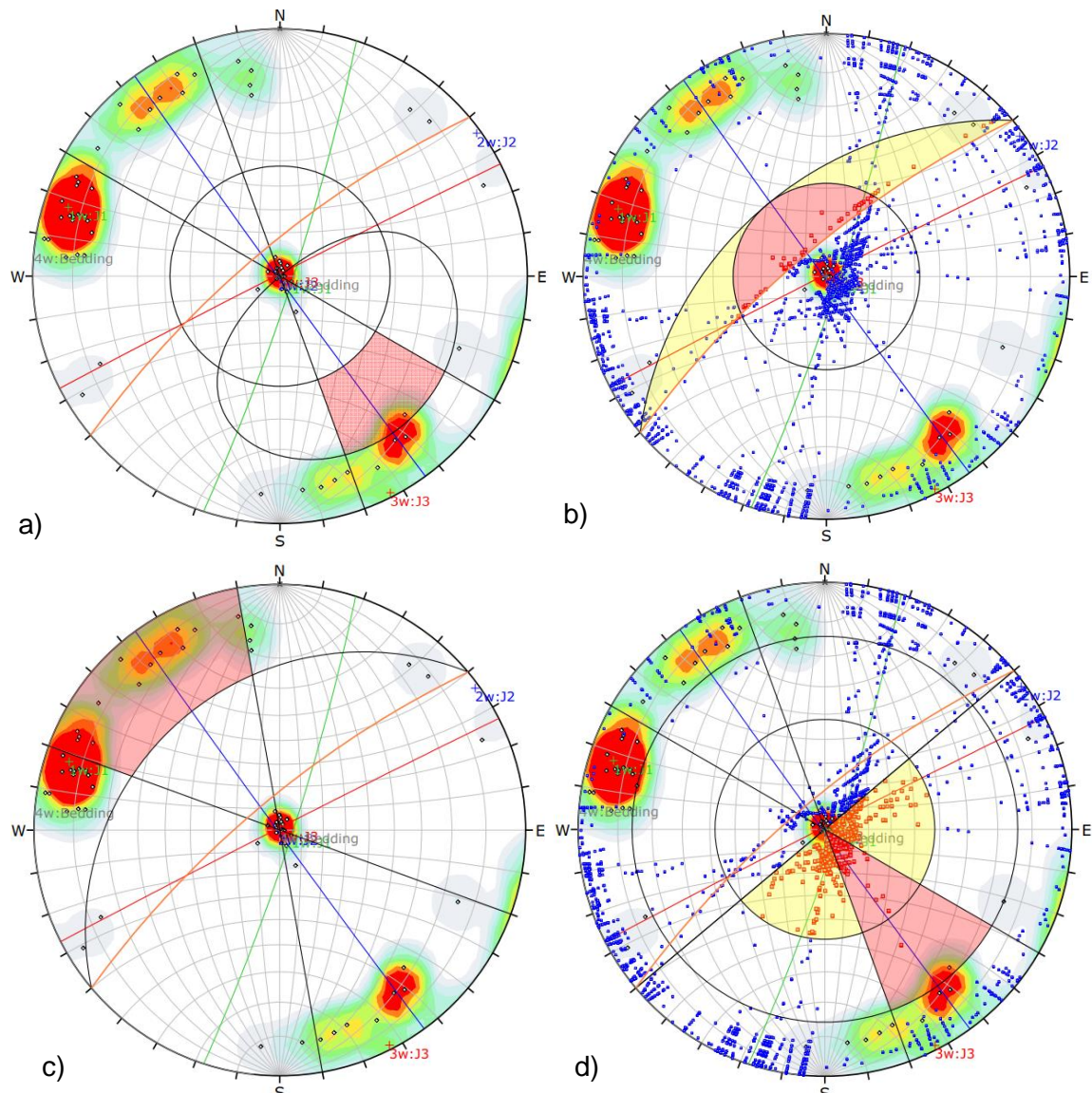


Figure 6-8: Kinematic analysis in DIPS for Domain D4. Friction angle of 30, quantity of data points scaled based on relative joint quantity. a) Planar sliding; b) Wedge sliding; c) Flexural toppling; d) Direct toppling.

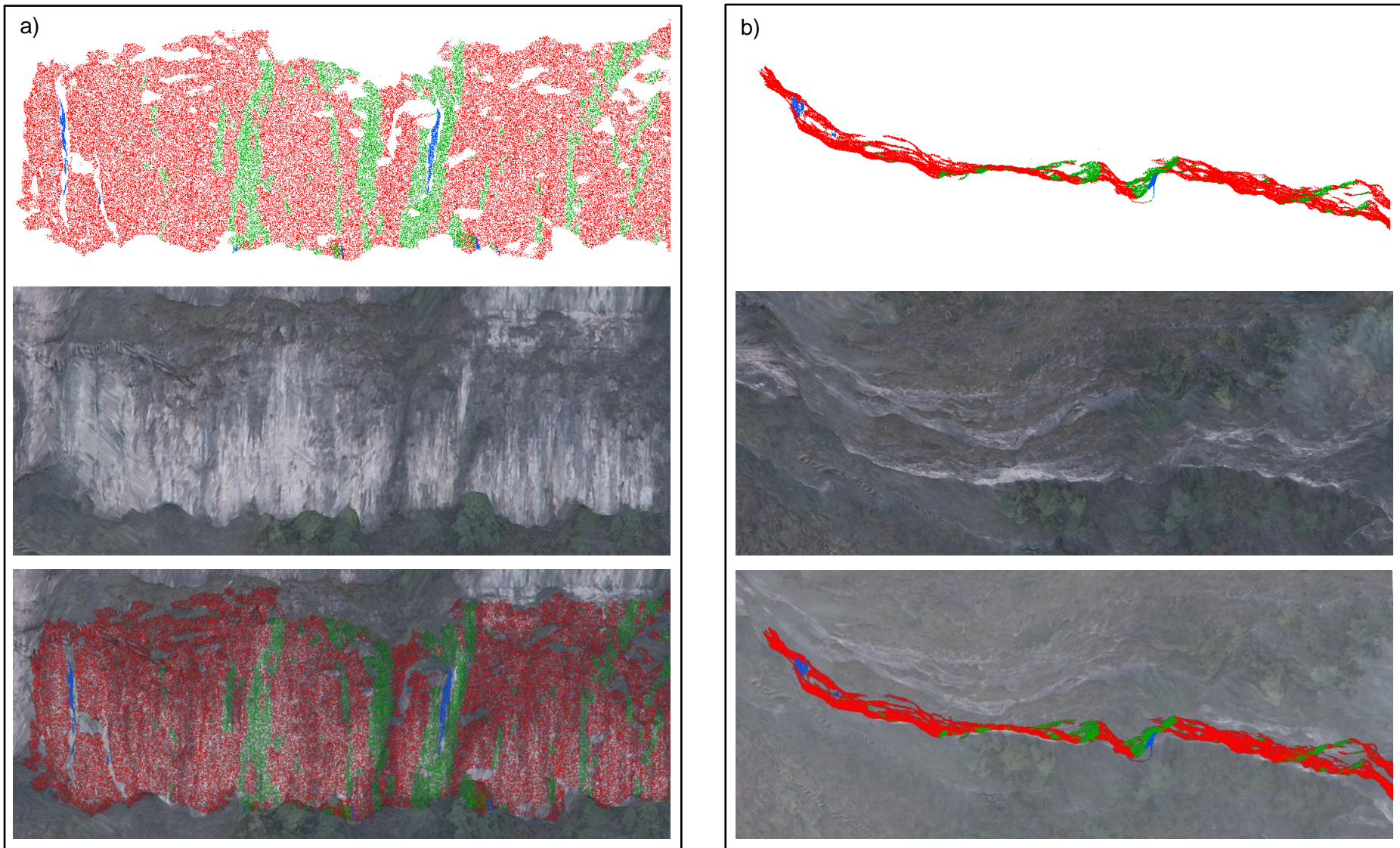


Figure 6-9: Typical slope face within Domain D4, presenting an example of toppling failure along Joint Set J3 (red) a) viewed perpendicular to slope; b) viewed from above;

Flexural toppling occurred along both joint sets J1 and J3. This is reflected in the shape of the surface, where minor variations in the slope orientation from the east to west are clearly defined in a change in dominant joint set from J3 to J1, along which toppling has occurred. Figure 6-9 presents locations within Domain D4 in which toppling was judged to have occurred along Joint Set J3. Output pages from the D4 DIPS Kinematic analysis are included in Appendix B4.

6.2 Probabilistic Analysis

Probabilistic analysis was undertaken in the RocScience software, RocPlane, SWedge and RocTopple in order to determine the probability of failure for planar sliding, wedge sliding and toppling respectively. This analysis was undertaken in domains where DIPS kinematic analysis determined that the failure mechanism was kinematically admissible in more than 10% of poles or intersections. A summary of the analysis undertaken is shown in Table 6-3.

Table 6-3: Types of probabilistic analysis undertaken in each domain

Domain	Planar Sliding	Wedge Sliding	Direct Toppling ¹	Flexural Toppling
D1	x	x	x	x
D2	-	x	x	x
D3	-	x	x	x
D4	-	-	x	x

Notes:

1. Direct toppling analysis here includes direct toppling and base plane sliding/toppling only.

These programs all allow the consideration of probabilistic distributions of parameters including slope orientation, joint orientation, spacing, waviness and shear strength. The resulting analysis then returns a factor of safety distribution, from which a probability of failure is calculated.

The weakness in these programs is the inability to refine the slope geometry. It is not possible to include the undercut situations so common within the Study Area. The orientation of the slope face has been taken as the overall slope face orientation within each domain. As discussed in Section 6.1, to appropriately reflect the geometric complexity of the slope face and the detachment of failing blocks, a 3D DEM model would be required, which is beyond the scope of this thesis.

Additionally, for sub-vertical joints, the probabilistic distribution does not consider that a portion of the joint set orientation extends to the “other side of vertical” from the set mean orientation, essentially only considering one half of any sub-vertical joint set.

All analyses assume no water pressure, tension cracks or additional external forces (such as surcharge or seismic) are present. Waviness values for joint sets were adopted based on a 9.8% reduction from measured mean peak dilation angles for each set. All defects were assumed to be fully persistent.

Probabilistic parameters adopted for analyses are outlined in Table 6-4 below. Normal statistical distributions were adopted for all parameters other than defect orientations, for which Fishers K distribution was used.

Table 6-4: Summary of probabilistic defect parameters used in analysis

Parameter	J1	J2	J3	Bedding
Mean Dip	86.2°	88.7°	88.8°	0.4°
Mean Dip Direction	113.0°	55.7°	338.3°	330.7°
Fishers K	45.72	37.74	27.33	136.78
Base Friction Angle	30°	30°	30°	30°
Mean Peak Dilation Angle	18.42°	20.99°	22.30°	20.86°
Reduced Dilation Angle	16.61°	18.93°	20.12°	18.81°
Dilation Standard Deviation	5.63°	4.01°	4.44°	4.96°
Dilation Relative Minimum & Maximum (2xSD)	11.26°	8.01°	8.89°	9.93°
Base Friction Angle	30°	30°	30°	30°
Base Friction Angle Standard Deviation	2°	2°	2°	2°
Base Friction Angle Relative Minimum & Maximum (2xSD)	4°	4°	4°	4°
Cohesion	0	0	0	0
Mean Spacing	5.58 m	4.39 m	3.60 m	12.09 m
Spacing Standard Deviation	4.61 m	3.55 m	2.30 m	5.22 m
Spacing Relative Minimum & Maximum (2xSD)	9.23 m	7.10 m	4.60 m	10.44 m
Unit Weight	24.5 kN/m ³	24.5 kN/m ³	24.5 kN/m ³	24.5 kN/m ³

6.2.1 Planar Sliding (RocPlane)

Planar sliding analysis was undertaken in Domain D1, where the basic DIPS kinematic analysis indicated that 12.8% of measured planes were kinematically able to fail in planar sliding. DIPS specified that were planar sliding to occur, it would occur along Joint Set J2.

RocPlane does not consider relative azimuth between the sliding plane and the slope face – the slope face and joint must have the same strike. Within Domain D1, the slope face has an extremely similar strike to Joint Set J2. Therefore it was assumed that the planes were of the same strike, and the relative dip values were utilised for the slope and J2.

Probabilistic joint set parameters were utilised as outlined in Table 6-4. Geometric inputs were utilised as outlined in Table 6-5 below.

Table 6-5: Geometry as input into planar analysis for Domain D1.

Parameter	Value	Standard Deviation	Relative Minimum	Relative Maximum	Comment
Slope Dip	78.9°	14.17°	23.34°	23.34°	From J2 68% and 95% variability cones
Slope Height	12.09 m	5.22 m	10.44 m	10.44 m	From bedding spacing
Upper Face Dip	1°	7.43°	12.20°	12.20°	Bedding 68% and 95% variability cones
Bench Width	3 m	2 m	4 m	4 m	Measured across the Study Area

RocPlane analysis indicated that there was a 24.85% chance of planar sliding along Joint Set J2 within Domain D1. This analysis is not considered to appropriately reflect the likelihood of planar failure. The method of analysis in RocPlane assumes that sliding will occur through the slope surface, which is comprised of planes from Joint Set J2. Based on the geometry of the RocPlane analysis, the only situation in which planar sliding could occur would be where joints of the same set cross each other. The high potential for planar sliding here likely reflects the statistical distribution of the slope dip and joint dip, which gives the false impression that the two regularly cross.

Despite this, the likelihood of planar sliding is still considered to be high, because where thinly bedded regions erode and undercutting occurs, joint surfaces further back in the slope intersect the undercut slope space and so may fail in sliding. This is true for all domains which have a dominant joint set (D1, D3, D4). However, the likelihood cannot be calculated in RocPlane, as undercutting cannot be modelled.

A visualisation of this failure is displayed in Figure 6-10 below. Output reports for each planar sliding analysis are included in Appendix C.

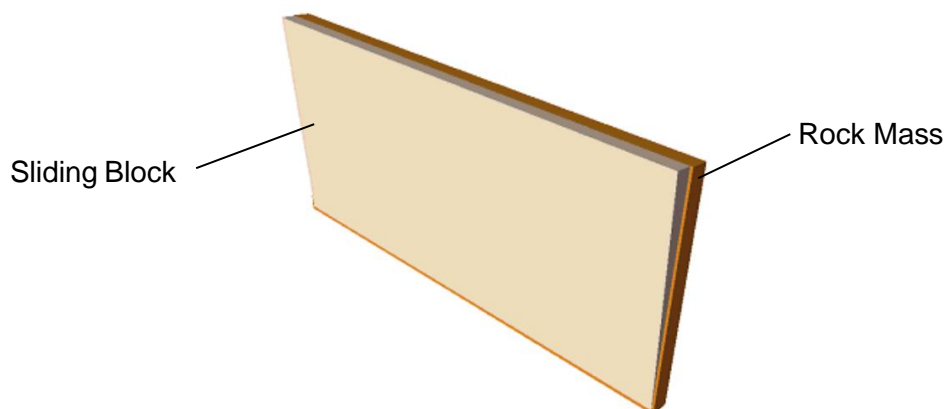


Figure 6-10: Visualisation of planar sliding within Domain D1, along Joint Set J2.

6.2.2 Wedge Sliding (SWedge)

Wedge sliding analysis was undertaken in Domains D1, D2 and D3 where the basic DIPS kinematic analysis indicated that 14.80%, 17.40% and 12.70% of measured intersections respectively were kinematically able to fail in wedge sliding.

Probabilistic analysis with a basal joint was adopted for this analysis. Analyses were run twice, once considering that the slope face was overhanging, once not. As discussed, this was required because SWedge is unable to consider sub-vertical joint sets going “to the other side of vertical” (switching their dip direction 180°) in their probabilistic distributions.

Standard geometries were adopted for all wedge sliding analyses as outlined in Table 6-6. Domain-specific geometries were adopted as outlined in Table 6-7.

Probabilistic analysis for wedge sliding in all domains returned a surprisingly low percentage probability of failure – less than 5% in all situations. It should be noted that the slope geometries input into SWedge do not, and can not, account for any undercutting, as is present in the Study Area. Where slope faces dip away from the slope this undercutting would act to shift the centre of gravity back into the slope while destabilising the toe of potential wedges, increasing the likelihood of wedge sliding. Conversely, where slope faces overhang, and dip back into the slope, undercutting would act to further shift the centre of gravity away from the rock mass, increasing the likelihood of toppling.

Table 6-6: Standard slope geometry as input into wedge sliding analysis for all domains.

Parameter	Value	Standard Deviation	Relative Minimum/Maximum	Comment
Slope Height	12.09 m	-	-	Measured mean bedding spacing
Upper Face Dip	1°	7.43°	12.20°	From bedding. Std. Dev. and relative min/max taken from 68% and 95% variability cones respectively.
Upper Face Dip Direction	330.7°	7.43°	12.20°	
Bench Width	3 m	-	-	Measured across the Study Area

Table 6-7: Geometry as input into wedge sliding analysis for each domain.

Domain	Slope Dip	Slope Dip Direction	Standard Deviation	Relative Minimum/Minimum	Comment
D1	78.79°	61.42°	14.17°	23.34°	St. Dev. from J2 68% and 95% variability cones
D2	81.8°	21.73°	15°	25°	Nominal
D3	80.86	343.81	16.66°	27.5°	St. Dev. from J3 68% and 95% variability cones

Table 6-8 below displays the major joint sets considered for each analysis, and the resulting percentage probability of failure calculated for each scenario. On the assumption that all sets have a vertical mean value, with uniform scatter, it follows that the overhanging and standard slope conditions each represent one half of the joint data set. The overall percentage probability of wedge sliding can therefore be taken as the average of the two percentage probabilities.

Table 6-8: Percentage probability of wedge sliding in each domain.

Parameter	Joint Sets	Percentage Probability – Standard Slope	Percentage Probability – Overhanging Slope	Average Percentage Probability
D1	J1, J2	2.09%	1.78%	1.94%
D2	J2, J3	1.98%	2.73%	2.36%
D3	J1, J3	2.76%	3.16%	2.96%
D3	J2, J3	4.49%	4.96%	4.73%

Figure 6-11 displays a visual representation of the wedge failure for each scenario, with both a standard (left) and overhanging (right) slope. Output reports for each wedge sliding analysis are included in Appendix D.

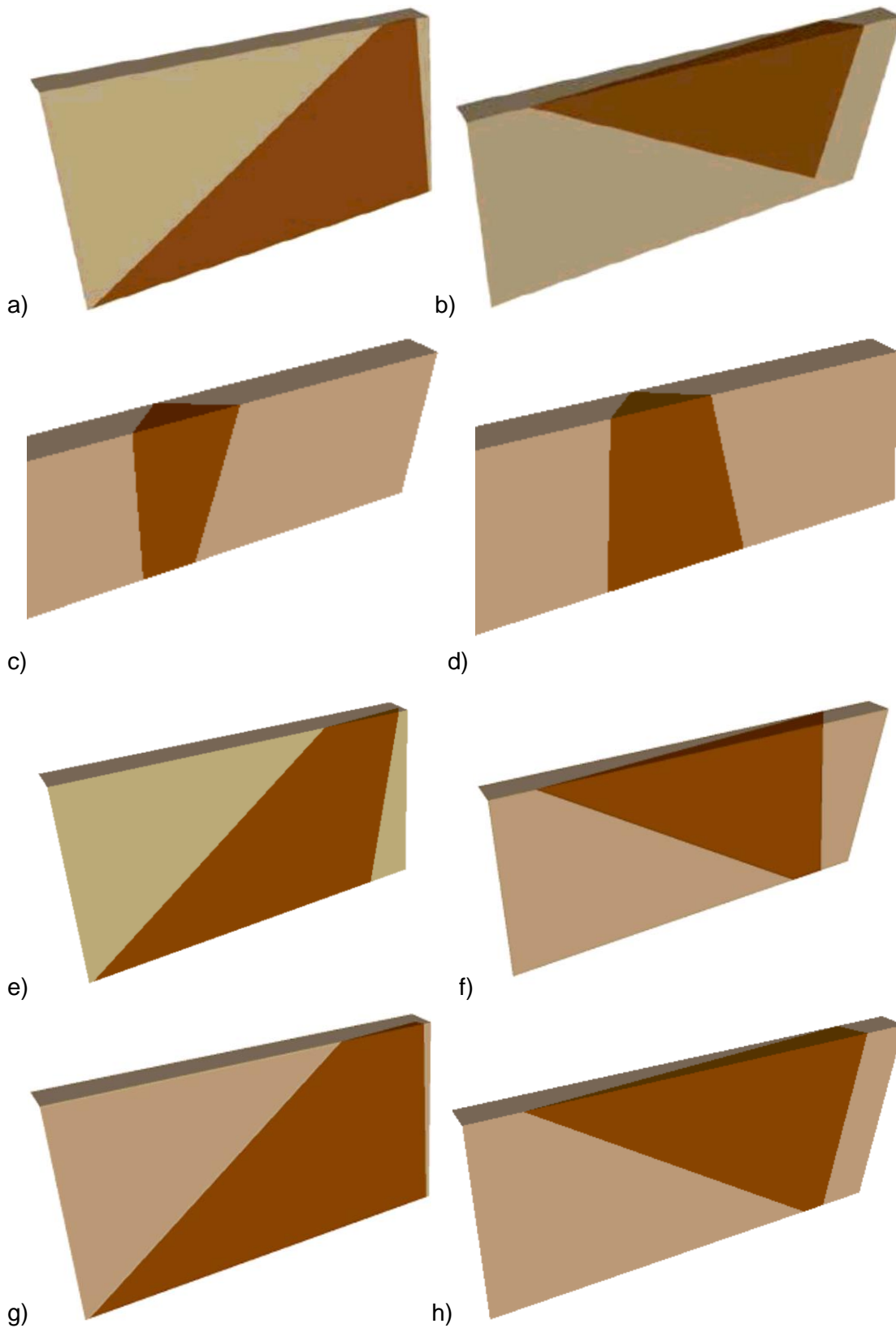


Figure 6-11: Wedge sliding failures as modelled in SWedge; a) D1, standard slope; b) D1, overhanging slope; c) D2, standard slope; d) D2, overhanging slope; e) D3_1, standard slope; f) D3_1, overhanging slope; g) D3_2, standard slope; h) D3_2, overhanging slope;

6.2.3 Toppling Failure (RocTopple)

Toppling analysis was undertaken in all domains. The basic DIPS kinematic analysis found that all toppling mechanisms (flexural toppling, backwards toppling, oblique toppling, and base plane sliding/toppling) were shown to be kinematically possible in a significant percentage of cases within each domain (>10%). Direct toppling was found to be kinematically possible in less than 6% of cases.

Probabilistic analysis was considered in two ways using the RocTopple program:

- Direct Toppling: based on the limit equilibrium block toppling method of Goodman and Bray (1976). This is only able to consider direct toppling and base sliding; and
- Flexural Toppling: based on the block flexure toppling method of Amini, Majdi and Veshadi (2012).

As RocTopple is a 2D program, it is not possible to consider oblique toppling, overhanging slopes, or undercut geometries. It is also not possible to consider joint sets which dip out of the slope face, and so it is not possible to consider backwards toppling.

RocTopple does not allow there to be any difference in strike between the joint plane and the slope face. Within most domains, the slope face is dominated by one joint set, which essentially controls the slope face geometry and orientation. The strike of the slope face and dominant joint set in each domain have therefore been assumed to be equal for the purposes of this analysis. For Domain D4, the domain has been split into two regions – one dominated by Joint Set J1, the other dominated by J3.

The flexural toppling analysis requires the input of intact rock strength in order to consider shear failure of blocks, which must be input according to the Mohr-Coulomb failure criterion. The RocScience program RocData was used to calculate the required Mohr-Coulomb parameters, using the inputs outlined in Table 6-4, and a maximum slope height of 140 m. This resulted in a friction angle of 48°, and a cohesion of 6 MPa. This output is included in Appendix E.

Point of force applications were maintained at default values. These ratios mark where the normal force from the block above will act for equilibrium calculations of sliding, shearing and flexural bending. Default values were maintained of 0.75 for sliding and shearing, and 0.9 for flexural bending. The entire slope height (140 m) was adopted, and as is visually displayed in Figure 6-12, this looks extremely similar to the actual stepped geometry of the slope face.

Standard geometries were adopted for all toppling analyses as outlined in Table 6-9. Domain-specific geometries were adopted as outlined in Table 6-10.

Table 6-9: Standard slope geometry as input into toppling analysis for all domains.

Parameter	Value	Standard Deviation	Relative Minimum/Maximum	Comment
Upper Face Dip	-28°	9.04°	14.85°	Back slope face, 68% and 95% variability cones
Overall Base Inclination ¹	10°	9°	9°	Lowest allowable value. Base inclination + Joint Dip must equal 90°
Base Joint Friction Angle ¹	48.81°	6.96°	13.93°	Base friction angle and dilation angle of bedding (average of all sets)
Bench Width ²	Domain slope height			To reflect geometry of back slope.

Notes:

1. Valid or adjustable for direct toppling analysis only
2. Input for flexural toppling analysis only

Table 6-10: Geometry as input into toppling analysis for each domain.

Domain	Dominant Joint Set	Slope Height	Slope Dip	Standard Deviation	Relative Minimum/Minimum	Comment
D1	J2	55 m	78.79°	14.17°	23.34°	St. Dev. from J2 68% and 95% variability cones
D2	J2, J3	90 m	81.80°	15.00°	25.00°	Nominal
D3	J3	140 m	80.86°	16.66°	27.50°	St. Dev. from J3 68% and 95% variability cones
D4_J1	J1	80 m	76.00°	12.86°	21.18°	St. Dev. from J1 68% and 95% variability cones
D4_J3	J3	80 m	76.00°	16.66°	27.5°	St. Dev. from J3 68% and 95% variability cones

The probabilistic distribution for sub-vertical joints in RocTopple also cannot consider fluctuations about the vertical where planes may dip in the opposite direction to the mean orientation – i.e., wrapped joint sets. In this case it is not possible to define most statistical distributions about the mean dip value. RocTopple does not compute where the addition of standard deviation and mean value is above 89, which is the case for all joint sets within the Study Area. RocTopple therefore only considers half of each joint set.

A visual inspection of stereonet in Figure 4-18 shows that all dominant joint sets have a roughly evenly distributed dip between 70° and 90°. Therefore, for all dominant joint sets in the toppling analysis a dip of 80° has been adopted in RocTopple, with a uniform probabilistic distribution defining a relative minimum and relative maximum of 10° and 9° respectively. This results in an equal distribution of joint dip between 70° and 89° (the maximum angle allowed for input).

The probability of failure calculated through this methodology considers only one half of the dataset for each joint set – the portion of the set which is oriented with a dip opposite to the dip of the slope face. For the purposes of this thesis, each defect set has been assumed to be distributed evenly about a vertical mean value. The probability of toppling failure for the whole joint set can then be calculated as one half of the probability calculated by RocTopple.

Table 6-11 below displays the results of the RocTopple analysis. These results are considered to be, at best, approximate figures. A number of assumptions (both geometric and probabilistic) were required in order to run the model, and arguably the most dominating forms of toppling (oblique and backwards toppling) were not included in this analysis.

Table 6-11: Percentage probability for toppling failure for each domain

Parameter	Dominant Joint Set	Flexural Toppling	Direct Toppling	0.5 x Flexural Toppling	0.5 x Direct Toppling
D1	J2	5.8%	9.5%	3.3%	4.8%
D2	J2, J3	22.7%	28.3%	11.4%	14.2%
D3	J3	45.8%	49.0%	22.9%	24.5%
D4_J1	J1	23.7%	27.9%	11.9%	14.0%
D4_J3	J3	31.9%	35.3%	16.0%	17.7%

These results do not initially appear to align well with the basic DIPS kinematic assessment. For example, DIPS assessment determined that, of all the planes and intersections considered, a maximum of 6% of intersections were kinematically able to fail through direct toppling. The RocTopple analysis assigns a probability of failure of generally above 14% (other than Domain D1). However, these two numbers are not comparable - the DIPS assessment does not return a probability of failure. It would be expected that of the subset of data which DIPS judged to be kinematically able to topple, only a portion of that subset would fail, once geometric factors, spacing, slope height etc. were taken into consideration.

Additionally, the probability of failure calculated in RocTopple considers base sliding/toppling together with direct toppling. It is not possible to segregate the two mechanisms within the “probability of failure” output. Although the probabilistic analysis in RocTopple considers all combinations of input variables, the results presented visually (and in a tabulated format block by block) display the mean situation only. As per the DIPS analysis, it is already known that the mean situation is not kinematically able to fail in base plane sliding/toppling in any domain. It is the outliers of each parameter which interact to allow this failure mechanism. No base plane sliding can therefore be seen in the RocTopple analysis, although it is likely there, contributing to the probability of failure.

The dataset input into RocTopple is also far more focused than the dataset input into DIPS. The RocTopple analysis considered only the dominant joint set of a domain and the base plane (bedding), effectively viewing a smaller dataset which had a higher likelihood of kinematic admissibility than the rest of the dataset as a whole.

Considering these factors, the results of the RocTopple analysis are reasonable. The analysis generally returns a lower percentage probability of failure than the percentage of kinematically admissible failures, for both flexural and direct (direct + base) toppling. Table 6-12 displays a comparison of the DIPS and probabilistic analysis.

Table 6-12: Comparison of the percentage of intersections/normals kinematically able to fail (DIPS), and percentage probability for failure (RocTopple)

Parameter	DIPS Direct Toppling	DIPS Base Toppling	0.5 x Direct Toppling	DIPS Flexural Toppling	0.5 x Flexural Toppling
D1	1.1%	18.2%	4.8%	22.4%	3.3%
D2	4.3%	12.0%	14.2%	13.9%	11.4%
D3	4.5%	12.9%	24.5%	21.0%	22.9%
D4 (J1, J3)	5.7%	11.0%	14.0% (17.7%)	27.2%	11.9% (16.0%)

The percentage probability of failure is above 10% for toppling mechanisms in all domains other than D1 (<5%). Domain D3 was most at risk of toppling failure, with flexural toppling at a 22.9% risk, and direct toppling at 24.5%. However, overall toppling percentage probability is likely to be significantly higher, once including oblique and backwards toppling.

Figure 6-12 displays a visual representation of the toppling failure for each scenario, including both direct (left) and flexural (right) toppling. Output reports for each RocTopple analysis are included in Appendix E.

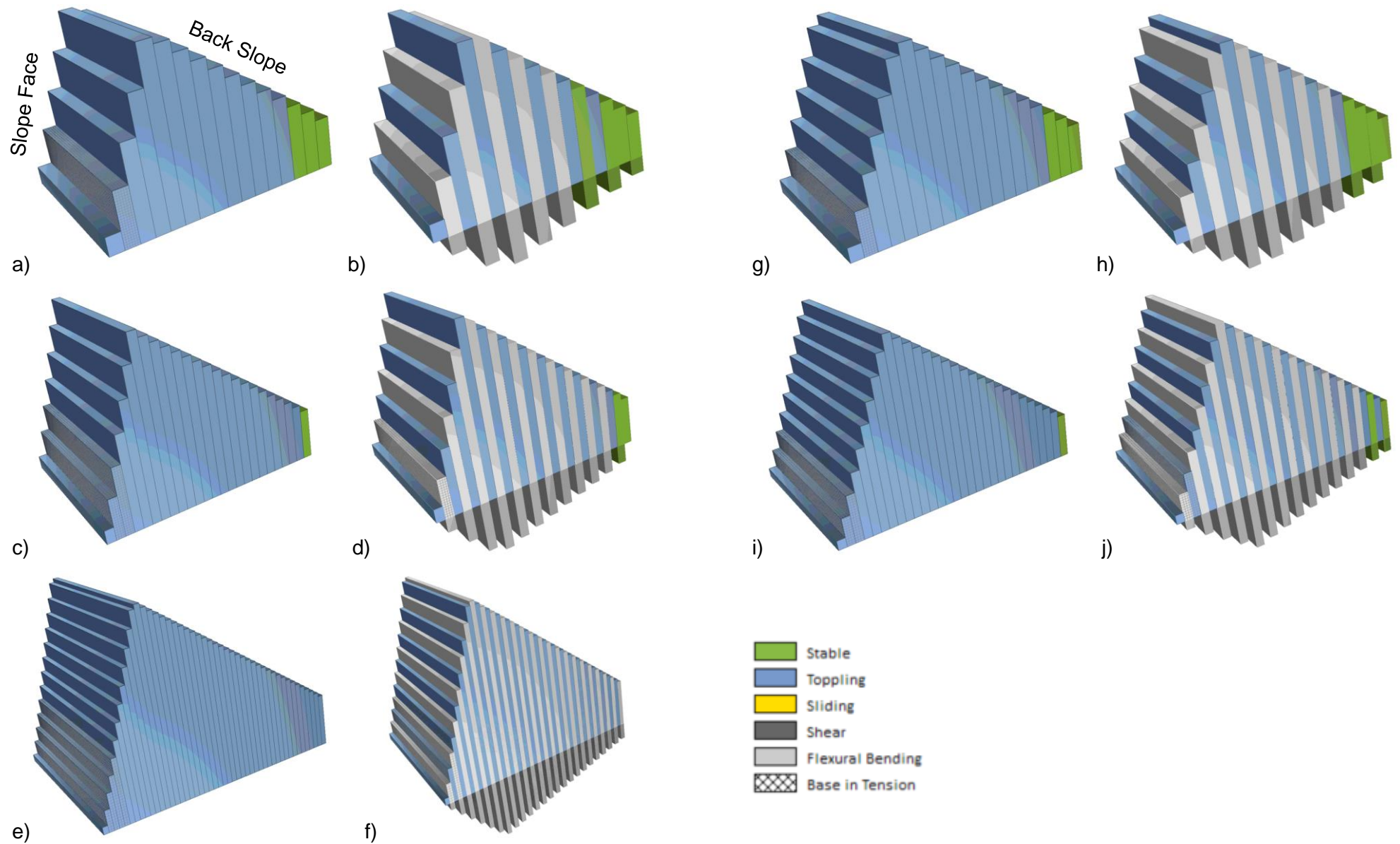


Figure 6-12: Visualisation of toppling analysis by domain; a) D1 Direct Toppling (J2); b) D1 Flexural Toppling (J2); c) D2 Direct Toppling (J2/J3); d) D2 Flexural Toppling (J2/J3); e) D3 Direct Toppling (J3); f) D3 Flexural Toppling (J3); g) D4 Direct Toppling (J1); h) D4 Flexural Toppling (J1); i) D4 Direct Toppling (J3); j) D4 Flexural Toppling (J3).

7 Conclusion

The behaviour of a rock mass is governed by both the properties of intact rock and the properties of defects which occur throughout the rock mass. In order to analyse the way in which a rock mass will behave, it is necessary to evaluate the defect orientations and identify if discrete sets are present. The various properties of present sets must then be characterised, including orientation, spacing, persistence, termination, roughness and waviness.

The purpose of this thesis was to develop a workflow to remotely characterise set-based joint parameters in slopes using three-dimensional data sets. The effect of these defects on slope stability was then investigated through a kinematic analysis.

7.1 Characterisation of Defect Sets

The provided dataset comprised a 3D point cloud of the Study Area and a 3D real scene model. The 3D point cloud had been processed using ContextCapture and MATLAB, to assign a Hough Normal and associated unique HSV colour to each point within the cloud.

Defect sets within the Study Area were defined by grouping defects with similar orientations into the same set. The most appropriate methodology for defect orientation measurement was assessed. It was determined that the two automated orientation tools in CloudCompare (FACETS Kd and FM), were less accurate than manual measurements taken using the Compass plugin in CloudCompare. The compass tool was used to take measurements manually across the study area on exposed defect planes. These manual measurements were assessed based on engineering and geological judgement by cross-referencing the HSV coloured point cloud and the 3D real scene model. Analysis of plane orientations in DIPS suggested the presence of three wrapped, sub-vertical joint sets (J1, J2, and J3) striking approximately 60° from each other, all orthogonal to a sub-horizontal bedding set.

This preliminary analysis provided sufficient information to define the outer extents of each joint set orientation. These orientation ranges were input into the qFACETS plugin in CloudCompare to segregate the dataset into four separate point clouds – one for each joint set and one for bedding

Considering the size of the Study Area (with a face area of approximately 70,000 m²), a number of analyses were conducted to reflect potential variations in location-based set distribution. The Study Area was therefore separated into four discrete domains, each of which had a consistent slope face orientation, and each with a unique combination of defect sets. It was observed that the joint sets exposed in each domain were dependant largely upon the orientation of the slope face relative to the joint set. Table 7-1 summarises slope orientation and the dominant defect sets for each domain.

Table 7-1: Summary of domain slope orientation and dominant joint sets.

Domain	Slope Dip	Slope Dip Direction	J1	J2	J3	Bedding
D1	78	61	Present	Dominant	Minor	Present
D2	81	21	Minor	Present	Present	Present
D3	80	343	Present	Present	Dominant	Present
D4	76	320	Present	Minor	Present	Present

An analysis of set orientation across the four domains was undertaken, however little variation was observed between domains. Final set orientations were calculated using data from across the entire study area, with Terzaghi weighting applied to each data point based on the appropriate domain slope face. Bedding orientation was defined in an outcrop-scale analysis, where planes were fitted to bedding traces along the slope face. Set mean values were defined, together with confidence and variability cones for each joint set, and Fisher's K. A summary of the parameters for the four defect sets is included in Table 7-2.

Normal set spacing was measured for each defect set, using a virtual scanline method to define five lines in each domain. The two-point thickness tool in CloudCompare was used to measure spacing between defects of the same set, using the mean set orientation as a reference plane. A basic statistical analysis was undertaken to define the spacing of the set, assuming a normal distribution. Analysis across the site determined that spacing was broadly consistent between domains for each set, and so was calculated on a site-wide basis. Spacing was a similar order of magnitude for each joint set, with Joint Set J1 having the widest spacing overall.

The wide spacing measured for the bedding planes is believed to reflect the distance between beds of a significantly different nature – i.e. thinly bedded zones vs. massive zones. Bedding structure likely still exists within the “massive” zones, but is not visible with the current imaging resolution.

Table 7-2: Summary of probabilistic defect parameters

Parameter	J1	J2	J3	Bedding
Mean Dip	86.2°	88.7°	88.8°	0.4°
Mean Dip Direction	113.0°	55.7°	338.3°	330.7°
Fishers K	45.72	37.74	27.33	136.78
Mean Spacing	5.58 m	4.39 m	3.60 m	12.09 m
Spacing Standard Deviation	4.61 m	3.55 m	2.30 m	5.22 m
Persistence	>140 m	>140 m	>140 m	>140 m
Mean Amplitude (waviness)	783 mm	703 mm	600 mm	-
Amplitude Standard Deviation	350 mm	347 mm	259 mm	-
Mean Peak Dilation Angle	18.42°	20.99°	22.30°	20.86°
Reduced Dilation Angle	16.61°	18.93°	20.12°	18.81°
Dilation Standard Deviation	5.63°	4.01°	4.44°	4.96°
Base Friction Angle (assumed)	30°	30°	30°	30°
Cohesion (assumed)	0	0	0	0

There are several sources of error which were noted throughout this spacing analysis, and the reliability of the results is considered to be low due to the following:

1. The point cloud by its nature can only display joint surfaces, and cannot show where joint traces do not result in surface relief;
2. The resolution of the point cloud is not capable of picking up smaller joint surfaces;
3. Regions of vegetation or talus cover can obscure joint surfaces;
4. Spacing between non-parallel planes is location dependant; and
5. It can be difficult to define the difference between waviness and defect spacing.

A statistical analysis of the defect spacing indicated problems with the collected data, in that the standard deviation values were larger than mean values. The data set was affected strongly by a few extremely high spacing values which were not representative of the actual joint spacing, and were likely due to the points listed above. Engineering judgement was applied to define an upper cap on defect spacing for each set and the set based normal spacing was recalculated, however, it is not known how many values which appear reasonable were in fact affected by the same failings.

In an attempt to address some of these uncertainties, the dimensions of fallen blocks observed below the slope were measured. Although it is understood that these blocks may have broken as they fell, their general rectangular shape and high intact strength indicates that their measurement may be a fair guide to the standard block size, and therefore to

spacing. It was not possible to define which joint sets had formed each block. However, it was possible to determine that the mean fallen block side length was much smaller than the mean spacing measured for each joint set in the point cloud, supporting the theory that spacing values are overestimated.

The persistence of the defect sets was determined qualitatively. All defect sets, including bedding, were persistent beyond the extents of the outcrop. No further comment can therefore be made, other than that the mean trace length is a minimum of 140 m vertically. On the rare occasions that there are seemingly isolated planes from a given joint set in the point cloud data, it is considered likely that these continue as traces throughout the outcrop, and simply do not appear in the point cloud model as they do not present as surfaces. In terms of defect termination, the three joint sets and bedding were observed to regularly cross each other, and no termination against one another was observed.

Joint geometry, surface waviness and roughness were analysed qualitatively and quantitatively. On the outcrop scale, visual assessments of the defects indicated that they were all undulating on the scale of tens of meters. All joint sets (but particularly Joint Set J1) exhibit locations in which joints appear to split and re-join, resulting in apparent “stepped” features. The long joint traces observed likely formed from the connection of individual adjacent joints, allowing fractures to form through intact rock between joints, or along a joint of a different set.

The amplitude of waviness on the scale of exposed surfaces was calculated using a planar method, analogous to the straight edge method but utilising a best fit plane and measuring maximum amplitude from that plane. This method is considered to provide a better assessment of the geometry of the mechanism, and recognises that the whole block will dilate over an asperity. There were, however several sources of error considered in the analysis of waviness amplitude, as follows:

1. All exposed surfaces occur where blocks have previously failed. If that failure involved shear movement along the plane, asperities on the surface may have already been degraded;
2. A high variability in measured amplitude was observed, which related to the surface area over which amplitude was measured. This may indicate, a) that there is a large-scale waviness which is captured in larger surfaces which is not reflected in smaller surfaces (which is known to be true), or b) that larger sampling areas increase the likelihood of encountering unusually large amplitudes. To reduce this scale effect, exposed surfaces larger than 50 m² were disregarded; and

3. Planes were fitted to segmented point clouds of the dominant joint set for that plane. In some cases gaps appeared in the point cloud where the plane normals of that point did not fit within the original set boundaries. This may reflect extreme waviness, an intersecting joint, or a rock bridge. Although this did not affect the measurement of amplitude, it did affect the calculation of dilation angles.

Peak dilation angles were measured by plotting the Hough Normals of each point within a joint surface on a stereonet, and defining the 95th percentile variability cone. Similar peak dilation angles were defined for each joint set, within the standard deviation for each set. The peak dilation angle showed some slight size bias, being larger on planes with a higher surface area. However, this was not as pronounced as for waviness amplitude.

The dilation angle was heavily influenced by voids in the segmented point cloud. If those “missing” points are included in the analysis, the scatter of normals increases drastically, increasing the dilation angle proportionally. From the defect planes inspected, voids were largely judged to be due to extreme waviness, with some rarer instances of intersecting joints. No rock bridges were directly observed. As all joint sets are sub-vertical and the direction of movement is likely sub-vertical, joint intersection is unlikely to cause significant dilation. Any rock bridges represented by the scatter would represent a cohesive component of shear strength and therefore would not be considered in calculations of dilation angle.

The defined parameters of each joint set were analysed in order to make comment on joint nature and formation. The joint sets were assessed to be regional in scale, of high persistence, and presented no termination against one another. They are judged to have formed in a state of near constant stress, with the primary stress direction being vertical from overburden weight. Assuming no horizontal regional stress, the minor and intermediate stresses may have been equal, both in the horizontal plane. The joints would therefore have been able to form perpendicular to the sub-horizontal bedding.

Uplift episodes, weathering, and erosion from the surface have created the current topography, where open joint sets can be observed often leading from diatremes at the top of the slope. It can be theorised that joint surfaces may be open either due to the dissolution of carbonate rocks through water movement, or from a reduction in lateral stress from removal or vertical burial loads.

The probabilistic properties of the defect sets were used to represent the aggregate characterization of the in-situ fracture system, using the program FracMan 7.70.

7.2 Shear Strength Reduction Analysis

A recent rockfall (Rockfall Area) was recreated in an effort to back-calculate the shear strength of defects at equilibrium. The reconstruction determined that the rockfall was likely initiated by the failure of Block 1, which presented as a mould somewhat undercut by an underlying thinly bedded zone. The failure of this block then undercut overlying blocks, which likely failed simply by falling. Frustratingly, this therefore meant that the only possible location for back-analysis from equilibrium was Block 1.

The program RS3 was used to build a geometry representative of the rock slope adjacent to Block 1, constructed from planes exported from CloudCompare. The joint surface was modelled as a planar approximation of the two joint surfaces (J2 and J3) defining the block. The planar approximation utilised an average of the two dilation angles measured directly from the joints (19.5°), and a base friction angle assumed from literature (30°). No cohesive component was considered, as there were no voids in the point cloud for either joint surface which would have indicated rock bridges were present.

The SSR analysis determined that the combined friction angles had been overestimated by 1.91° . It is possible that this result was due to factors such as incorrect block shape assumptions, surcharge loading, seismic loading, or water pressure. However, for the purposes of this thesis, it was considered that the required reduction value derives from an overestimation of the dilation angle. This then represents a reduction in 9.8% of the measured dilation angle, which was applied to mean peak dilation angles for each joint set.

7.3 Kinematic Analysis

Kinematic Analyses were undertaken for each domain, in order to define the dominant failure modes and their likelihood of failure. A basic assessment of kinematically possible failure mechanisms within each domain was undertaken in DIPS. This analysis considered the average slope orientation in each domain and used a scaled percentage of data points for each defect set, relative to the abundance of the joint set within that domain. The mean peak dilation angle of 18.8° was input, together with a base friction angle of 30° .

The basic DIPS analysis demonstrated a broad range of failure mechanisms within each domain. Toppling was the leading failure mechanism for all domains, having the highest relative percentage of kinematically admissible poles/intersections. Backwards, flexural and oblique toppling were particularly common. The dominance of toppling is not unexpected,

considering the sub-vertical jointing and pervasive base plane generated by the sub-horizontal bedding. Wedge sliding also had a high relative percentage of kinematically admissible intersections in Domains D1, D2 and D3. Planar sliding was kinematically possible for a moderate number of poles in Domain D1.

The RocScience software RocPlane, SWedge and RocTopple were used to analyse the probability of failure in domains for which planar sliding, wedge sliding and toppling respectively were considered to be likely (>10% of poles/intersections kinematically admissible). Geometric and joint set parameters were entered with probabilistic distributions, including slope orientation, joint orientation, spacing and waviness.

Table 7-3 summarises the percentage of poles/intersections which are kinematically admissible for each failure mode, compared with the probabilistic assessments.

Table 7-3: Summary of DIPS percentage of kinematically admissible poles/intersections, and probability of failure from RocPlane, SWedge and RocTopple.

	D1		D2		D3		D4	
	DIPS	PROB.	DIPS	PROB.	DIPS	PROB.	DIPS	PROB.
Planar Sliding	12.8%	24.9%	3.9%	-	6.9%	-	3.6%	-
Wedge Sliding	14.8%	1.9%	17.4%	2.4%	12.7%	4.7%	5.9%	-
Flexural Toppling	22.4%	3.3%	13.9%	11.4%	21.0%	22.9%	27.2%	16.0%
Direct Toppling	1.1%	4.8%	4.3%	14.2%	4.5%	24.5%	5.7%	14.0%
Base Plane Sliding	18.2%		12.9%		12.9%		11.0%	
Oblique Toppling	14.1%	-	16.3%	-	20.9%	-	24.3%	-
Backward Toppling	15.2%	-	20.6%	-	25.4%	-	30.0%	-

Planar sliding was only significant in Domain D1. RocPlane analysis indicated a 24.9% chance of planar sliding along Joint Set J2 within Domain D1. This analysis is not considered to appropriately reflect the likelihood of planar failure, as the method of analysis in RocPlane essentially assumes that joints of the set J2 will cross each other. The potential for planar sliding here likely reflects the statistical distribution of slope dip and joint dip, which gives the false impression that the two regularly cross. However, the likelihood of planar sliding is still considered high, due to slope geometry which would not be modelled in RocPlane. Where thinly bedded regions erode and undercutting occurs, joint surfaces further back in the slope may be exposed and can then fail in sliding. This is true for all domains with a dominant joint set (D1, D3, D4). The likelihood of failure in this situation cannot be calculated in RocPlane, as undercutting cannot be modelled.

SWedge analysis defined probabilities for wedge sliding failures of less than 5% for all domains. This is a surprising result, considering that although no mean plane intersections lay within the critical zone for wedge failure in the DIPS analysis, there was a high proportion of kinematically admissible intersections within the wedge sliding critical zone. It should be noted that the slope geometries input into SWedge cannot account for any undercutting, as is present on site (neither can DIPS). Where slope faces dip away from the slope, undercutting would act to shift the centre of gravity back into the slope while destabilising the toe of potential wedges, increasing the likelihood of wedge sliding. Conversely, where slope faces overhang, undercutting would act to further shift the centre of gravity away from the face, increasing the likelihood of toppling.

The inability of the RocScience suite to incorporate complex slope geometry also had a significant impact upon the RocTopple analysis. There were several issues in the RocTopple analysis which led to the results being considered questionable:

1. As a 2D program, RocTopple assumes that the slope face and joint set have the same strike. It is therefore unable to calculate the probability of oblique toppling;
2. RocTopple cannot consider joint sets which dip in the same direction as the slope face, and therefore cannot consider backwards toppling;
3. The probability of failure calculated in RocTopple does not report results that differentiate between base sliding/toppling and direct toppling for any cases other than the mean case;
4. RocTopple is not able to consider any overhanging slopes or undercutting; and
5. The probabilistic distribution for sub-vertical joints in RocTopple cannot consider fluctuations about the vertical where planes may dip in the opposite direction to the mean orientation – i.e., wrapped joint sets. This means that, for the sub-vertical sets within the study area, the calculation considers only one half of the data set.

The RocTopple analysis is based on a narrower dataset than was input into DIPS - a dataset which has a higher probability of kinematic admissibility. Considering this, the results of the RocTopple analysis are reasonable. Results generally return a lower percentage probability of failure (from RocTopple) than the percentage of kinematically admissible failures (from DIPS), for both flexural and direct (direct + base) toppling.

It is particularly difficult to define the dominant kinematic modes of failure due to the sub-vertical nature of all joint sets, and their scatter around vertical. The overhanging and undercut nature of the slope makes modelling in any simple 2D software inaccurate. This means that at best only a rough estimation of potential failure mechanisms can be gathered.

Visually, it is difficult to define whether the “stairway” geometry of the slope is due to direct toppling, or whether the overhanging nature of many faces is a reflection of flexural toppling. Many locations show two joint sets meeting approximately orthogonal to each other, with a sub-vertical intersection. This could reflect either wedge sliding, toppling of a wedge, or toppling along one joint set, with the other set simply acting as a release plane. Which failure mechanisms occur in a particular location depends essentially on the precise orientation of both the joint set in question and the slope face at that location.

From the visual geometry of the slope face, the kinematic DIPS analysis, and the probabilistic analysis, it is considered that flexural toppling is likely the dominant form of failure in most domains. However, backwards toppling, base plane sliding/toppling and wedge sliding are also present in significant proportions.

Whilst the probabilistic analysis does not accurately reflect the likelihood of potential failure mechanisms, the problem does not rest directly with either the data set or the analysis procedure. Rather, the data set would lend itself to a different kinematic and probabilistic methodology, capable of considering complex slope geometry and sub-vertical joint sets. This may include a 3D DEM analysis. The applied kinematic and probabilistic methodology would be appropriate for a dataset with a simple slope geometry and non-vertical joint sets.

7.4 Potential Future Works

Potential topics for future research may include the following:

- Higher resolution imaging, to allow a combined dataset where joint traces as well as surfaces could be considered;
- A statistical sensitivity analysis of measured spacing values, to account for errors due to waviness (on the small scale) and obstruction of joint surfaces (on the large scale). This could be achieved by defining percentage upper and lowerbound limits which could be applied to measured spacing data;
- Further investigation into the appropriateness of measuring defect surface amplitude using a mean orientation plane;
- Further investigation into the calculation of dilation angle from Hough Normals – how to define which points on the plane to consider where they may be voids in data. How to quantify the proportion of these voids;
- Attempts were made to import the imaged surface directly into RS3 for SSR analysis. However, the complexity of the mesh (even when reduced) was such that the model was not able to resolve in a timely manner. The idea behind this import

had been to directly model, in effect, the dilation angle, meaning that any reduction in shear strength should be applicable to the base friction angle only. Future studies could attempt this calculation, perhaps with a more powerful computer or program. It should be noted that this would not account for small-scale roughness, which the point cloud is not able to define;

- SSR calculations on additional blocks, in order to gather a statistically defensible dataset for dilation angle and base shear strength;
- Develop a 3D DEM model to appropriately reflect the geometric complexity of the slope face (both vertically and horizontally) and to determine the modes of failure in a more rigorous fashion;
- Quantification of the effect of wrapped sets on the probabilistic analyses undertaken in RocPlane, SWedge and RocTopple;
- RockFall backanalysis of fallen blocks in the Rockfall Area, and use of this analysis to then calculate the expected trajectory of potential future failures;
- Consideration of the effects of the diolines within the study area on introducing block stability;
- Consideration of the effects of weathering on joint set properties;
- Investigate the effect of surcharge loading from overlying blocks; and
- Investigate the possibility of seismic impacts on slope stability in this region.

Many of these potential future works would be best undertaken on a sub-set of the Study Area. This would allow for a more focused approach, where data could be rigorously interrogated, analysed and modelled.

8 Bibliography

- Anon., 2020. *Cloud Compare: 3D point cloud and mesh processing software*. [Online] Available at: <https://www.danielgm.net/cc/>
- Barton, N., 2012. Shear strength criteria for rock, rock joints, rockfill and rock masses: Problems and solutions. *Journal of Rock Mechanics and Geotechnical Engineering*, Volume 5, pp. 249-261.
- Barton, N. & Bandis, S., 1990. *Review of predictive capabilities of JRC-JCS model in engineering practice*. Rotterdam, Rock Joints; Proceedings of the International Symposium on Rock Joints.
- Barton, N. R. & Choubey, V., 1977. The shear strength of rock joints in theory and practice. *Rock Mechanics and Rock Engineering*, 10(1), pp. 1-54.
- Boulch, A. & Marlet, R., 2016. Deep learning for robust normal estimation in unstructured point clouds. *Eurographics Symposium on Geometry Processing*, 35(5).
- Brady, B. H. & Brown, E. T., 2005. *Rock Mechanics for Underground Mining*. 3 ed. Dordrecht: Springer Science.
- Devkota, K., 2019. *Characteristics of discontinuity spacing in a rock mass*. Tucson, Arizona, USA, s.n.
- Dewez, T., 2020. *Facets (plugin)*. [Online] Available at: [https://www.cloudcompare.org/doc/wiki/index.php?title=Facets_\(plugin\)](https://www.cloudcompare.org/doc/wiki/index.php?title=Facets_(plugin))
- Dewez, T. J., Girardeau-Montaut, D., Allanic, C. & Rohmer, J., 2016. Facets: A CloudCompare plugin to extract geological planes from unstructured 3D point clouds. *The International Archives of the Photogrammetry, Remote Sensing and Spatial Information Sciences*, pp. XLI-B5.
- Diederichs, M. S., 1990. *DIPS: An interactive and graphical approach to the analysis of orientation based data*, University of Toronto: Masters Thesis .
- Dong, X. et al., 2020. Reconstruction of Suröcial Rock Blocks by Means of Rock Structure Modelling of 3D TLS Point Clouds: The 2013 Long-Chang Rockfall. 53(671–689).
- Duncan, J. M., 1996. State of the art: Limit equilibrium and finite element analysis of slopes. *Journal of Geotechnical Engineering, ASCE*, Volume 122, pp. 577-596.
- Einstein, H. H., 1996. Risk and Risk Analysis in Rock Engineering. *Tunnelling and Underground Space Technology*, 11(2), pp. 141-155.
- Fabio, R., 2004. From point cloud to surface: the modelling and visualization problem. *International Archives of the Photogrammetry, Remote Sensing and Spatial Information Sciences*, Volume XXXIV-5/W10.
- Ghosh, S. et al., 2010. Rock slope instability assessment using spatially distributed structural orientation data in Darjeeling Himalaya (India). *Earth Surface Processes and Landforms*, Volume 35, pp. 1773-1792.
- Ghosh, S., Milad, B. & Ghosh, S. S., 2018. Origin and characterization of joints in sedimentary rocks: a review. *Petroleum and Petrochemical Engineering Journal*, 2(2), pp. 2578-4846.
- Gigli, G. & Casagli, N., 2011. Semi-automatic extraction of rock mass structural data from high resolution LIDAR point clouds. *International Journal of Rock Mechanics and Mining Sciences*, Volume 48, pp. 187-198.
- Goodman, R. E. & Bray, J. W., 1976. *Toppling of rock slopes*. Boulder, CO, American Society of Civil Engineers.

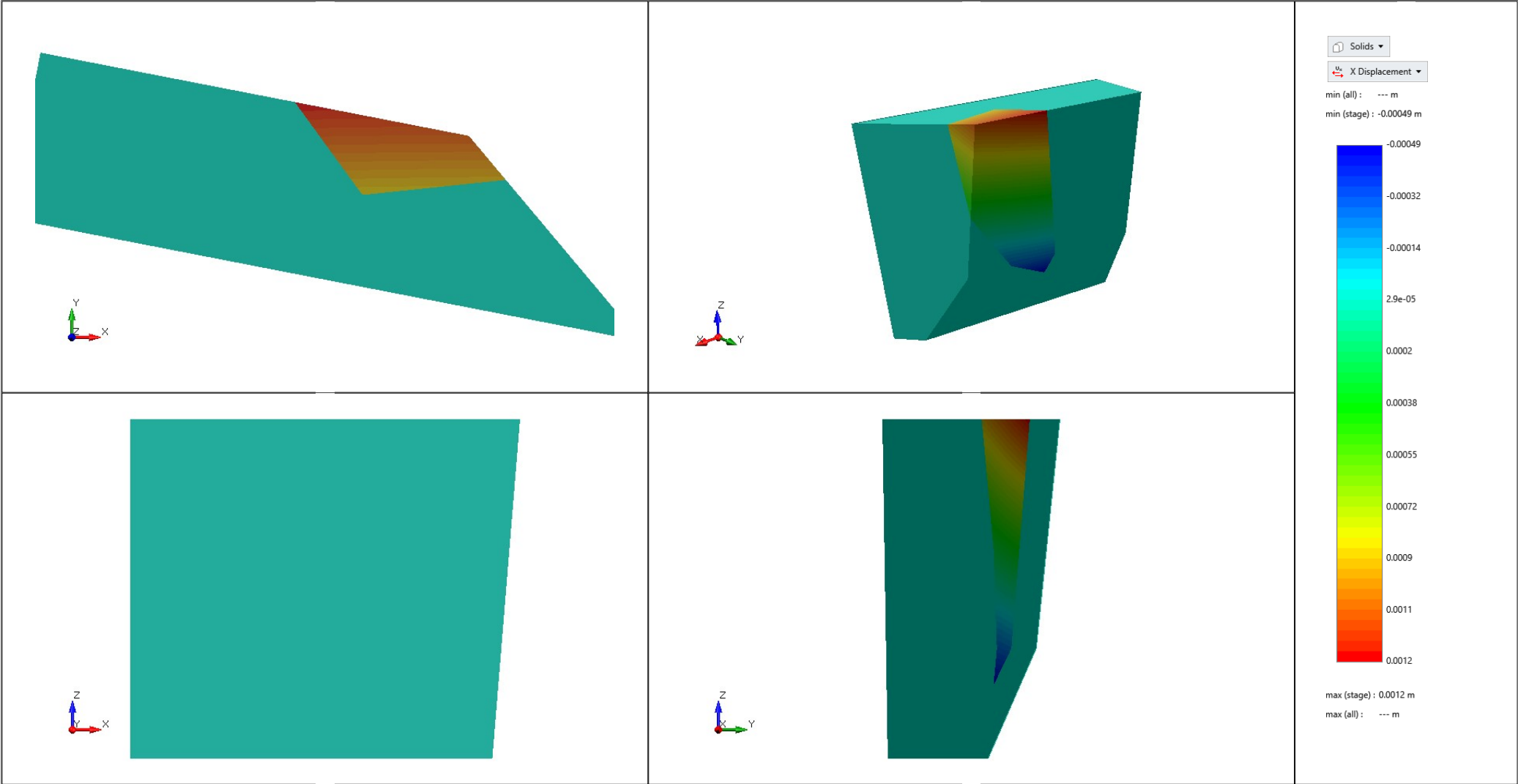
- Google Earth Pro, 2014-2020. *Shuangyan, Kaili Region, China, 7.3.3.7786* (64-bit): s.n.
- Grasselli, G. & Egger, P., 2003. Constitutive law for the shear strength of rock joints based on three-dimensional surface parameters. *International Journal of Rock Mechanics and Mining Sciences*, Volume 40, pp. 25-40.
- Gutiérrez, F., Parise, M., Waele, J. D. & Jourde, H., 2014. A review on natural and human-induced geohazards and impacts in karst. *Earth-Science Reviews*, Volume 138, pp. 61-88.
- Hammah, R. & Corkum, B., 2004. *Stability analysis of rock slopes using the finite element method*. Salzburg, Austria, EUROCK 2004 & 53rd Geomechanics Colloquium.
- Hammah, R. E., Yacoub, T., Corkum, B. & Curran, J. H., 2008. The Practical Modelling of Discontinuous Rock Masses with Finite Element Analysis. *American Rock Mechanics Association*, pp. 08-180.
- Hammah, R. E. et al., 2007. *Analysis of blocky rock slopes with finite element shear strength reduction analysis*. Vancouver, American Rock Mechanics Association.
- Hammah, R., Yacoub, T., Corkum, B. & Curran, J., 2005. *A comparison of finite element slope stability analysis with conventional limit-equilibrium investigation*. Saskatoon, Saskatchewan, Canada, Proceedings of the 58th Canadian Geotechnical and 6th Joint IAH-CNC and CGS Groundwater Specialty Conferences.
- Hencher, S. R., 1995. *Interpretation of direct shear tests on rock joints*. Reno, Nevada, American Rock Mechanics Association.
- Hencher, S. R. & Richards, L. R., 2015. Assessing the shear strength of rock discontinuities at laboratory and field scales. *Rock Mechanics and Rock Engineering*, Volume 48, pp. 883-905.
- Hoek, E. & Bray, J., 1977. *Rock Slope Engineering*. London: Institute of Mining and Metallurgy.
- Hoek, E., 2006. *Practical Rock Engineering*. 2 ed. Vancouver: Evert Hoek Consulting Engineer Inc..
- Hudson, J. A. & Harrison, J. P., 1997. *Engineering Rock Mechanics: An Introduction to the Principals*. London: Pergamon.
- Hudson, J. A. & Priest, S. D., 1979. Discontinuities and Rock Mass Geometry. *International Journal of Rock Mechanics, Mining Sciences & Geomechanics Abstracts*, Volume 16, pp. 339-362.
- Hudson, J. A. & Priest, S. D., 1983. Discontinuity frequency in rock masses. *International Journal of Rock Mechanics*, 20(2), pp. 73-89.
- Joshi, D., 2019. Here are the world's largest drone companies and manufacturers to watch and stocks to invest in 2020. *Business Insider*, 21 12, pp. <https://www.businessinsider.com/drone-manufacturers-companies-invest-stocks?r=AU&IR=T>.
- Kong, D., Wu, F. & Saroglou, C., 2020. Automatic identification and characterization of discontinuities in rock masses from 3D point clouds. *Engineering Geology*, Volume 265, p. 105442.
- Kulatilake, P. H. et al., 2003. Stochastic fracture geometry modelling in 3-D including validations for a part of Arrowhead East Tunnel, California, USA. *Engineering Geology*, Volume 70, pp. 131-155.
- Laux, D. & Henk, A., 2015. Terrestrial laser scanning and fracture network characterisation - Perspectives for a (semi-) automatic analysis of point cloud data from outcrops. *Zeitschrift der Deutschen Gesellschaft für Geowissenschaften*, Volume 10, pp. 1860-1804.

- Liu, Q., 2019. *Field Methods in Rock Mass Characterization*. TU Graz, s.n., pp. 1-18.
- Liu, Q., 2019. *Rock Mass Characterisation - Chapter 2: Basic Approaches*. TU Graz, Institute of Applied Geosciences.
- Liu, Q., 2020. *Modelling in Engineering Geology*. TU Graz, Institute of Applied Geosciences.
- Liu, Q. & Kaufmann, V., 2015. Integrated assessment of cliff rockfall hazards by means of rock structure modelling applied to TLS data: New developments. *Future Development of Rock Mechanics*, pp. 139-144.
- Li, Z. H., Dong, S. W. & Qu, H. J., 2014. Timing of the initiation of the Jurassic Yanshan movement on the North China Craton: evidence from sedimentary cycles, heavy minerals, geochemistry, and zircon U-Pb geochronology. *International Geology Review*, 56(3), pp. 288-312.
- Lu, Y., Liu, Q. & Zhang, F., 2013. Environmental characteristics of karst in China and their effect on engineering. *Carbonates Evaporites*, Volume 28, pp. 251-258.
- Lyman, G., Poropat, G. V. & Elmouttie, M., 2008. *Uncertainty in rock mass jointing characterisation*. Perth, Australian Centre for Geomechanics, pp. 419-432.
- Marcher, T. & Potsch, M., 2019. *220.102 Rock Mechanics and Tunnelling*. TU Graz, Institute of Rock Mechanics and Tunnelling.
- Morelli, G. L., 2014. On joint roughness: Measurements and use in rock mass characterization. *Geotechnical and Geological Engineering*, Volume 32, pp. 345-362.
- National Research Council, 1996. *Rock Fractures and Fluid Flow: Contemporary Understanding and Applications*. Washington DC: The National Academies Press.
- Noroozi, M., Kakaie, R. & Jalali, S. E., 2015. 3D Geometrical-stochastical modelling of rock mass joint networks: Case study of the right bank of Rudbar Lorestan Dam plant. *Journal of Geology and Mining Research*, 7(1), pp. 1-10.
- Norrish, N. I. & Wyllie, D. C., 1996. Chapter 15 - Rock Slope Stability Analysis. In: *Landslides: Investigation and Mitigation*. Washington DC: Transportation Research Board (National Research Council), pp. 391-425.
- Pahl, P. J., 1981. Estimating the mean length of discontinuity traces. *International Journal of Rock Mechanics, Mineral Science and Geomechanics*, Volume 18, pp. 221-228.
- Patton, F. D., 1966. *Multiple modes of shear failure in rock*. Lisbon, Proceeding of the 1st Congress of International Society of Rock Mechanics.
- Phoon, K.-K., 2019. The story of statistics in geotechnical engineering. *Georisk: Assessment and Management of Risk for Engineered Systems and Geohazards*, Volume 14:1, pp. 3-25.
- Poropat, G. V., 2009. *Measurement of surface roughness of rock discontinuities*. Toronto, Proceedings of the 3rd CANUS Rock Mechanics Symposium.
- Priest, S. D., 1985. *Hemispherical projection methods in rock mechanics*. 1 ed. London: Allen & Unwin.
- Priest, S. D., 1993. *Discontinuity Analysis for Rock Engineering*. Dordrecht: Springer.
- Riquelme, A. J., Abellán, A., Tomás, R. & Jaboyedoff, M., 2014. A new approach for semi-automatic rock mass joints recognition from 3D point clouds. *Computers & Geosciences*, Issue 68, pp. 38-52.
- RocScience, 2020. *Overview of Kinematic Analysis in DIPS*. [Online] Available at: https://www.rocsience.com/help/dips/dips/kinematic_analysis_overview.htm [Accessed 11 9 2020].

- RocScience, 2020. RS3. [Online]
Available at: <https://www.rocscience.com/software/rs3>
[Accessed 25 11 2020].
- Santo, A., Del Prete, S., Di Crescenzo, G. & Rotella, M., 2007. Karst processes and slope instability: some investigations in the carbonate Apennine of Campania (southern Italy). *Geological Society, London*, Volume 279, pp. 59-72.
- Sauro, U., 2003. Dolines and sinkholes: Aspects of evolution and problems of classification. *ACTA Carsol*, 32(2), pp. 4-52.
- Shigui, D., Yunjin, H., Xiaofei, H. & Xiao, G., 2011. Comparison between empirical estimation by JRC-JCS model and direct shear test for joint shear strength. *Journal of Earth Sciences*, 22(3), pp. 411-420.
- Singh, B. & Goel, R. K., 2012. *Engineering Rock Mass Classification: Tunnelling, Foundations and Landslides*. s.l.:Elsevier.
- Sturzenegger, M. & Stead, D., 2009. Close-range terrestrial digital photogrammetry and terrestrial laser scanning for discontinuity characterization on rock cuts. *Engineering Geology*, Issue 106, p. 163–182.
- Terzaghi, R. D., 1965. Sources of errors in joint surveys. *Geotechnique*, Volume 15, pp. 287-304.
- Thiele, S. T. et al., 2017. Rapid, semi-automatic fracture and contact mapping for point clouds, images and geophysical data. *Solid Earth*, Issue 8, p. 1241–1253.
- Thiele, S. T. et al., 2020. *Compass (plugin)*. [Online]
Available at:
[https://www.cloudcompare.org/doc/wiki/index.php?title=Compass_\(plugin\)#Introduction](https://www.cloudcompare.org/doc/wiki/index.php?title=Compass_(plugin)#Introduction)
- Thiele, S. T., Micklethwaite, S., Bourke, P. & Verrall, M., 2015. Insights into the mechanics of en-echelon sigmoidal vein formation using ultra-high resolution photogrammetry and computed tomography. *Journal of Structural Geology*, pp. 27-44.
- Turner, A. K., Slob, S. & Hack, H. R., 2006. Evaluation, and management of unstable rock slopes by 3D laser scanning. *International Association for Engineering Geology and the Environment*, pp. 1-11.
- Wang, X. & Mauldon, M., 2006. *Proportional errors of the Terzaghi correction factor*. Colorado, American Rock Mechanics Association, p. 1055.
- Wyllie, D. C. & Mah, C. W., 2004. *Rock Slope Engineering: Civil and Mining*. 4 ed. New York: Spoon Press.
- Yuan, D. X., Li, B. & Liu, Z. H., 1995. Karst in China. *Episodes*, 18(1), pp. 62-65.
- Zhang, L. & Einstein, H. H., 1998. Estimating the mean trace length of rock discontinuities. *Rock Mechanics and Rock Engineering*, 31(4), pp. 217-235.
- Zhang, P. et al., 2019. 3D mapping of discontinuity traces using fusion of point cloud and image data. *Bulletin of Engineering Geology and the Environment*, Volume 78, pp. 2789-2801.
- Zhao, H. J., Ma, F. S. & Guo, J., 2012. Regularity and formation mechanisms of large-scale abrupt karst collapse in southern China in the first half of 2010. *Natural Hazards*, Volume 60, pp. 1037-1054.

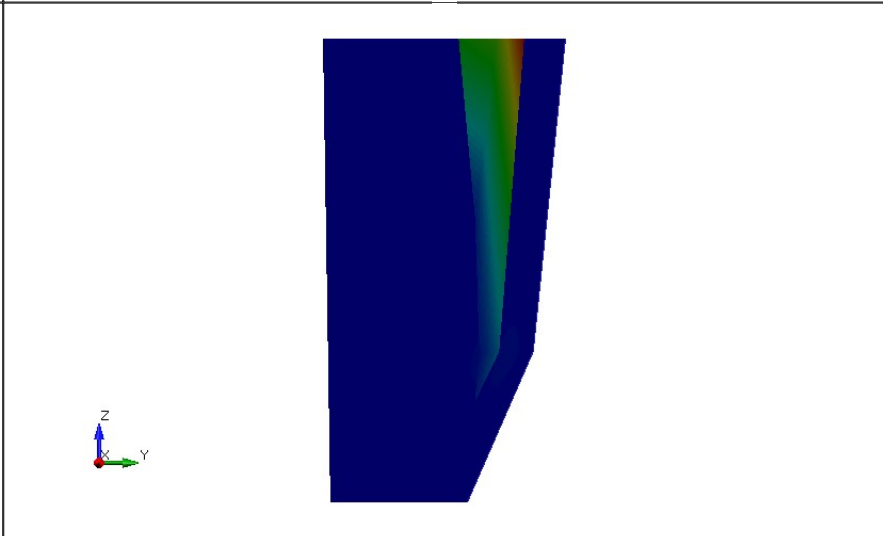
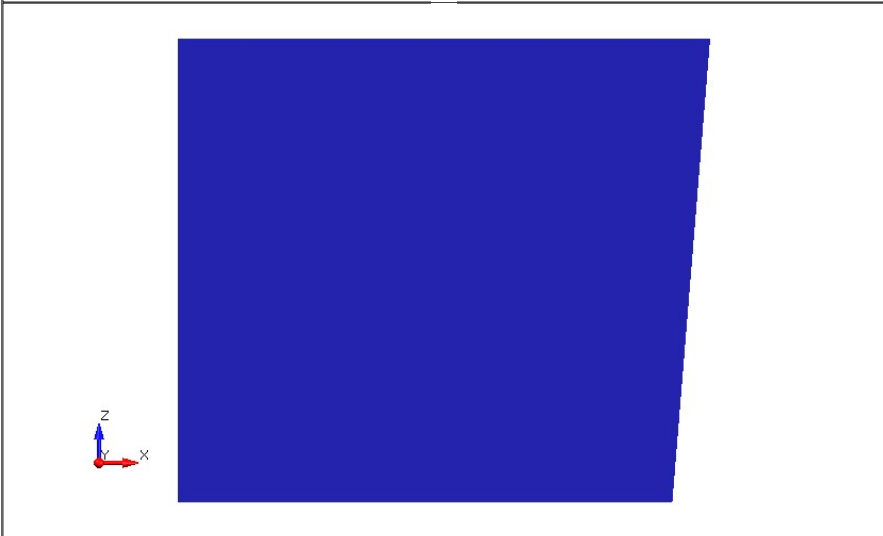
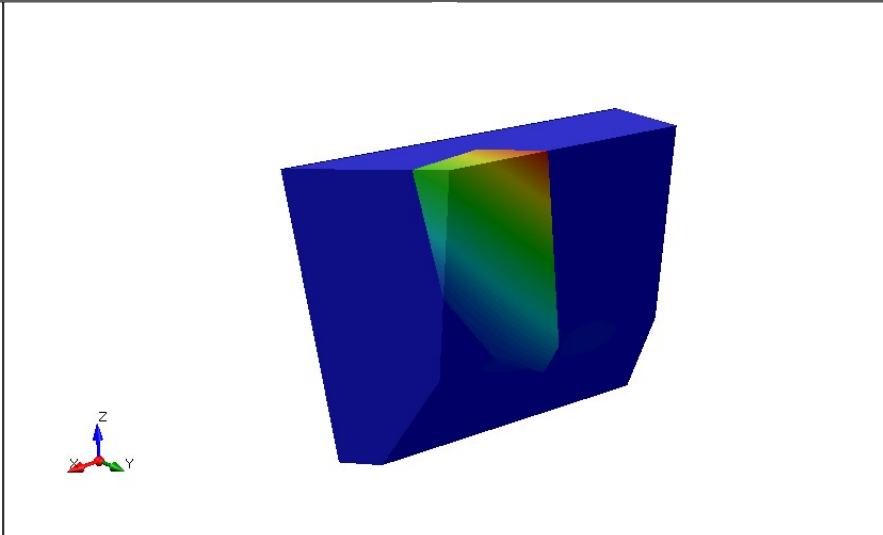
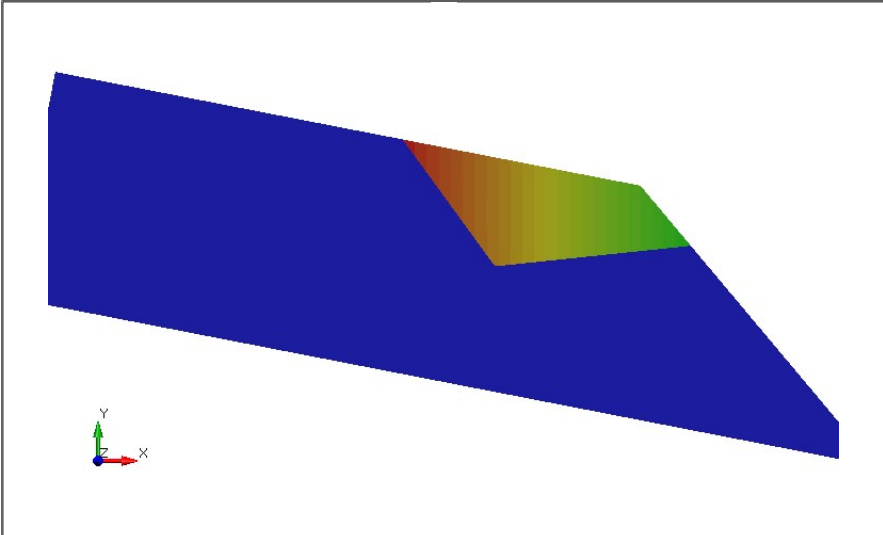
Appendix A – RS3 SSR Analysis

Project1 - Stage 1 - X Displacement



<i>Project</i>	Project1		
<i>Author</i>		<i>Company</i>	
<i>Date</i>	November 26 2020, 05:50 AM	<i>File Name</i>	Block_1_Planes.rs3v3
<i>Analysis</i>			

Project1 - Stage 1 - Y Displacement



Solids ▾

Y Displacement ▾

min (all) : --- m

min (stage) : 0 m

0

0.00017

0.00035

0.00052

0.0007

0.00087

0.001

0.0012

0.0014

0.0016

0.0017

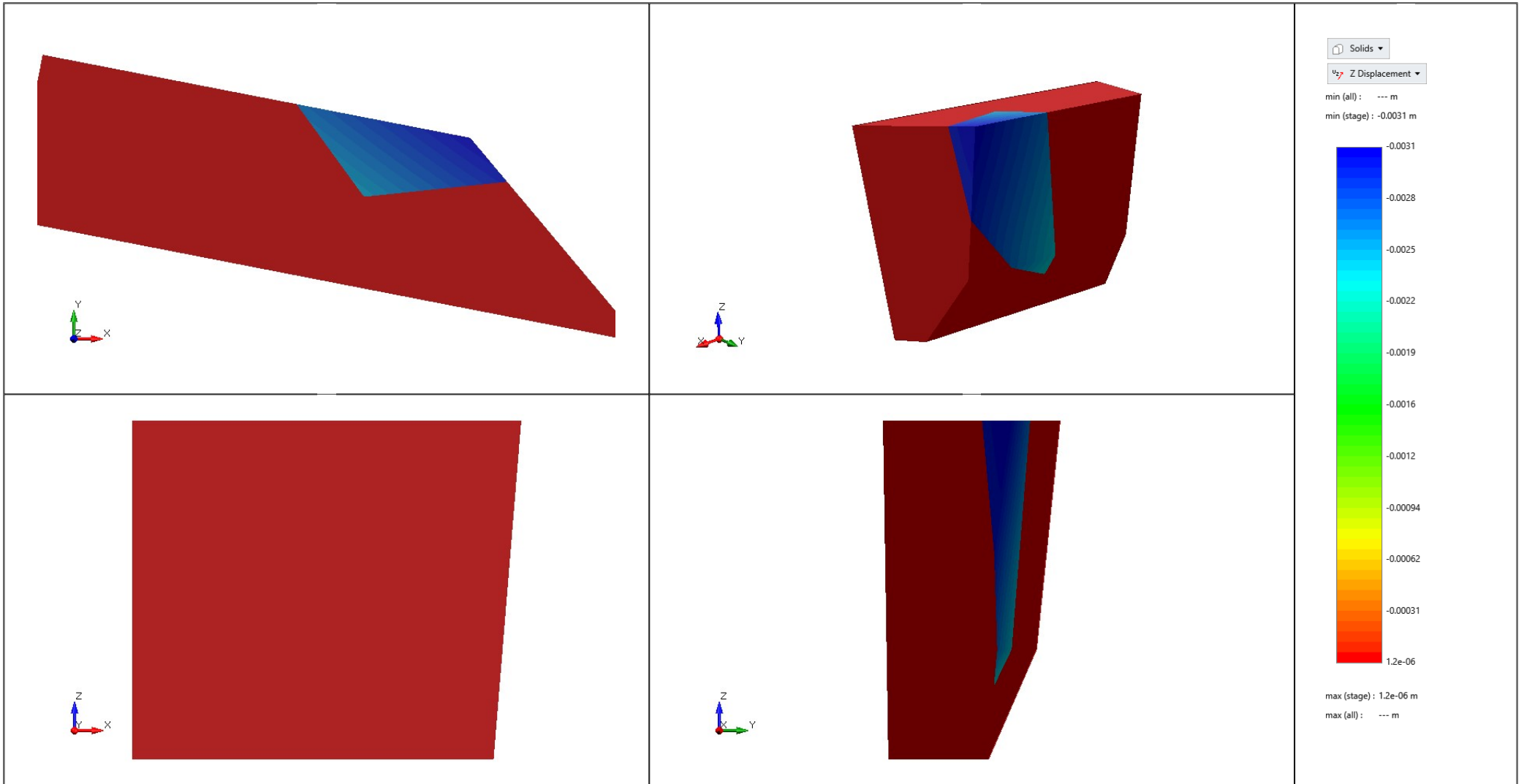
max (stage) : 0.0017 m

max (all) : --- m



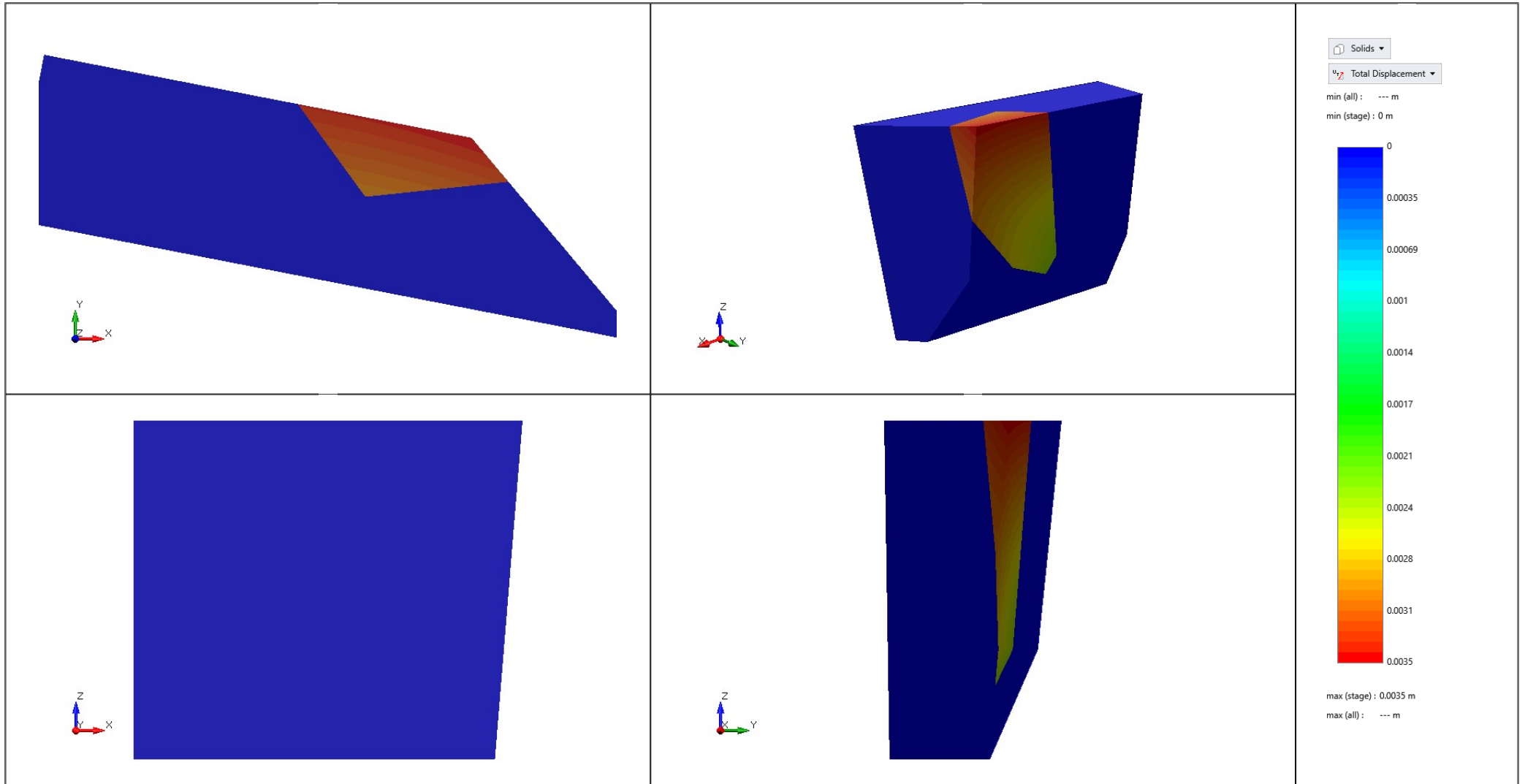
<i>Project</i>	Project1		
<i>Author</i>		<i>Company</i>	
<i>Date</i>	November 26 2020, 05:50 AM	<i>File Name</i>	Block_1_Planes.rs3v3
<i>Analysis</i>			

Project1 - Stage 1 - Z Displacement



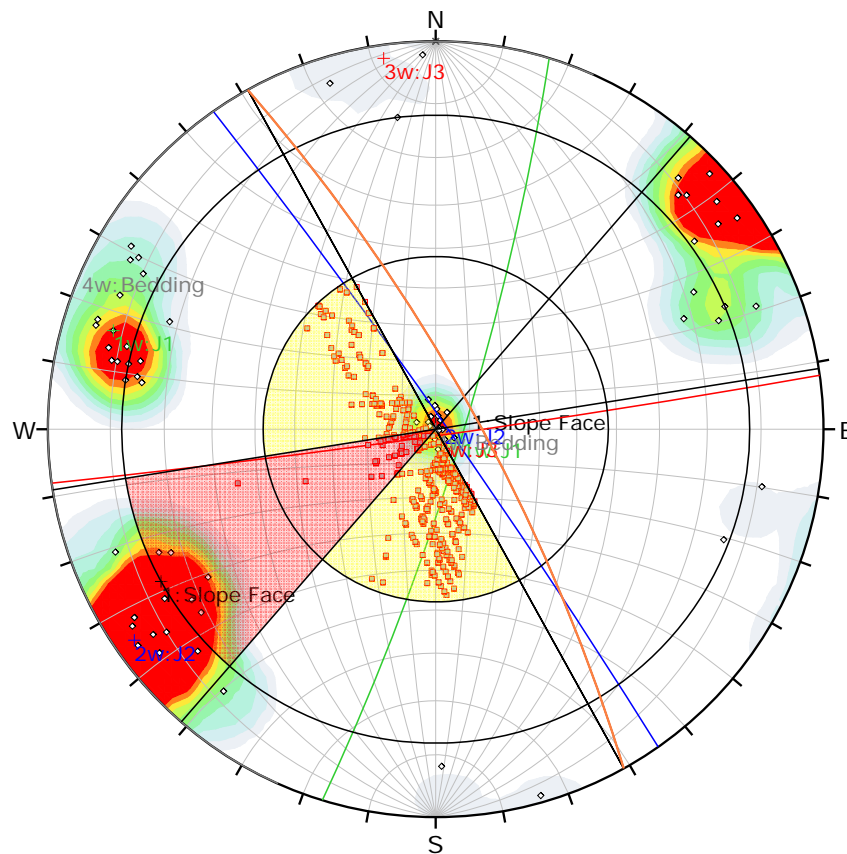
<i>Project</i>	Project1		
<i>Author</i>		<i>Company</i>	
<i>Date</i>	November 26 2020, 05:50 AM	<i>File Name</i>	Block_1_Planes.rs3v3
<i>Analysis</i>			

Project1 - Stage 1 - Total Displacement



<i>Project</i>	Project1		
<i>Author</i>		<i>Company</i>	
<i>Date</i>	November 26 2020, 05:50 AM	<i>File Name</i>	Block_1_Planes.rs3v3
<i>Analysis</i>			

Appendix B – DIPS Kinematic Analysis



Symbol	Feature
◇	Pole Vectors
■	Critical Intersection

Color	Density Concentrations
	0.00 - 1.00
	1.00 - 2.00
	2.00 - 3.00
	3.00 - 4.00
	4.00 - 5.00
	5.00 - 6.00
	6.00 - 7.00
	7.00 - 8.00
	8.00 - 9.00
	9.00 <

Contour Data	Pole Vectors
Maximum Density	23.85%
Contour Distribution	Fisher
Counting Circle Size	1.0%

Kinematic Analysis	Direct Toppling
Slope Dip	78
Slope Dip Direction	61
Friction Angle	48°
Lateral Limits	20°

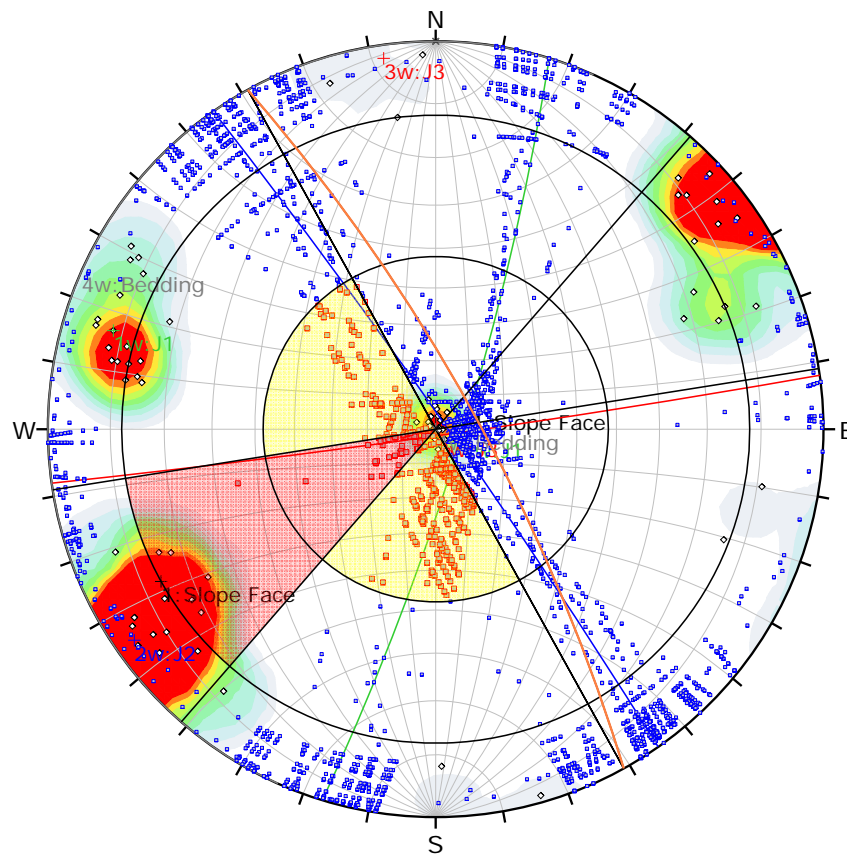
Weighted Results	Critical	Total	%
Direct Toppling (Intersection)	120	11110	1.08%
Oblique Toppling (Intersection)	1564	11110	14.08%
Base Plane (All)	27	151	18.15%
Base Plane (Set 2: J2)	19	97	19.92%
Base Plane (Set 4: Bedding)	8	20	40.00%

Color	Dip	Dip Direction	Label
User Planes			
1	78	61	Slope Face
Mean Set Planes			
1w	82	107	J1
2w	87	55	J2
3w	88	172	J3
4w	0	294	Bedding

Plot Mode	Pole Vectors
Vector Count (Weighted)	151 (75 Entries)
Terzaghi Weighting	Minimum Bias Angle 15°
Intersection Mode	Grid Data Planes
Intersections Count (Weighted)	11110
Hemisphere	Lower
Projection	Equal Angle



Project	Kinematic Analysis for D1		
Analysis Description	Direct Toppling		
Drawn By	Kara Stariha	Company	
Date	27/08/2020, 2:08:20 PM	File Name	Kinematic_D1_Wrapped_Scaled_20201104.dips8



Symbol	Feature
◇	Pole Vectors
■	Critical Intersection
■	Intersection

Color	Density Concentrations
	0.00 - 1.00
	1.00 - 2.00
	2.00 - 3.00
	3.00 - 4.00
	4.00 - 5.00
	5.00 - 6.00
	6.00 - 7.00
	7.00 - 8.00
	8.00 - 9.00
	9.00 <

Contour Data	Pole Vectors
Maximum Density	23.85%
Contour Distribution	Fisher
Counting Circle Size	1.0%

Kinematic Analysis	Direct Toppling
Slope Dip	78
Slope Dip Direction	61
Friction Angle	48°
Lateral Limits	20°

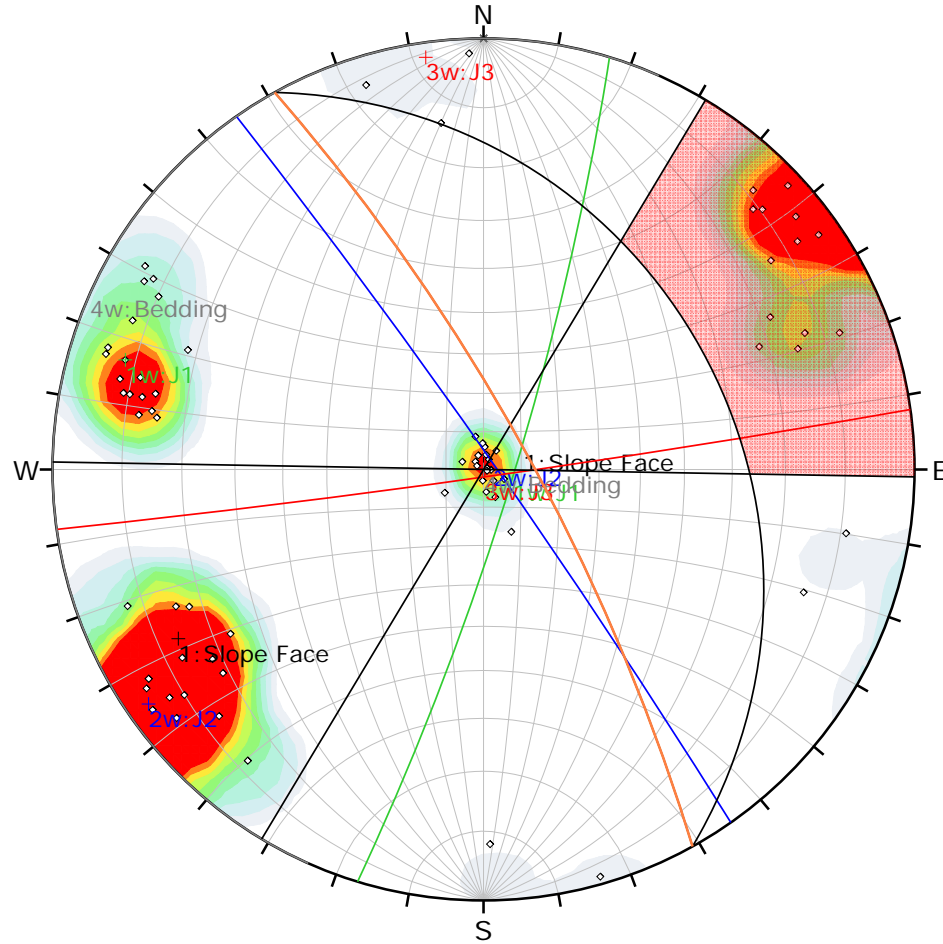
Weighted Results	Critical	Total	%
Direct Toppling (Intersection)	120	11110	1.08%
Oblique Toppling (Intersection)	1564	11110	14.08%
Base Plane (All)	27	151	18.15%
Base Plane (Set 2: J2)	19	97	19.92%
Base Plane (Set 4: Bedding)	8	20	40.00%

	Color	Dip	Dip Direction	Label
User Planes				
1	■	78	61	Slope Face
Mean Set Planes				
1w	■	82	107	J1
2w	■	87	55	J2
3w	■	88	172	J3
4w	■	0	294	Bedding

Plot Mode	Pole Vectors
Vector Count (Weighted)	151 (75 Entries)
Terzaghi Weighting	Minimum Bias Angle 15°
Intersection Mode	Grid Data Planes
Intersections Count (Weighted)	11110
Hemisphere	Lower
Projection	Equal Angle



Project	Kinematic Analysis for D1		
Analysis Description	Direct Toppling		
Drawn By	Kara Stariha	Company	
Date	27/08/2020, 2:08:20 PM	File Name	Kinematic_D1_Wrapped_Scaled_20201104.dips8



Symbol	Feature
◇	Pole Vectors

Color	Density Concentrations
	0.00 - 1.00
	1.00 - 2.00
	2.00 - 3.00
	3.00 - 4.00
	4.00 - 5.00
	5.00 - 6.00
	6.00 - 7.00
	7.00 - 8.00
	8.00 - 9.00
	9.00 <


Contour Data	Pole Vectors
Maximum Density	23.85%
Contour Distribution	Fisher
Counting Circle Size	1.0%

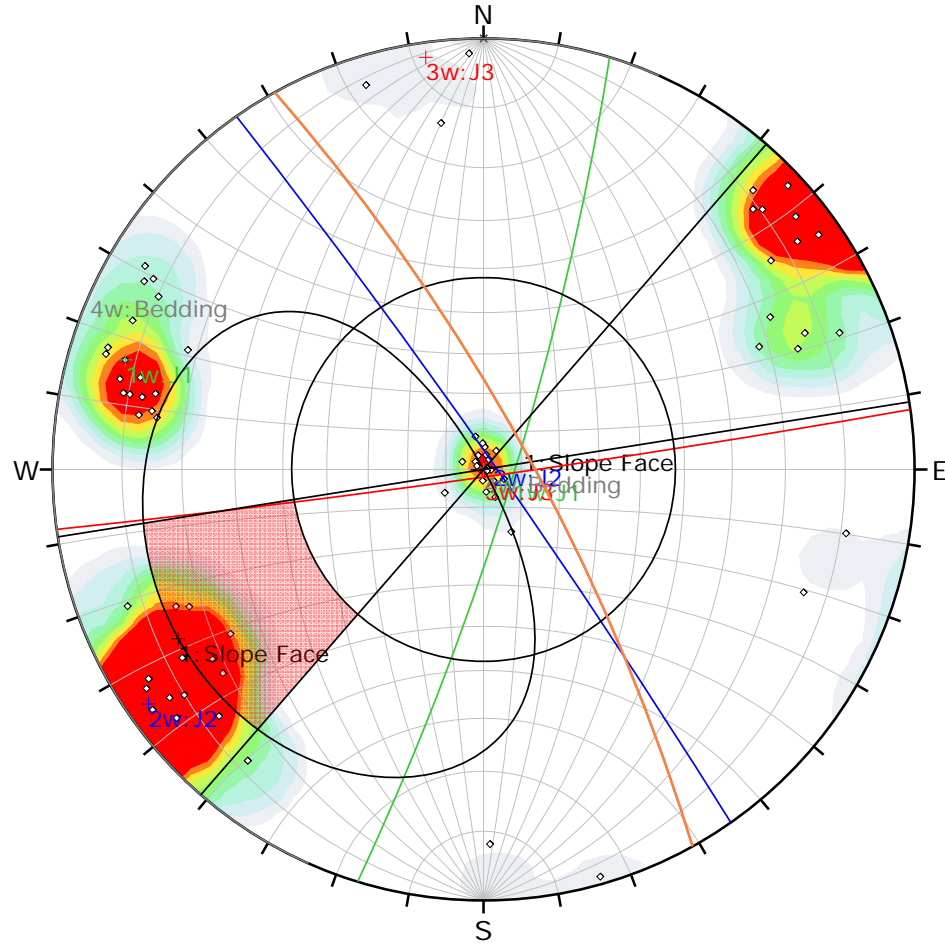
Kinematic Analysis	Flexural Toppling
Slope Dip	78
Slope Dip Direction	61
Friction Angle	48°
Lateral Limits	30°

Weighted Results	Critical	Total	%
Flexural Toppling (All)	34	151	22.36%
Flexural Toppling (Set 2: J2)	34	97	34.70%

	Color	Dip	Dip Direction	Label
User Planes				
1	■	78	61	Slope Face
Mean Set Planes				
1w	■	82	107	J1
2w	■	87	55	J2
3w	■	88	172	J3
4w	■	0	294	Bedding

Plot Mode	Pole Vectors
Vector Count (Weighted)	151 (75 Entries)
Terzaghi Weighting	Minimum Bias Angle 15°
Hemisphere	Lower
Projection	Equal Angle

	Project	Kinematic Analysis for D1	
	Analysis Description	Flexural Toppling	
	Drawn By	Kara Stariha	Company
	Date	27/08/2020, 2:08:20 PM	File Name



Symbol	Feature
◇	Pole Vectors


Color	Density Concentrations	
		0.00
	1.00	- 2.00
	2.00	- 3.00
	3.00	- 4.00
	4.00	- 5.00
	5.00	- 6.00
	6.00	- 7.00
	7.00	- 8.00
	8.00	- 9.00
	9.00	<

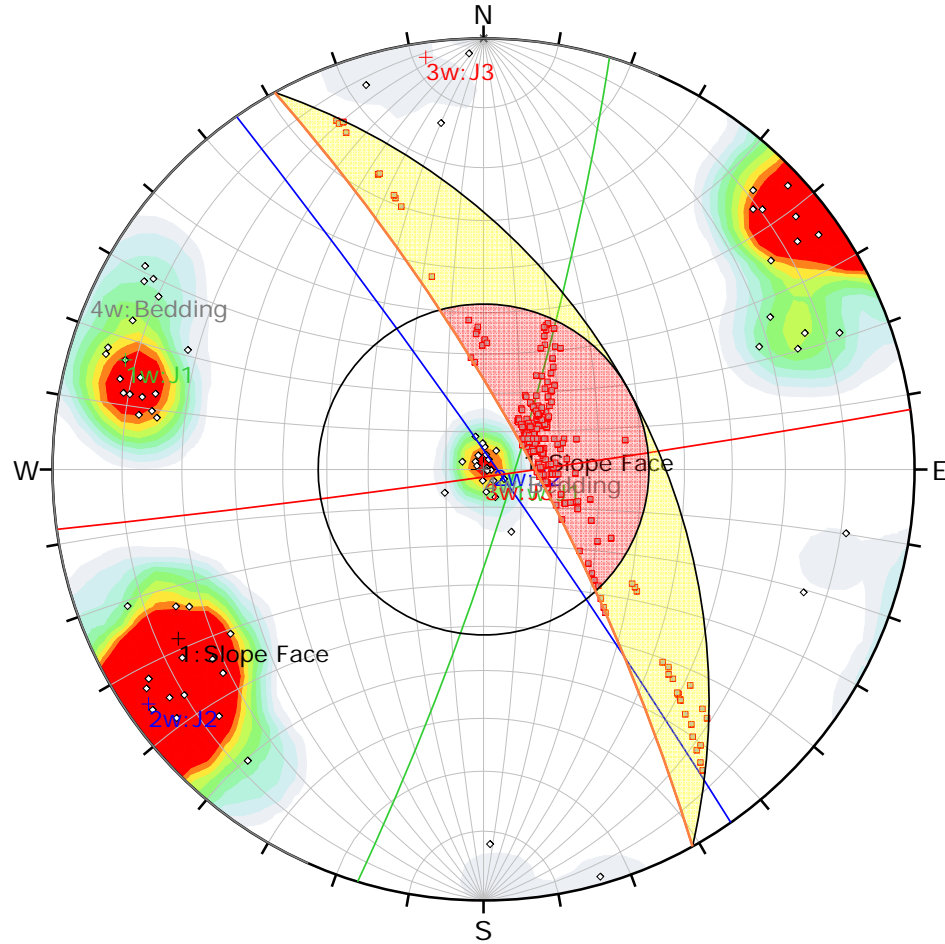
Contour Data	Pole Vectors
Maximum Density	23.85%
Contour Distribution	Fisher
Counting Circle Size	1.0%

Kinematic Analysis	Planar Sliding		
Slope Dip	78		
Slope Dip Direction	61		
Friction Angle	48°		
Lateral Limits	20°		
Weighted Results	Critical	Total	%
Planar Sliding (All)	19	151	12.83%
Planar Sliding (Set 2: J2)	19	97	19.92%

	Color	Dip	Dip Direction	Label
User Planes				
1	■	78	61	Slope Face
Mean Set Planes				
1w	■	82	107	J1
2w	■	87	55	J2
3w	■	88	172	J3
4w	■	0	294	Bedding

Plot Mode	Pole Vectors
Vector Count (Weighted)	151 (75 Entries)
Terzaghi Weighting	Minimum Bias Angle 15°
Hemisphere	Lower
Projection	Equal Angle

	<i>Project</i>	Kinematic Analysis for D1		
	<i>Analysis Description</i>	Planar Sliding		
	<i>Drawn By</i>	Kara Stariha	<i>Company</i>	
	<i>Date</i>	27/08/2020, 2:08:20 PM	<i>File Name</i>	Kinematic_D1_Wrapped_Scaled_20201104.dips8



Symbol	Feature
◇	Pole Vectors
■	Critical Intersection


Color	Density Concentrations
	0.00 - 1.00
	1.00 - 2.00
	2.00 - 3.00
	3.00 - 4.00
	4.00 - 5.00
	5.00 - 6.00
	6.00 - 7.00
	7.00 - 8.00
	8.00 - 9.00
	9.00 <

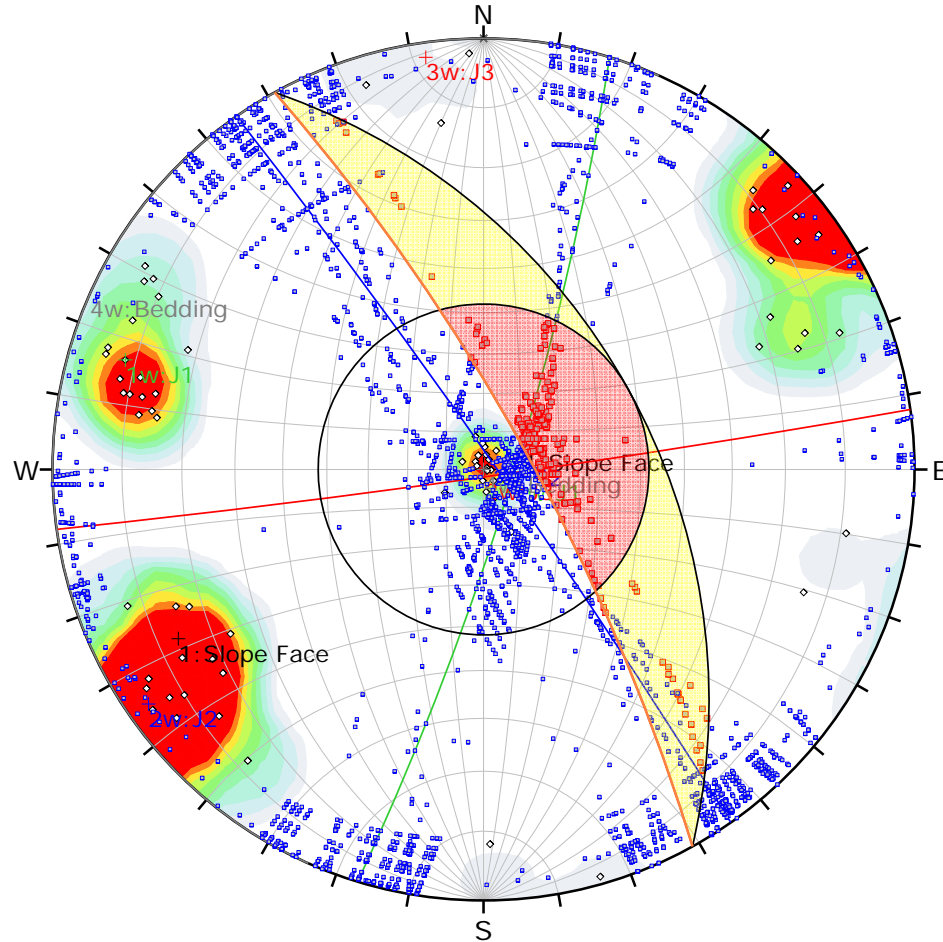
Contour Data	Pole Vectors
Maximum Density	23.85%
Contour Distribution	Fisher
Counting Circle Size	1.0%

Kinematic Analysis	Wedge Sliding		
Slope Dip	78		
Slope Dip Direction	61		
Friction Angle	48°		
Weighted Results	Critical	Total	%
Wedge Sliding	1646	11110	14.82%

	Color	Dip	Dip Direction	Label
User Planes				
1	■	78	61	Slope Face
Mean Set Planes				
1w	■	82	107	J1
2w	■	87	55	J2
3w	■	88	172	J3
4w	■	0	294	Bedding

Plot Mode	Pole Vectors
Vector Count (Weighted)	151 (75 Entries)
Terzaghi Weighting	Minimum Bias Angle 15°
Intersection Mode	Grid Data Planes
Intersections Count (Weighted)	11110
Hemisphere	Lower
Projection	Equal Angle

	<i>Project</i>	Kinematic Analysis for D1	
	<i>Analysis Description</i>	Wedge Sliding	
	<i>Drawn By</i>	Kara Stariha	<i>Company</i>
	<i>Date</i>	27/08/2020, 2:08:20 PM	<i>File Name</i>



Symbol	Feature
◇	Pole Vectors
■	Critical Intersection
□	Intersection


Color	Density Concentrations
	0.00 - 1.00
	1.00 - 2.00
	2.00 - 3.00
	3.00 - 4.00
	4.00 - 5.00
	5.00 - 6.00
	6.00 - 7.00
	7.00 - 8.00
	8.00 - 9.00
	9.00 <

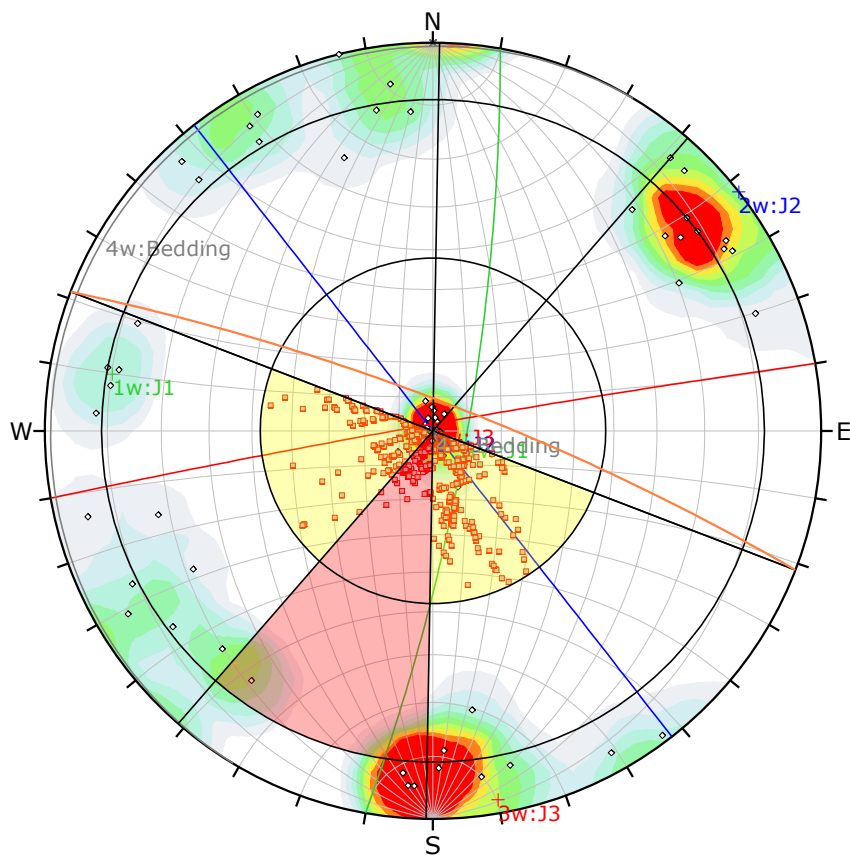
Contour Data	Pole Vectors
Maximum Density	23.85%
Contour Distribution	Fisher
Counting Circle Size	1.0%

Kinematic Analysis	Wedge Sliding		
Slope Dip	78		
Slope Dip Direction	61		
Friction Angle	48°		
Weighted Results	Critical	Total	%
Wedge Sliding	1646	11110	14.82%

	Color	Dip	Dip Direction	Label
User Planes				
1	■	78	61	Slope Face
Mean Set Planes				
1w	■	82	107	J1
2w	■	87	55	J2
3w	■	88	172	J3
4w	■	0	294	Bedding

Plot Mode	Pole Vectors
Vector Count (Weighted)	151 (75 Entries)
Terzaghi Weighting	Minimum Bias Angle 15°
Intersection Mode	Grid Data Planes
Intersections Count (Weighted)	11110
Hemisphere	Lower
Projection	Equal Angle

	<i>Project</i>	Kinematic Analysis for D1	
	<i>Analysis Description</i>	Wedge Sliding	
	<i>Drawn By</i>	Kara Stariha	<i>Company</i>
	<i>Date</i>	27/08/2020, 2:08:20 PM	<i>File Name</i>



Symbol	Feature
◇	Pole Vectors
■	Critical Intersection

Color	Density Concentrations
	0.00 - 1.00
	1.00 - 2.00
	2.00 - 3.00
	3.00 - 4.00
	4.00 - 5.00
	5.00 - 6.00
	6.00 - 7.00
	7.00 - 8.00
	8.00 - 9.00
	9.00 <


Contour Data	Pole Vectors
Maximum Density	15.43%
Contour Distribution	Fisher
Counting Circle Size	1.0%

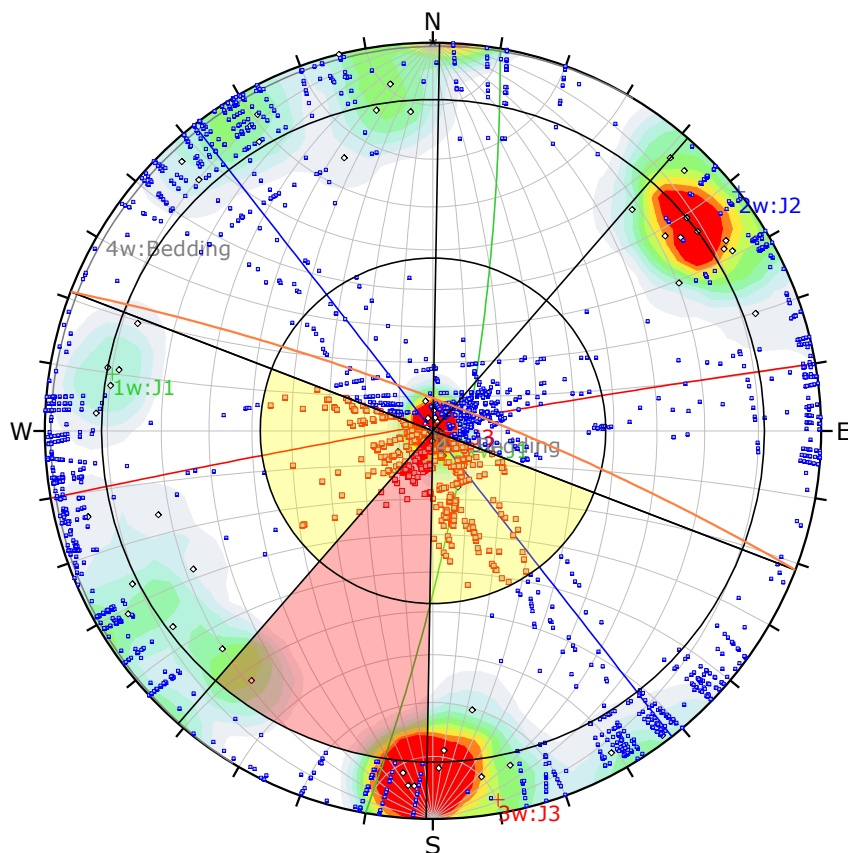
Kinematic Analysis	Direct Toppling
Slope Dip	81
Slope Dip Direction	21
Friction Angle	48°
Lateral Limits	20°

Weighted Results	Critical	Total	%
Direct Toppling (Intersection)	209	4877	4.28%
Oblique Toppling (Intersection)	794	4877	16.28%
Base Plane (All)	13	100	12.90%
Base Plane (Set 2: J2)	4	36	10.65%
Base Plane (Set 4: Bedding)	9	20	45.00%

	Color	Dip	Dip Direction	Label
Mean Set Planes				
1w	■	80	100	J1
2w	■	90	232	J2
3w	■	88	350	J3
4w	■	1	301	Bedding

Plot Mode	Pole Vectors
Vector Count (Weighted)	100 (65 Entries)
Terzaghi Weighting	Minimum Bias Angle 15°
Intersection Mode	Grid Data Planes
Intersections Count (Weighted)	4877
Hemisphere	Lower
Projection	Equal Angle

	<i>Project</i>	Kinematic Analysis for D2	
	<i>Analysis Description</i>	Direct Toppling	
	<i>Drawn By</i>	Kara Stariha	<i>Company</i>
	<i>Date</i>	27/08/2020, 2:08:20 PM	<i>File Name</i>



Symbol	Feature
◇	Pole Vectors
■	Critical Intersection
■	Intersection

Color	Density Concentrations
	0.00 - 1.00
	1.00 - 2.00
	2.00 - 3.00
	3.00 - 4.00
	4.00 - 5.00
	5.00 - 6.00
	6.00 - 7.00
	7.00 - 8.00
	8.00 - 9.00
	9.00 <

Contour Data	Pole Vectors
Maximum Density	15.43%
Contour Distribution	Fisher
Counting Circle Size	1.0%

Kinematic Analysis	Direct Toppling
Slope Dip	81
Slope Dip Direction	21
Friction Angle	48°
Lateral Limits	20°

Weighted Results	Critical	Total	%
Direct Toppling (Intersection)	209	4877	4.28%
Oblique Toppling (Intersection)	794	4877	16.28%
Base Plane (All)	13	100	12.90%
Base Plane (Set 2: J2)	4	36	10.65%
Base Plane (Set 4: Bedding)	9	20	45.00%

	Color	Dip	Dip Direction	Label
Mean Set Planes				
1w	■	80	100	J1
2w	■	90	232	J2
3w	■	88	350	J3
4w	■	1	301	Bedding

Plot Mode	Pole Vectors
Vector Count (Weighted)	100 (65 Entries)
Terzaghi Weighting	Minimum Bias Angle 15°
Intersection Mode	Grid Data Planes
Intersections Count (Weighted)	4877
Hemisphere	Lower
Projection	Equal Angle



Project

Kinematic Analysis for D2

Analysis Description

Direct Toppling

Drawn By

Kara Stariha

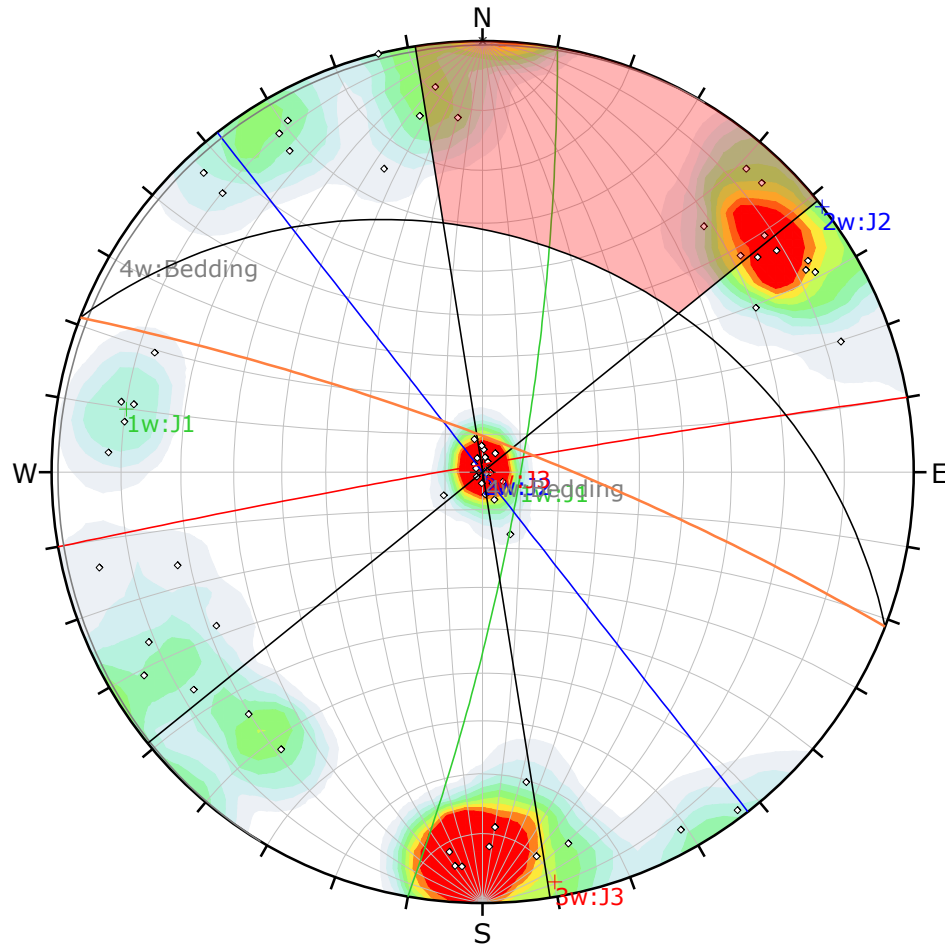
Company

Date

27/08/2020, 2:08:20 PM

File Name

Kinematic_D2_Wrapped_Scaled_20201104.dips8



Symbol	Feature
◇	Pole Vectors

Color	Density Concentrations
	0.00 - 1.00
	1.00 - 2.00
	2.00 - 3.00
	3.00 - 4.00
	4.00 - 5.00
	5.00 - 6.00
	6.00 - 7.00
	7.00 - 8.00
	8.00 - 9.00
	9.00 <


Contour Data	Pole Vectors
Maximum Density	15.43%
Contour Distribution	Fisher
Counting Circle Size	1.0%

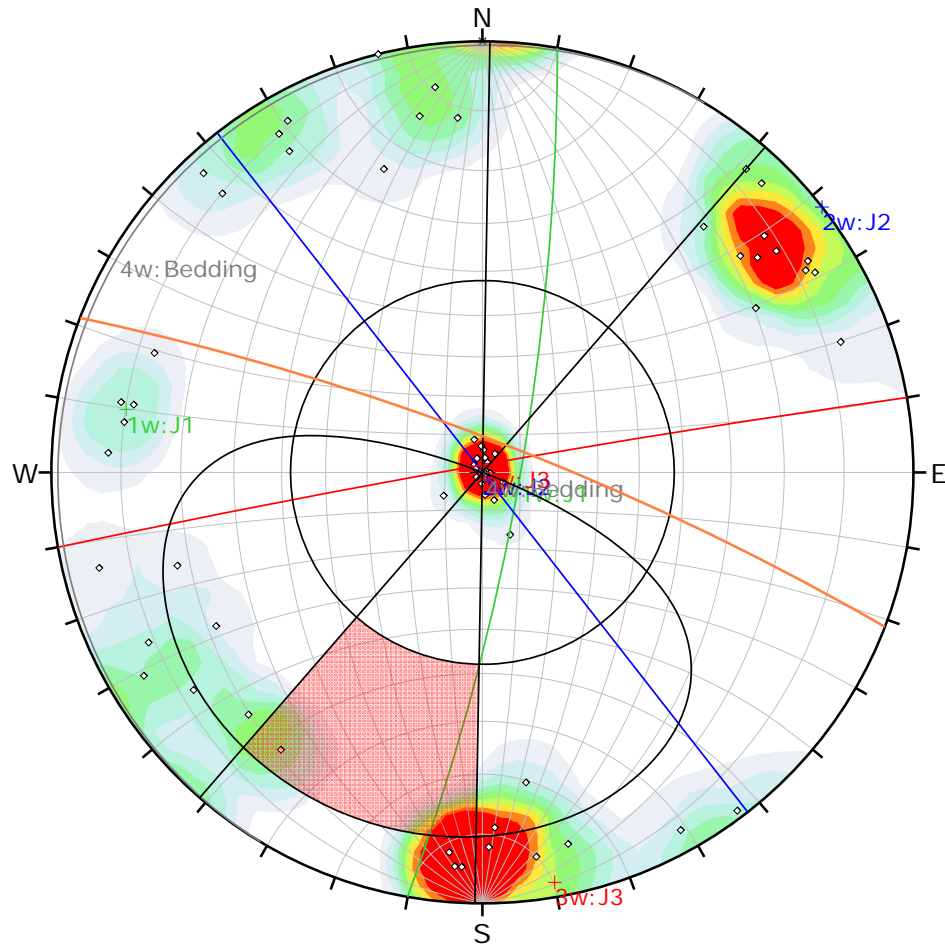
Kinematic Analysis	Flexural Toppling
Slope Dip	81
Slope Dip Direction	21
Friction Angle	48°
Lateral Limits	30°

Weighted Results	Critical	Total	%
Flexural Toppling (All)	14	100	13.86%
Flexural Toppling (Set 2: J2)	10	36	27.78%
Flexural Toppling (Set 3: J3)	4	38	9.76%

	Color	Dip	Dip Direction	Label
Mean Set Planes				
1w	Green	80	100	J1
2w	Blue	90	232	J2
3w	Red	88	350	J3
4w	Grey	1	301	Bedding

Plot Mode	Pole Vectors
Vector Count (Weighted)	100 (65 Entries)
Terzaghi Weighting	Minimum Bias Angle 15°
Hemisphere	Lower
Projection	Equal Angle

	<i>Project</i>	Kinematic Analysis for D2	
	<i>Analysis Description</i>	Flexural Toppling	
	<i>Drawn By</i>	Kara Stariha	<i>Company</i>
	<i>Date</i>	27/08/2020, 2:08:20 PM	<i>File Name</i>



Symbol	Feature
◇	Pole Vectors

Color	Density Concentrations
	0.00 - 1.00
	1.00 - 2.00
	2.00 - 3.00
	3.00 - 4.00
	4.00 - 5.00
	5.00 - 6.00
	6.00 - 7.00
	7.00 - 8.00
	8.00 - 9.00
	9.00 <


Contour Data	Pole Vectors
Maximum Density	15.43%
Contour Distribution	Fisher
Counting Circle Size	1.0%

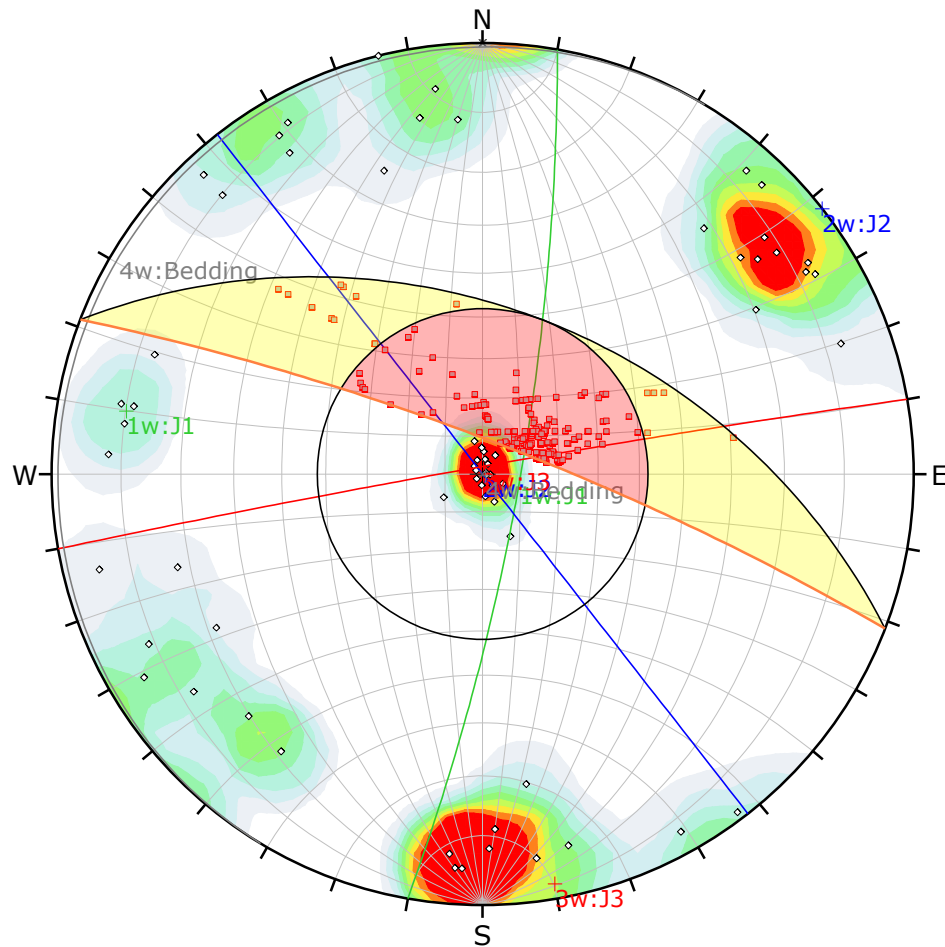
Kinematic Analysis	Planar Sliding
Slope Dip	81
Slope Dip Direction	21
Friction Angle	48°
Lateral Limits	20°

Weighted Results	Critical	Total	%
Planar Sliding (All)	4	100	3.88%
Planar Sliding (Set 2: J2)	4	36	10.65%

	Color	Dip	Dip Direction	Label
Mean Set Planes				
1w	■	80	100	J1
2w	■	90	232	J2
3w	■	88	350	J3
4w	■	1	301	Bedding

Plot Mode	Pole Vectors
Vector Count (Weighted)	100 (65 Entries)
Terzaghi Weighting	Minimum Bias Angle 15°
Hemisphere	Lower
Projection	Equal Angle

	<i>Project</i>	Kinematic Analysis for D2		
	<i>Analysis Description</i>	Planar Sliding		
	<i>Drawn By</i>	Kara Stariha	<i>Company</i>	
	<i>Date</i>	27/08/2020, 2:08:20 PM	<i>File Name</i>	Kinematic_D2_Wrapped_Scaled_20201104.dips8



Symbol	Feature
◇	Pole Vectors
■	Critical Intersection

Color	Density Concentrations
	0.00 - 1.00
	1.00 - 2.00
	2.00 - 3.00
	3.00 - 4.00
	4.00 - 5.00
	5.00 - 6.00
	6.00 - 7.00
	7.00 - 8.00
	8.00 - 9.00
	9.00 <


Contour Data	Pole Vectors
Maximum Density	15.43%
Contour Distribution	Fisher
Counting Circle Size	1.0%

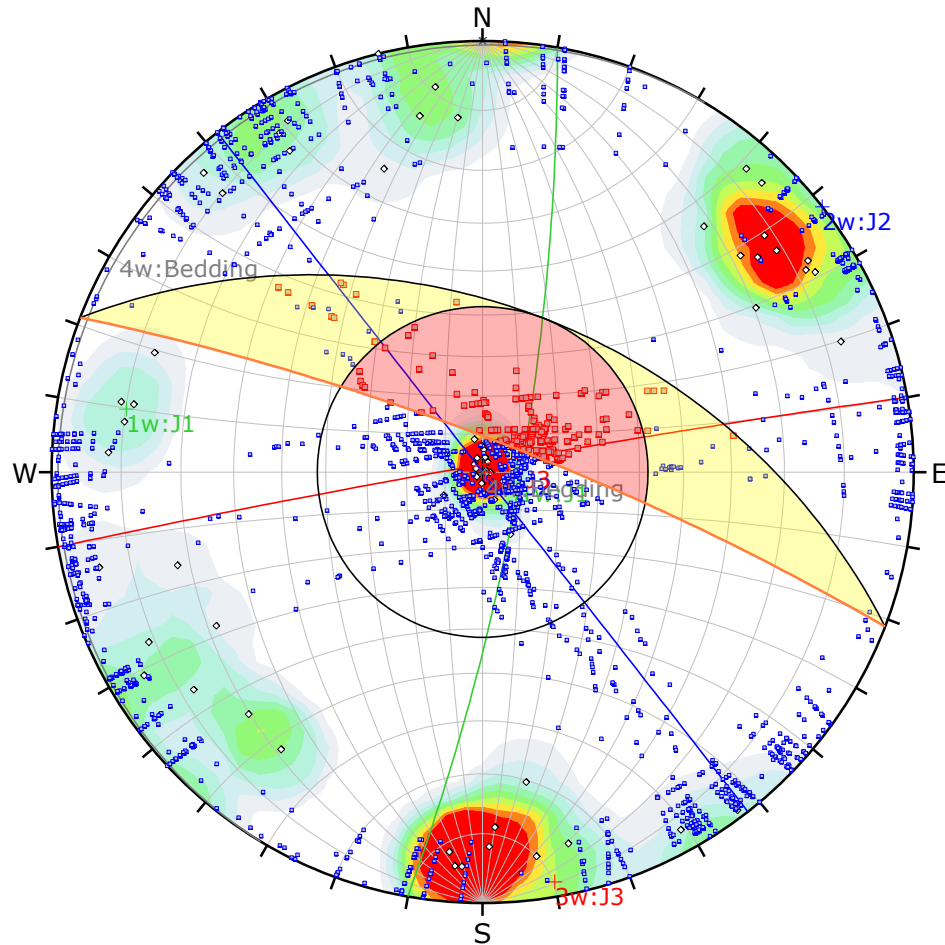
Kinematic Analysis	Wedge Sliding		
Slope Dip	81		
Slope Dip Direction	21		
Friction Angle	48°		

Weighted Results	Critical	Total	%
Wedge Sliding	850	4877	17.42%

	Color	Dip	Dip Direction	Label
Mean Set Planes				
1w	■	80	100	J1
2w	■	90	232	J2
3w	■	88	350	J3
4w	■	1	301	Bedding

Plot Mode	Pole Vectors
Vector Count (Weighted)	100 (65 Entries)
Terzaghi Weighting	Minimum Bias Angle 15°
Intersection Mode	Grid Data Planes
Intersections Count (Weighted)	4877
Hemisphere	Lower
Projection	Equal Angle

	Project	Kinematic Analysis for D2	
	Analysis Description	Wedge Sliding	
	Drawn By	Kara Stariha	Company
	Date	27/08/2020, 2:08:20 PM	File Name



Symbol	Feature
◇	Pole Vectors
■	Critical Intersection
■	Intersection

Color	Density Concentrations
	0.00 - 1.00
	1.00 - 2.00
	2.00 - 3.00
	3.00 - 4.00
	4.00 - 5.00
	5.00 - 6.00
	6.00 - 7.00
	7.00 - 8.00
	8.00 - 9.00
	9.00 <


Contour Data	Pole Vectors
Maximum Density	15.43%
Contour Distribution	Fisher
Counting Circle Size	1.0%

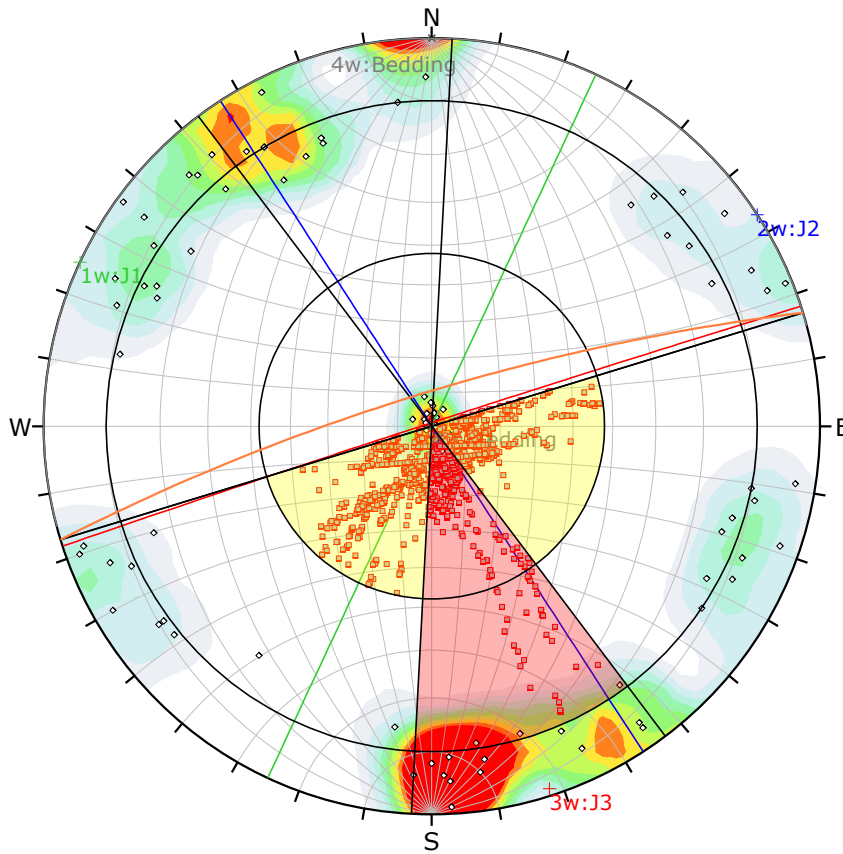
Kinematic Analysis	Wedge Sliding
Slope Dip	81
Slope Dip Direction	21
Friction Angle	48°

Weighted Results	Critical	Total	%
Wedge Sliding	850	4877	17.42%

	Color	Dip	Dip Direction	Label
Mean Set Planes				
1w	■	80	100	J1
2w	■	90	232	J2
3w	■	88	350	J3
4w	■	1	301	Bedding

Plot Mode	Pole Vectors
Vector Count (Weighted)	100 (65 Entries)
Terzaghi Weighting	Minimum Bias Angle 15°
Intersection Mode	Grid Data Planes
Intersections Count (Weighted)	4877
Hemisphere	Lower
Projection	Equal Angle

	Project	Kinematic Analysis for D2	
	Analysis Description	Wedge Sliding	
	Drawn By	Kara Stariha	Company
	Date	27/08/2020, 2:08:20 PM	File Name



Symbol	Feature
◊	Pole Vectors
■	Critical Intersection

Color	Density Concentrations
	0.00 - 1.00
	1.00 - 2.00
	2.00 - 3.00
	3.00 - 4.00
	4.00 - 5.00
	5.00 - 6.00
	6.00 - 7.00
	7.00 - 8.00
	8.00 - 9.00
	9.00 <

Contour Data	Pole Vectors
Maximum Density	18.61%
Contour Distribution	Fisher
Counting Circle Size	1.0%

Kinematic Analysis	Direct Toppling
Slope Dip	80
Slope Dip Direction	343
Friction Angle	48°
Lateral Limits	20°

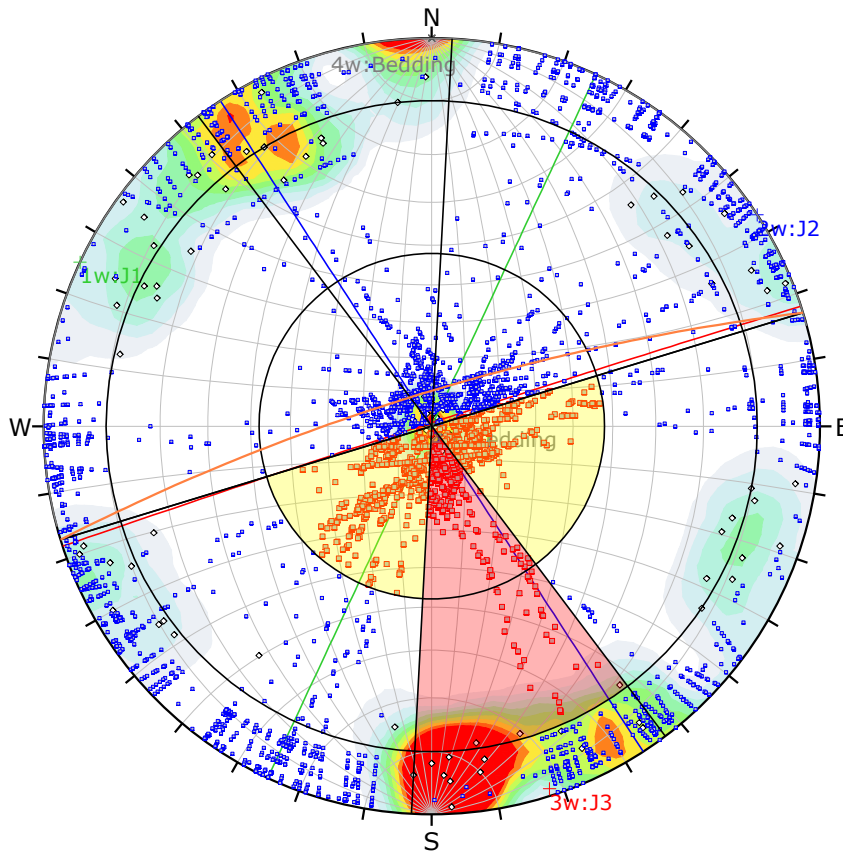
Weighted Results	Critical	Total	%
Direct Toppling (Intersection)	549	12230	4.49%
Oblique Toppling (Intersection)	2557	12230	20.90%
Base Plane (All)	20	158	12.88%
Base Plane (Set 3: J3)	11	90	12.07%
Base Plane (Set 4: Bedding)	9	21	46.05%

Color	Dip	Dip Direction	Label
Mean Set Planes			
1w	90	115	J1
2w	90	237	J2
3w	89	342	J3
4w	0	345	Bedding

Plot Mode	Pole Vectors
Vector Count (Weighted)	158 (90 Entries)
Terzaghi Weighting	Minimum Bias Angle 15°
Intersection Mode	Grid Data Planes
Intersections Count (Weighted)	12230
Hemisphere	Lower
Projection	Equal Angle



Project	Kinematic Analysis for D3		
Analysis Description	Direct Toppling		
Drawn By	Kara Stariha	Company	
Date	27/08/2020, 2:08:20 PM	File Name	Kinematic_D3_Wrapped_Scaled_20201104.dips8



Symbol	Feature
◊	Pole Vectors
■	Critical Intersection
□	Intersection


Color	Density Concentrations
	0.00 - 1.00
	1.00 - 2.00
	2.00 - 3.00
	3.00 - 4.00
	4.00 - 5.00
	5.00 - 6.00
	6.00 - 7.00
	7.00 - 8.00
	8.00 - 9.00
	9.00 <

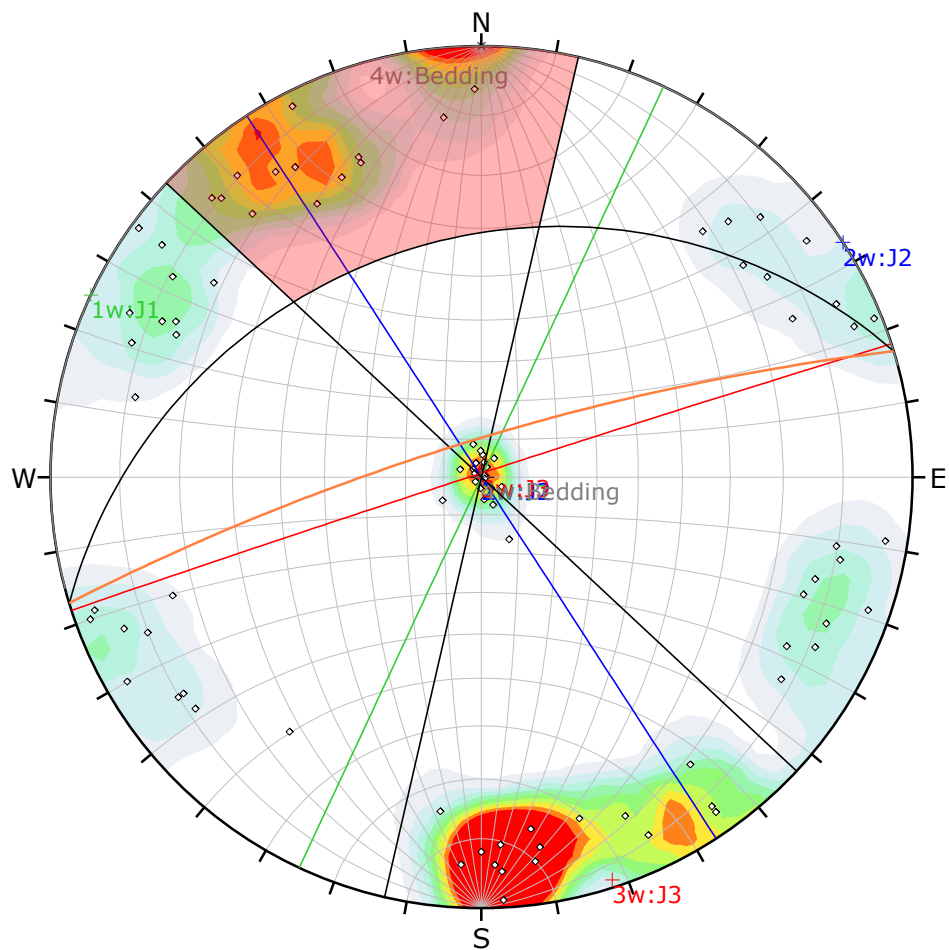
Contour Data	Pole Vectors
Maximum Density	18.61%
Contour Distribution	Fisher
Counting Circle Size	1.0%

Kinematic Analysis		Direct Toppling		
Slope Dip	80			
Slope Dip Direction	343			
Friction Angle	48°			
Lateral Limits	20°			
Weighted Results		Critical	Total	%
Direct Toppling (Intersection)		549	12230	4.49%
Oblique Toppling (Intersection)		2557	12230	20.90%
Base Plane (All)		20	158	12.88%
Base Plane (Set 3: J3)		11	90	12.07%
Base Plane (Set 4: Bedding)		9	21	46.05%

Color	Dip	Dip Direction	Label
Mean Set Planes			
1w	90	115	J1
2w	90	237	J2
3w	89	342	J3
4w	0	345	Bedding

Plot Mode	Pole Vectors
Vector Count (Weighted)	158 (90 Entries)
Terzaghi Weighting	Minimum Bias Angle 15°
Intersection Mode	Grid Data Planes
Intersections Count (Weighted)	12230
Hemisphere	Lower
Projection	Equal Angle

	Project	Kinematic Analysis for D3	
	Analysis Description	Direct Toppling	
	Drawn By	Kara Stariha	Company
	Date	27/08/2020, 2:08:20 PM	File Name



Symbol	Feature
◇	Pole Vectors

Color	Density Concentrations
	0.00 - 1.00
	1.00 - 2.00
	2.00 - 3.00
	3.00 - 4.00
	4.00 - 5.00
	5.00 - 6.00
	6.00 - 7.00
	7.00 - 8.00
	8.00 - 9.00
	9.00 <


Contour Data	Pole Vectors
Maximum Density	18.61%
Contour Distribution	Fisher
Counting Circle Size	1.0%

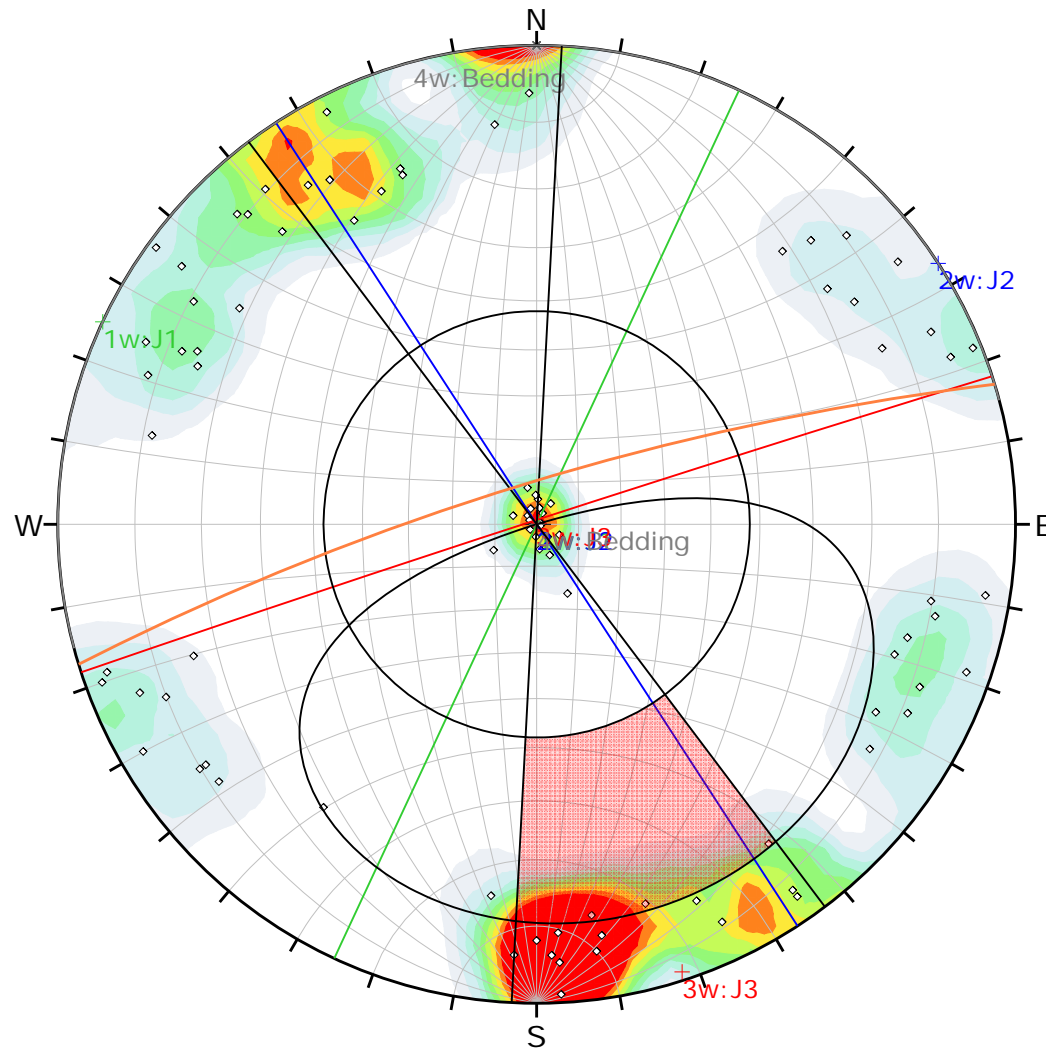
Kinematic Analysis	Flexural Toppling
Slope Dip	80
Slope Dip Direction	343
Friction Angle	48°
Lateral Limits	30°

Weighted Results	Critical	Total	%
Flexural Toppling (All)	33	158	21.04%
Flexural Toppling (Set 3: J3)	33	90	37.03%

	Color	Dip	Dip Direction	Label
Mean Set Planes				
1w	■	90	115	J1
2w	■	90	237	J2
3w	■	89	342	J3
4w	■	0	345	Bedding

Plot Mode	Pole Vectors
Vector Count (Weighted)	158 (90 Entries)
Terzaghi Weighting	Minimum Bias Angle 15°
Hemisphere	Lower
Projection	Equal Angle

	<i>Project</i>	Kinematic Analysis for D3	
	<i>Analysis Description</i>	Flexural Toppling	
	<i>Drawn By</i>	Kara Stariha	<i>Company</i>
	<i>Date</i>	27/08/2020, 2:08:20 PM	<i>File Name</i>



Symbol	Feature
◇	Pole Vectors

Color	Density Concentrations
	0.00 - 1.00
	1.00 - 2.00
	2.00 - 3.00
	3.00 - 4.00
	4.00 - 5.00
	5.00 - 6.00
	6.00 - 7.00
	7.00 - 8.00
	8.00 - 9.00
	9.00 <


Contour Data		Pole Vectors
Maximum Density	18.61%	
Contour Distribution	Fisher	
Counting Circle Size	1.0%	

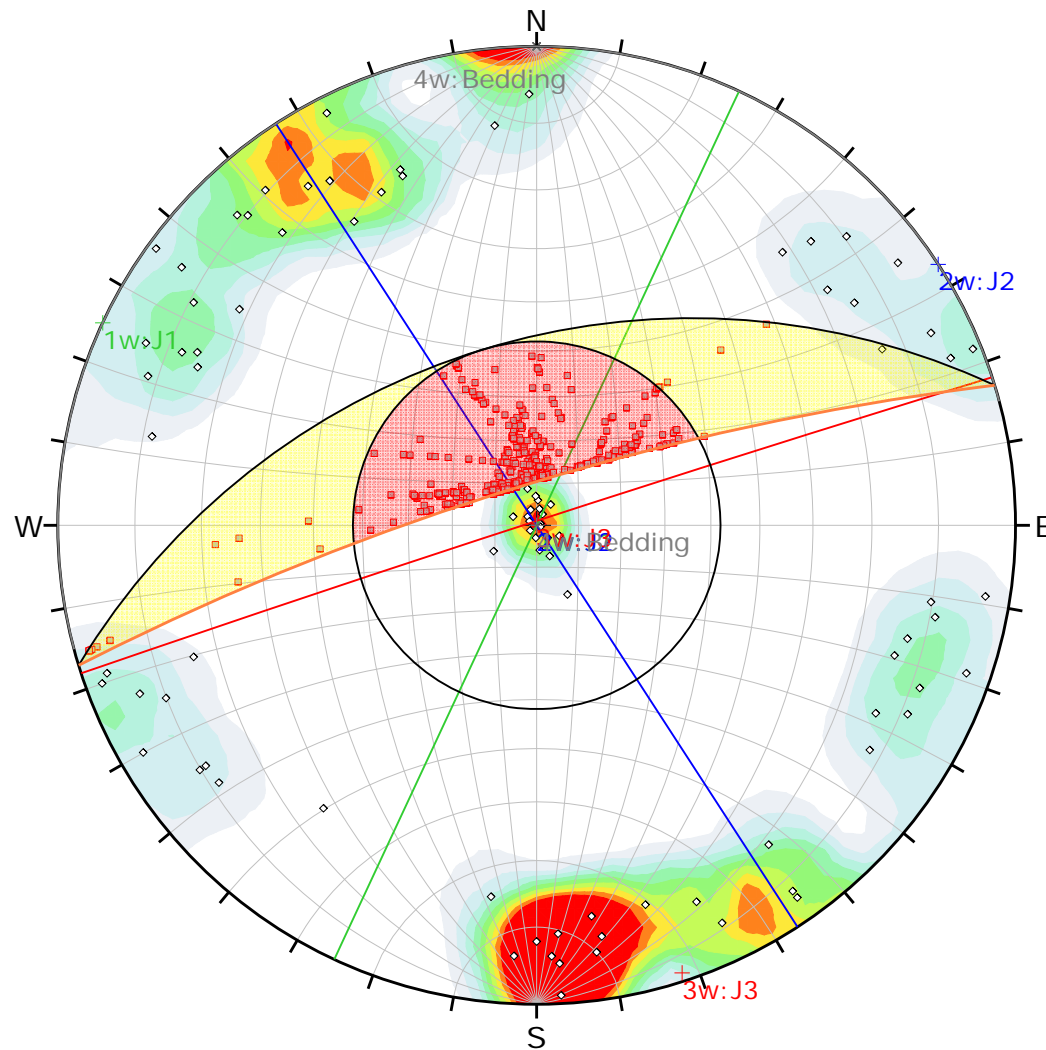
Kinematic Analysis	Planar Sliding
Slope Dip	80
Slope Dip Direction	343
Friction Angle	48°
Lateral Limits	20°

Weighted Results	Critical	Total	%
Planar Sliding (All)	11	158	6.86%
Planar Sliding (Set 3: J3)	11	90	12.07%

	Color	Dip	Dip Direction	Label
Mean Set Planes				
1w	■	90	115	J1
2w	■	90	237	J2
3w	■	89	342	J3
4w	■	0	345	Bedding

Plot Mode	Pole Vectors
Vector Count (Weighted)	158 (90 Entries)
Terzaghi Weighting	Minimum Bias Angle 15°
Hemisphere	Lower
Projection	Equal Angle

	Project	Kinematic Analysis for D3	
	Analysis Description	Planar Sliding	
	Drawn By	Kara Stariha	Company
	Date	27/08/2020, 2:08:20 PM	File Name



Symbol	Feature
◇	Pole Vectors
■	Critical Intersection

Color	Density Concentrations
	0.00 - 1.00
	1.00 - 2.00
	2.00 - 3.00
	3.00 - 4.00
	4.00 - 5.00
	5.00 - 6.00
	6.00 - 7.00
	7.00 - 8.00
	8.00 - 9.00
	9.00 <


Contour Data	Pole Vectors
Maximum Density	18.61%
Contour Distribution	Fisher
Counting Circle Size	1.0%

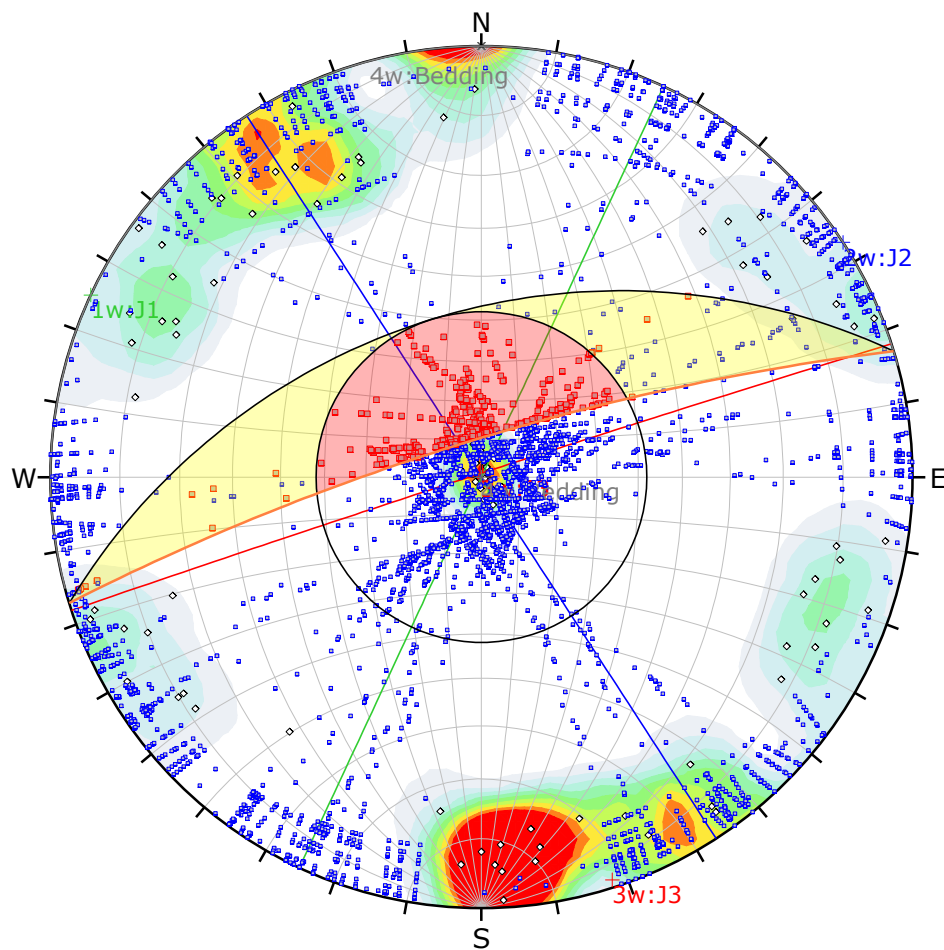
Kinematic Analysis	Wedge Sliding
Slope Dip	80
Slope Dip Direction	343
Friction Angle	48°

	Weighted Results	Critical	Total	%
Wedge Sliding	1551	12230	12.69%	

	Color	Dip	Dip Direction	Label
Mean Set Planes				
1w	■	90	115	J1
2w	■	90	237	J2
3w	■	89	342	J3
4w	■	0	345	Bedding

Plot Mode	Pole Vectors
Vector Count (Weighted)	158 (90 Entries)
Terzaghi Weighting	Minimum Bias Angle 15°
Intersection Mode	Grid Data Planes
Intersections Count (Weighted)	12230
Hemisphere	Lower
Projection	Equal Angle

	<i>Project</i>	Kinematic Analysis for D3	
	<i>Analysis Description</i>	Wedge Sliding	
	<i>Drawn By</i>	Kara Stariha	<i>Company</i>
	<i>Date</i>	27/08/2020, 2:08:20 PM	<i>File Name</i>



Symbol	Feature
◇	Pole Vectors
■	Critical Intersection
■	Intersection

Color	Density Concentrations
	0.00 - 1.00
	1.00 - 2.00
	2.00 - 3.00
	3.00 - 4.00
	4.00 - 5.00
	5.00 - 6.00
	6.00 - 7.00
	7.00 - 8.00
	8.00 - 9.00
	9.00 <


Contour Data	Pole Vectors
Maximum Density	18.61%
Contour Distribution	Fisher
Counting Circle Size	1.0%

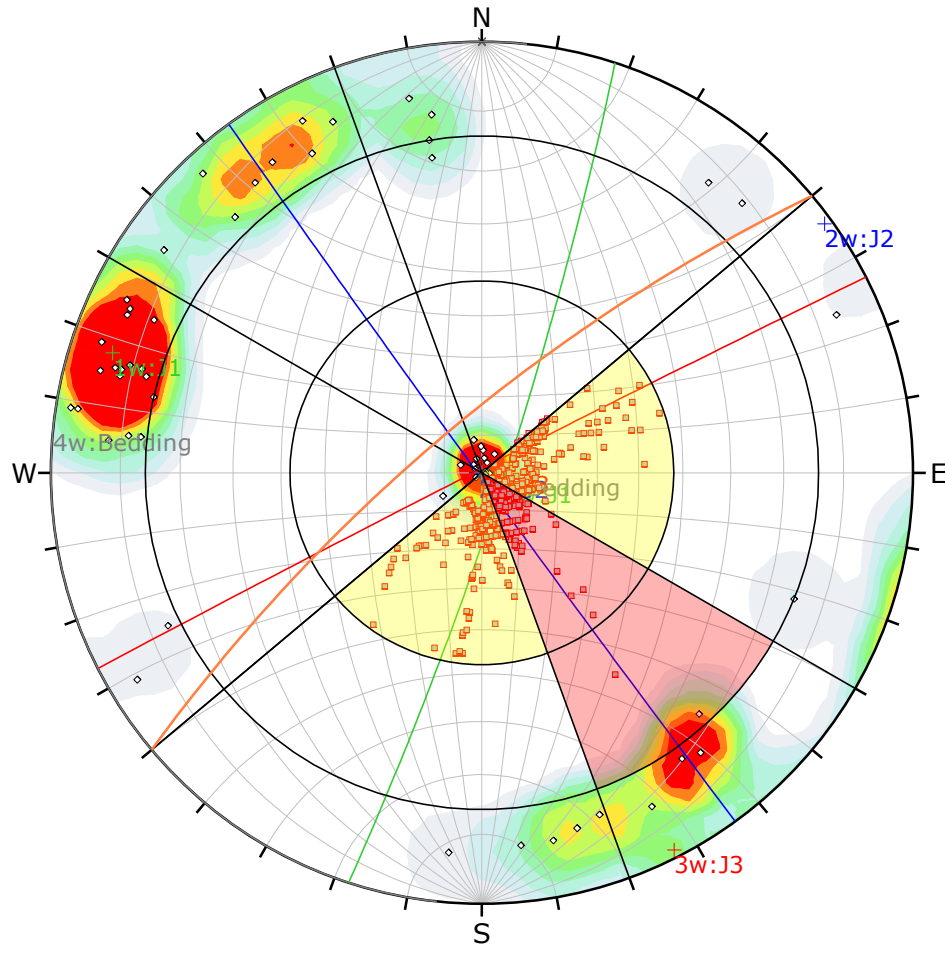
Kinematic Analysis	Wedge Sliding
Slope Dip	80
Slope Dip Direction	343
Friction Angle	48°

	Weighted Results	Critical	Total	%
Wedge Sliding	1551	12230	12230	12.69%

	Color	Dip	Dip Direction	Label
Mean Set Planes				
1w	■	90	115	J1
2w	■	90	237	J2
3w	■	89	342	J3
4w	■	0	345	Bedding

Plot Mode	Pole Vectors
Vector Count (Weighted)	158 (90 Entries)
Terzaghi Weighting	Minimum Bias Angle 15°
Intersection Mode	Grid Data Planes
Intersections Count (Weighted)	12230
Hemisphere	Lower
Projection	Equal Angle

	Project	Kinematic Analysis for D3	
	Analysis Description	Wedge Sliding	
	Drawn By	Kara Stariha	Company
	Date	27/08/2020, 2:08:20 PM	File Name



Symbol	Feature
◇	Pole Vectors
■	Critical Intersection

Color	Density Concentrations
	0.00 - 1.00
	1.00 - 2.00
	2.00 - 3.00
	3.00 - 4.00
	4.00 - 5.00
	5.00 - 6.00
	6.00 - 7.00
	7.00 - 8.00
	8.00 - 9.00
	9.00 <

Contour Data	Pole Vectors
Maximum Density	16.51%
Contour Distribution	Fisher
Counting Circle Size	1.0%

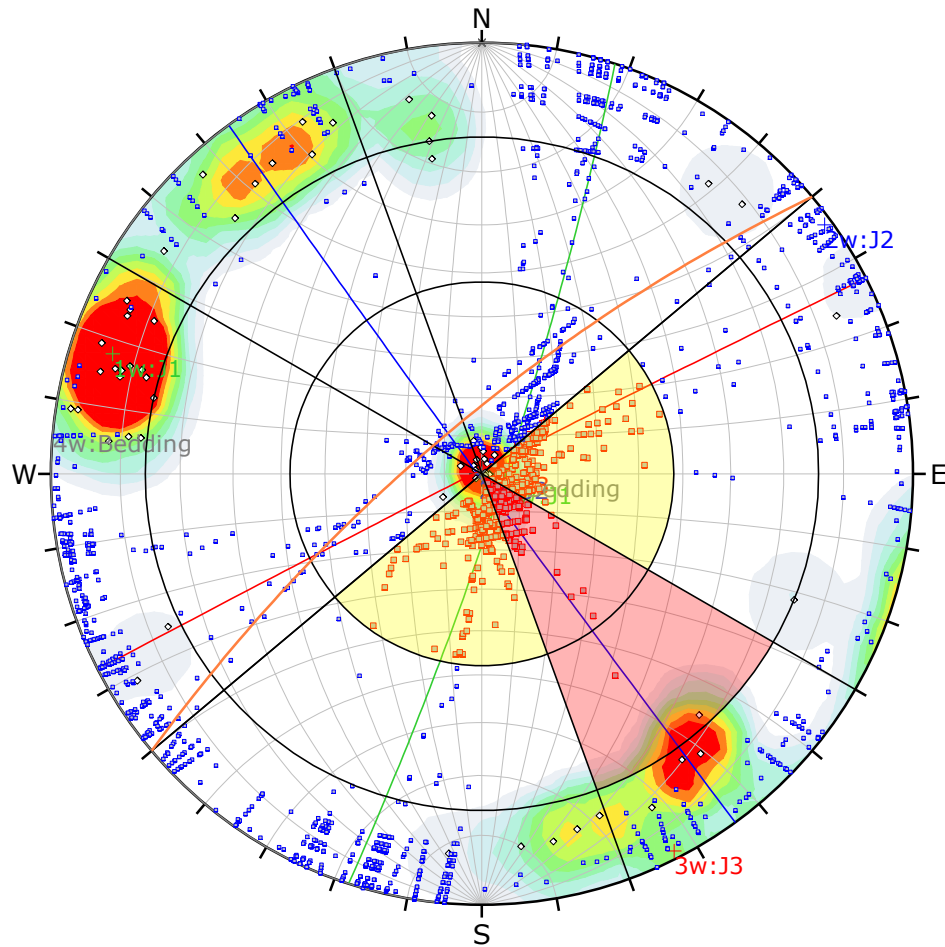
Kinematic Analysis	Direct Toppling		
Slope Dip	76		
Slope Dip Direction	320		
Friction Angle	48°		
Lateral Limits	20°		
Weighted Results	Critical	Total	%
Direct Toppling (Intersection)	323	5687	5.69%
Oblique Toppling (Intersection)	1383	5687	24.31%
Base Plane (All)	12	108	11.02%
Base Plane (Set 3: J3)	4	50	7.75%
Base Plane (Set 4: Bedding)	8	20	40.00%

	Color	Dip	Dip Direction	Label
Mean Set Planes				
1w	■	84	108	J1
2w	■	89	234	J2
3w	■	89	333	J3
4w	■	0	276	Bedding

Plot Mode	Pole Vectors
Vector Count (Weighted)	108 (65 Entries)
Terzaghi Weighting	Minimum Bias Angle 15°
Intersection Mode	Grid Data Planes
Intersections Count (Weighted)	5687
Hemisphere	Lower
Projection	Equal Angle



<i>Project</i>	Kinematic Analysis for D4		
<i>Analysis Description</i>	Direct Toppling		
<i>Drawn By</i>	Kara Stariha	<i>Company</i>	
<i>Date</i>	27/08/2020, 2:08:20 PM	<i>File Name</i>	Kinematic_D4_Wrapped_Scaled_20201104.dips8



Symbol	Feature
◇	Pole Vectors
■	Critical Intersection
■	Intersection

Color	Density Concentrations
	0.00 - 1.00
	1.00 - 2.00
	2.00 - 3.00
	3.00 - 4.00
	4.00 - 5.00
	5.00 - 6.00
	6.00 - 7.00
	7.00 - 8.00
	8.00 - 9.00
	9.00 <

Contour Data	Pole Vectors
Maximum Density	16.51%
Contour Distribution	Fisher
Counting Circle Size	1.0%

Kinematic Analysis	Direct Toppling
Slope Dip	76
Slope Dip Direction	320
Friction Angle	48°
Lateral Limits	20°

	Weighted Results	Critical	Total	%
Direct Toppling (Intersection)	323	5687	5687	5.69%
Oblique Toppling (Intersection)	1383	5687	5687	24.31%
Base Plane (All)	12	108	108	11.02%
Base Plane (Set 3: J3)	4	50	50	7.75%
Base Plane (Set 4: Bedding)	8	20	20	40.00%

	Color	Dip	Dip Direction	Label
Mean Set Planes				
1w	■	84	108	J1
2w	■	89	234	J2
3w	■	89	333	J3
4w	■	0	276	Bedding

Plot Mode	Pole Vectors
Vector Count (Weighted)	108 (65 Entries)
Terzaghi Weighting	Minimum Bias Angle 15°
Intersection Mode	Grid Data Planes
Intersections Count (Weighted)	5687
Hemisphere	Lower
Projection	Equal Angle



Project

Kinematic Analysis for D4

Analysis Description

Direct Toppling

Drawn By

Kara Stariha

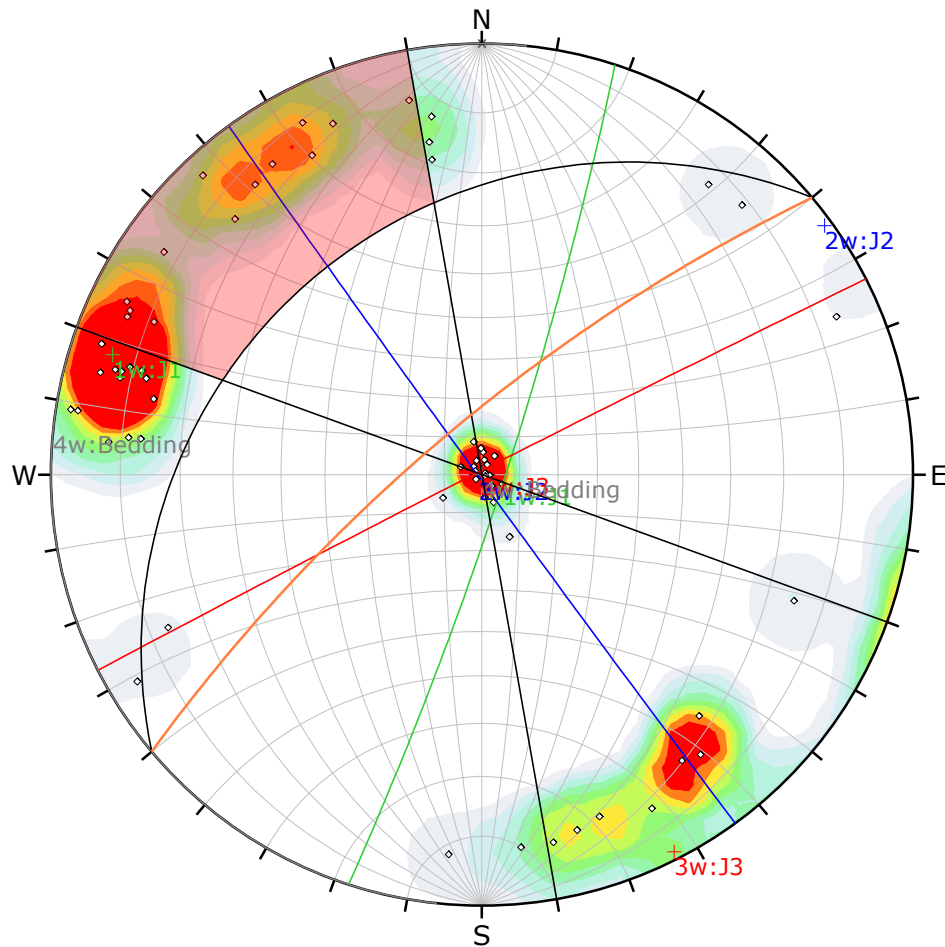
Company

Date

27/08/2020, 2:08:20 PM

File Name

Kinematic_D4_Wrapped_Scaled_20201104.dips8



Symbol	Feature
◇	Pole Vectors

Color	Density Concentrations
	0.00 - 1.00
	1.00 - 2.00
	2.00 - 3.00
	3.00 - 4.00
	4.00 - 5.00
	5.00 - 6.00
	6.00 - 7.00
	7.00 - 8.00
	8.00 - 9.00
	9.00 <


Contour Data	Pole Vectors
Maximum Density	16.51%
Contour Distribution	Fisher
Counting Circle Size	1.0%

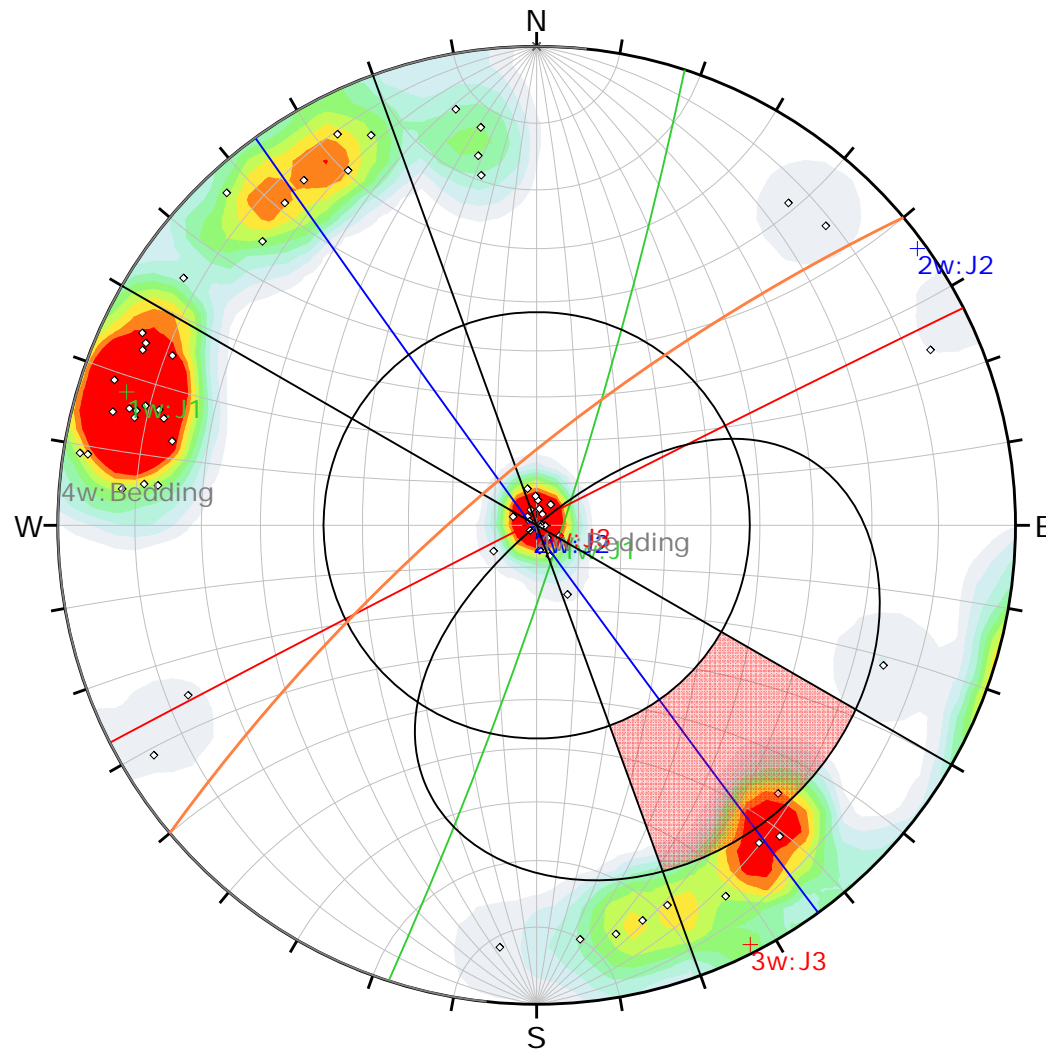
Kinematic Analysis	Flexural Toppling
Slope Dip	76
Slope Dip Direction	320
Friction Angle	48°
Lateral Limits	30°

Weighted Results	Critical	Total	%
Flexural Toppling (All)	29	108	27.21%
Flexural Toppling (Set 1: J1)	10	33	30.24%
Flexural Toppling (Set 3: J3)	19	50	38.90%

	Color	Dip	Dip Direction	Label
Mean Set Planes				
1w	Green	84	108	J1
2w	Blue	89	234	J2
3w	Red	89	333	J3
4w	Grey	0	276	Bedding

Plot Mode	Pole Vectors
Vector Count (Weighted)	108 (65 Entries)
Terzaghi Weighting	Minimum Bias Angle 15°
Hemisphere	Lower
Projection	Equal Angle

	Project	Kinematic Analysis for D4	
	Analysis Description	Flexural Toppling	
	Drawn By	Kara Stariha	Company
	Date	27/08/2020, 2:08:20 PM	File Name



Symbol	Feature
◇	Pole Vectors

Color	Density Concentrations
	0.00 - 1.00
	1.00 - 2.00
	2.00 - 3.00
	3.00 - 4.00
	4.00 - 5.00
	5.00 - 6.00
	6.00 - 7.00
	7.00 - 8.00
	8.00 - 9.00
	9.00 <


Contour Data		Pole Vectors
Maximum Density	16.51%	
Contour Distribution	Fisher	
Counting Circle Size	1.0%	

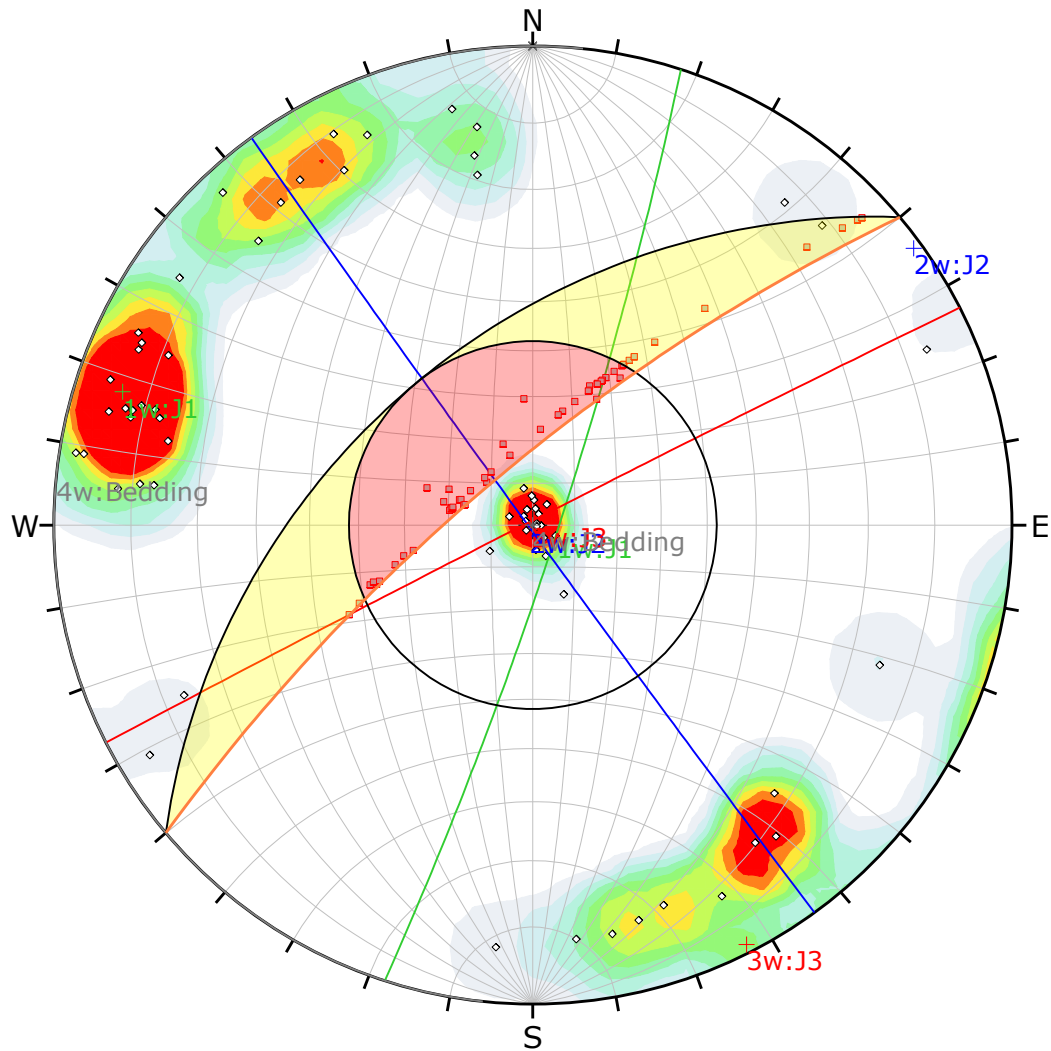
Kinematic Analysis		Planar Sliding	
Slope Dip	76		
Slope Dip Direction	320		
Friction Angle	48°		
Lateral Limits	20°		

Weighted Results		Critical	Total	%
Planar Sliding (All)		4	108	3.59%
Planar Sliding (Set 3: J3)		4	50	7.75%

Color	Dip	Dip Direction	Label
Mean Set Planes			
1w	84	108	J1
2w	89	234	J2
3w	89	333	J3
4w	0	276	Bedding

Plot Mode		Pole Vectors
Vector Count (Weighted)	108 (65 Entries)	
Terzaghi Weighting	Minimum Bias Angle 15°	
Hemisphere	Lower	
Projection	Equal Angle	

	Project	Kinematic Analysis for D4	
	Analysis Description	Planar Sliding	
	Drawn By	Kara Stariha	Company
	Date	27/08/2020, 2:08:20 PM	File Name



Symbol	Feature
◇	Pole Vectors
■	Critical Intersection


Color	Density Concentrations
	0.00 - 1.00
	1.00 - 2.00
	2.00 - 3.00
	3.00 - 4.00
	4.00 - 5.00
	5.00 - 6.00
	6.00 - 7.00
	7.00 - 8.00
	8.00 - 9.00
	9.00 <

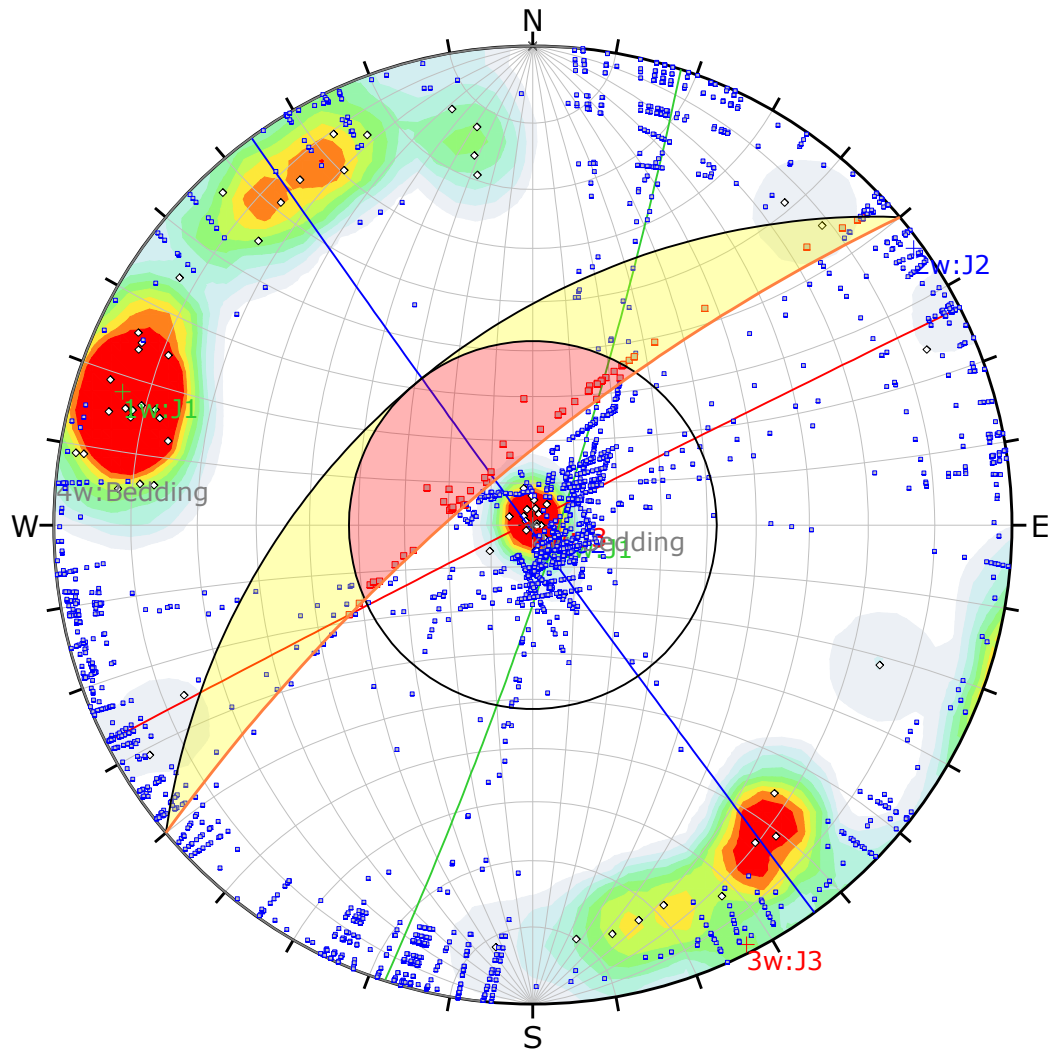
Contour Data	Pole Vectors
Maximum Density	16.51%
Contour Distribution	Fisher
Counting Circle Size	1.0%

Kinematic Analysis	Wedge Sliding			
Slope Dip	76			
Slope Dip Direction	320			
Friction Angle	48°			
	Weighted Results	Critical	Total	%
	Wedge Sliding	337	5687	5.93%

	Color	Dip	Dip Direction	Label
Mean Set Planes				
1w	■	84	108	J1
2w	■	89	234	J2
3w	■	89	333	J3
4w	■	0	276	Bedding

Plot Mode	Pole Vectors
Vector Count (Weighted)	108 (65 Entries)
Terzaghi Weighting	Minimum Bias Angle 15°
Intersection Mode	Grid Data Planes
Intersections Count (Weighted)	5687
Hemisphere	Lower
Projection	Equal Angle

	<i>Project</i>	Kinematic Analysis for D4	
	<i>Analysis Description</i>	Wedge Sliding	
	<i>Drawn By</i>	Kara Stariha	<i>Company</i>
	<i>Date</i>	27/08/2020, 2:08:20 PM	<i>File Name</i>



Symbol	Feature
◇	Pole Vectors
■	Critical Intersection
□	Intersection

Color	Density Concentrations
	0.00 - 1.00
	1.00 - 2.00
	2.00 - 3.00
	3.00 - 4.00
	4.00 - 5.00
	5.00 - 6.00
	6.00 - 7.00
	7.00 - 8.00
	8.00 - 9.00
	9.00 <


Contour Data	Pole Vectors
Maximum Density	16.51%
Contour Distribution	Fisher
Counting Circle Size	1.0%

Kinematic Analysis	Wedge Sliding
Slope Dip	76
Slope Dip Direction	320
Friction Angle	48°

	Weighted Results	Critical	Total	%
Wedge Sliding		337	5687	5.93%

	Color	Dip	Dip Direction	Label
Mean Set Planes				
1w	■	84	108	J1
2w	■	89	234	J2
3w	■	89	333	J3
4w	■	0	276	Bedding

Plot Mode	Pole Vectors
Vector Count (Weighted)	108 (65 Entries)
Terzaghi Weighting	Minimum Bias Angle 15°
Intersection Mode	Grid Data Planes
Intersections Count (Weighted)	5687
Hemisphere	Lower
Projection	Equal Angle

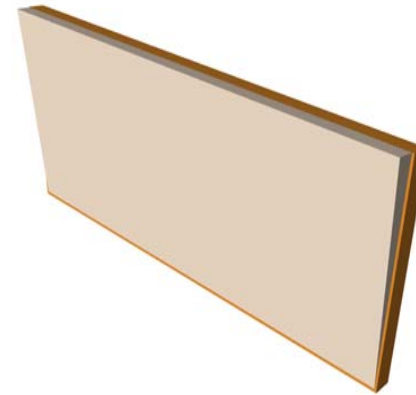
	<i>Project</i>	Kinematic Analysis for D4		
	<i>Analysis Description</i>	Wedge Sliding		
	<i>Drawn By</i>	Kara Stariha	<i>Company</i>	
	<i>Date</i>	27/08/2020, 2:08:20 PM	<i>File Name</i>	Kinematic_D4_Wrapped_Scaled_20201104.dips8

Appendix C – RocPlane Probabilistic Assessment

Probability of Failure: 0.2482



Top



Perspective



Front



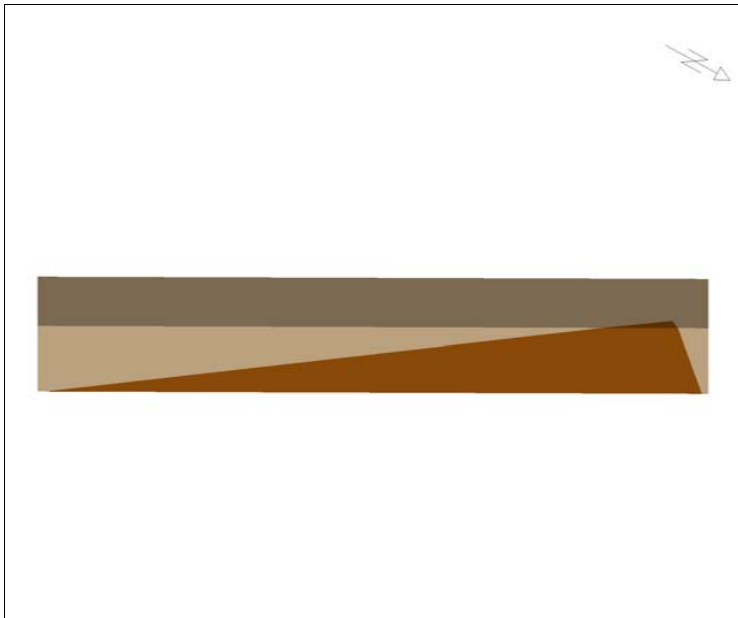
Side



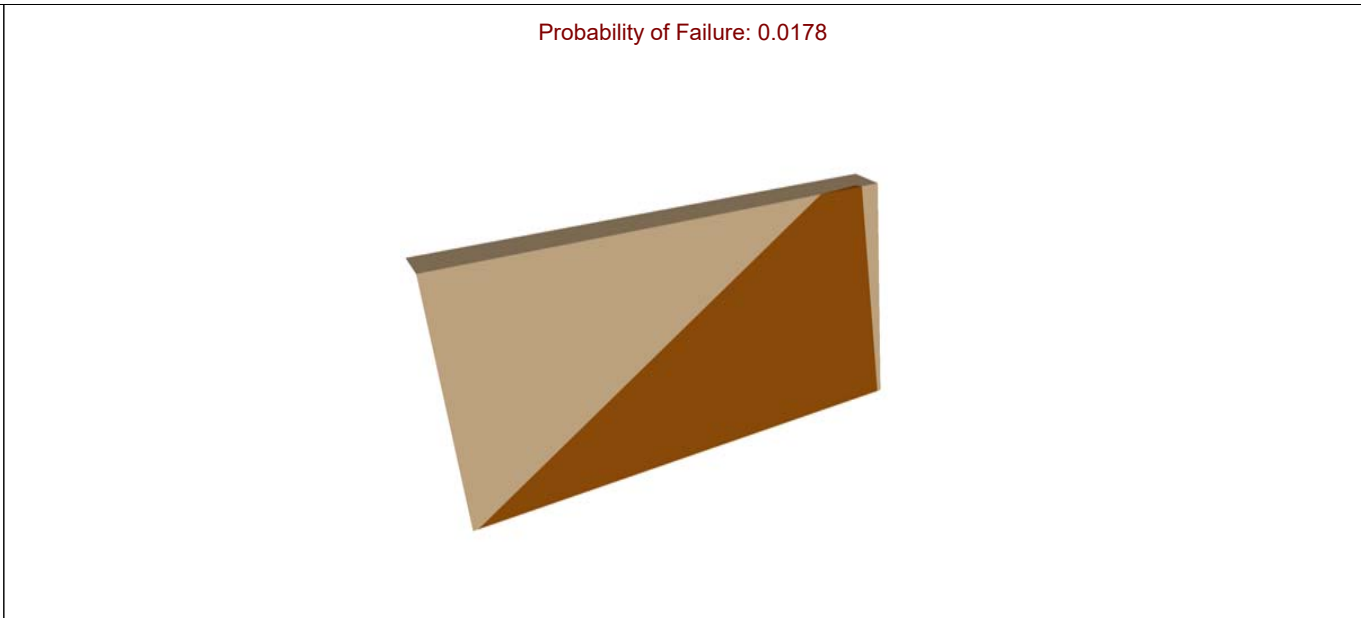
ROCPANE 4.006

<i>Project</i>	RocPlane - Planar Wedge Stability Analysis		
<i>Analysis Description</i>	D1 - Planar Sliding		
<i>Drawn By</i>	Kara Stariha	<i>Company</i>	
<i>Date</i>	28.11.2020, 09:18:41	<i>File Name</i>	RocPlane1.pln4

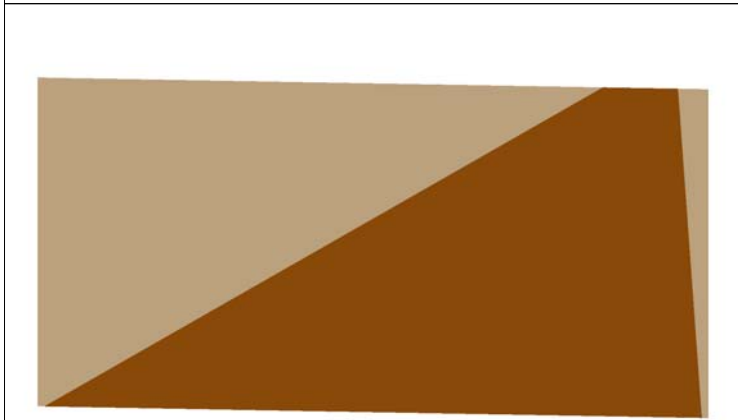
Appendix D – SWedge Probabilistic Assessment



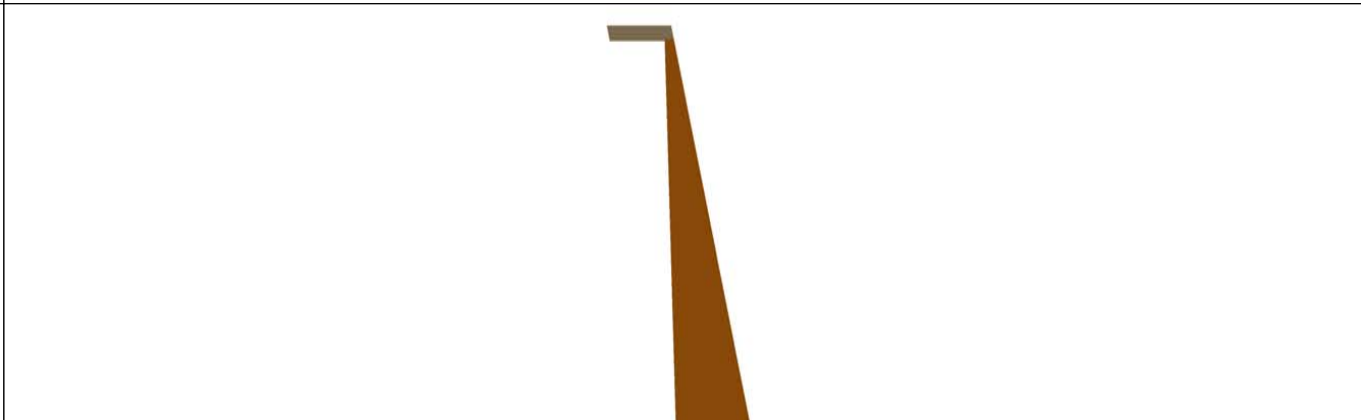
Top




Perspective

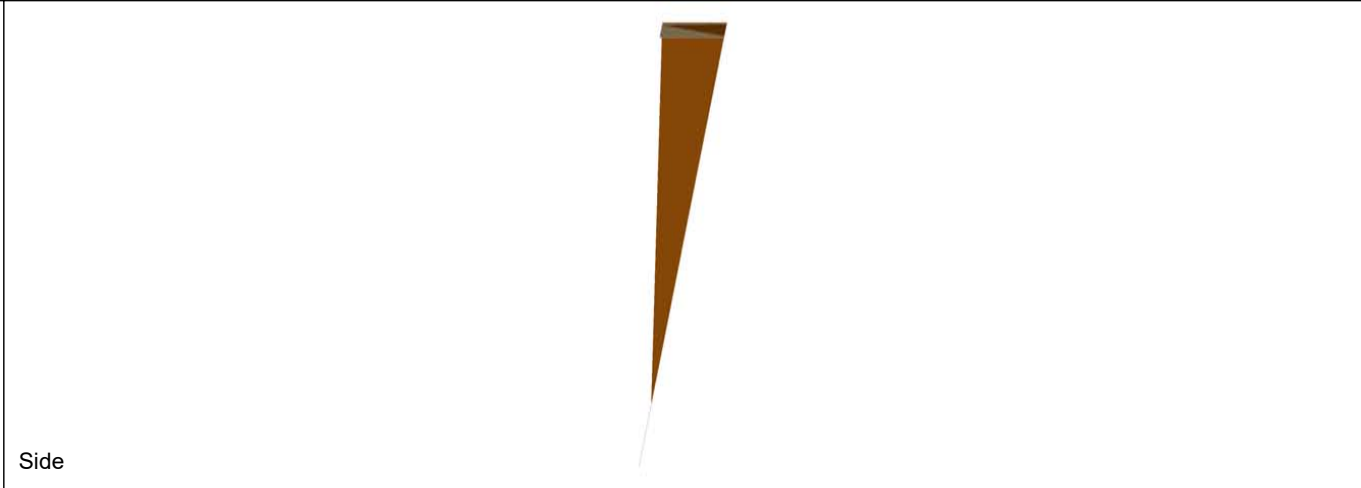
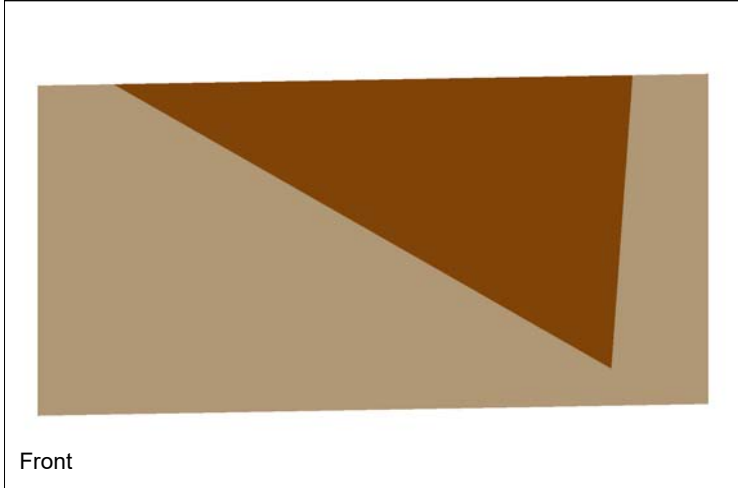
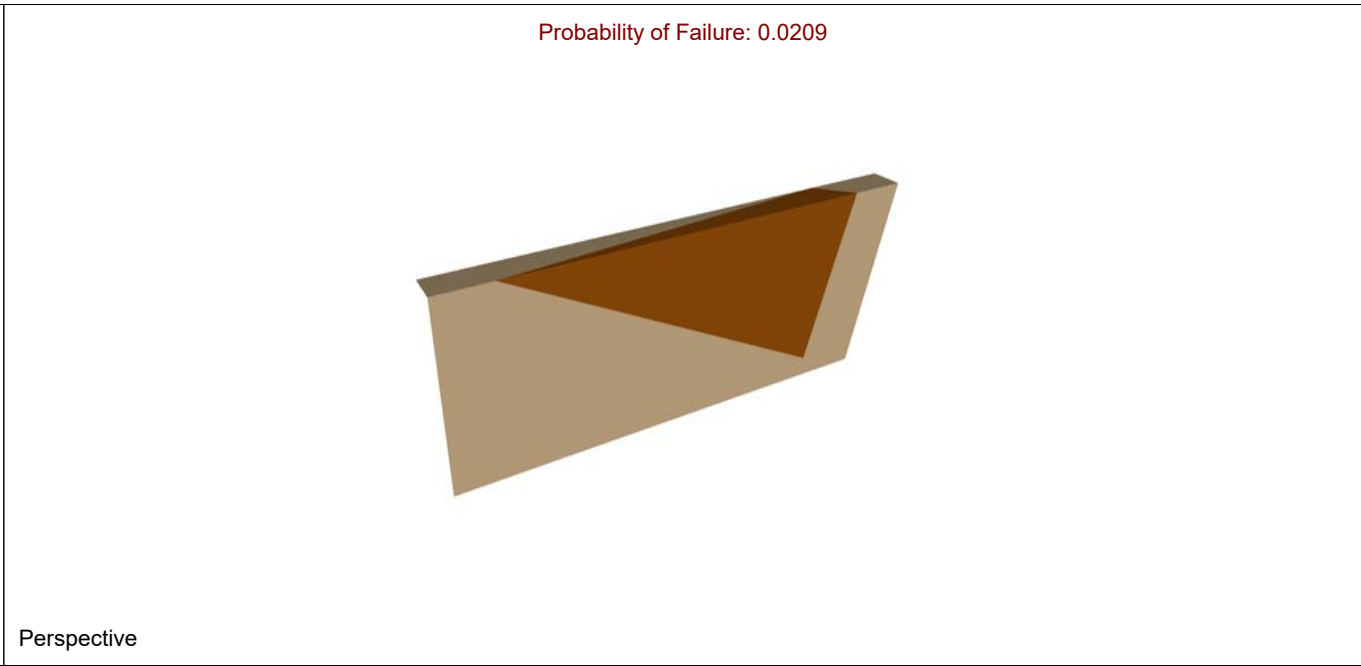
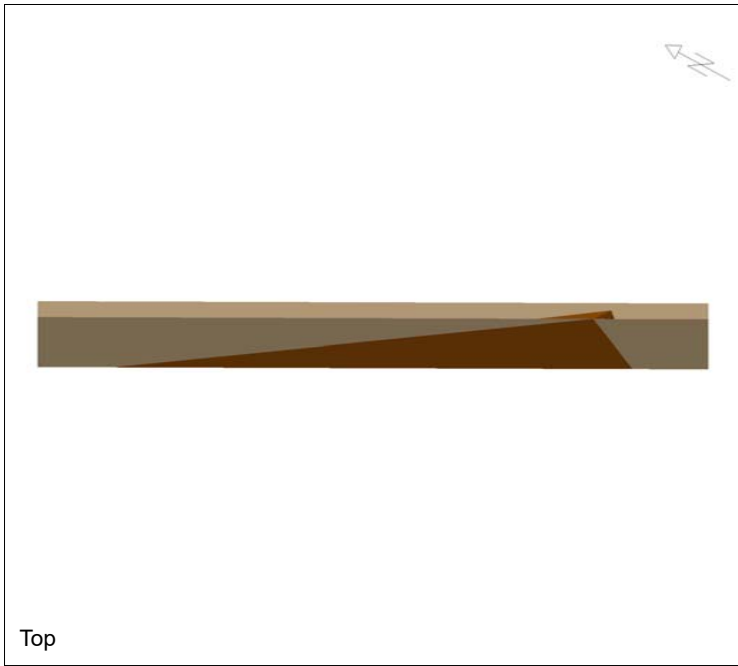



Front

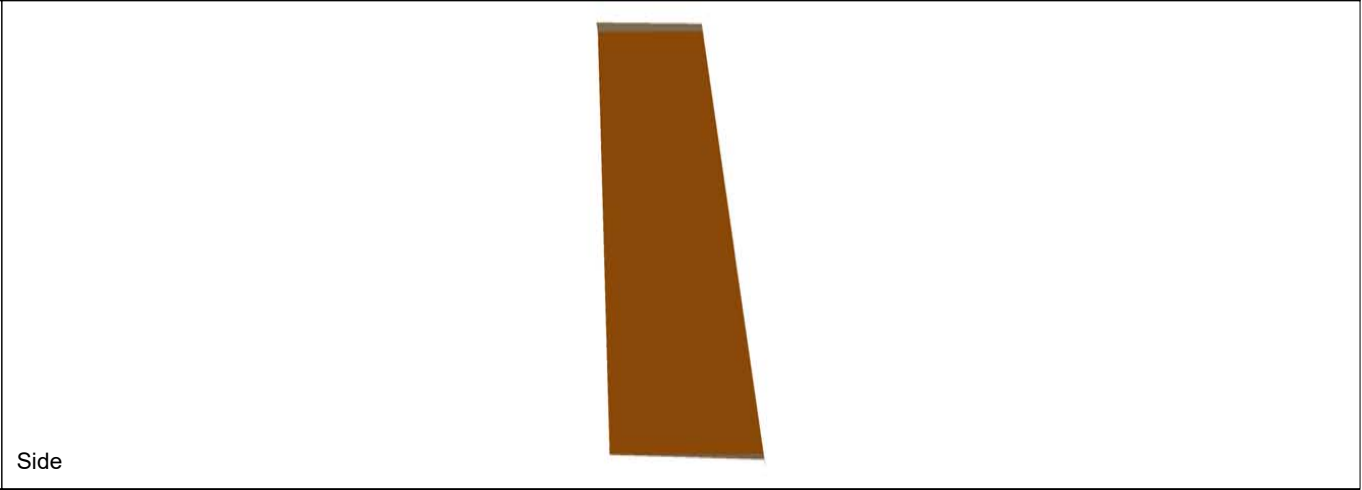
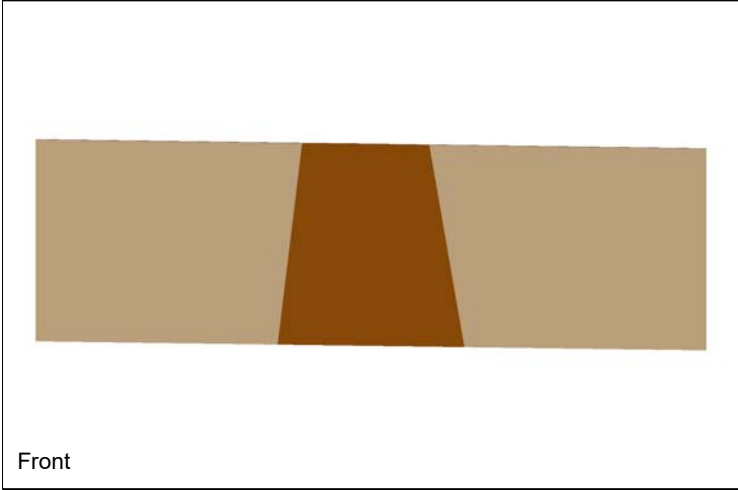
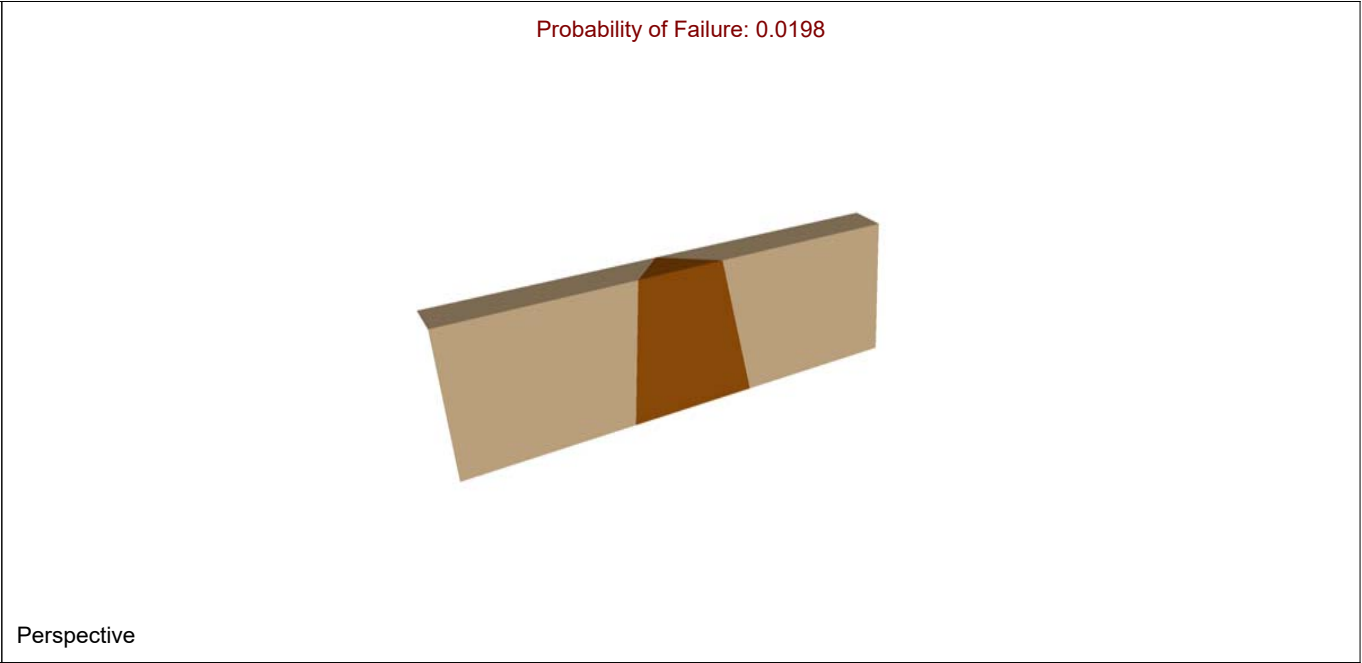
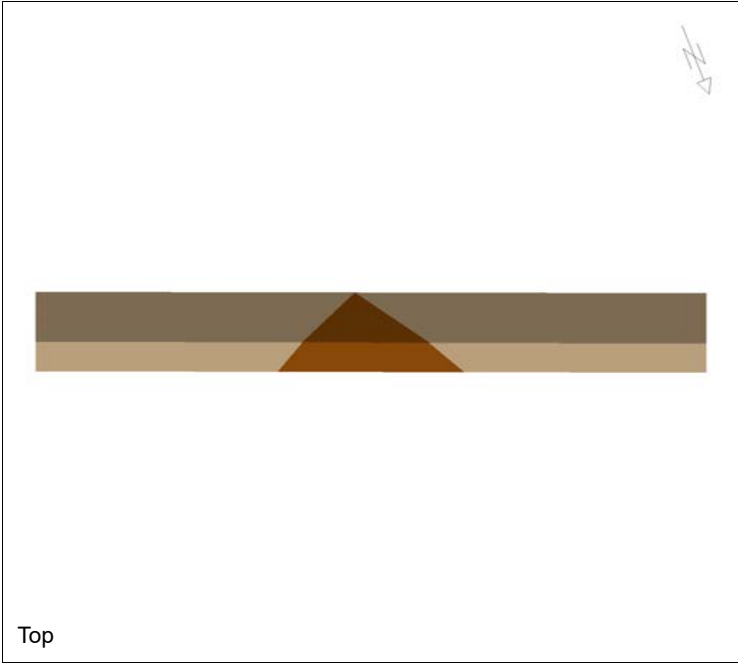



Side

	<i>Project</i> SWEDGE - Surface Wedge Stability Analysis		
	<i>Analysis Description</i> D1 - Wedge Sliding		
	<i>Drawn By</i> Kara Stariha	<i>Company</i>	
	<i>Date</i> 26.11.2020, 08:08:23	<i>File Name</i>	D1.swd7



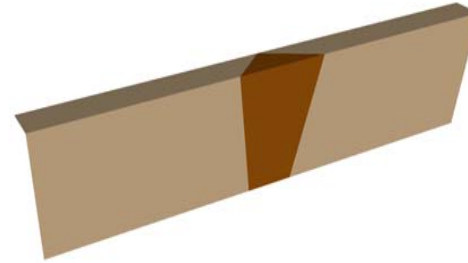
	<i>Project</i> SWEDGE - Surface Wedge Stability Analysis		
	<i>Analysis Description</i> D1 - Wedge Sliding - Overhanging		
	<i>Drawn By</i> Kara Stariha	<i>Company</i>	
	<i>Date</i> 26.11.2020, 08:08:23	<i>File Name</i>	D1.swd7



	<i>Project</i>		
	SWEDGE - Surface Wedge Stability Analysis		
	<i>Analysis Description</i>		
	D2 Wedge Sliding		
<i>Drawn By</i>		Kara Stariha	<i>Company</i>
<i>Date</i>		26.11.2020, 08:08:23	<i>File Name</i>
SWEDGE 7.008			D2.swd7

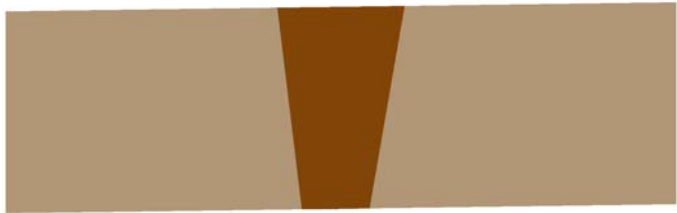


Probability of Failure: 0.0273



Top

Perspective

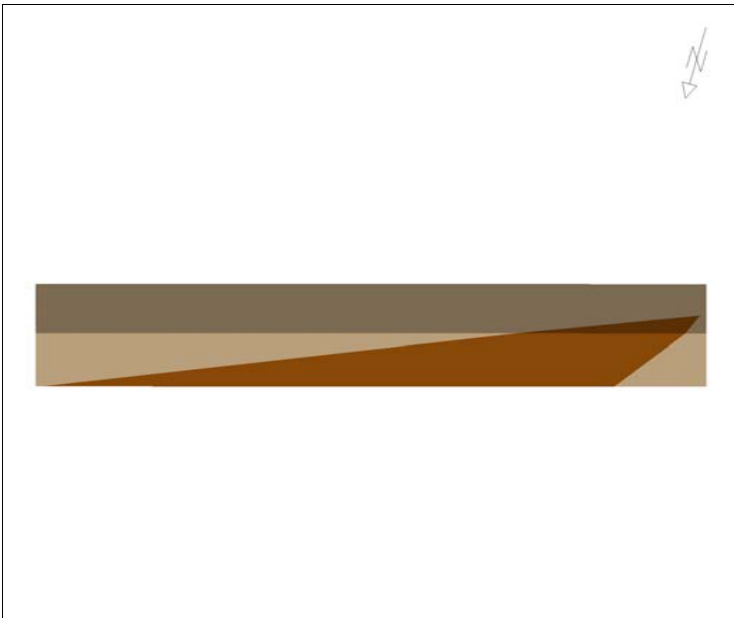


Front

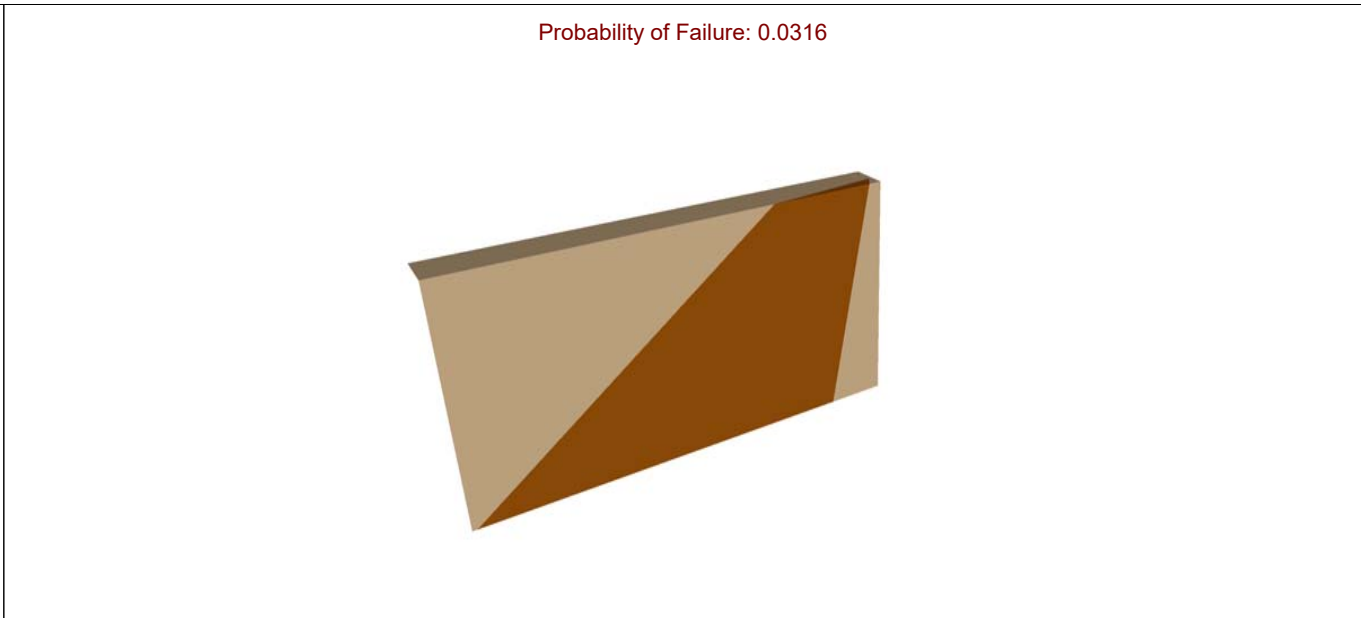
Side



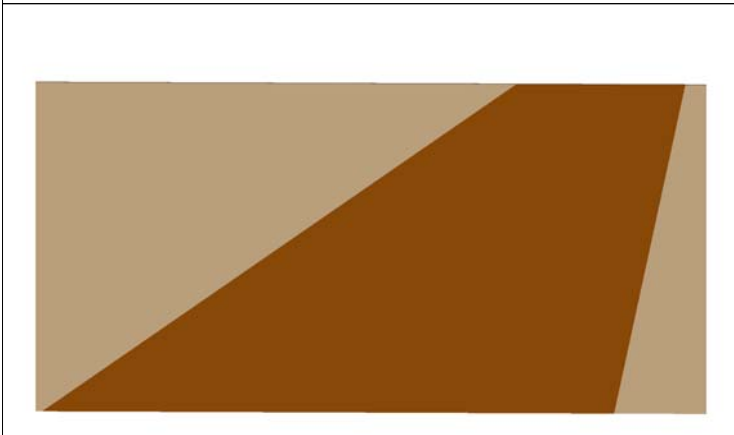
<i>Project</i>	SWEDGE - Surface Wedge Stability Analysis		
<i>Analysis Description</i>	D2 Wedge Sliding - Overhang		
<i>Drawn By</i>	Kara Stariha	<i>Company</i>	
<i>Date</i>	26.11.2020, 08:08:23	<i>File Name</i>	D2.swd7



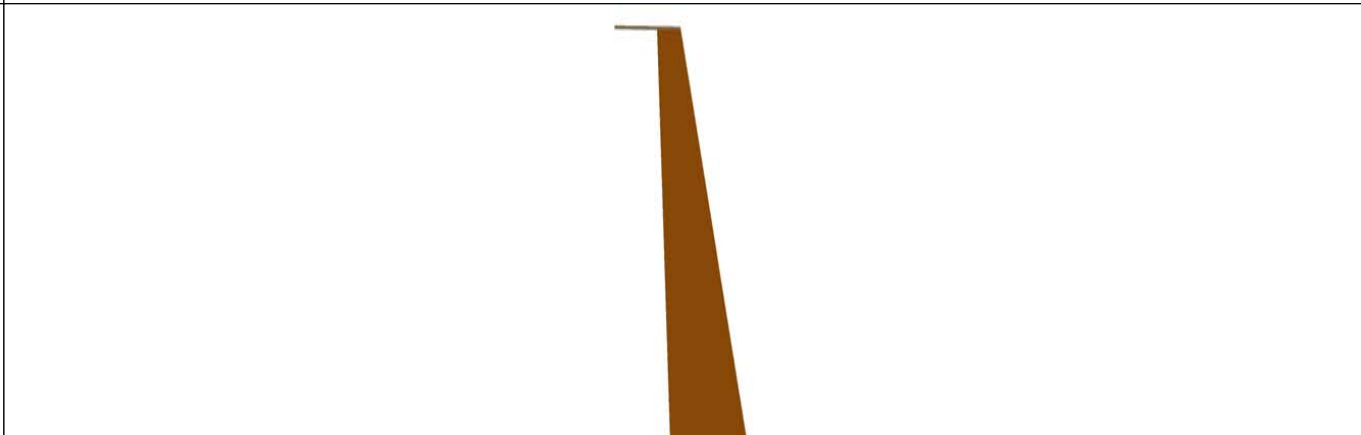
Top




Perspective



Front



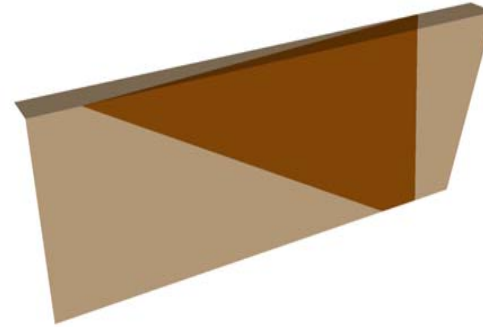
Side

	<i>Project</i> SWEDGE - Surface Wedge Stability Analysis		
	<i>Analysis Description</i> D3 - Wedge Sliding		
	<i>Drawn By</i> Kara Stariha	<i>Company</i>	
	<i>Date</i> 26.11.2020, 08:08:23	<i>File Name</i>	D3_1.swd7

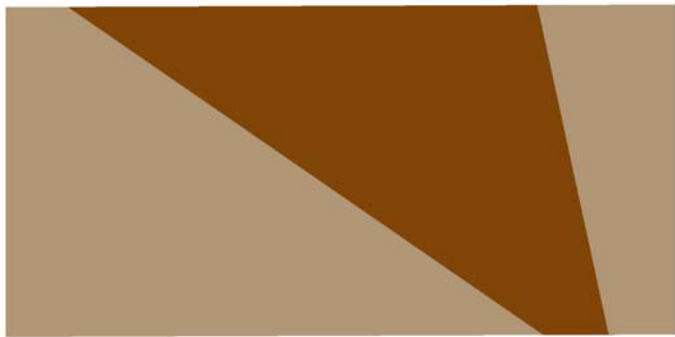


Top

Probability of Failure: 0.0276



Perspective



Front

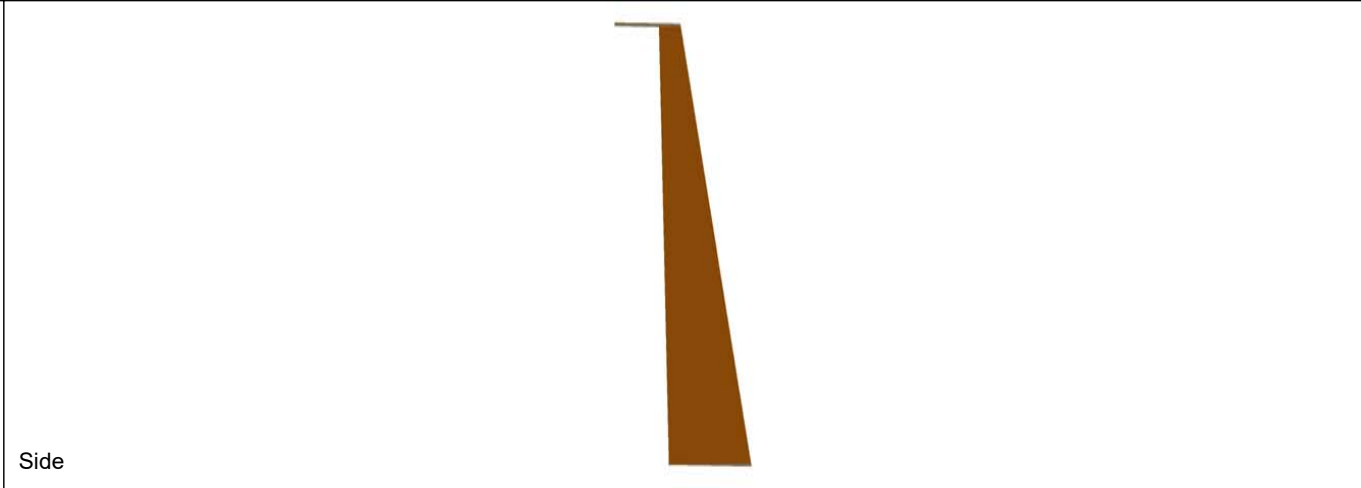
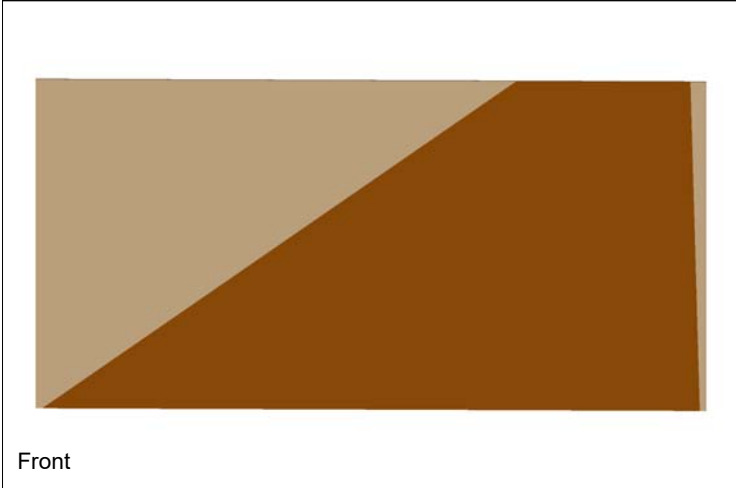
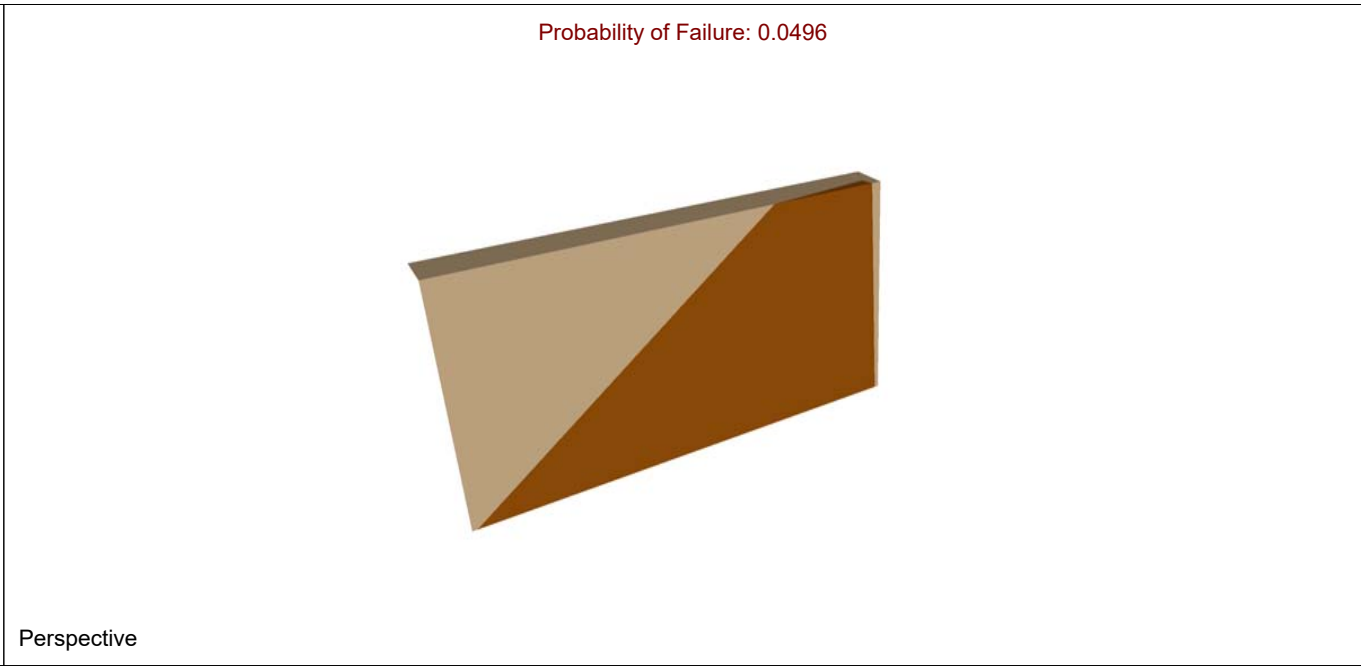
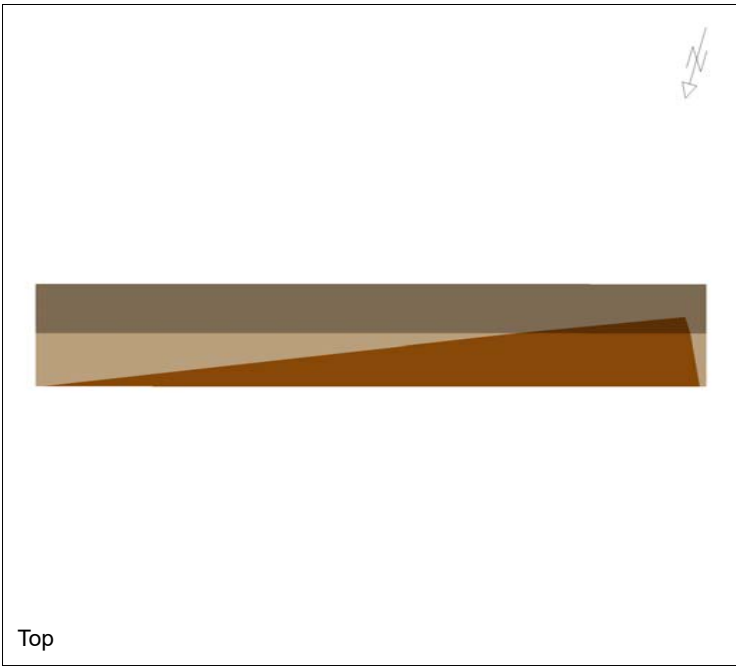



Side



SWEDGE 7.008

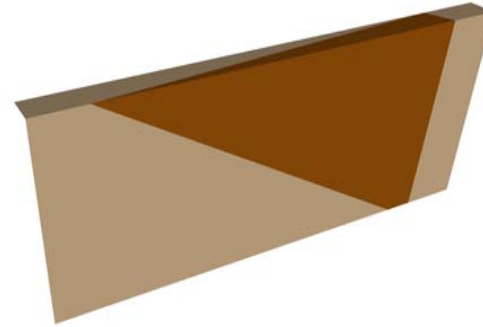
<i>Project</i>	SWEDGE - Surface Wedge Stability Analysis		
<i>Analysis Description</i>	D3 - Wedge Sliding - Overhanging		
<i>Drawn By</i>	Kara Stariha	<i>Company</i>	
<i>Date</i>	26.11.2020, 08:08:23	<i>File Name</i>	D3_1.swd7



	<i>Project</i> SWEDGE - Surface Wedge Stability Analysis		
	<i>Analysis Description</i> D3_2 - Wedge Sliding		
	<i>Drawn By</i> Kara Stariha	<i>Company</i>	
	<i>Date</i> 26.11.2020, 08:08:23	<i>File Name</i>	D3_2.swd7

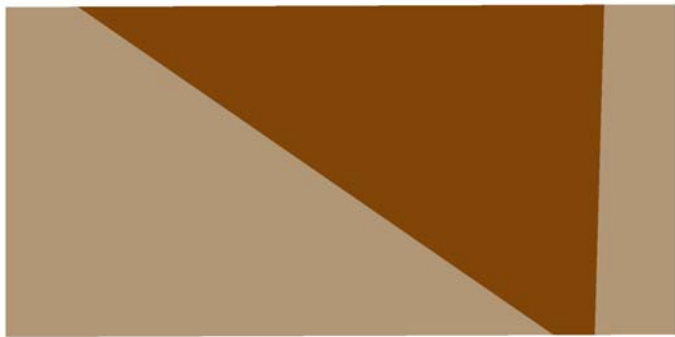


Probability of Failure: 0.0449



Top

Perspective



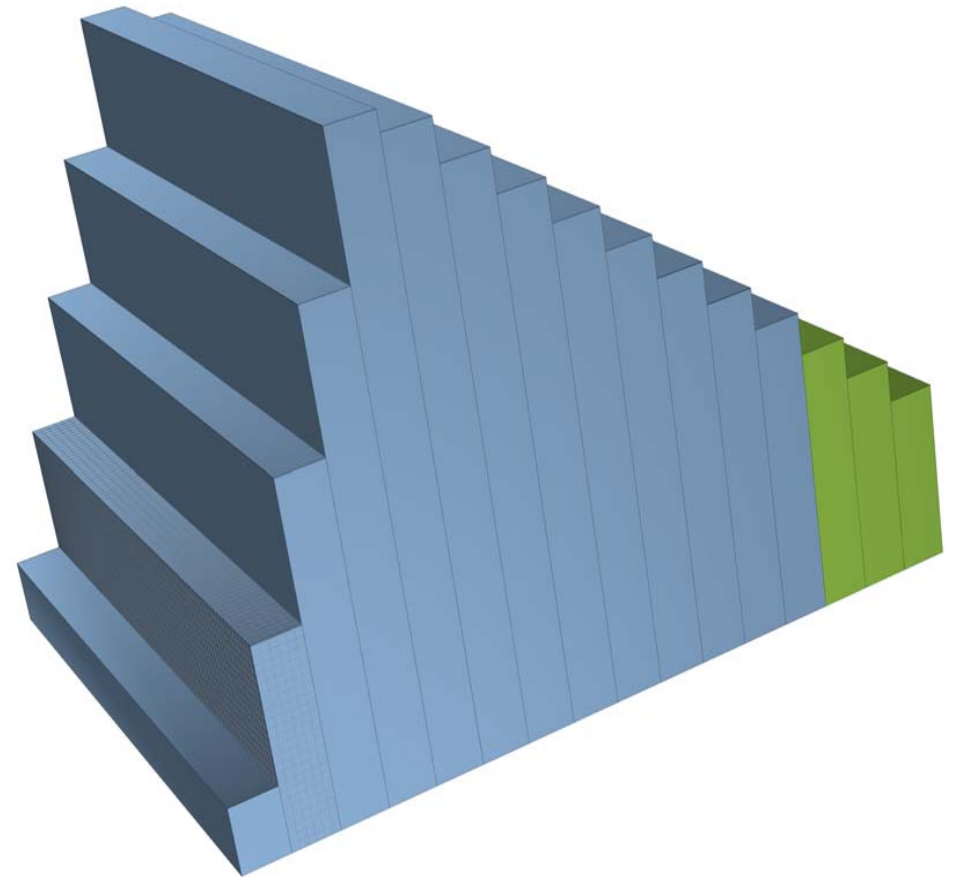
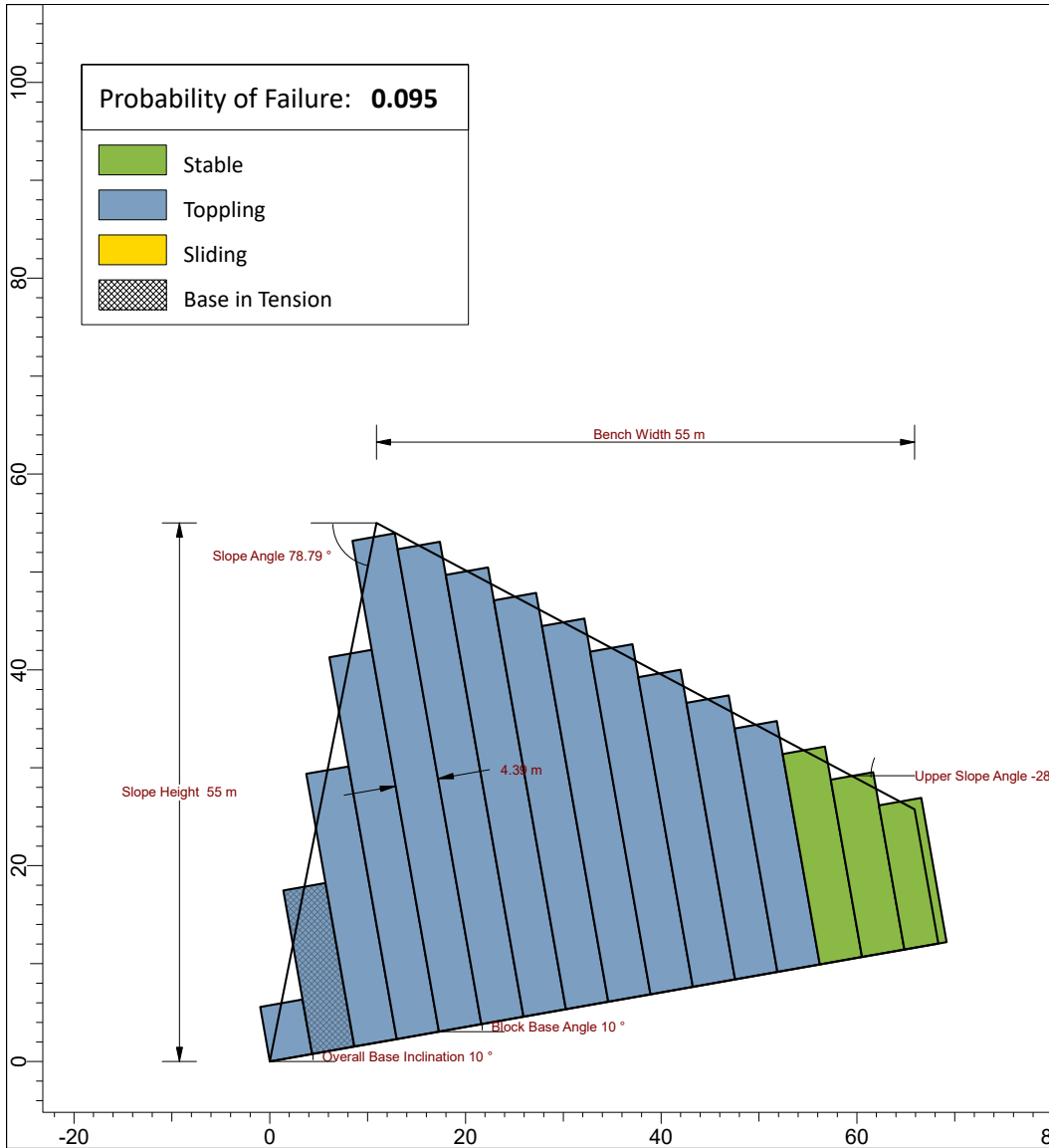
Front


Side

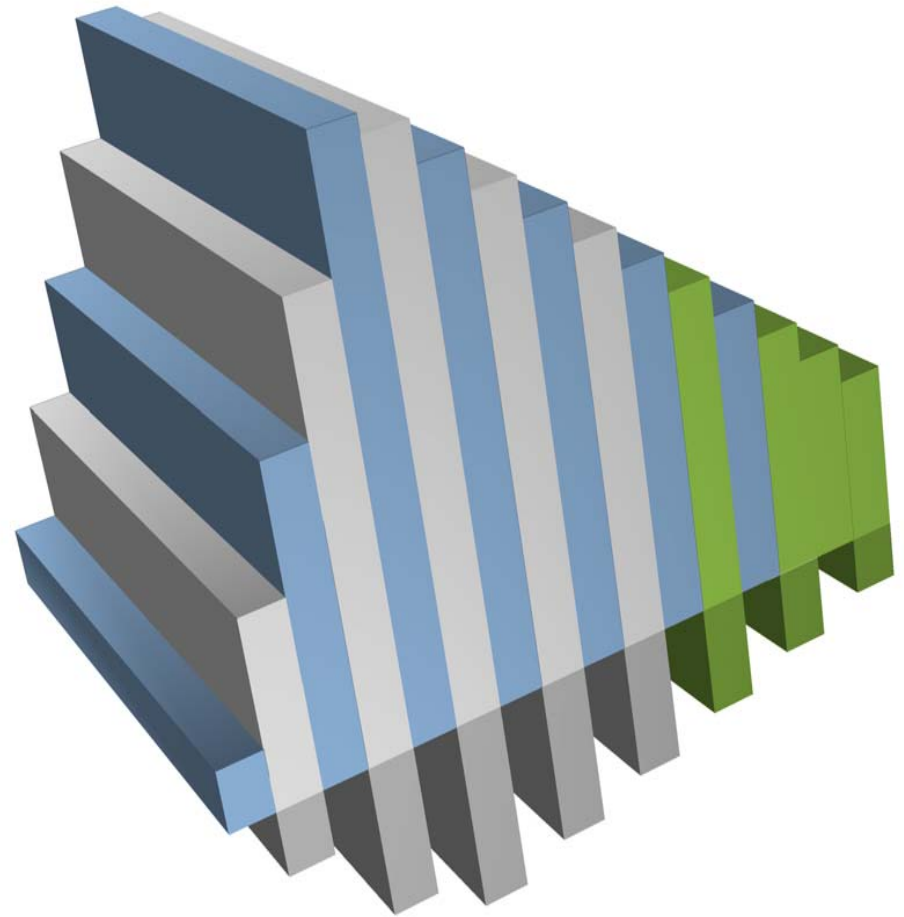
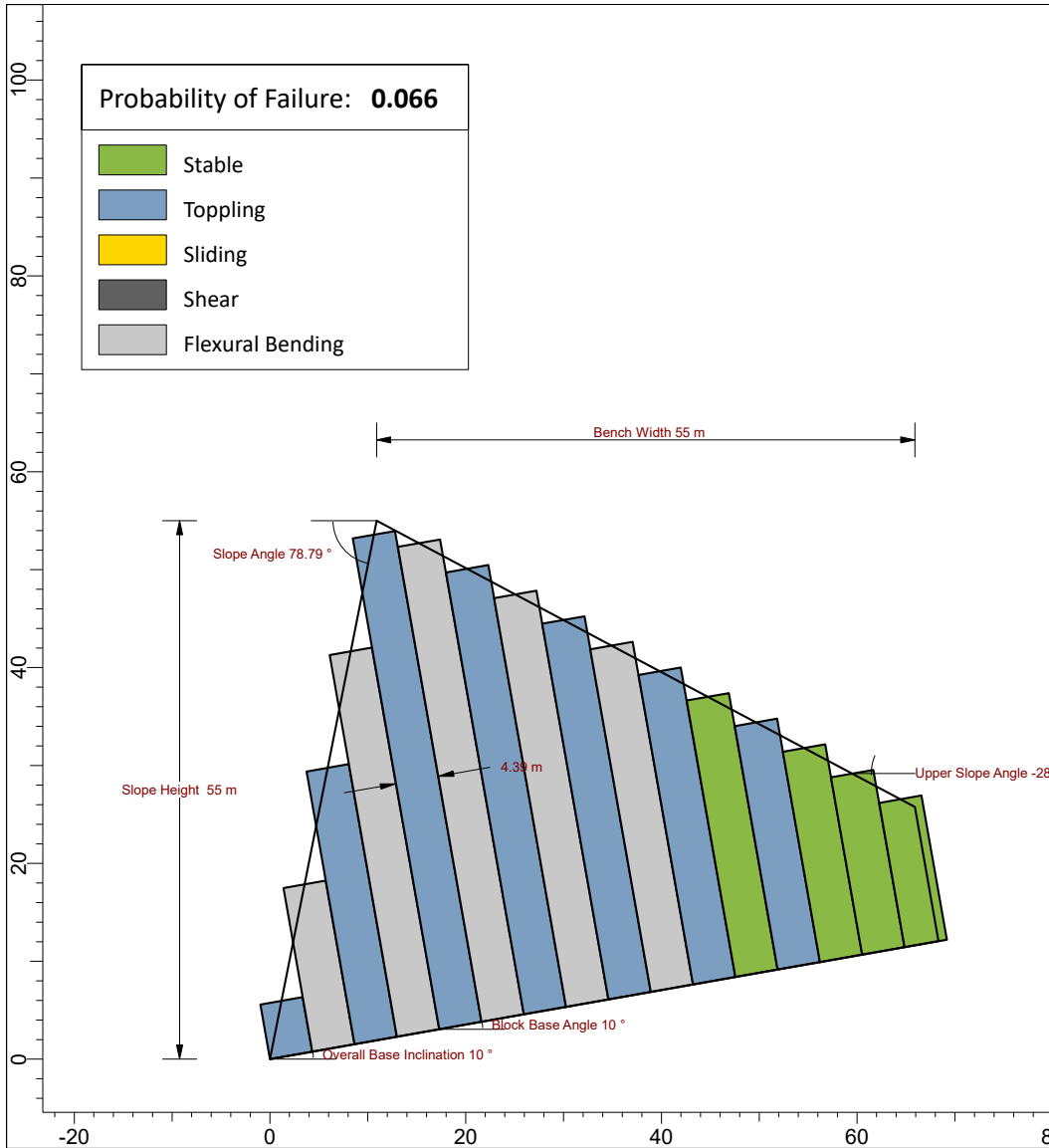



<i>Project</i>	SWEDGE - Surface Wedge Stability Analysis		
<i>Analysis Description</i>	D3_2 - Wedge Sliding - Overhanging		
<i>Drawn By</i>	Kara Stariha	<i>Company</i>	
<i>Date</i>	26.11.2020, 08:08:23	<i>File Name</i>	D3_2.swd7

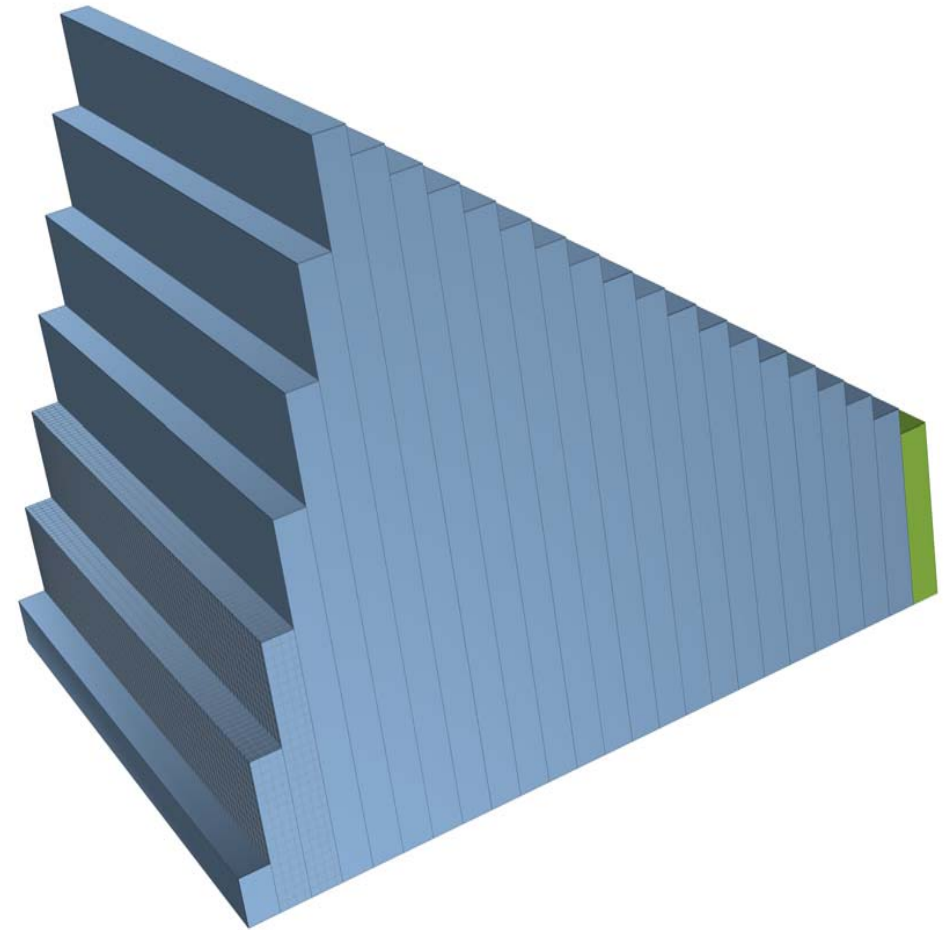
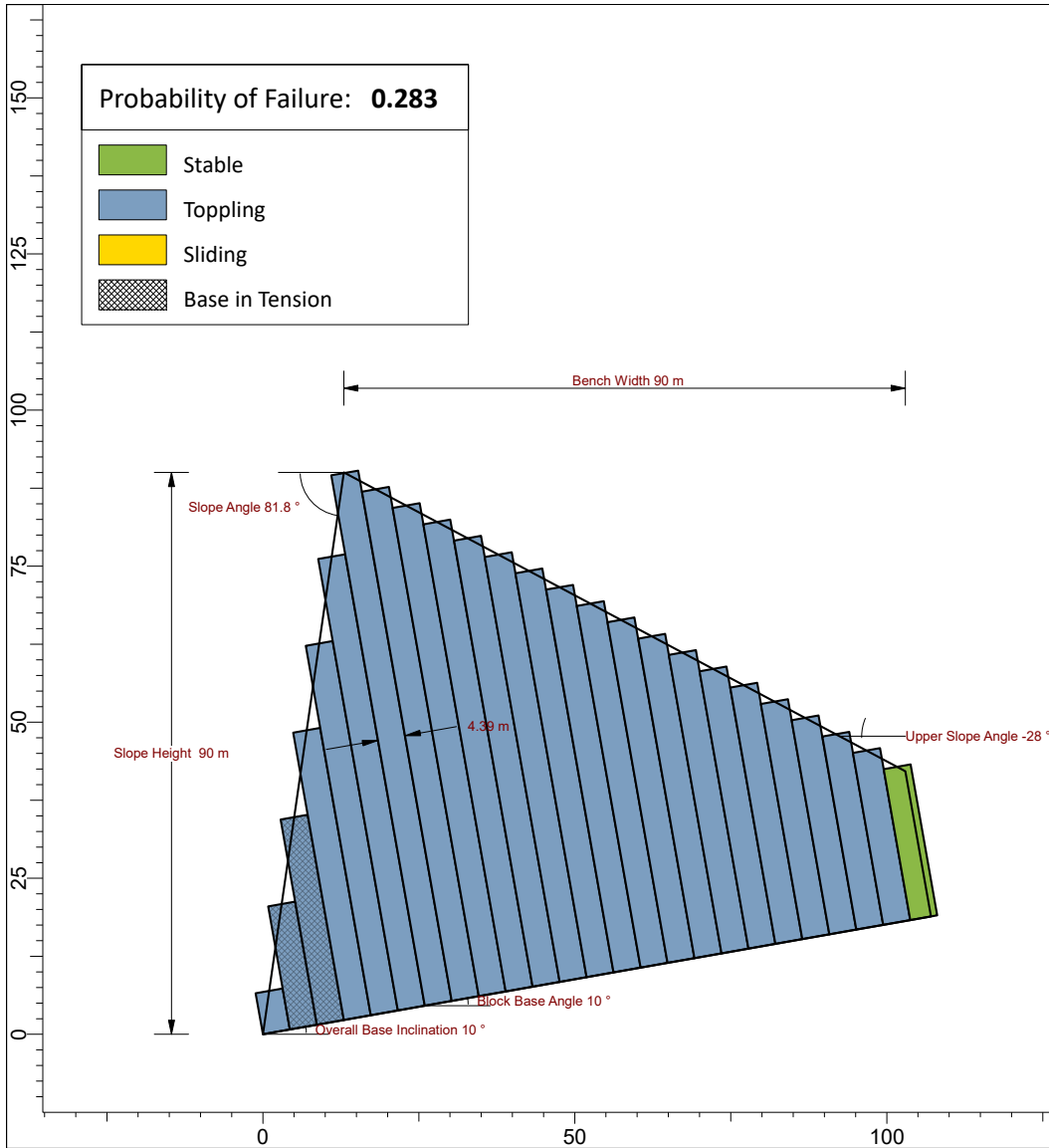
Appendix E – RocTopple Probabilistic Assessment




	Project			ROCTOPPLE - Rock Toppling Analysis
	Analysis Description			D1 - Direct Topple
	Drawn By		Kara Stariha	Company
	Date		28.11.2020, 12:37:00	File Name
ROCTOPPLE 2.003				D1_Topple.rtop



	Project	ROCTOPPLE - Rock Toppling Analysis	
	Analysis Description	D1 - Flexural Topple	
	Drawn By	Kara Stariha	Company
	Date	28.11.2020, 12:37:00	File Name

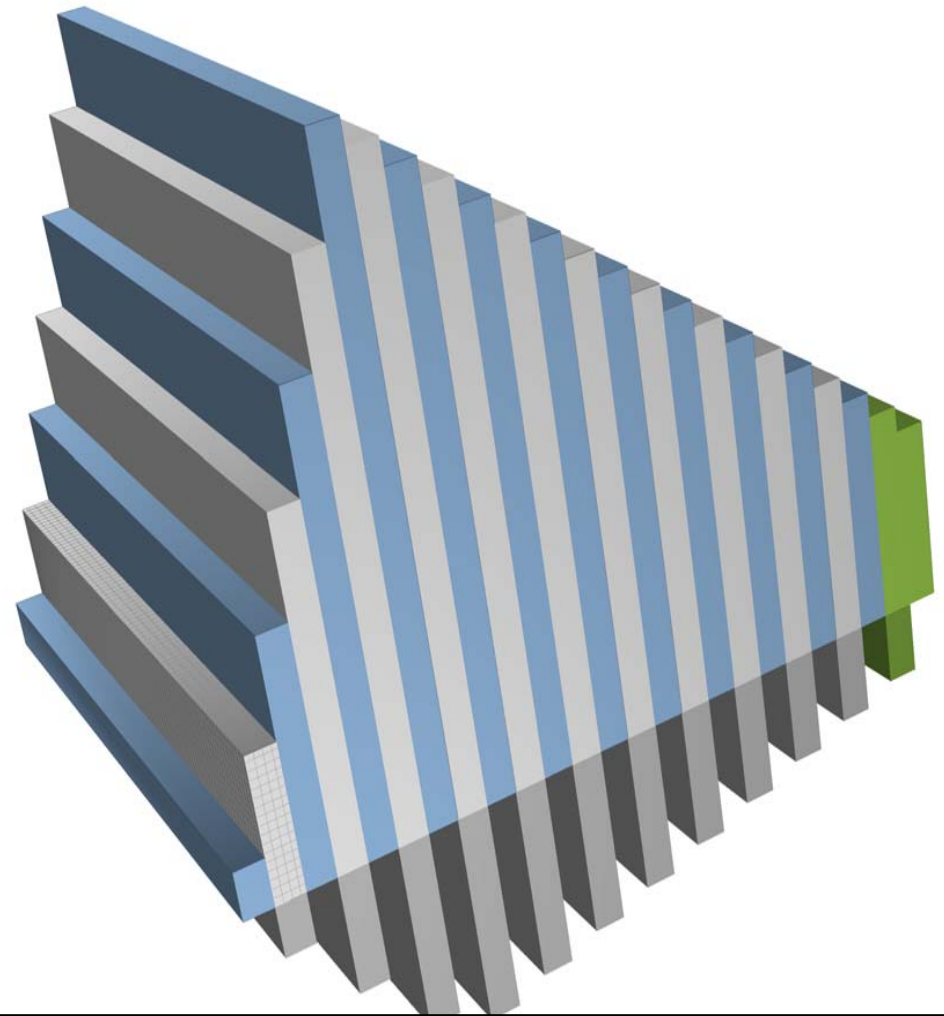
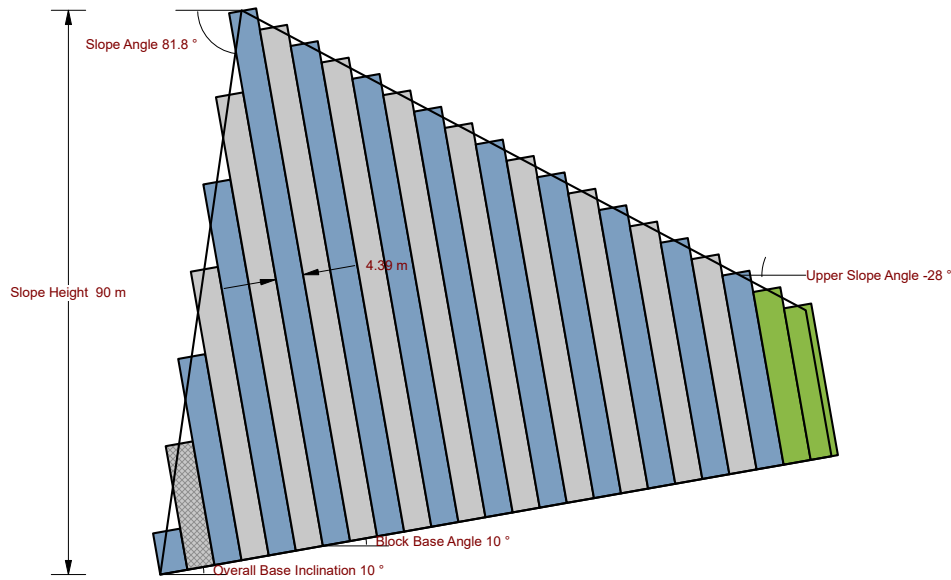


	Project		ROCTOPPLE - Rock Toppling Analysis	
	Analysis Description		D2 -Direct Topple	
	Drawn By	Kara Stariha	Company	
	Date	28.11.2020, 12:37:00	File Name	D2_Topple.rtop

Probability of Failure: **0.227**

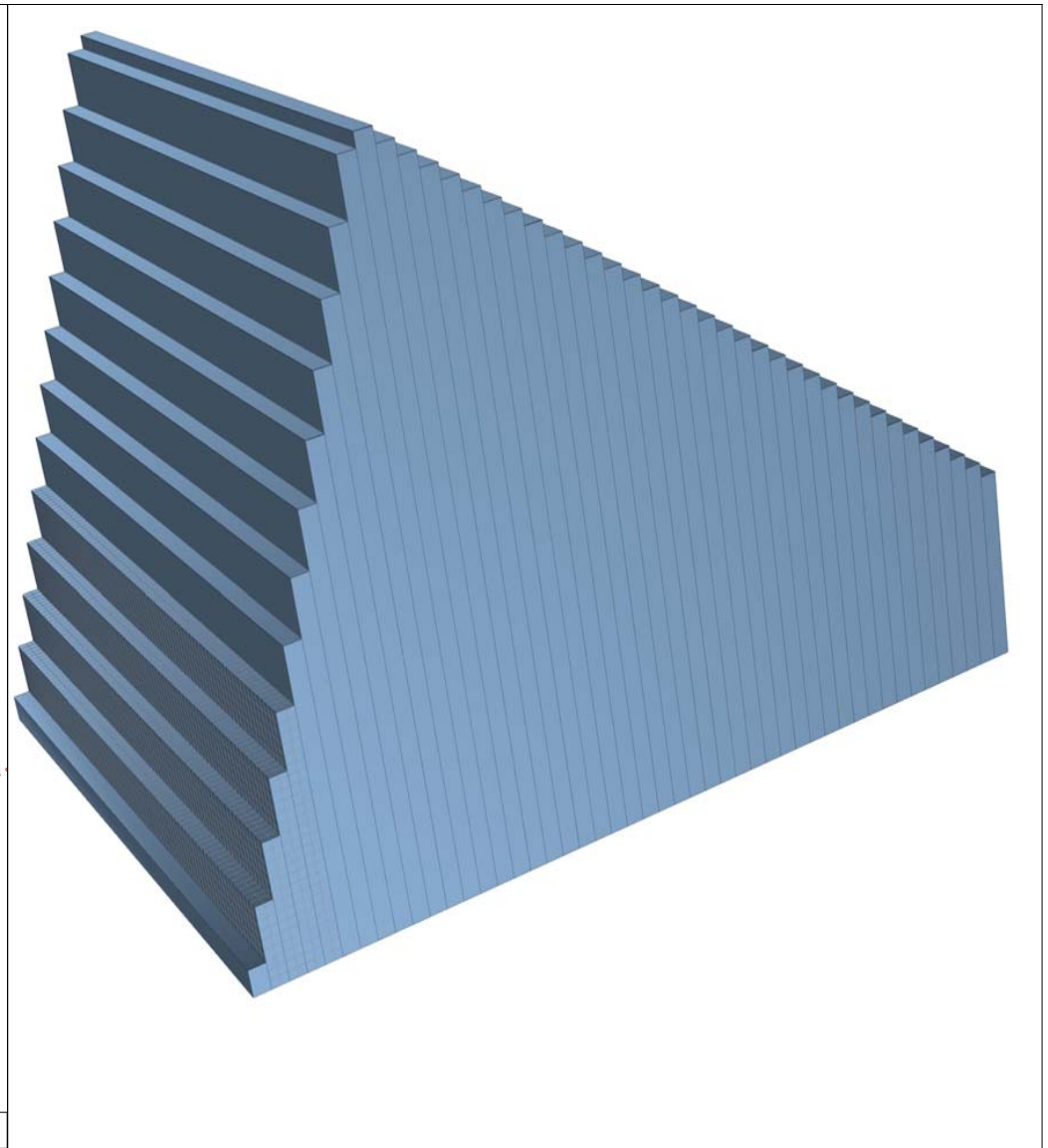
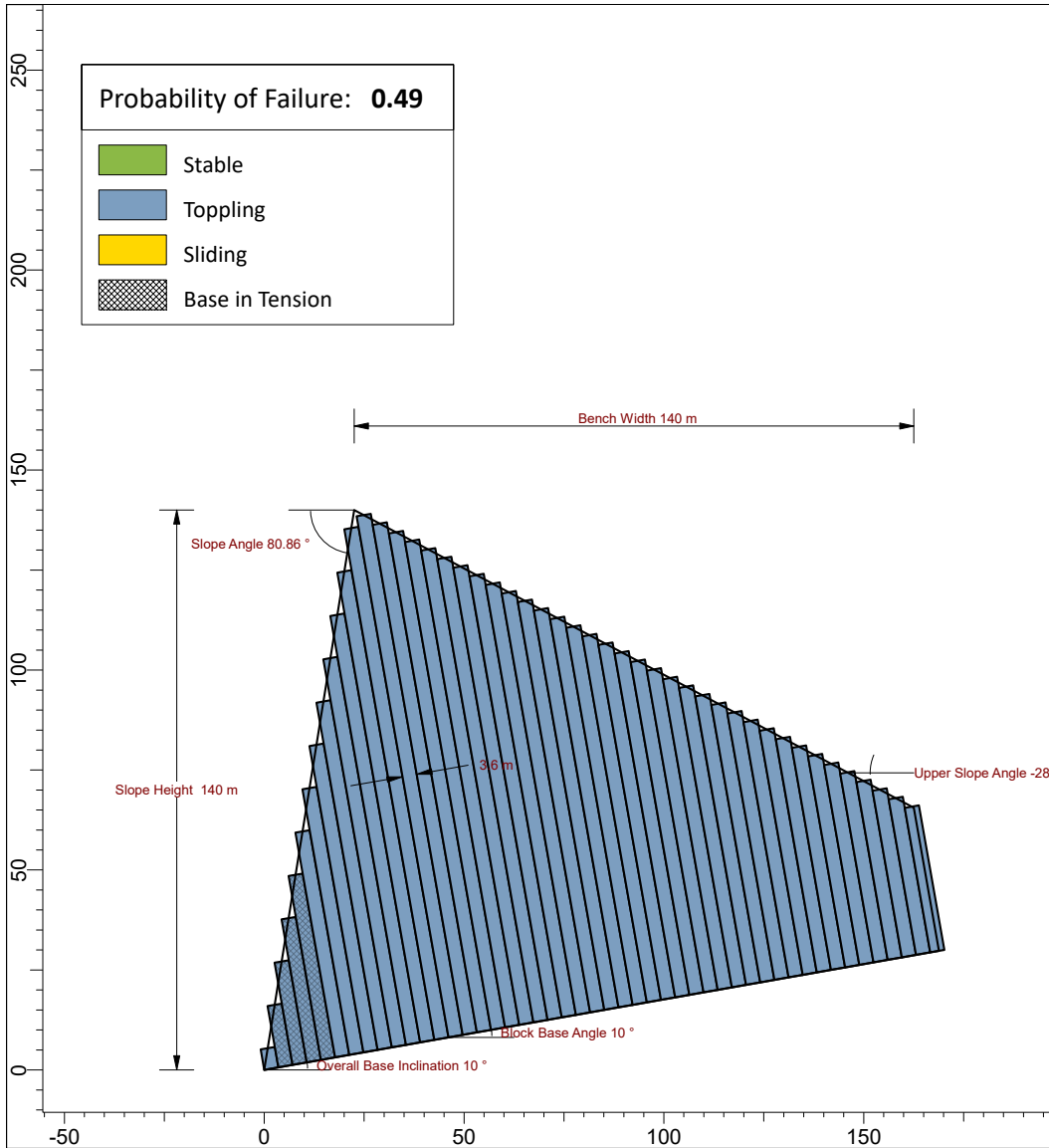
- Stable
- Toppling
- Sliding
- Shear
- Flexural Bending
- Base in Tension


Bench Width 90 m

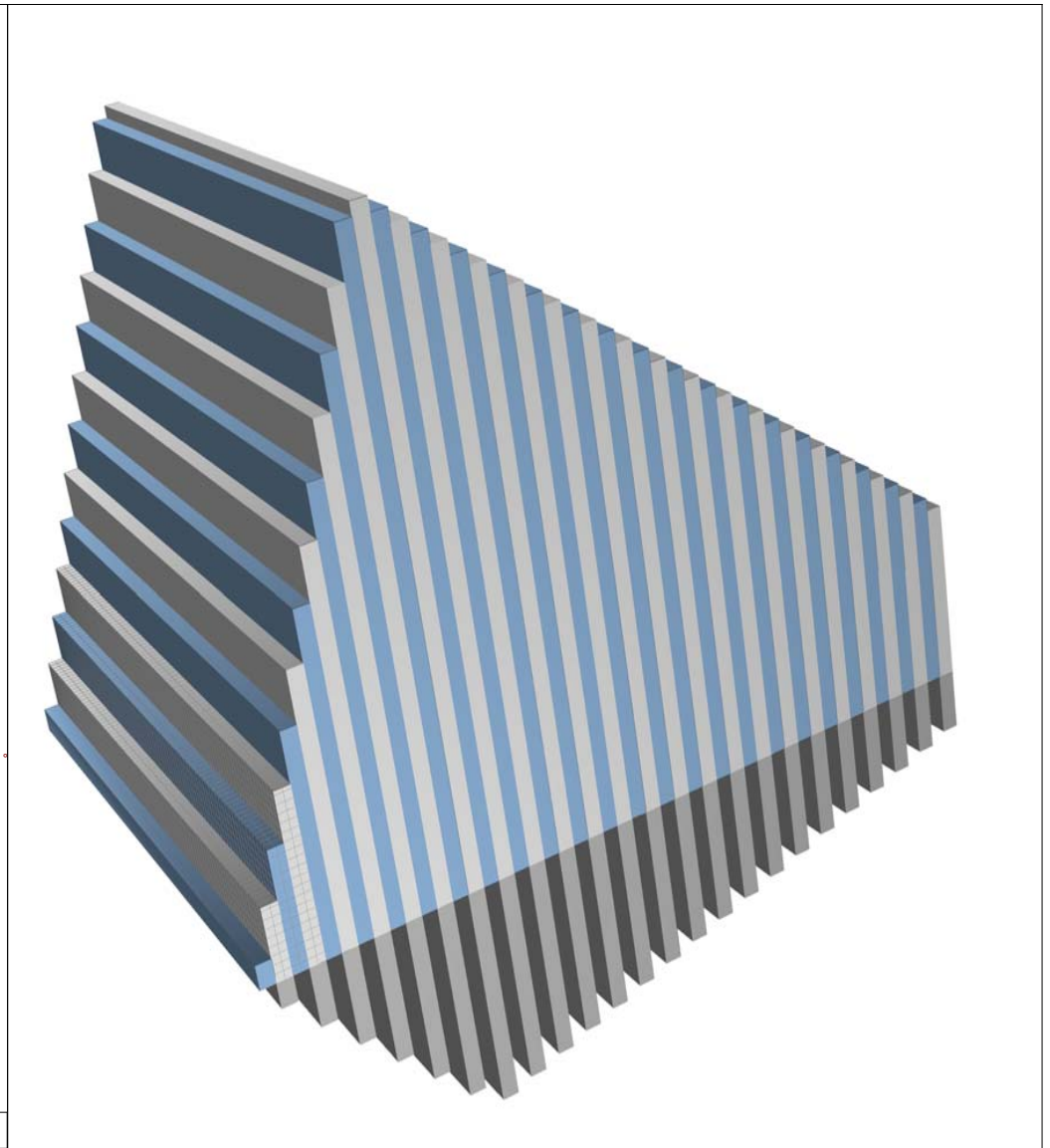
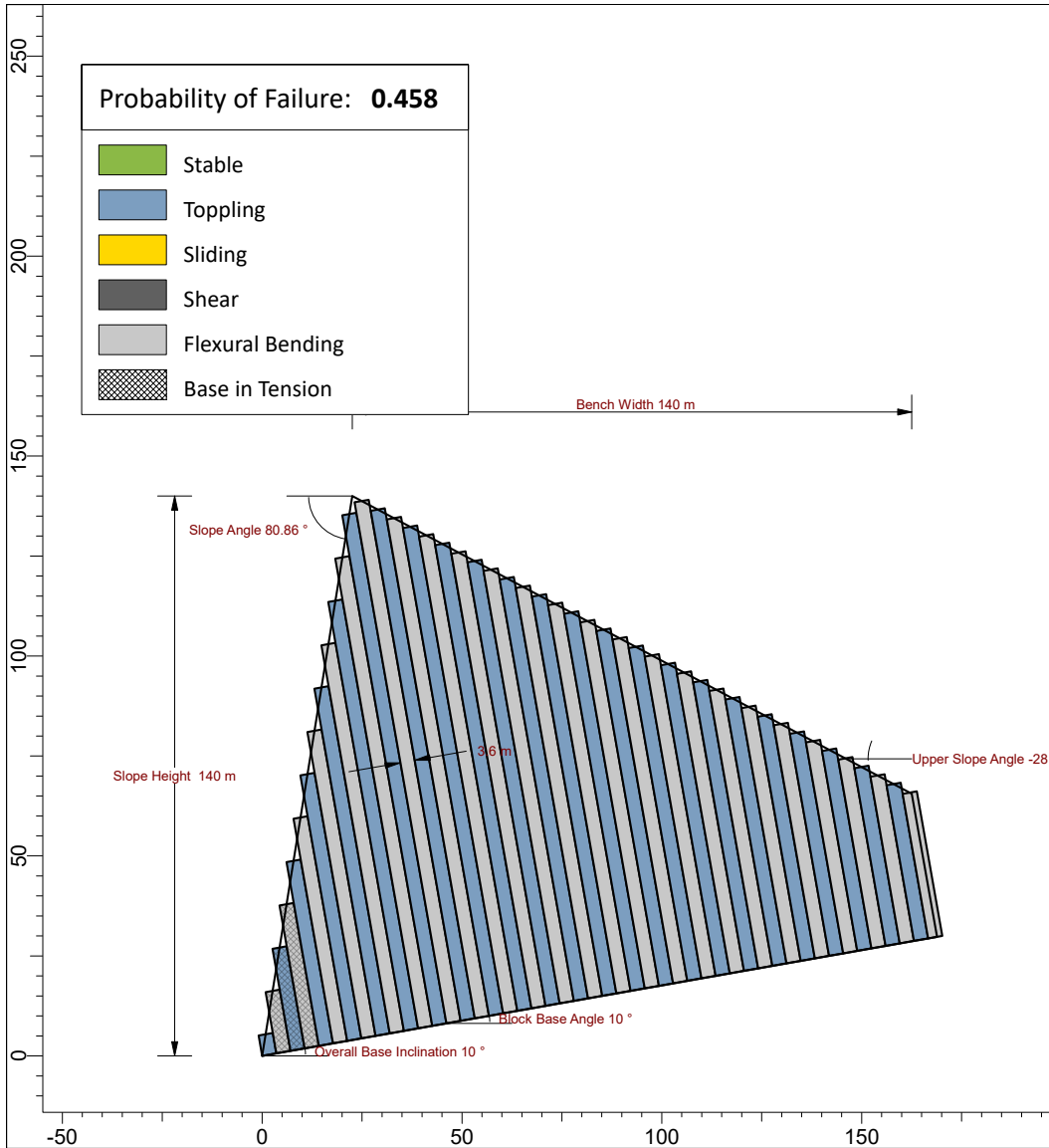



ROCTOPPLE 2.003

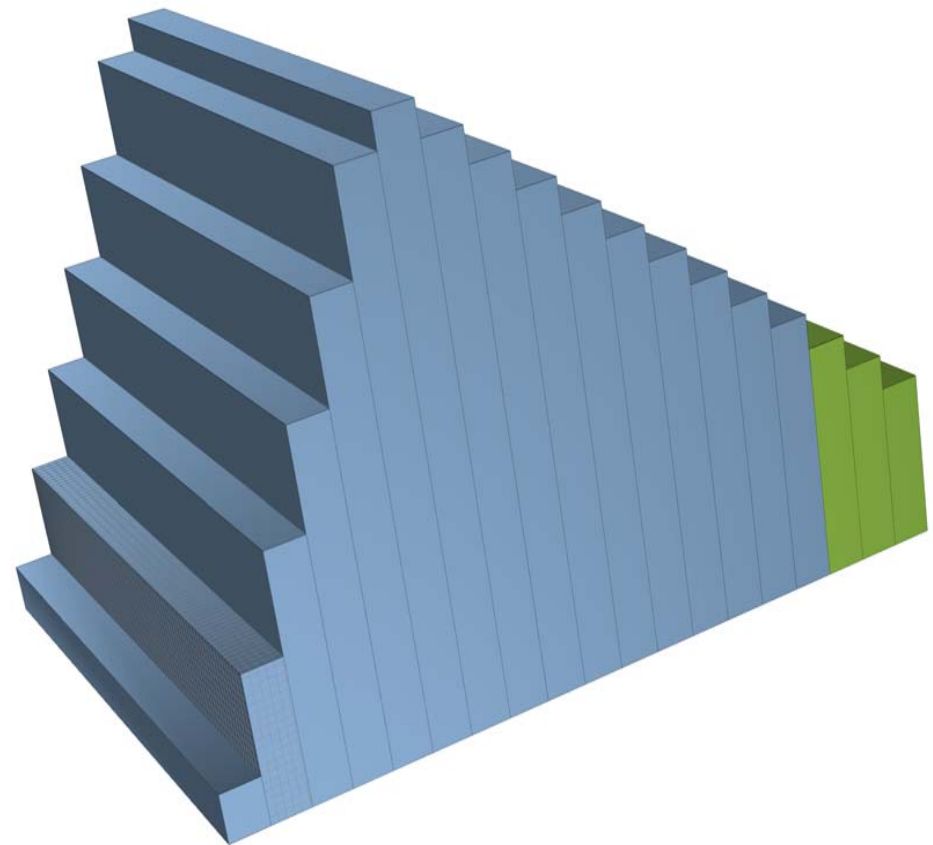
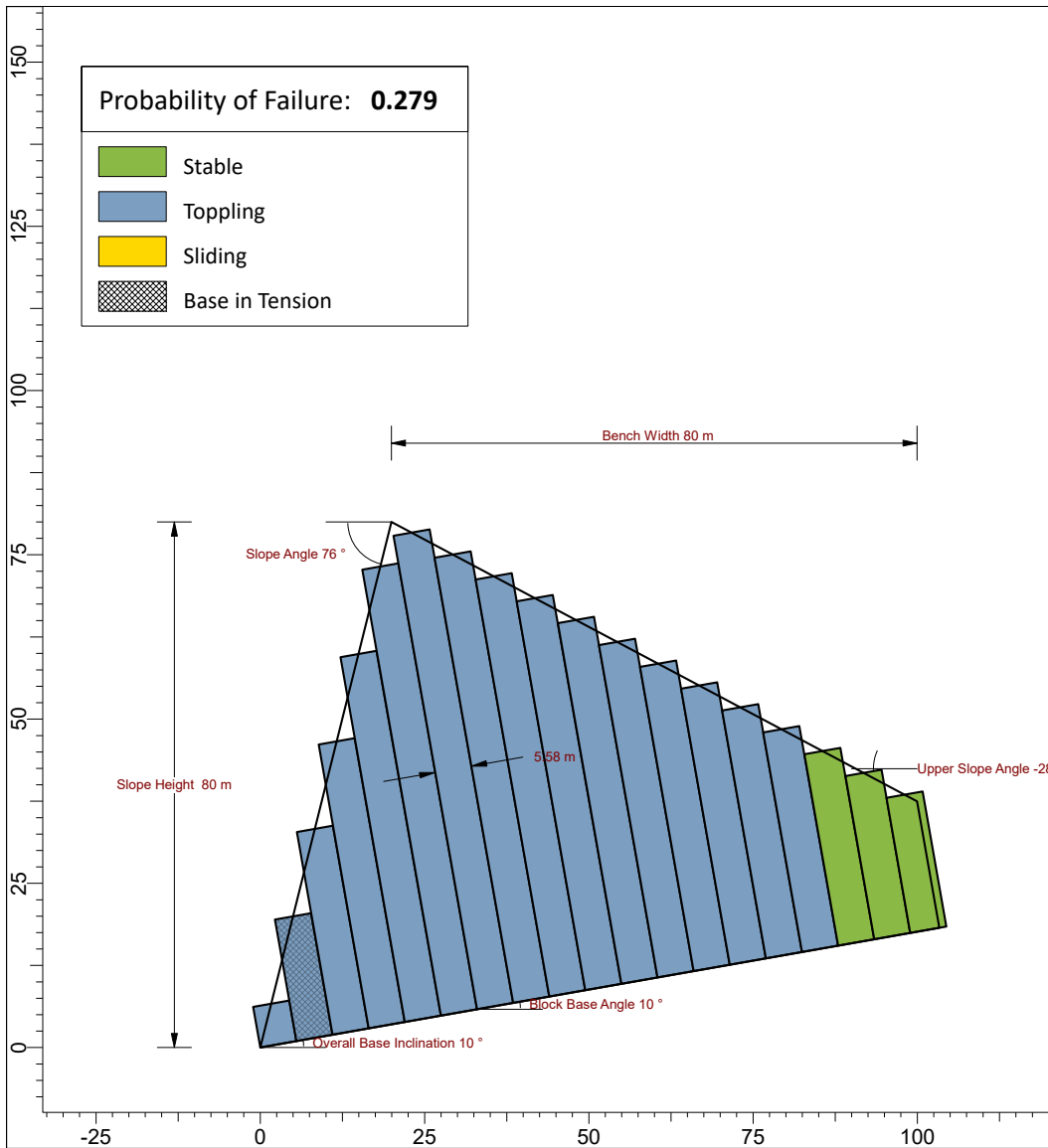
<i>Project</i>	ROCTOPPLE - Rock Toppling Analysis		
<i>Analysis Description</i>	D2 - Flexural Topple		
<i>Drawn By</i>	Kara Stariha	<i>Company</i>	
<i>Date</i>	28.11.2020, 12:37:00	<i>File Name</i>	D2_Topple.rtop




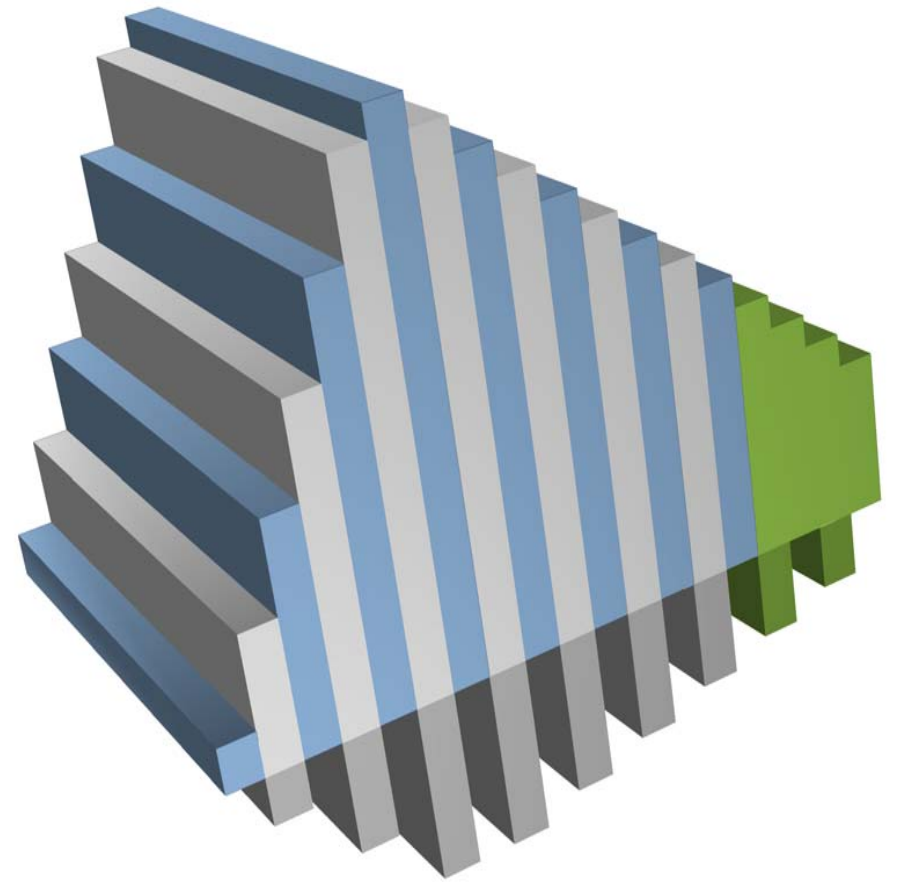
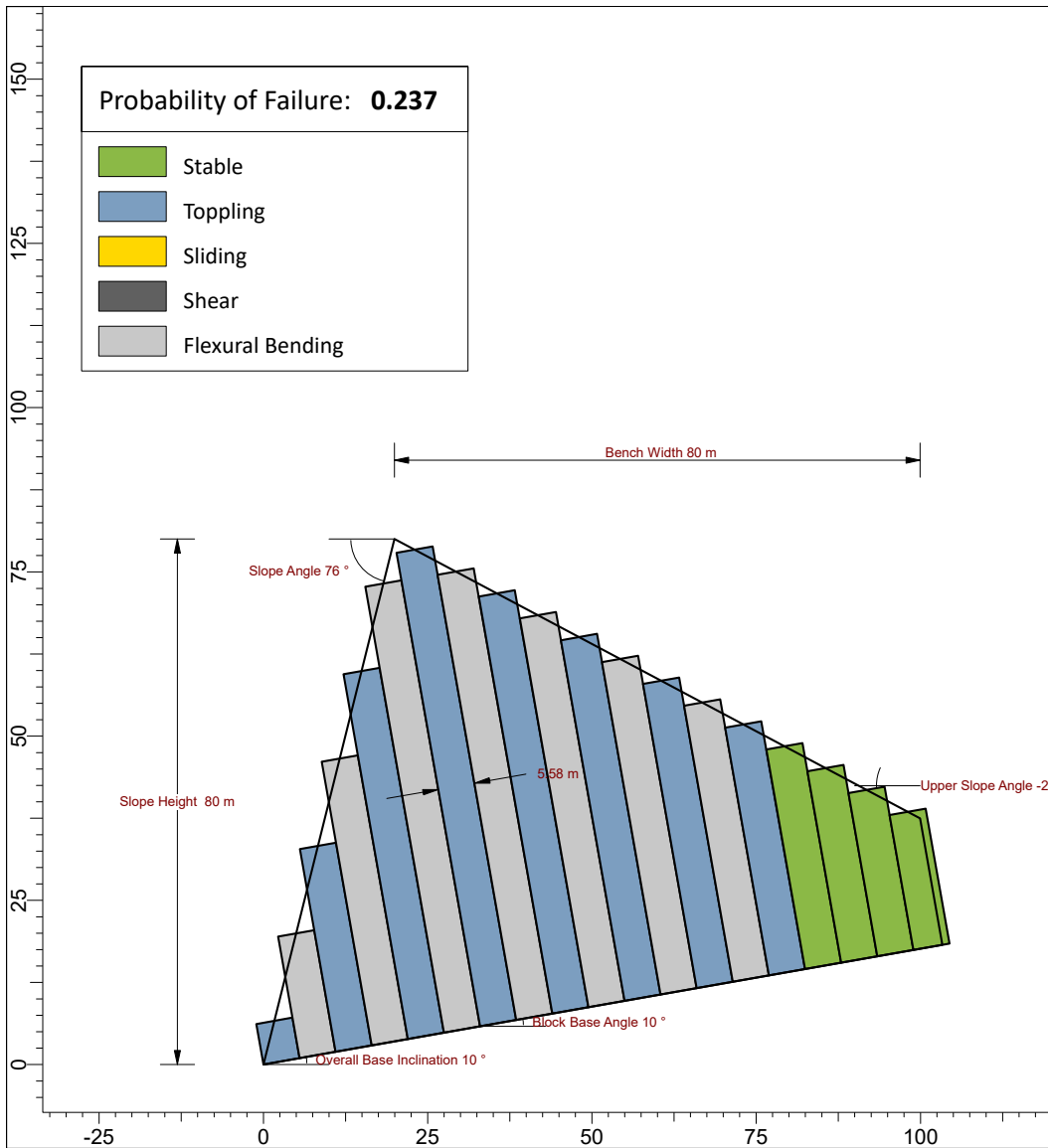
	Project	ROCTOPPLE - Rock Toppling Analysis	
	Analysis Description	D3 -Direct Topple	
	Drawn By	Kara Stariha	Company
	Date	28.11.2020, 12:37:00	File Name




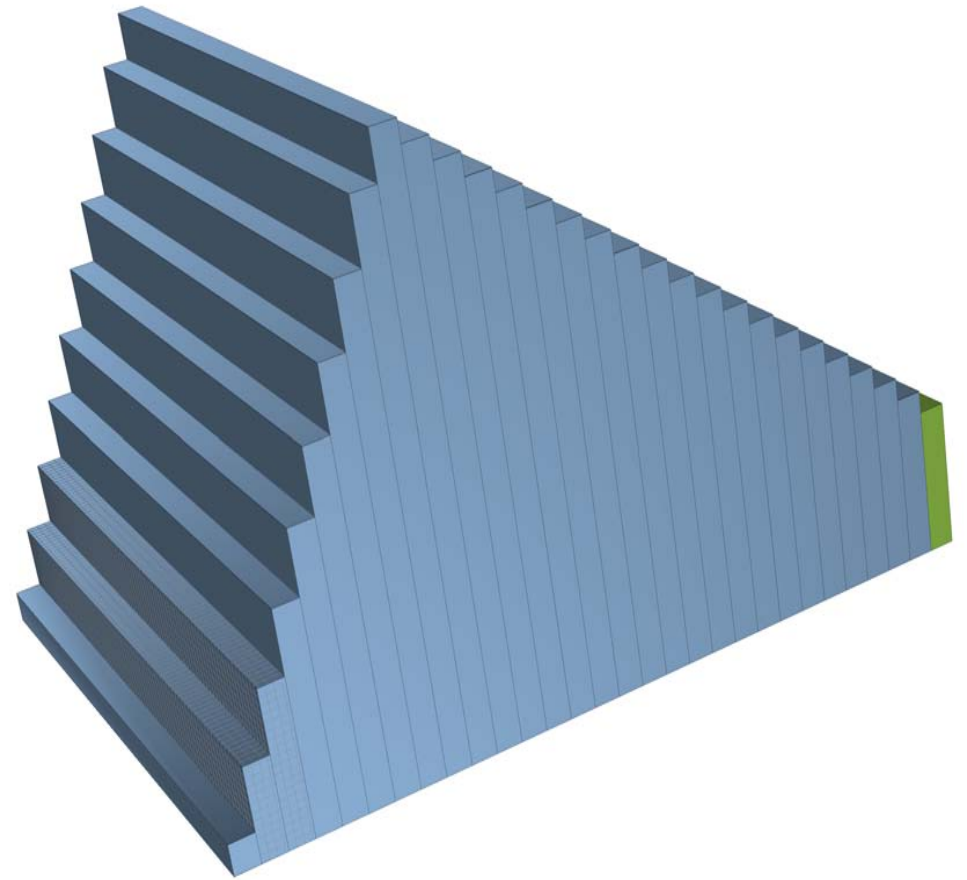
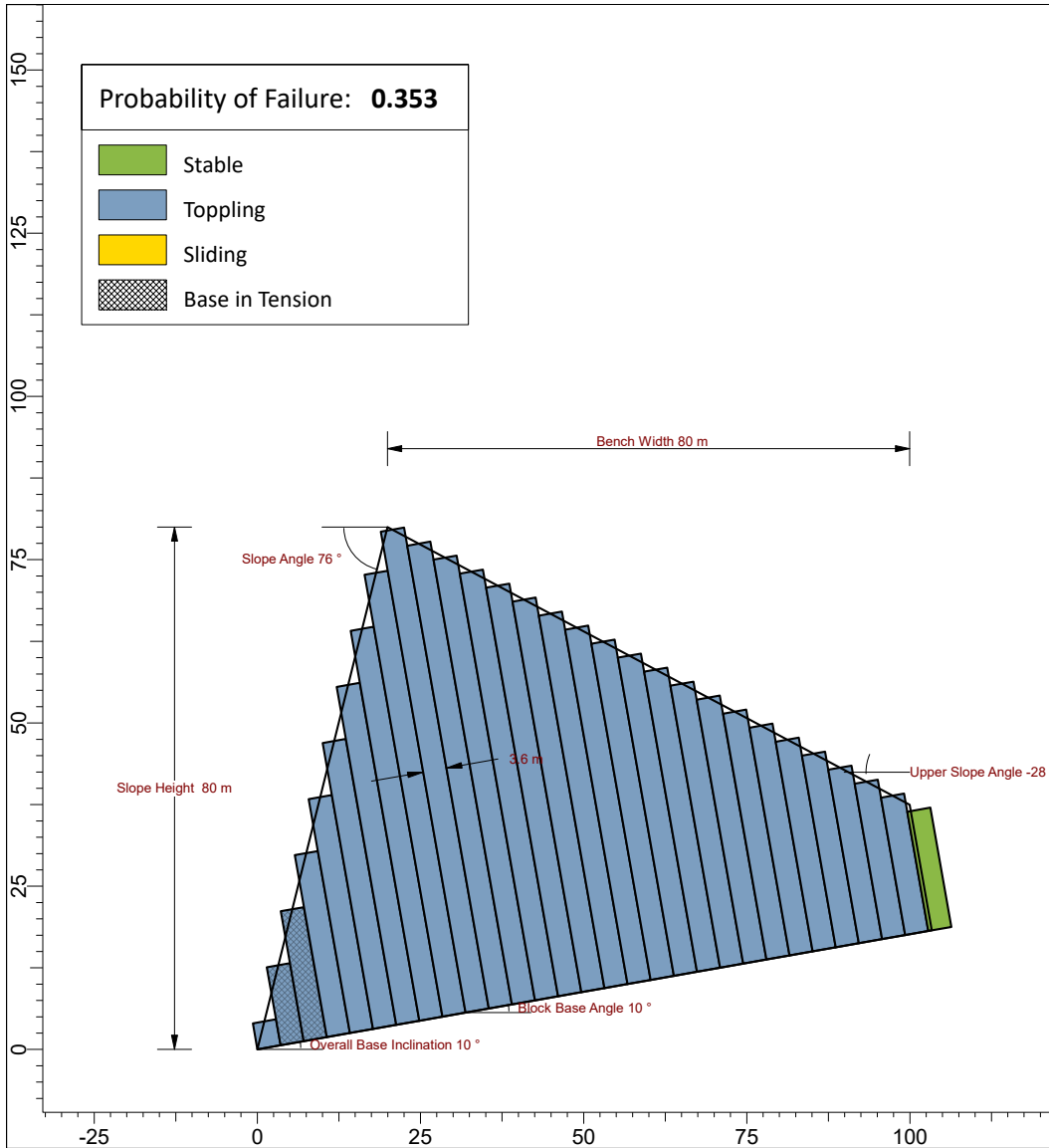
	Project		ROCTOPPLE - Rock Toppling Analysis
	Analysis Description		D3 - Flexural Topple
	Drawn By	Kara Stariha	Company
	Date	28.11.2020, 12:37:00	File Name




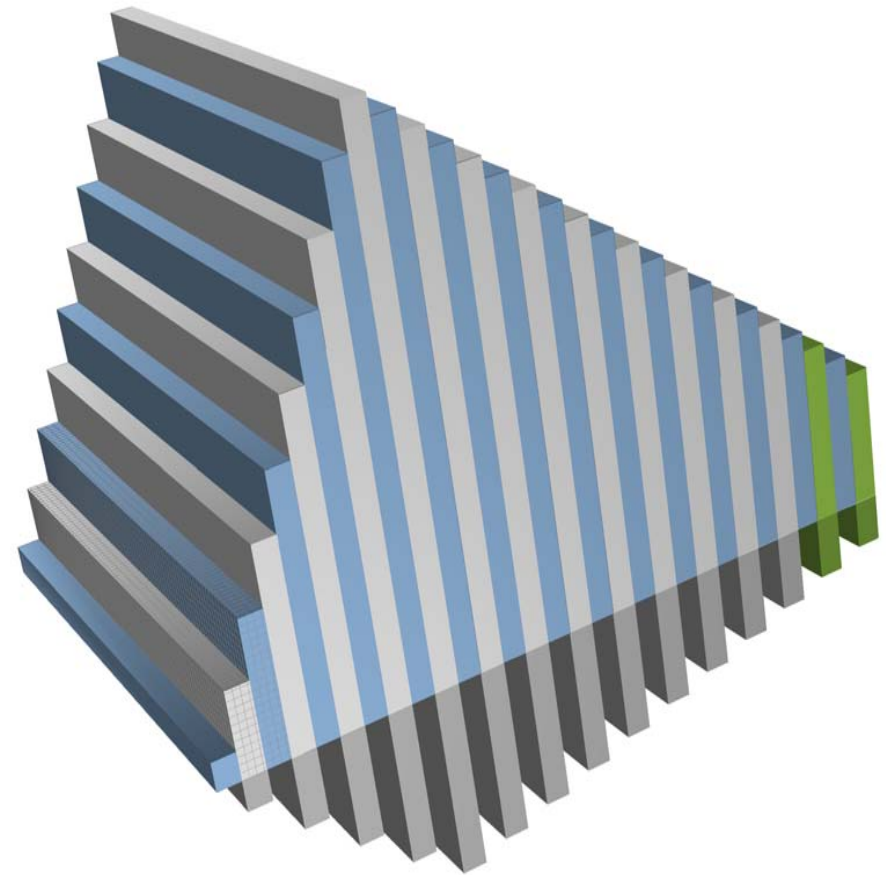
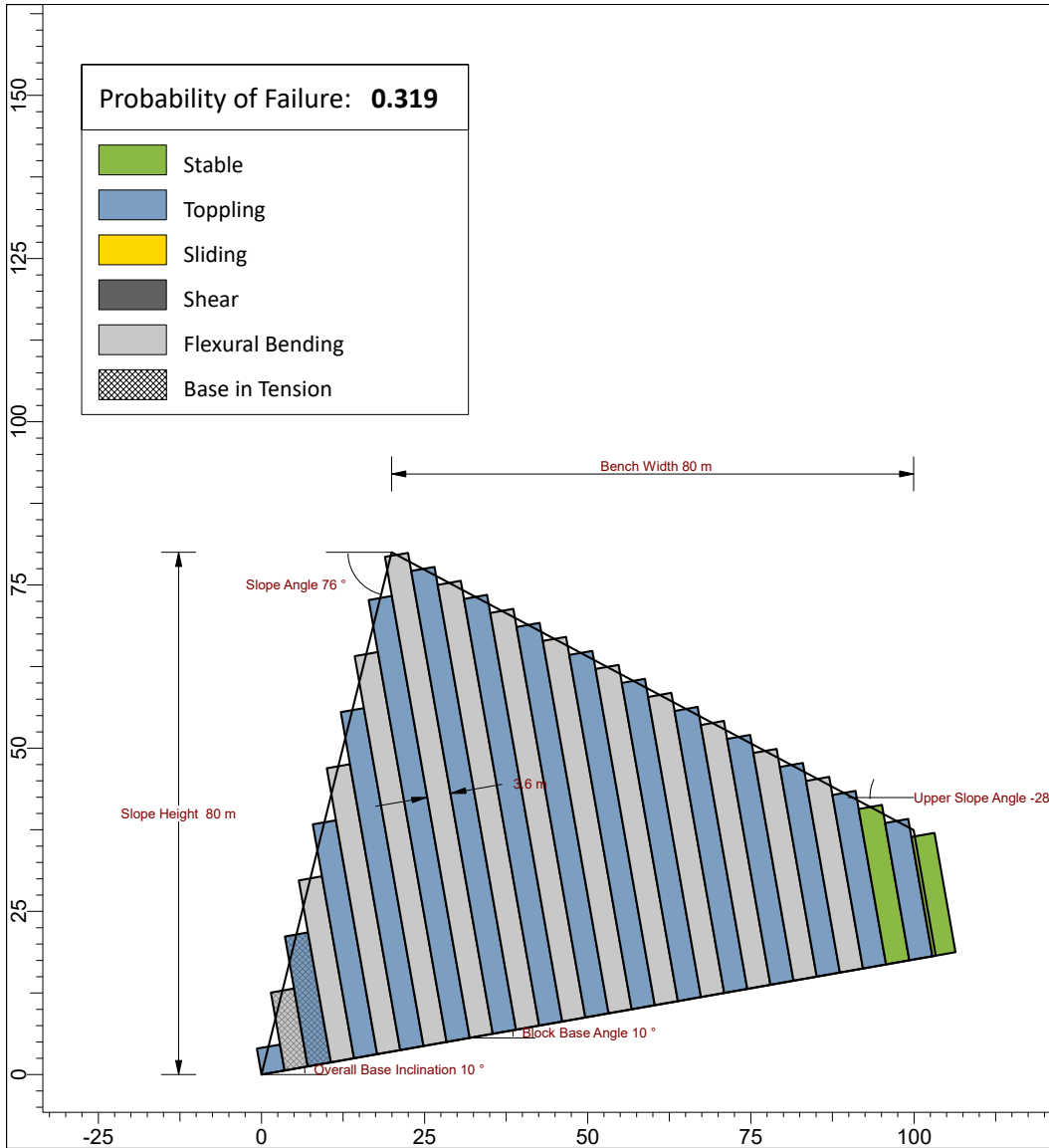
	Project	ROCTOPPLE - Rock Toppling Analysis	
	Analysis Description	D4_J1 -Direct Topple	
	Drawn By	Kara Stariha	Company
	Date	28.11.2020, 12:37:00	File Name



	Project ROCTOPPLE - Rock Toppling Analysis
	Analysis Description D4_J1 - Flexural Topple
	Drawn By Kara Stariha
	Date 28.11.2020, 12:37:00
	Company
	File Name D4_J1_Topple.rtop



	Project	ROCTOPPLE - Rock Toppling Analysis	
	Analysis Description	D4_J3 - Block Topple	
	Drawn By	Kara Stariha	Company
	Date	28.11.2020, 12:37:00	File Name



	Project	ROCTOPPLE - Rock Toppling Analysis	
	Analysis Description	D4_J3 - Flexural Topple	
	Drawn By	Kara Stariha	Company
	Date	28.11.2020, 12:37:00	File Name